DESY 96-204
September 1996
ISSN 0418-9833

Photoproduction of Jets at HERA in Next-To-Leading Order QCD

M. Klasen
II. Institut für Theoretische Physik
Universität Hamburg
D - 22761 Hamburg, Germany

Abstract

Photoproduction of jets is one of the most important processes investigated at the electron-proton collider HERA. It not only allows to test the theory of strong interactions, quantum chromodynamics (QCD), but it also permits to measure the proton and photon structure functions with high precision. This requires exact theoretical predictions for the observed one- and two-jet cross sections. These cross sections are given here for the first time for direct and resolved photoproduction in next-to-leading order of perturbation theory. We present the complete analytical results for the Born terms, the virtual, and the real corrections. Here, we use the phase space slicing method to separate singular and regular regions of phase space by an invariant mass cut. In this way, all soft and collinear singularities can be either cancelled, or absorbed into the structure functions. Using a flexible Monte Carlo program, we evaluate the cross sections numerically and compare them to data from the experiments H1 and ZEUS.

Contents

1 Introduction **1**

2 Photoproduction of Jets at HERA **5**

2.1 Photon Spectrum in the Electron 6

2.2 Parton Distributions in the Proton 9

2.3 Parton Distributions in the Photon 13

2.4 Jet Definitions 18

2.5 Hard Photoproduction Cross Sections 22

3 Leading Order Cross Sections **27**

3.1 Phase Space for Two-Particle Final States 28

3.2 Born Matrix Elements for Direct Photons 29

3.3 Born Matrix Elements for Resolved Photons 30

4 Next-To-Leading Order Cross Sections **33**

4.1 Virtual Corrections 34

4.1.1 Virtual Corrections for Direct Photons 35

4.1.2 Virtual Corrections for Resolved Photons 37

4.2 Real Corrections 40

4.2.1 Phase Space for Three-Particle Final States 42

4.2.2 Final State Corrections for Direct Photons 44

4.2.3 Final State Corrections for Resolved Photons 47

4.2.4 Phase Space for Three-Particle Final States Revisited 52

4.2.5 Photon Initial State Corrections for Direct Photons 54

4.2.6 Proton Initial State Corrections for Direct Photons 57

4.2.7 Photon Initial State Corrections for Resolved Photons 60

4.2.8 Proton Initial State Corrections for Resolved Photons 66

4.3 Finite Next-To-Leading Order Cross Sections 67

5 Numerical Results **71**

5.1 Check of the Analytical Results 73

5.2 Renormalization- and Factorization-Scale Dependences 78

5.3 One-Jet Cross Sections 84

5.4 Two-Jet Cross Sections 91

5.5 Comparison to H1 and ZEUS Data 98

6 Summary and Outlook **103**

Acknowledgements **105**

A Phase Space Integrals for Final State Singularities **107**

B Phase Space Integrals for Initial State Singularities **109**

References **122**

List of Figures **124**

List of Tables **125**

1 Introduction

Since the beginning of operation in 1992, the electron-proton collider HERA at DESY in Hamburg has produced a wide range of results on the physics of elementary particles and fundamental interactions. One of the most interesting classes of events that was studied by the experiments H1 and ZEUS is the photoproduction of jets, where the electron and the proton interact through a photon with small virtuality $Q^2 \simeq 0$ [Ahm92, Ahm93, Abt93, Aid96, Der92, Der94, Der95, Der95a, Der95b, Der96, Der96a]. The importance of this process is due to the facts that the event rates are largest at small Q^2 and that the debris of hadrons in the final state can be well observed. Real photons provide a tool complementary to virtual photons in deep inelastic scattering and are well suited to investigate the structure of the proton. On the other hand, real photons can dissolve so that one can also study the photon structure at HERA. This complements the information obtained from deep inelastic $\gamma\gamma^*$ scattering at e^+e^- colliders.

The modern fundamental theory for microscopic particles and interactions is quantum field theory. In quantum electrodynamics (QED), the electromagnetic interaction between the electron and the proton is described through a single photon exchange. The photon radiated by the electron is spacelike and almost real in photoproduction, so that the electron is only weakly deflected. Using the Weizsäcker-Williams or Equivalent Photon Approximation, one can then approximate the electron-proton cross section by a photon spectrum in the electron with point-like coupling and the photon-proton cross section [Wei34, Wil34, Wil35]. The admixture of a weak Z^0 boson to the photon, which is predicted by the electroweak Glashow-Salam-Weinberg (GSW) model, is largely suppressed and can be neglected. The same holds for multiple-photon exchange between the electron and the proton.

Due to the hadronic structure of the proton, the coupling of the photon to the proton is not point-like but an incoherent superposition of the scattering off the proton constituents. In the parton model, the proton consists of three valence quarks, which are free at the large center-of-mass energies reached at HERA ($\sqrt{s_H} \simeq 300$ GeV) [Fey69, Bjo69]. It is, however, well-known that the quarks in the proton are bound by gluons (the gauge particles of the strong interaction) and surrounded by a virtual quark sea. Thus, the parton model is improved by quantum chromodynamics (QCD). The partons in the proton, that do not participate in the hard scattering process, form a so-called remnant or spectator jet. It has only little transverse energy and stays mostly in the proton beam pipe.

In a non-abelian gauge theory like QCD, it is possible that the gluons couple not only to the quarks, but also to themselves. An important consequence is the asymptotic freedom of QCD [tHo72a, Gro73, Pol73]. It allows the application of perturbation theory not only to QED but also to QCD, since the strong coupling constant α_s is small at large energies. Perturbative QCD is, however, no longer valid at hadronic scales. Therefore, every hadronic scattering process must be separated into a non-perturbative part at large distances and a perturbative part at small distances through an artificial factorization scale. The perturbative part is calculable from partonic Feynman diagrams and scattering matrix elements. The non-perturbative parton densities in the proton can be parametrized with the Altarelli-Parisi method [Par76, Alt77]. Similarly, the transformation of scattered partons in the final state into hadrons can be described with so-called fragmentation functions. However, we consider in this study not specific hadrons but beams of partons or hadrons, i.e. jets with large transverse momenta.

As the fundamental gauge boson of QED, the photon couples directly to the charged elementary particles like leptons and quarks. It can, however, also exhibit hadronic properties and dissolve into quarks and gluons, which then interact with the partons in the proton. Both contributions are of the same order in perturbation theory and have to be added to give the complete photoproduction cross

section. Beyond leading order of perturbation theory, the distinction between direct and resolved processes becomes theoretically ambiguous, as both components are related to each other through the factorization scale at the photon leg. Experimentally, the fraction of the longitudinal momentum of the photon in the hard scattering is cut to maintain the distinction. The distribution of partons in the photon is not calculable perturbatively and is parametrized in a similar way as in the proton case. The unscattered partons in the photon will also form a remnant jet similar to the proton remnant.

A dijet event, that was observed recently with the ZEUS detector, is shown in figure 1. The right side of the plot only contains the tracks of the two hard jets and the proton remnant jet to the left, but no track to the right. Since there is no photon remnant, this is a direct photon event. The transverse energies of the jets are $E_T = 40$ GeV and $E_T = 34$ GeV. Figure 2 shows a recent resolved photoproduction event from the ZEUS collaboration. One observes several tracks and energy deposition to the right, which can be identified with the photon remnant. Two jets with transverse energies of 30 GeV and 25 GeV are produced. Only 20% of the initial photon longitudinal momentum go into the hard scattering. From the typical events in figures 1 and 2 we can already see that direct photoproduction dominates at large E_T and resolved photoproduction dominates at low E_T. In the latter case, it is also more difficult to find the hard jets.

The high precision of the data, that have already been delivered or are still to be expected from HERA, requires equally high precision in the theoretical predictions which are compared to the data. This is the motivation of the calculation presented here, where existing cross sections in leading order (LO) of the strong coupling constant α_s [Owe80, Bae89] are improved considerably by next-to-leading order (NLO) corrections to these cross sections. In quantum chromodynamics, these corrections can have a very sizeable effect of up to a factor of two, as we will see especially in the case of resolved photoproduction. This is due to the dependence of these cross sections on the strong coupling α_s, which is much larger than than the electric or weak couplings even in the domain of asymptotic freedom. Furthermore, the theoretical uncertainties coming from the links between the soft (hadronic) and hard (partonic) scattering process are generally reduced in next-to-leading order of perturbation theory through reduced scale dependence and the possible implementation of a jet algorithm.

Higher order corrections in quantum field theory can be subdivided into virtual corrections with internal particle loops and real corrections, where an additional particle is radiated, which can eventually become soft or collinear to another particle. In the virtual corrections, one encounters ultraviolet (UV) divergencies when integrating over the internal loop momenta up to infinity. Since QCD is a renormalizable field theory, they can, however, be absorbed into the Lagrangian order by order in α_s. Theories with massless bosons like the photon in QED and the gluon in QCD have additional infrared (IR) divergencies at the lower end of the loop integration. Similar singularities occur in the real corrections, when the emitted particle has infinitely low energy or two particles become collinear. For the case of QED it has been proven, that the virtual and real infrared singularities have to cancel [Blo37, Nor37, Yen61]. A similar mechanism applies for QCD, if only so-called "infrared safe" quantities are calculated or measured [Kin62, Lee64]. However, collinear singularities in the initial state will not necessarily cancel. They must then be absorbed into the parton densities in the photon and the proton. This is stated in the factorization theorem [Pol77, Pol77a, Ell78, Ell79, Ama78, Ama78a, Lib79, Hum81, Hum81a], which was proven in [Mue78, Mue81, Hum82]. The redefinition of the parton densities is universal, i.e. independent of the considered process, and only specific for the hadron under consideration.

Several groups have performed next-to-leading order calculations for photoproduction in the past, mostly for inclusive single-jet cross sections. The Tallahassee collaboration of Baer, Ohnemus, and Owens published the first NLO cross sections for the direct photoproduction of one jet in 1989 [Bae89a]. They used the phase space slicing method with a collinear and a soft cut to isolate the singularities

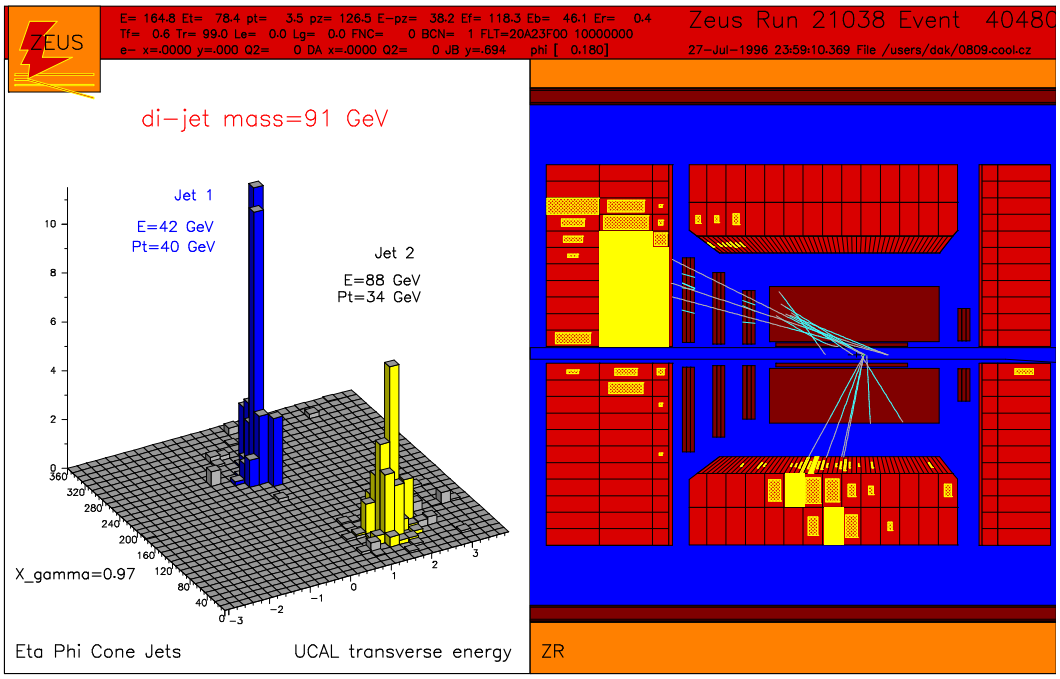

Figure 1: *A recent direct photoproduction event as seen by the ZEUS detector. Two jets with* $E_T = 40$ *GeV and* $E_T = 34$ *GeV are produced, and no hadronic cluster is seen to the right [Kra96].*

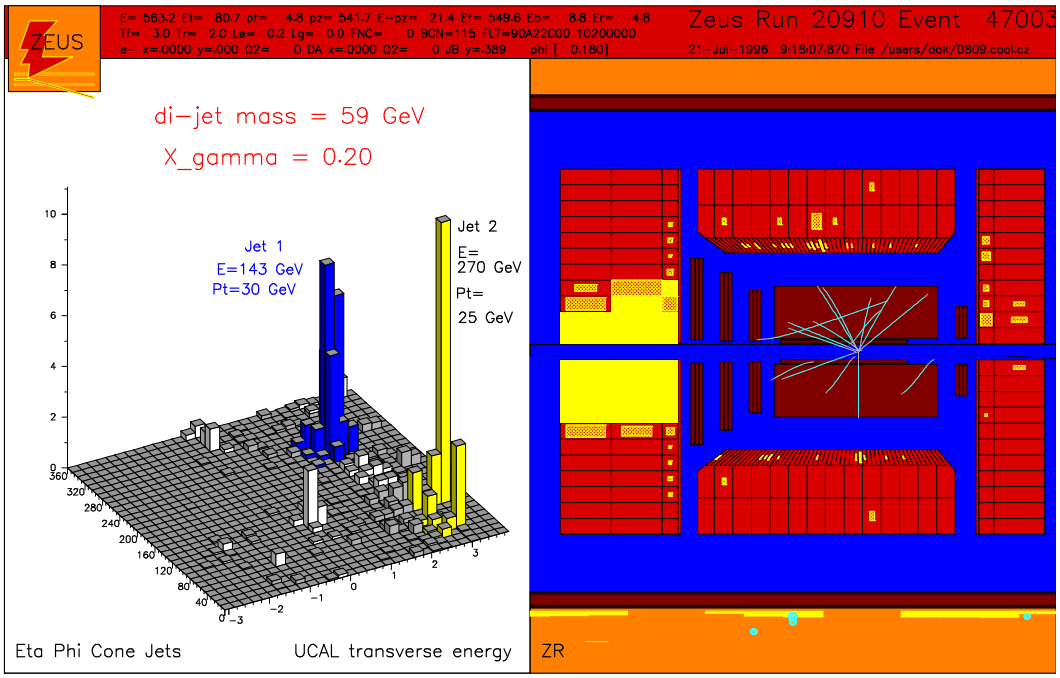

Figure 2: *A recent resolved photoproduction event as seen by the ZEUS detector. The hard jets have transverse energies of* $E_T = 30$ *GeV and* $E_T = 25$ *GeV. The tracks and the energy deposition to the right belong to the photon remnant. The fraction of longitudinal momentum from the photon in the event is only* $x_\gamma = 0.20$ *[Kra96a].*

in the real corrections. Cross sections for dijet production with direct photons were presented by Bödeker in 1992 [Böd92, Böd92a, Böd93] based on the subtraction method of Ellis, Kunszt, and Soper [Ell89, Kun92]. We calculated the same direct dijet cross section with the phase space slicing method using an invariant mass cut [Kla93, Kla95a] and compared it to data from ZEUS [Kla96]. However, this study included only leading order results for the resolved part. The same method was used by Kleinwort and Kramer for $\gamma\gamma$ collisions at e^+e^- colliders. They published a theoretical study [Kle96a] and a comparison to data from TOPAZ and AMY [Kle96]. Resolved single-jet production was first studied in next-to-leading order of QCD by Salesch in 1993 [Sal93] and then superimposed with the direct contribution [Böd94]. The complete NLO single-jet prediction was successfully compared to experimental data from H1 [Bou95] and ZEUS [Kla95]. Similar results were obtained by Gordon and Storrow in Manchester [Gor92a] and by the French collaboration of Aurenche, Fontannaz, and Guillet [Aur94a]. The results of Aurenche et al. are, however, overestimated by a factor of two in the resolved contribution [Fon96]. We present here for the first time the resolved dijet contribution and a complete calculation of direct and resolved photoproduction of one and two jets.

We organize this thesis into six main sections: After this introduction, we relate the experimental electron-proton scattering to photon-parton scattering in section 2. We derive the Weizsäcker-Williams approximation, discuss the proton and photon structure functions, and explain the experimental and theoretical properties of various jet definitions. Furthermore, section 2 contains the master formulæ for one- and two-jet cross sections. These will be calculated in section 3 in leading order and in section 4 in next-to-leading order of perturbative QCD. In both sections, we calculate the relevant phase space for $2 \to 2$ and $2 \to 3$ scattering, respectively. The Born matrix elements for direct and resolved photons are contained in section 3. In section 4 we present the virtual one-loop matrix elements and the tree-level $2 \to 3$ matrix elements, which are then integrated over singular regions of phase space. We again give the results for direct and resolved photoproduction. Next, we demonstrate how all ultraviolet and infrared poles in the next-to-leading order calculation cancel or are removed through renormalization. A detailed numerical evaluation of jet cross sections in photoproduction follows in section 5. Here, we check our analytical results numerically, study the renormalization and factorization scale dependences of the cross section, and present theoretical predictions for one- and two-jet cross sections. We also compare our results to one- and two-jet data from the H1 and ZEUS collaborations, before we draw our final conclusions in section 6.

2 Photoproduction of Jets at HERA

In this section we set up the general framework for theoretical predictions of the photoproduction of jets in electron-proton scattering. This includes the separation of the perturbatively calculable parts from the non-perturbative parts of the cross section and linking the electron-proton to photon-proton scattering. This link will be discussed first in section 2.1 and consists in the Weizsäcker-Williams or Equivalent Photon Approximation.

The framework of the QCD improved parton model for protons will be discussed in section 2.2. This is necessary, since protons are not pointlike but composed of three valence quarks and sea quarks and gluons. Perturbative QCD is not applicable at distances comparable to the size of the proton, but only at small partonic scales due to the asymptotic freedom of QCD. Therefore, the parton content of the proton is the domain of non-perturbative QCD and has to be described with universal distribution functions. The scale dependence of these functions is governed by the Altarelli-Parisi equations.

A similar concept applies for resolved photons, which are discussed in section 2.3. Contrary to direct photons, which are obviously pointlike, resolved photons can be considered to have a complicated hadronic structure like protons. However, they have a different valence structure than protons. Furthermore, a complex relationship between direct and resolved photons will show up in next-to-leading order of QCD.

Having related the initial state particles electron and proton in the experiment to the photons and partons in perturbative QCD, we can turn our attention to the final state particles. Section 2.4 describes how the interpretation of partons as jets changes from leading to next-to-leading order of QCD. Several jet definition schemes are discussed with respect to their theoretical and experimental behavior.

The last section 2.5 summarizes the different ingredients of the calculation and contains the master formulæ for one- and two-jet photoproduction. Also, the numerous analytical contributions in leading and next-to-leading order of QCD are organized in a tabular form for transparency.

2.1 Photon Spectrum in the Electron

In photoproduction, one would like to study the hard scattering of real photon beams off nuclear targets. This can be done in fixed target experiments, like NA14 at CERN [Aug86] or E683 at Fermilab [Ada94], where real photons are produced e.g. in pion decay with energies of up to 400 GeV [Pau92]. If higher energies are required, one must resort to spacelike, almost real photons radiated from electrons. This method is employed at the electron-proton collider HERA. There, electrons of energy $E_e = 26.7$ GeV produce photons with small virtuality Q^2, which then collide with a proton beam of energy $E_p = 820$ GeV. This corresponds to photon energies of up to 50 TeV in fixed target experiments.

On the theoretical side, the calculation of the electron-proton cross section can be considerably simplified by using the Weizsäcker-Williams or Equivalent Photon Approximation. Here, one uses current conservation and the small photon virtuality to factorize the electron-proton cross section into a broad-band photon spectrum in the electron and the hard photon-proton cross section. Already in 1924, Fermi discovered the equivalence between the perturbation of distant atoms by the field of charged particles flying by and the one due to incident electromagnetic radiation [Fer24]. His semi-classical treatment was then extended to high-energy electrodynamics in 1933-1935 by Weizsäcker [Wei34] and Williams [Wil34, Wil35] independently, who used a Fourier analysis to unravel the predominance of transverse over longitudinal photons radiated from a relativistic charged particle. In the fifties, Curtis [Cur56] and Dalitz and Yennie [Dal57] gave the first field-theoretical derivations and applied the approximation to meson production in electron-nucleon collisions. Chen and Zerwas used infinite-momentum-frame techniques for an extension to photon bremsstrahlung and photon splitting processes [Che75].

Let us consider the electroproduction process

$$\text{electron}(k) + \text{proton}(p) \to \text{electron}(k') + X \tag{2.1}$$

as shown in figure 3, where k, k', and p are the four-momenta of the incoming and outgoing electron

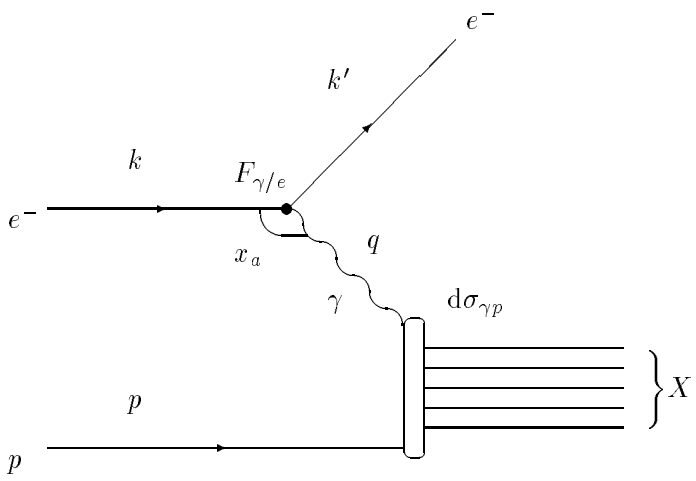

Figure 3: *Electron-proton scattering with single photon exchange.*

and the proton, respectively. X denotes a generic hadronic system not specified here. $q = k - k'$ is the momentum transfer of the electron to the photon with virtuality $Q^2 = -q^2 \simeq 0$, and the center-of-mass energy of the process is $\sqrt{s_H} = \sqrt{(k+p)^2} = 295.9$ GeV. We restrict ourselves to one-photon exchange

without electroweak Z^0 admixture. Two-photon exchange is suppressed by an additional order of α, and Z^0 exchange is suppressed by the pole in the Z^0 mass $1/m^2_{Z^0}$.

The cross section of this process is

$$\mathrm{d}\sigma_{ep}(ep \to eX) = \int \frac{1}{8k.p} \frac{e^2 W^{\mu\nu} T_{\mu\nu}}{Q^4} \frac{\mathrm{d}^3 k'}{(2\pi)^3 2E'_e}, \tag{2.2}$$

where $W^{\mu\nu}$ and $T_{\mu\nu}$ are the usual hadron and lepton tensors. Exploiting current conservation and the small photon virtuality, we find

$$W^{\mu\nu} T_{\mu\nu} = 4W_1(Q^2 = 0, q.p) \left[Q^2 \frac{1 + (1 - x_a)^2}{x_a^2} - 2m_e^2 \right], \tag{2.3}$$

where

$$x_a = \frac{q.p}{k.p} = 1 - \frac{k'.p}{k.p} \in [0, 1] \tag{2.4}$$

is the fraction of longitudinal momentum carried by the photon. Next, we have to calculate the phase space for the scattered electron. Using

$$k' = (E'_e, 0, E'_e \beta' \sin\theta, E'_e \beta' \cos\theta) \quad , \quad k = (E_e, 0, 0, E_e \beta), \tag{2.5}$$

$$\beta' = \sqrt{1 - \frac{m_e^2}{E'^2_e}} \quad , \quad \beta = \sqrt{1 - \frac{m_e^2}{E_e^2}}, \tag{2.6}$$

and integrating over the azimuthal angle, we find

$$\begin{aligned} \frac{\mathrm{d}^3 k'}{E'_e} &= 2\pi \beta'^2 E'_e \mathrm{d}k' \mathrm{d}\cos\theta \\ &= \pi \mathrm{d}q^2 \mathrm{d}x_a. \end{aligned} \tag{2.7}$$

Combining eq. (2.3) and (2.7) and integrating over the photon virtuality, we can factorize the electron-proton cross section into

$$\mathrm{d}\sigma_{ep}(ep \to eX) = \int_0^1 \mathrm{d}x_a F_{\gamma/e}(x_a) \mathrm{d}\sigma_{\gamma p}(\gamma p \to X), \tag{2.8}$$

where

$$F_{\gamma/e}(x_a) = \frac{\alpha}{2\pi} \left[\frac{1 + (1 - x_a)^2}{x_a} \ln \frac{Q^2_{\max}}{Q^2_{\min}} + 2m_e^2 x_a \left(\frac{1}{Q^2_{\min}} - \frac{1}{Q^2_{\max}} \right) \right] \tag{2.9}$$

is the renowned Weizsäcker-Williams approximation and where

$$\sigma_{\gamma p}(\gamma p \to X) = -\frac{g_{\mu\nu} W^{\mu\nu}}{8q.p} = \frac{W_1(Q^2 = 0, q.p)}{4q.p} \tag{2.10}$$

is the photon-proton cross section. We will only use the leading logarithmic contribution and neglect the second term in eq. (2.9), first calculated by Frixione et al. [Fri93].

There exist two fundamentally different experimental situations. At HERA, the scattered electron is anti-tagged and must disappear into the beam pipe. For such small scattering angles of the electron, the integration bounds $Q_{\min}$ and $Q_{\max}$ can be calculated from the equation

$$Q^2 = \frac{m_e^2 x_a^2}{1 - x_a} + \frac{E_e(1 + \beta)(A^2 - m_e^2)^2}{4A^3} \theta^2 + \mathcal{O}(\theta^4), \tag{2.11}$$

where $A = E_e(1+\beta)(1-x_a)$. Using the minimum scattering angle $\theta = 0$, we obtain

$$Q^2_{\min} = \frac{m_e^2 x_a^2}{1-x_a}, \tag{2.12}$$

which leads us to the final form of the Weizsäcker-Williams approximation used here:

$$F_{\gamma/e}(x_a) = \frac{\alpha}{2\pi}\frac{1+(1-x_a)^2}{x_a}\ln\left(\frac{Q^2_{\max}(1-x_a)}{m_e^2\ x_a^2}\right). \tag{2.13}$$

At H1 and ZEUS, the maximum virtualities of the photon are given directly as $Q^2_{\max} = 0.01$ GeV^2 and 4 GeV^2, respectively. If only the maximum scattering angle of the electron is known, we obtain

$$Q^2_{\max} = E_e^2(1-x_a)\theta^2_{\max} \tag{2.14}$$

with $\theta_{\max}$ being of the order of 5°. Except in equation (2.13), we will assume all particles to be massless in this thesis. Therefore, all results are only valid in the high-energy limit.

When no information about the scattered electron is available, one has to integrate over the whole phase space thus allowing large transverse momenta and endangering the factorization property of the cross section. Then, one only knows that the invariant mass of the produced hadronic system X has to be bounded from below, e.g. by minimal transverse momenta or heavy quark mass thresholds, which constrains the maximum virtuality of the photon only weakly. Possible choices are

$$Q_{\max} = \frac{\sqrt{s_H}}{2}, \frac{\sqrt{x_a s_H}}{2}, E_e, \cdots. \tag{2.15}$$

At e^+e^- colliders, bremsstrahlung of electrons is not the only source of almost real photons. Through the bending of the particle trajectories, beamstrahlung is produced that is quite similar to synchrotron radiation and causes a tail in the luminosity spectrum towards low energies. Even higher luminosities can be achieved by colliding the electron beam at some distance from the interaction point with a dense laser beam [Aur95].

2.2 Parton Distributions in the Proton

The first evidence that the proton has a substructure came from deep inelastic electron-proton scattering $ep \to eX$. Together with muon- and neutrino-scattering, this process provides us with information on the distribution of partons (quarks and gluons) in the proton. In the parton model, scattering off hadrons is interpreted as an incoherent superposition of scattering off massless and pointlike partons [Fey69, Bjo69]. This is shown in figure 4, where p_b is the four-momentum of the scattered parton b. If

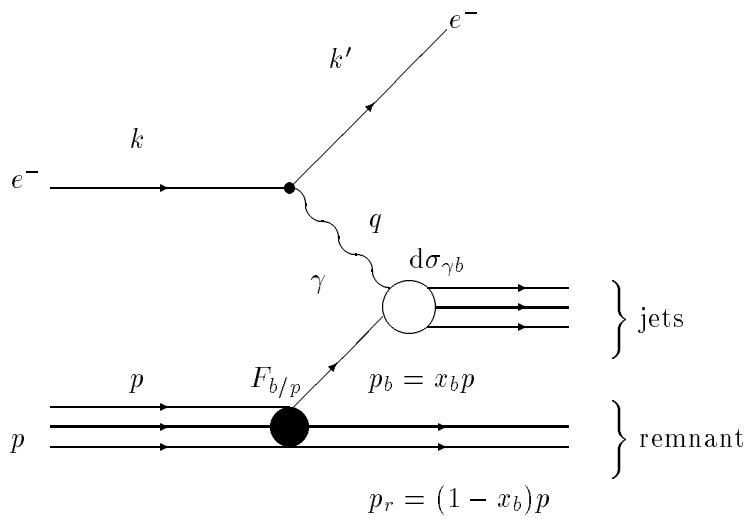

Figure 4: *Electron-proton scattering in the parton model.*

the scale M_b, at which the proton is probed, is large enough, the transverse momentum of the parton will be small and its phase space can be described by a single variable

$$x_b = \frac{qp_b}{qp} \in [0, 1], \tag{2.16}$$

the longitudinal momentum fraction of the proton carried by the parton. The other partons in the proton will then not notice the interaction but form a so-called remnant or spectator jet. Multiple scattering is suppressed by factors of $1/M_b^2$, and only the leading twist contributes for large M_b^2. The proton remnant carries the four-momentum p_r, which again depends only on x_b and the proton momentum p. The proton remnant will not be counted as a jet in the following.

We can now factorize the photon-proton cross section into

$$\mathrm{d}\sigma_{\gamma p}(\gamma p \to \text{jets} + \text{remnant}) = \sum_b \int_0^1 \mathrm{d}x_b F_{b/p}(x_b, M_b^2) \mathrm{d}\sigma_{\gamma b}(\gamma b \to \text{jets}), \tag{2.17}$$

where $F_{b/p}(x_b, M_b^2)$ is the probability of finding a parton b (where b may be a quark, an antiquark, or a gluon) within the proton carrying a fraction x_b of its momentum when probed at the hard scale M_b. The usual choice for deep inelastic scattering, $M_b = Q$, is not possible for photoproduction, as $Q^2 \simeq 0$ here. Instead, one takes $M_b = \xi E_T$ with E_T being the transverse energy of the outgoing parton or observed jet and ξ being of order 1. Contrary to the hard photon-parton scattering cross section $\mathrm{d}\sigma_{\gamma b}$, the parton densities $F_{b/p}(x_b, M_b^2)$ are not calculable in perturbative QCD and have to be taken from

experiment.

At high energies, the deep inelastic scattering (DIS) cross section takes the differential form

$$\frac{\mathrm{d}^2\sigma}{\mathrm{d}x_B\mathrm{d}Q^2} = \frac{4\pi\alpha^2}{x_B Q^4}\left[y^2 x_B F_1(x_B,Q^2) + (1-y)F_2(x_B,Q^2)\right] \tag{2.18}$$

with the Bjorken variable $x_B = Q^2/(2q.p)$ and $y = Q^2/(x_B s_H)$. The observable proton structure function $F_2(x_B,Q^2)$ is related to the parton densities $F_{b/p}(x_b,Q^2)$ through

$$\begin{aligned} F_2(x_B,Q^2) &= x_B \sum_q e_q^2 \int_{x_B}^1 \frac{\mathrm{d}x_b}{x_b}\left\{F_{q/p}(x_b,Q^2)\left[\delta\left(1-\frac{x_B}{x_b}\right) + \frac{\alpha_s}{2\pi}C_q\left(\frac{x_B}{x_b}\right)\right]\right. \\ &\quad \left. + F_{g/p}(x_b,Q^2)\frac{\alpha_s}{2\pi}C_g\left(\frac{x_B}{x_b}\right)\right\}, \end{aligned} \tag{2.19}$$

where e_q is the fractional quark charge. The partonic subprocesses are shown in figure 5. For the

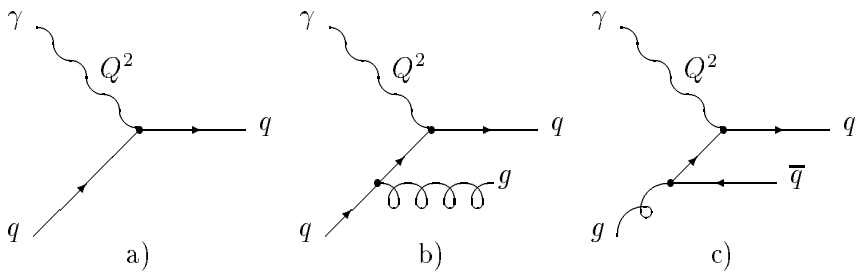

Figure 5: *Partonic subprocesses contributing to deep inelastic scattering: a) LO diagram, b) NLO quark contribution, c) NLO gluon contribution.*

leading order subprocess a), only the δ-function remains and eq. (2.19) simplifies to the Callan-Gross relation

$$F_2(x_B) = 2x_B F_1(x_B) = \sum_q x_B e_q^2 (F_{q/p}(x_B) + F_{\overline{q}/p}(x_B)). \tag{2.20}$$

The structure functions then depend only on x_B and not explicitly on Q^2, which is the Bjorken scaling property of the naïve parton model. The $\mathcal{O}(\alpha_s)$ QCD subprocesses b) and c) contain initial state singularities (cf. sections 4.2.6 and 4.2.8). These are factored off into the parton densities causing them to run, i.e. to depend on Q^2, leaving the coefficient functions C_q and C_g well-behaved. The explicit Q^2 dependence is given by the DGLAP equations found by Dokshitzer [Dok77], Gribov and Lipatov [Gri72, Gri72a], and Altarelli and Parisi [Alt77]:

$$\frac{\mathrm{d}F_{q/p}(x_b,Q^2)}{\mathrm{d}\ln Q^2} = \frac{\alpha_s}{2\pi}\int_{x_b}^1 \frac{\mathrm{d}z_b}{z_b}\left[P_{q\leftarrow q}\left(\frac{x_b}{z_b}\right)F_{q/p}(z_b,Q^2) + P_{q\leftarrow g}\left(\frac{x_b}{z_b}\right)F_{g/p}(z_b,Q^2)\right], \tag{2.21}$$

$$\frac{\mathrm{d}F_{g/p}(x_b,Q^2)}{\mathrm{d}\ln Q^2} = \frac{\alpha_s}{2\pi}\int_{x_b}^1 \frac{\mathrm{d}z_b}{z_b}\left[P_{g\leftarrow q}\left(\frac{x_b}{z_b}\right)F_{q/p}(z_b,Q^2) + P_{g\leftarrow g}\left(\frac{x_b}{z_b}\right)F_{g/p}(z_b,Q^2)\right]. \tag{2.22}$$

These equations contain the splitting functions $P_{b\leftarrow b'} = P^{(0)}_{b\leftarrow b'} + \alpha_s P^{(1)}_{b\leftarrow b'} + \cdots$. As only $P^{(0)}_{b\leftarrow b'}$ and $P^{(1)}_{b\leftarrow b'}$ have been calculated so far [Cur80, Fur80], the resummation of $\ln Q^2$ terms is truncated, which

introduces a factorization scheme dependence for the parton densities $F_{b/p}(x_b, Q^2)$.

In the leading twist approximation, the parton densities extracted from deep inelastic scattering can be used for any other process with incoming nucleons like photoproduction or proton-antiproton scattering – they are universal. As stated above, they have to be determined by experiment at some scale $Q^2 = Q_0^2$, where one parametrizes the x dependence before evolving up to any value of Q^2 according to the DGLAP equations. The input parameters are then determined by a global fit to the data. The u, d, and s quark densities are rather well known today from muon scattering (BCDMS, NMC, E665) and neutrino scattering (CCFR) experiments, and the c quark is constrained by open charm production at EMC. The small-x region, where the gluon and the sea quarks become important, could, however, not be studied by these experiments. As figure 6 illustrates, this is mainly the domain of the HERA experiments H1 and ZEUS in DIS as well as in photoproduction.

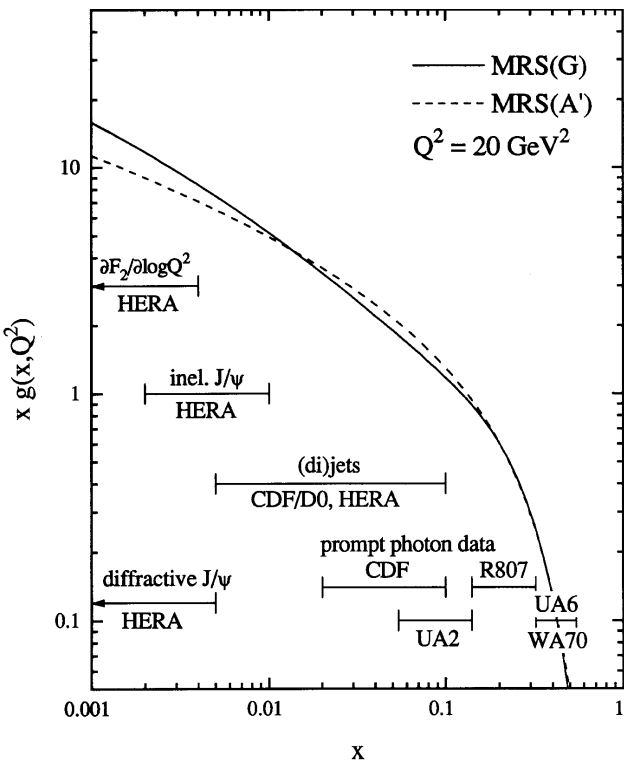

Figure 6: *The x intervals in which the gluon may be constrained by various sets of data. Also shown are the MRS(G) and MRS(A') gluon distributions (see below) [Mar96].*

There exist over 80 different sets of parton density functions. Most of them are easily accessible in the CERN library PDFLIB kept up to date by Plothow-Besch [Plo95]. We will now briefly compare the three parametrizations mainly in use today: CTEQ [Lai95], MRS [Mar94, Mar95], and GRV [Glü95]. The first two are very similar to each other, and both take $Q_0^2 = 4$ GeV^2. The starting distributions are taken to be of the form

$$x_b F_{b/p}(x_b, Q_0^2) = A_b x_b^{-\lambda_b}(1 - x_b)^{\beta_b}(1 + \gamma_b\sqrt{x_b} + \delta_b x_b) \tag{2.23}$$

for $b = u_v, d_v$, and g. The parameters in eq. (2.23) are only weakly constrained by flavor and momentum sum rules. In addition, CTEQ use this functional form also for $(\overline{d} + \overline{u})$ and $(\overline{d} - \overline{u})$, whereas MRS use it for the total quark sea $S = 2(\overline{u} + \overline{d} + \overline{s} + \overline{c} + \cdots)$. Very recently, CTEQ and MRS presented

new parametrizations (set 4 and set R, respectively) including new HERA and TEVATRON inclusive jet data [Lai96, Mar96a]. The GRV approach is rather different from the two mentioned above. In order to avoid any free additional parameters, their original version was based on the assumption that all gluon and sea distributions are generated dynamically from measured valence quark densities at a very low scale $Q_0 \simeq \mathcal{O}(\Lambda)$. The QCD coupling scale Λ also has to be fitted to the data and ranges from 200 to 255 MeV for the parametrizations considered here and for four quark flavors. As the assumption

$$g(x_b, Q_0^2) = \overline{q}(x_b, Q_0^2) = 0 \tag{2.24}$$

leads to much too steep distributions in the low x regime, the approach of GRV is modified using valence-like distributions for the gluon and the sea at the starting scale Q_0:

$$x_b g(x_b, Q_0^2) = A x_b^{\alpha}(1-x_b)^{\beta} \quad , \quad x_b \overline{q}(x_b, Q_0^2) = A' x_b^{\alpha'}(1-x_b)^{\beta'}. \tag{2.25}$$

Figure 7 displays the best next-to-leading fits from the three groups. In the large-x region, where the valence quarks dominate and high-precision data has been available for quite some time, all three singlet parametrizations lie on top of each other, and the gluon varies only weakly. Towards smaller x, however, the gluons as well as the sea quark driven singlet distribution start to differ between the various parametrizations, and here lies the main potential for a comparison of the NLO calculation presented here with existing and coming high-precision HERA data of the photoproduction of jets.

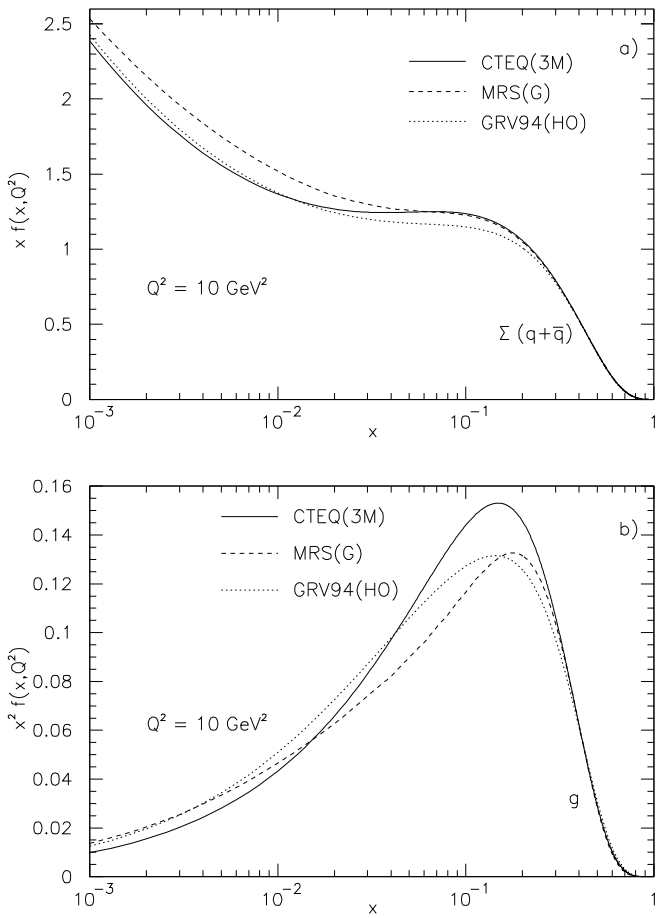

Figure 7: *Different parametrizations for a) the singlet parton density and b) the gluon density in the proton. We compare the CTEQ(3M), MRS(G), and GRV94(HO) results.*

2.3 Parton Distributions in the Photon

The photon is the fundamental gauge boson of quantum electrodynamics (QED), which is the most accurately tested field theory. Surprisingly, many reactions involving photons are much less well understood. This is due to the fact that the photon can fluctuate into $q\overline{q}$ pairs which in turn evolve into a complicated hadronic structure. At HERA, the photon radiated from the electron can thus interact either directly with a parton in the proton (direct component) or act as a hadronic source of partons which collide with the partons in the proton (resolved component, see figure 8). In the latter case, one does not test the proton structure alone but also the photon structure.

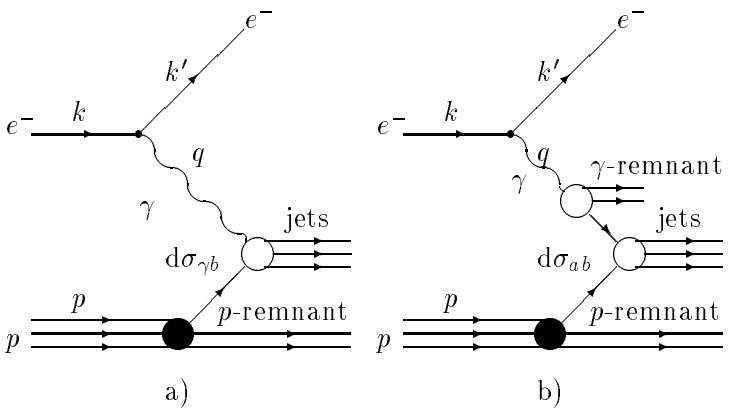

Figure 8: *Generic diagrams for a) direct and b) resolved photoproduction.*

Using the factorization theorem, the cross section for photon-parton scattering can be written as

$$\mathrm{d}\sigma_{\gamma b}(\gamma b \to \text{jets}) = \sum_a \int_0^1 \mathrm{d}y_a F_{a/\gamma}(y_a, M_a^2) \mathrm{d}\sigma_{ab}(ab \to \text{jets}). \tag{2.26}$$

Here, $F_{a/\gamma}(y_a, M_a^2)$ stands for the probability of finding a parton a with momentum fraction y_a in the photon, which has to be universal in all processes. The scale M_a is a measure for the hardness of the parton-parton cross section $\mathrm{d}\sigma_{ab}$ calculable in perturbative QCD and is again taken to be of $\mathcal{O}(E_T)$. The particle a can also be a direct photon. Then, $F_{\gamma/\gamma}(y_a, M_a^2)$ is simply given by the δ-function $\delta(1-y_a)$ and does not depend on the hard scale M_a, which is also expressed by the DGLAP equation (2.32) (see below).

Before HERA started taking data, information on the hadronic structure of the photon came almost exclusively from deep inelastic $\gamma^*\gamma$ scattering at e^+e^- colliders. Similarly to deep inelastic ep scattering, this is a totally inclusive process well suited to define a photon structure function. Using $y = Q^2/(x_B s_H)$, where Q^2 denotes the virtuality of the probing photon γ^*, and replacing F_1 by the longitudinal structure function $F_L(x_B, Q^2) = F_2(x_B, Q^2) - 2x_B F_1(x_B, Q^2)$, we can rewrite eq. (2.18) in the form

$$\frac{\mathrm{d}^2\sigma}{\mathrm{d}x_B \mathrm{d}y} = \frac{2\pi\alpha^2 s_H}{Q^4} \left\{ \left[1 + (1-y)^2\right] F_2^\gamma(x_B, Q^2) - y^2 F_L^\gamma(x_B, Q^2) \right\}, \tag{2.27}$$

where in LO $F_2^\gamma(x_B, Q^2)$ is related to the singlet quark parton density in the photon

$$F_2^\gamma(x_B, Q^2) = \sum_q x_B e_q^2 (F_{q/\gamma}(x_B, Q^2) + F_{\overline{q}/\gamma}(x_B, Q^2)). \tag{2.28}$$

But there are also important differences from ep scattering. First, the longitudinal structure function is non-zero even in the quark parton model. Second, the x_B dependence of the photon structure functions can be computed in perturbative QCD at large x_B and asymptotically large Q^2. In the naïve parton model, only the quark box diagram a) in figure 9 contributes. For the QCD improved

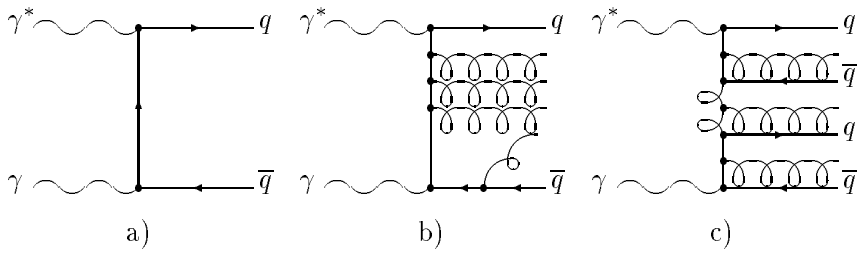

Figure 9: *a) Parton model diagram, b) nonsinglet and b) singlet corrections to* $F_2^\gamma(x_B, Q^2)$.

model, one adds nonsinglet and singlet diagrams of type b) and c) giving

$$F_2^\gamma(x_B, Q^2) = \alpha \left[\frac{1}{\alpha_s(Q^2)} a(x_B) + b(x_B) \right]. \tag{2.29}$$

This is the so-called "asymptotic pointlike" contribution to the resolved photon process not to be confused with the generic direct process. The first term is the LO result of Witten [Wit77] and the second term its NLO correction [Bar79]. Note that scaling is violated here already in LO. Obviously, eq. (2.29) is of $\mathcal{O}(\alpha/\alpha_s)$, which is usually claimed to be the order of the total photon structure function. As the parton-parton cross section is of $\mathcal{O}(\alpha_s^2)$, the resolved contribution is of the same order $\mathcal{O}(\alpha\alpha_s)$ as the direct contribution. Unfortunately, the necessary approximations leading to eq. (2.29) are not valid in the presently accessible range of Q^2, which gives rise to divergencies and negative counting rates at small x_B. Obviously, this problem can only be cured by assuming additional non-perturbative contributions.

A possible phenomenological and non-perturbative description of resolved photons is the so-called Vector Meson Dominance (VMD) model. It can well explain the production of vector mesons V in elastic photon-proton scattering ($\gamma p \to Vp$) at low energies [Sak60, Joo67, Joo67a]. As shown in figure 10 for deep inelastic $\gamma^*\gamma$ scattering, the photon can be regarded as a superposition of ρ, ω, and ϕ

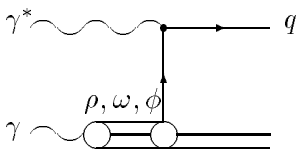

Figure 10: *The Vector Meson Dominance (VMD) model applied to* $\gamma^*\gamma$ *scattering.*

mesons. The cross section for this process can be written as

$$\mathrm{d}\sigma_{\gamma p} = \sum_{V=\rho,\omega,\phi} \frac{\pi\alpha}{\gamma_V^2} \mathrm{d}\sigma_{Vp}, \tag{2.30}$$

and the constants γ_V are determined to $\gamma_\rho : \gamma_\omega : \gamma_\phi = 1 : 3 : -3/\sqrt{2}$. This follows partly from symmetry properties. However, meson-proton cross sections are finite and hence cannot cancel the

asymptotic divergency. This can be done by including a boundary condition at a low reference scale Q_0^2 [Glü84], giving

$$F_2^\gamma(n,Q^2) = \frac{\alpha a(n)}{\alpha_s(Q^2)}\left[1-\left(\frac{\alpha_s(Q^2)}{\alpha_s(Q_0^2)}\right)^{1+d(n)}\right] + F_2^\gamma(n,Q_0^2)\left(\frac{\alpha_s(Q^2)}{\alpha_s(Q_0^2)}\right)^{d(n)} \tag{2.31}$$

in n-moment space. The second term in the square brackets regularizes the singularity and the last term is the usual hadronic contribution. Strictly, eq. (2.31) only holds for the nonsinglet part, whereas the singlet and gluon distributions are coupled. Thus, one has to introduce input distributions for the quarks and even for the gluon at the scale Q_0^2 as in the proton case. The evolution to higher scales is then given by the inhomogeneous DGLAP equations

$$\frac{\mathrm{d}F_{\gamma/\gamma}(y_a,Q^2)}{\mathrm{d}\ln Q^2} = 0, \tag{2.32}$$

$$\begin{aligned}\frac{\mathrm{d}F_{q/\gamma}(y_a,Q^2)}{\mathrm{d}\ln Q^2} &= \frac{\alpha_s}{2\pi}\int\limits_{y_a}^1 \frac{\mathrm{d}z_a}{z_a}\left[P_{q\leftarrow q}\left(\frac{y_a}{z_a}\right)F_{q/\gamma}(z_a,Q^2) + P_{q\leftarrow g}\left(\frac{y_a}{z_a}\right)F_{g/\gamma}(z_a,Q^2)\right] \\ &\quad + \frac{\alpha}{2\pi}P_{q\leftarrow\gamma}(y_a),\end{aligned} \tag{2.33}$$

$$\frac{\mathrm{d}F_{g/\gamma}(y_a,Q^2)}{\mathrm{d}\ln Q^2} = \frac{\alpha_s}{2\pi}\int\limits_{y_a}^1 \frac{\mathrm{d}z_a}{z_a}\left[P_{g\leftarrow q}\left(\frac{y_a}{z_a}\right)F_{q/\gamma}(z_a,Q^2) + P_{g\leftarrow g}\left(\frac{y_a}{z_a}\right)F_{g/\gamma}(z_a,Q^2)\right], \tag{2.34}$$

where $P_{q\leftarrow\gamma}(x) = 2N_C e_q^2(x^2+(1-x)^2)/2$ is the LO QED splitting function corresponding to the lower vertex in figure 9a) and $P_{a\leftarrow a'}$ are again the QCD splitting functions.

Fitting the input parameters to data is not as easy as in the proton case. First, no momentum sum rule applies for the photonic parton densities as they are all of LO in QED. This and the subleading nature of the gluonic process makes a determination of the gluon from F_2^γ very difficult. However, a momentum sum rule exists for mesons so that the VMD part of the gluon is reasonably well constrained. Second, the cross section for F_2^γ is quite small and falls rapidly with increasing Q^2 (see eq. (2.27)) leading to large statistical errors. This can be seen in figure 11, where the most recent data from TRISTAN and LEP are shown as a function of x for various Q^2 bins. The data are compared to the GRV and LAC parametrizations (see below), which were fitted to older data from PETRA, PEP, TRISTAN, and LEP1. Third, the target photon usually escapes undetected so that its energy can only be determined from the hadronic system. This leads to additional large systematic errors.

Presently, over 20 different parton distributions exist for the photon, and most of them are available in the PDFLIB [Plo95]. We compare the most commonly used ones in figures 12 (u-quark) and 13 (gluon). The VMD input is insufficient to fit the data at higher Q^2 offering two alternatives: GRV [Glü92], AFG [Aur92, Aur94], and SaS [Sch95] follow the same "dynamical" philosophy as in the GRV proton case starting from a simple valence-like input at a low scale $Q_0^2 = 0.25 \ldots 0.36$ GeV^2. On the other hand, LAC [Abr91, Abr92] and GS [Gor92] take a larger value for $Q_0^2 = 4 \ldots 5.3$ GeV^2, assume a more complicated ansatz there, and fit the free parameters to F_2^γ data. LAC intended to demonstrate the poor constraints on the gluon assuming a very soft gluon (fits 1 and 2) as well as a very hard one (fit 3). However, LAC 3 is ruled out now by recent e^+e^- and HERA data. In their latest parametrization, GS lowered their input scale to $Q_0^2 = 3$ GeV^2, included all available data on F_2^γ, and constrained the gluon from jet production at TRISTAN [Gor96].

The distinction between direct and resolved photon is only meaningful in LO of perturbation theory. In NLO, collinear singularities arise from the photon initial state that have to be absorbed

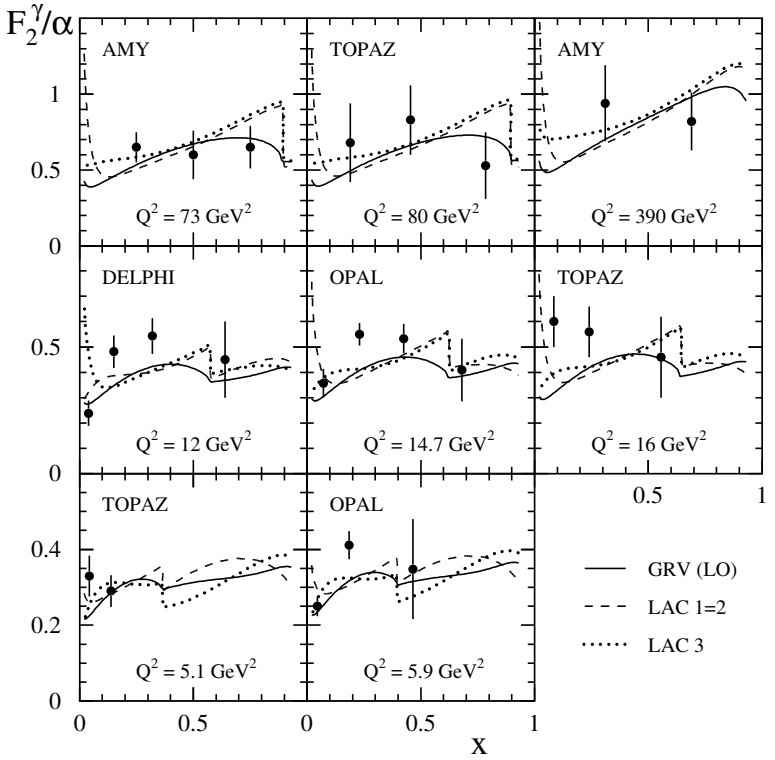

Figure 11: *Recent data on F_2^γ from TRISTAN and LEP compared to the LO fits of LAC and GRV to older data [Sjö96].*

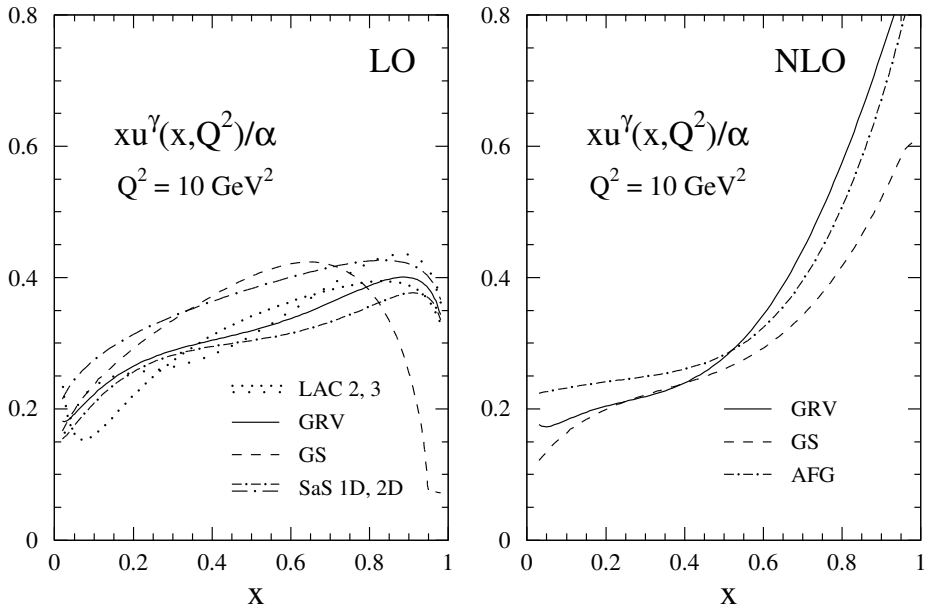

Figure 12: *Different u-quark parametrizations in LO (LAC(2,3), GRV, GS, SaS(1D,2D)) and NLO (GRV, GS, AFG). The latter are given in the $\overline{MS}$ scheme [Sjö96].*

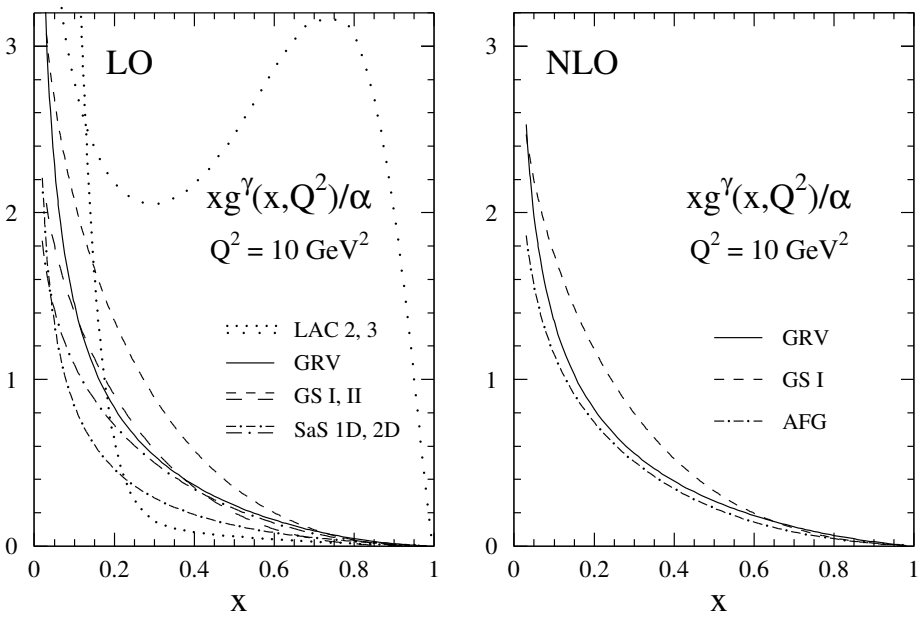

Figure 13: *Different gluon parametrizations in LO (LAC(2,3), GRV, GS(I,II), SaS(1D,2D)) and NLO (GRV, GS(I), AFG) [Sjö96].*

into the photon structure function (cf. sections 4.2.5 and 4.2.7) and produce a factorization scheme dependence as in the proton case. If one requires approximately the same F_2^γ in LO and NLO, the quark distributions in the $\overline{\text{MS}}$-scheme have quite different shapes in LO and NLO (see figure 12). This is not the case if the DIS$_\gamma$-scheme of GRV is used, where the direct-photon contribution to F_2^γ is absorbed into the photonic quark distributions. This allows for perturbative stability between LO and NLO results. Therefore, the separation between direct and resolved process is an artifact of finite order perturbation theory and depends on the factorization scheme and scale M_a. Experimentally, one tries to get a handle on this by introducing kinematical cuts, e.g. on the photon energy fraction taking part in the hard cross section.

2.4 Jet Definitions

Due to the confinement of color charge, neither incoming nor outgoing partons can be observed directly in experiment, but rather transform into colorless hadrons. This transformation is a long-distance process and is not calculable in perturbative QCD. For the incoming particles, we have already described how the ignorance of universal parton distributions in hadrons is parametrized. A similar method can be used for the final state partons, employing so-called fragmentation functions for the inclusive production of single hadrons [Bin95, Bin96]. The transformation of partons into individual hadrons forming part of the total final state was first studied by [Fie78, Hoy79, And80, Ali80]. Alternatively, one can observe beams of many hadrons going approximately into the same direction without the need to specify individual hadrons. The hadrons are then combined into so-called jets by cluster algorithms, where one starts from an initial cluster in phase space and ends at stable fixed points for the jet coordinates. These jet definitions should fulfill a number of important properties. They should [Ell89a]

- be simple to implement in the experimental analysis,
- be simple to implement in the theoretical calculation,
- be defined at any order of perturbation theory,
- yield a finite cross section at any order of perturbation theory,
- yield a cross section that is relatively insensitive to hadronization.

Although, in principle, hadronization of the final state should be factorizable from the hard cross section and the initial state, jets do indeed look quite different in e^+e^- and in, at least partly, hadronic collisions like ep scattering. This can be attributed to the "underlying event" of remnant jet production from the initial state, which can interfere with the hard jets in the final state. The main problem here is the determination of the true jet energy and the subtraction of the remnant pedestal.

In LO QCD, there is a one-to-one correspondence between partons and jets. This results in a complete insensitivity of theory to the experimentally used algorithm or to the resolution parameters. The experimental results depend, however, on these parameters as well as on detector properties and have to be corrected stepwise from detector level to hadron level to parton level. At this stage, one has to rely heavily on phenomenological Monte Carlo (MC) models like HERWIG [Mar92] or PYTHIA [Ben87], which model, e.g., parton-showers or color coherence. The situation can only be improved by going to NLO in perturbation theory. Here, the emission of one additional soft or collinear parton is calculable with correct treatment of the occurring singularities. A hadron jet can then consist not only of one, but also of two partons. It acquires a certain substructure, and will depend on the experimental algorithm and resolution.

Historically, the first resolution criterion was proposed by Sterman and Weinberg [Ste77]. It adds a particle to a jet if its energy is smaller than εM^2 or its angle with the jet is less than 2δ, which provides a close link to the radiation of secondary partons. The energy cut handles the soft divergencies and the angular cut the collinear divergencies. There is some freedom in the choice for M^2. Usually, one takes the hard scale of the process, e.g. Q^2 in e^+e^- annihilation.

The PETRA experiments used the so-called JADE cluster algorithm [Bar86], which has the advantage of being invariant under boosts along the beam axis. Two particles are combined into a cluster, if their invariant mass $s_{ij} = (p_i + p_j)^2$ is smaller than yM^2 [Kra84], where M^2 is again a typical scale and y is of $\mathcal{O}(10^{-2})$. In this way, the soft and collinear divergencies can be described by a single cut-off y. There exist a number of different schemes for this algorithm regarding the invariant mass of the

combination of the two particles and the combination of the particle four-momenta (JADE-, E-, $E0$-, P-, and $P0$-scheme).

At hadron colliders, cluster algorithms tend to include hadrons from the remnant jet, which is not present in e^+e^- collisions, into the current jet. Therefore, algorithms are preferred here which use a cone in rapidity-azimuth $(\eta - \phi)$ space, quite similar to the δ-condition of Sterman and Weinberg. The (pseudo-)rapidity $\eta = -\ln[\tan(\theta/2)]$ parametrizes the polar angle θ between the hard jet and the beam axis, and ϕ is the azimuthal angle of the jet around the beam axis. In the case of cone algorithms, only inclusive cross sections are infrared safe, where an arbitrary number of particles outside the jet cone can be radiated as long as they are softer than the observed jets. According to the standardization of the Snowmass meeting in 1990, calorimeter cells or partons i may have a distance R_i from the jet center provided that

$$R_i = \sqrt{(\eta_i - \eta_J)^2 + (\phi_i - \phi_J)^2} \leq R, \tag{2.35}$$

where η_i and ϕ_i are the coordinates of the parton or the center of the calorimeter cell [Hut92]. Typical values for the resolution parameter R range from 0.7 to 1, where the effects of hadronization and the underlying event are minimized. The transverse energy of the combined jet E_{T_J} is calculated from the sum of the particle E_{T_i}

$$E_{T_J} = \sum_{R_i \leq R} E_{T_i}, \tag{2.36}$$

and the jet axis is defined by the weighted averages

$$\eta_J = \frac{1}{E_{T_J}} \sum_{R_i \leq R} E_{T_i} \eta_i, \tag{2.37}$$

$$\phi_J = \frac{1}{E_{T_J}} \sum_{R_i \leq R} E_{T_i} \phi_i. \tag{2.38}$$

In perturbative QCD, the final state consists of a limited number of partons. For a single isolated parton i, the partonic and jet parameters agree ($(E_{T_i}, \eta_i, \phi_i) = (E_{T_J}, \eta_J, \phi_J)$) as shown in figure 14a), whereas two neighboring partons i, j will form a combined jet as shown in figure 14b). Equation

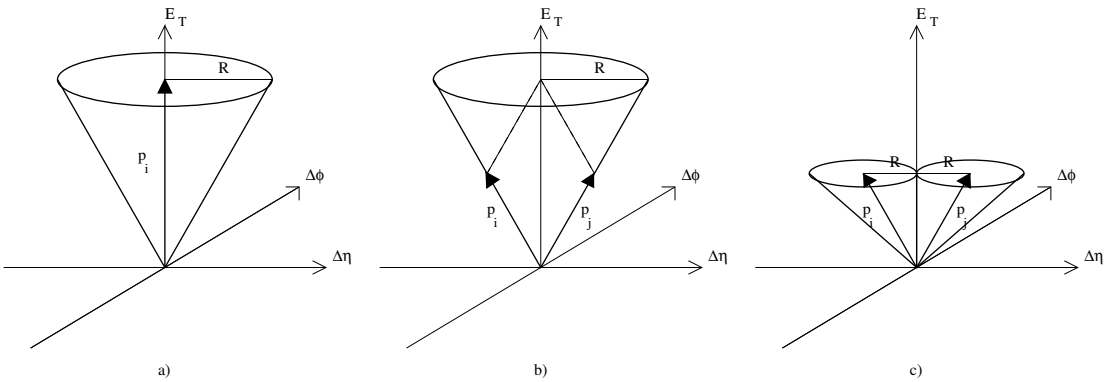

Figure 14: *Jet cone definition according to the Snowmass convention for a) a single parton, b) two combined partons with distance R from the jet axis, and c) two single partons.*

(2.35) only defines the distances R_i, R_j of each parton from the jet axis so that the two partons may be separated from each other by

$$R_{ij} = \sqrt{(\eta_i - \eta_j)^2 + (\phi_i - \phi_j)^2} \leq \frac{E_{T_i} + E_{T_j}}{\max(E_{T_i}, E_{T_j})} R. \tag{2.39}$$

This is just a consequence of the lever law of classical mechanics. If both partons have equal transverse energy, they may then be separated by as much as $2R$. As parton j does not lie inside a cone of radius R around parton i and vice versa, one might with some justification also count the two partons separately as shown in figure 14c). If one wants to study only the highest-E_T jet, this "double counting" must be excluded.

The selection of the initiating cluster, before a cone is introduced ("seed-finding"), is not fixed by the Snowmass convention, and different approaches are possible. The ZEUS collaboration at HERA uses two different cone algorithms: EUCELL takes the calorimeter cells in a window in $\eta - \phi$ space as seeds to find a cone with the highest E_T. The cells in this cone are then removed, and the algorithm continues. On the other hand, PUCELL was adapted from CDF and starts with single calorimeter cells. It then iterates cones around each of them, until the set of enclosed cells is stable. In this case it may happen that two stable jets overlap. If the overlapping transverse energy amounts to a large fraction of the jets, they are merged, otherwise the overlapping energy is split. Alternatively, the overlap could be attributed to the nearest, to the largest, or to both jets. The question of overlapping jets cannot be addressed in a next-to-leading order calculation of photoproduction. There, we only have up to three partons in the final state, which can form at most one recombined jet and no overlap.

Experimentally, jets of type b) in figure 14 are hard to find because of the missing seed in the jet center. This is a problem in particular with the PUCELL algorithm, which relies on initial clusters and does indeed find smaller cross sections than the less affected EUCELL algorithm. One possibility to model this theoretically is to introduce an additional parameter R_{sep} to restrict the distance of two partons from each other:

$$R_{ij} \leq \min\left[\frac{E_{T_i} + E_{T_j}}{\max(E_{T_i}, E_{T_j})} R, R_{\mathrm{sep}}\right]. \tag{2.40}$$

In figure 15, we can see that for two partons of similar or equal transverse energies E_T, R_{sep} is the

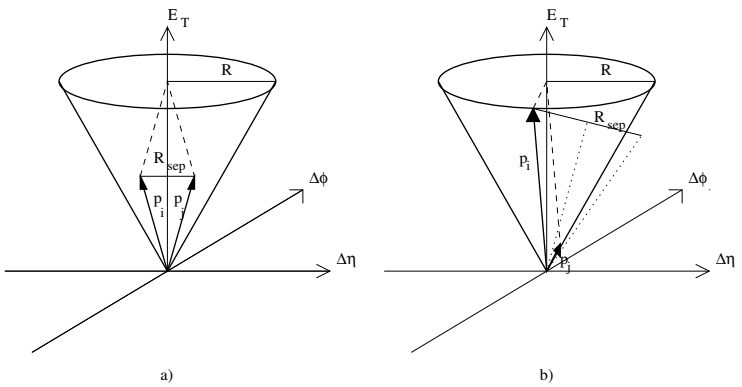

Figure 15: *Jet cone definition with an additional parameter for parton-parton separation R_{sep}: a) two partons with similar or equal transverse energies E_T, b) two partons with large E_T imbalance.*

limiting parameter, whereas it is the parton-jet distance R for two partons with large E_T imbalance. Numerical studies of the R and R_{sep} dependences will be given in sections 5.3 and 5.5 [But96].

The JADE algorithm clusters soft particles regardless of how far apart in angle they are, because only the invariant mass of the clusters is used. This is improved in the k_T or Durham clustering algorithm of Catani et al. [Cat91, Ell93, Sey95], where one defines the closeness of two particles by

$$d_{ij} = \min(E_{T_i}, E_{T_j})^2 R_{ij}^2. \tag{2.41}$$

R_{ij} is again defined in $(\eta - \phi)$ space. For small opening angles, $R_{ij} \ll 1$, eq. (2.41) reduces to

$$\min(E_{T_i}, E_{T_j})^2 R_{ij}^2 \simeq \min(E_i, E_j)^2 \Delta\theta^2 \simeq k_T^2, \tag{2.42}$$

the relative transverse momentum squared of the two particles in the jet. Similarly, one can define a closeness to the remnant jet particles b, if they are present:

$$d_{ib} = E_{T_i}^2 R_{ib}^2. \tag{2.43}$$

Particles are clustered into jets as long as they are closer than

$$d_{\{ij,ib\}} \leq d_i^2 = E_{T_i}^2 R^2, \tag{2.44}$$

where R is an adjustable parameter of $\mathcal{O}(1)$ analogous to the cone size parameter in the cone algorithm. Also, one chooses the same recombination scheme. Consequently, the k_T algorithm produces jets that are very similar to those produced by the cone algorithm with $R \simeq R_{\text{sep}}$.

2.5 Hard Photoproduction Cross Sections

We have now established the links between the experimentally observed initial and final states at HERA (electron, proton, and jets) and the partonic subprocess calculable in perturbative QCD. Formally, we can combine eqs. (2.8), (2.17), and (2.26) into

$$\begin{aligned} &\mathrm{d}\sigma_{ep}(ep \to e \ + \ \text{jets} + \text{remnants}) = \\ &= \sum_{a,b} \int_0^1 \mathrm{d}x_a F_{\gamma/e}(x_a) \int_0^1 \mathrm{d}y_a F_{a/\gamma}(y_a, M_a^2) \int_0^1 \mathrm{d}x_b F_{b/p}(x_b, M_b^2) \mathrm{d}\sigma_{ab}^{(n)}(ab \to \text{jets}), \end{aligned} \tag{2.45}$$

where x_a, y_a, and x_b denote the longitudinal momentum fractions of the photon in the electron, the parton in the photon, and the parton in the proton, respectively. From now on, we will use the variable x_a as the variable for the *parton in the electron* with the consequence that the incoming partons have momenta $p_a = x_a k$ and $p_b = x_b p$ and eq. (2.45) becomes

$$\begin{aligned} &\mathrm{d}\sigma_{ep}(ep \to e \ + \ \text{jets} + \text{remnants}) = \\ &= \sum_{a,b} \int_0^1 \mathrm{d}x_a F_{\gamma/e}\left(\frac{x_a}{y_a}\right) \int_{x_a}^1 \frac{\mathrm{d}y_a}{y_a} F_{a/\gamma}(y_a, M_a^2) \int_0^1 \mathrm{d}x_b F_{b/p}(x_b, M_b^2) \mathrm{d}\sigma_{ab}^{(n)}(ab \to \text{jets}). \end{aligned} \tag{2.46}$$

Next, one has to fix the kinematics for the photoproduction of jets. All particles are considered to be massless. In the HERA laboratory system, the positive z-axis is taken along the proton direction such that $k = E_e(1,0,0,-1)$ and $p = E_p(1,0,0,1)$. For the hard jets, we choose the decomposition of four-momenta into transverse energies, rapidities, and azimuthal angles $p_i = E_{T_i}(\cosh\eta_i, \cos\phi_i, \sin\phi_i, \sinh\eta_i)$. The boost from the HERA laboratory system into the ep center-of-mass system is then simply mediated by a shift in rapidity $\eta_{\text{boost}} = 1/2 \ln(E_e/E_p)$. Through energy and momentum conservation $p_a + p_b = \sum_i p_i$, the final partons are related kinematically to the invariant scaling variables x_a and x_b

$$x_a = \frac{1}{2E_e} \sum_i E_{T_i} e^{-\eta_i}, \tag{2.47}$$

$$x_b = \frac{1}{2E_p} \sum_i E_{T_i} e^{\eta_i}. \tag{2.48}$$

The cross section for the production of an n-parton final state from two initial partons a, b,

$$\mathrm{d}\sigma_{ab}^{(n)}(ab \to \text{jets}) = \frac{1}{2s} \overline{|\mathcal{M}|^2} \mathrm{dPS}^{(n)}, \tag{2.49}$$

depends on the flux factor $1/(2s)$, where $s = x_a x_b s_H$ is the partonic center-of-mass energy, the n-particle phase space

$$\mathrm{dPS}^{(n)} = \int (2\pi)^d \prod_{i=1}^n \frac{\mathrm{d}^d p_i \delta(p_i^2)}{(2\pi)^{d-1}} \delta^d \left(p_a + p_b - \sum_{i=1}^n p_i \right), \tag{2.50}$$

where $d = 4 - 2\varepsilon$ is the space-time dimension, and on the squared matrix element $\overline{|\mathcal{M}|^2}$. The latter is averaged over initial and summed over final spin and color states. Since we study almost-real photons with $Q^2 \simeq 0$ and treat quarks and gluons as massless, only transverse polarizations are possible giving spin average factors of $1/2$ for photons and quarks and $1/(2(1-\varepsilon))$ for gluons in dimensional regularization. The quarks form the fundamental representation of the SU(3) color symmetry group and can therefore carry $N_C = 3$ different colors. The gluons belong to the adjoint representation of dimension $2N_C C_F = N_C^2 - 1 = 8$. This is the defining equation for the so-called color factor C_F. We

therefore average the initial colors with factors of $1/N_C$ for quarks and $1/(2N_CC_F)$ for gluons. As the fundamental gauge bosons of QED, photons naturally are colorless.

In leading order QCD, the phase space for two partons $\mathrm{dPS}^{(2)}$ in the final state and the Born matrix elements T have to be computed as displayed in the first line of table 1. In next-to-leading order QCD, new contributions arise. Whereas the virtual corrections V also have a two-particle phase space (second line in table 1), the real corrections of the final state F, of the photon initial state I, and of the proton initial state J require the inclusion of a third outgoing parton into the phase space $\mathrm{dPS}^{(3)}$ (lines three to five in table 1). We will distinguish between direct and resolved photoproduction in the subsequent chapters and treat the two contributions in a completely parallel way.

Order	Phase Space $\mathrm{dPS}^{(n)}$	Direct Matrix Element $\overline{\lvert\mathcal{M}\rvert^2}$	Resolved Matrix Element $\overline{\lvert\mathcal{M}\rvert^2}$
LO	$\mathrm{dPS}^{(2)}$, sect. 3.1	$T_{\gamma b\to 12}$, sect. 3.2	$T_{ab\to 12}$, sect. 3.3
NLO		$V_{\gamma b\to 12}$, sect. 4.1.1	$V_{ab\to 12}$, sect. 4.1.2
	$\mathrm{dPS}^{(3)}$, sect. 4.2.1	$F_{\gamma b\to 123}$, sect. 4.2.2	$F_{ab\to 123}$, sect. 4.2.3
	$\mathrm{dPS}^{(3)}$, sect. 4.2.4	$I_{\gamma b\to 123}$, sect. 4.2.5	$I_{ab\to 123}$, sect. 4.2.7
		$J_{\gamma b\to 123}$, sect. 4.2.6	$J_{ab\to 123}$, sect. 4.2.8

Table 1: *Summary of phase space parametrizations and matrix elements needed for this NLO calculation of direct and resolved photoproduction.*

The two final state partons produced in a LO process have to balance their transverse energies $E_{T_1} = E_{T_2} = E_T$, so that relations (2.47) and (2.48) simplify to

$$x_a = \frac{E_T}{2E_e}\left(e^{-\eta_1} + e^{-\eta_2}\right), \tag{2.51}$$

$$x_b = \frac{E_T}{2E_p}\left(e^{\eta_1} + e^{\eta_2}\right). \tag{2.52}$$

The rapidity η_2 of the second jet is kinematically fixed by E_T, η_1, and x_a through the relation

$$\eta_2 = -\ln\left(\frac{2x_aE_e}{E_T} - e^{-\eta_1}\right). \tag{2.53}$$

In the HERA experiments, x_a is restricted to a fixed interval $x_{a,\min} \le x_a \le x_{a,\max} < 1$. We shall disregard this constraint and allow x_a to vary in the kinematically allowed range $x_{a,\min} \le x_a \le 1$, where

$$x_{a,\min} = \frac{E_pE_Te^{-\eta_1}}{2E_eE_p - E_eE_Te^{\eta_1}}. \tag{2.54}$$

From eqs. (2.51) and (2.52), we can express x_b as a function of E_T, η_1, and x_a:

$$x_b = \frac{x_aE_eE_Te^{\eta_1}}{2x_aE_eE_p - E_pE_Te^{-\eta_1}}. \tag{2.55}$$

This function is plotted in figure 16 for $E_T = 20$ GeV and four different values of η_1 in the range $0 \le \eta_1 \le 3$ as a function of x_a. Also shown is the envelope of these curves

$$x_{b,\mathrm{env}} = \frac{E_T^2}{x_aE_eE_p}, \tag{2.56}$$

which can be obtained from finding the minimum of x_b with respect to η_1 for fixed x_a. The minimal x_a-values for $\eta_1 = 0$, 1, 2, 3 are 0.379, 0.143, 0.0557, and 0.0247. The rapidity of the second jet is

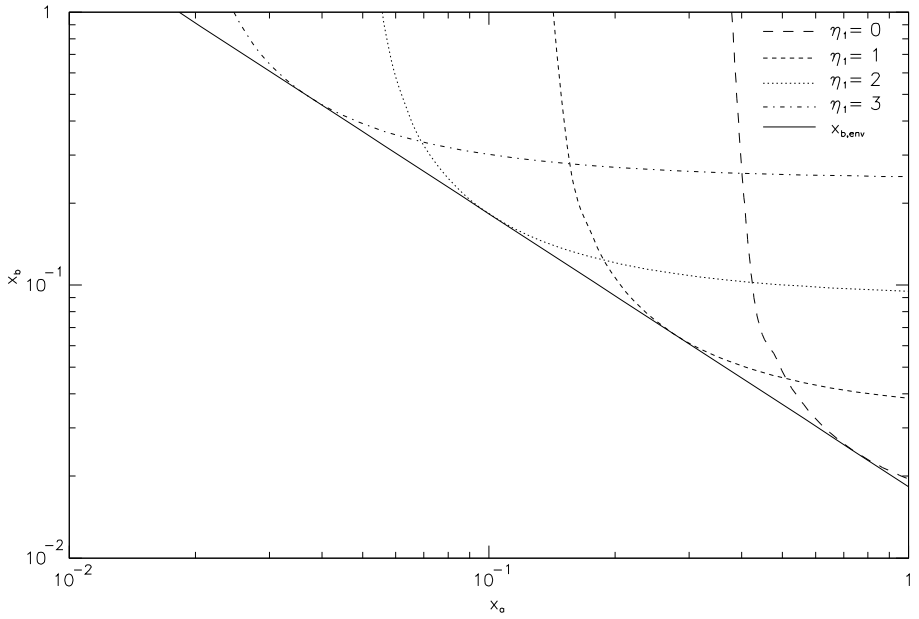

Figure 16: *Contours of constant η_1 in the $x_a - x_b$ plane for $E_T = 20$ GeV. $x_{b,env}$ (full curve) is the envelope of the curves.*

given by equation (2.53). Depending on x_a, different regions of x_b are explored. Small values of x_b are reached for negative η_1 and the maximal possible x_a, which is $x_a = 1$ in our case and $x_a = x_{a,\max}$ in the HERA experiments. This is of interest for determining the gluon structure function of the proton in the small-x region [For93]. Since x_a is not constrained very much under experimental conditions, it is possible to achieve minimal values of x_b by selecting the appropriate range in E_T, η_1, and η_2 according to (2.51) and (2.52).

Of course, studying the gluon structure of the proton in this way introduces a large dependence on the cross sections in the appropriate regions. The inclusive two-jet cross section for $ep \to e + \text{jet}_1 + \text{jet}_2 + X$ is obtained from

$$\frac{\mathrm{d}^3\sigma}{\mathrm{d}E_T^2 \mathrm{d}\eta_1 \mathrm{d}\eta_2} = \sum_{a,b} x_a F_{a/e}(x_a, M_a^2) x_b F_{b/p}(x_b, M_b^2) \frac{\mathrm{d}\sigma}{\mathrm{d}t}(ab \to \text{jets}), \tag{2.57}$$

where

$$F_{a/e}(x_a, M_a^2) = \int_{x_a}^{1} \frac{\mathrm{d}y_a}{y_a} F_{a/\gamma}(y_a, M_a^2) F_{\gamma/e}\left(\frac{x_a}{y_a}\right) \tag{2.58}$$

defines the parton content in the electron. $\mathrm{d}\sigma/\mathrm{d}t$ stands for the differential cross section of the partonic subprocess $ab \to$ jets. The invariants of this process are $s = (p_a + p_b)^2$, $t = (p_a - p_1)^2$, and $u = (p_a - p_2)^2$. They can be expressed by the final state variables E_T, η_1, and η_2 and the initial state momentum fractions x_a and x_b:

$$s = 4x_a x_b E_e E_p, \tag{2.59}$$

$$t = -2x_a E_e E_T e^{\eta_1} = -2x_b E_p E_T e^{-\eta_2}, \tag{2.60}$$

$$u = -2x_a E_e E_T e^{\eta_2} = -2x_b E_p E_T e^{-\eta_1}. \tag{2.61}$$

For the inclusive one-jet cross section, we must integrate over one of the rapidities in (2.57). We integrate over η_2 and transform to the variable x_a using (2.51). The result is the cross section for

$ep \to e + \text{jet} + X$, which depends on E_T and η:

$$\frac{\mathrm{d}^2\sigma}{\mathrm{d}E_T \mathrm{d}\eta} = \sum_{a,b} \int_{x_{a,\min}}^{1} \mathrm{d}x_a x_a F_{a/e}(x_a, M_a^2) x_b F_{b/p}(x_b, M_b^2) \frac{4E_e E_T}{2x_a E_e - E_T e^{-\eta}} \frac{\mathrm{d}\sigma}{\mathrm{d}t}(ab \to \text{jet}). \tag{2.62}$$

Here, x_b is given by (2.55) with $\eta_1 = \eta$.

3 Leading Order Cross Sections

In this section, we consider the leading order contributions to the photoproduction cross section $\mathrm{d}\sigma/\mathrm{d}t$. The leading order direct hard scattering process is of $\mathcal{O}(\alpha\alpha_s)$, and the leading order resolved hard scattering process is of $\mathcal{O}(\alpha_s^2)$. Since the latter has to be multiplied with the photon structure function of $\mathcal{O}(\alpha/\alpha_s)$, both contributions are of the the same order $\mathcal{O}(\alpha\alpha_s)$. To this order, it is necessary to calculate the phase space of two-particle final states, the tree-level matrix elements for direct photons $\gamma b \to 12$, and those for resolved photons $ab \to 12$. The two particles produced in the hard scattering then correspond directly to the two jets that can at most be observed. Either particle can be in jet one or jet two, so that the cross sections $\mathrm{d}\sigma/\mathrm{d}t$ have to be considered in their given form and with $(t \leftrightarrow u)$ to give the complete cross section $\mathrm{d}\sigma/\mathrm{d}t(s,t,u)+\mathrm{d}\sigma/\mathrm{d}t(s,u,t)$. Furthermore, one has to add symmetry factors of $1/n!$ for n identical particles in the final state. As we will later go from four to $d = 4 - 2\varepsilon$ dimensions to regularize the singularities showing up in next-to-leading order, we already give the results in this section in d dimensions. If one is only interested in leading order results, one can always set ε to zero in this section.

Section 3.1 contains the phase space for $2 \to 2$ scattering in d dimensions. It is calculated in the center-of-mass system of the incoming or equivalently outgoing particles. The matrix elements for direct photons are presented in section 3.2. Only one master diagram for the so-called QCD Compton scattering process $\gamma q \to gq$ contributes. The gluon initiated process is obtained by crossing. For resolved photons, we have four parton-parton master diagrams. The corresponding matrix elements are given in section 3.3. In addition, we show a table from which the matrix elements for all other processes can be deduced.

3.1 Phase Space for Two-Particle Final States

We give here a brief sketch of the phase space calculation for the scattering of two initial into two final particles in $d = 4 - 2\varepsilon$ dimensions. We start from the general expression [Byc73]

$$\mathrm{dPS}^{(2)} = \int (2\pi)^d \prod_{i=1}^{2} \frac{\mathrm{d}^d p_i \delta(p_i^2)}{(2\pi)^{d-1}} \delta^d \left(p_a + p_b - \sum_{i=1}^{2} p_i \right). \tag{3.1}$$

The dijet and single jet cross sections in eqs. (2.57) and (2.62) require partonic cross sections differential in the Mandelstam variable t. We therefore insert an additional δ-function with respect to t

$$\frac{\mathrm{dPS}^{(2)}}{\mathrm{d}t} = \int (2\pi)^d \prod_{i=1}^{2} \frac{\mathrm{d}^d p_i \delta(p_i^2)}{(2\pi)^{d-1}} \delta^d \left(p_a + p_b - \sum_{i=1}^{2} p_i \right) \delta(t + 2p_a p_1), \tag{3.2}$$

before we integrate over the d-dimensional δ-function leading to

$$\frac{\mathrm{dPS}^{(2)}}{\mathrm{d}t} = \int \frac{\mathrm{d}^d p_1 \delta(p_1^2)}{(2\pi)^{d-2}} \delta((p_a + p_b - p_1)^2) \delta(t + 2p_a p_1). \tag{3.3}$$

Next, we choose the center-of-mass system of the incoming partons a, b as shown in figure 17, where

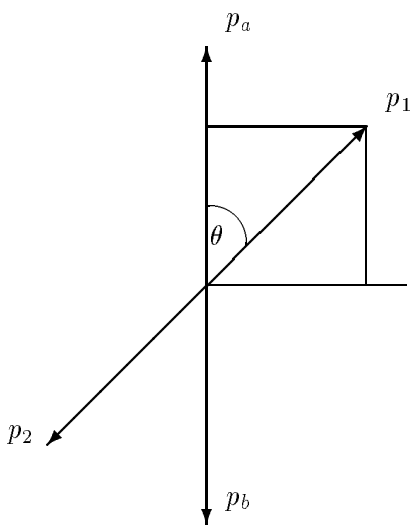

Figure 17: *Center-of-mass system for the scattering of two initial into two final partons.*

the outgoing partons are of the same energy and can be described by a single polar angle θ between p_1 and p_a. We integrate over the azimuthal angle ϕ

$$\frac{\mathrm{dPS}^{(2)}}{\mathrm{d}t} = \int \frac{\mathrm{d}E_1 E_1^{d-3} \mathrm{d}\cos\theta (1 - \cos^2\theta)^{\frac{d-4}{2}}}{2^{d-2}\pi^{\frac{d-2}{2}}\Gamma\left(\frac{d-2}{2}\right)} \delta(s - 2\sqrt{s}E_1) \delta(t + \sqrt{s}E_1(1 - \cos\theta)) \tag{3.4}$$

and over the remaining δ-functions. The final result is [Aur87, Arn89, Gra90]

$$\frac{\mathrm{dPS}^{(2)}}{\mathrm{d}t} = \frac{1}{\Gamma(1-\varepsilon)} \left(\frac{4\pi s}{tu} \right)^{\varepsilon} \frac{1}{8\pi s}. \tag{3.5}$$

3.2 Born Matrix Elements for Direct Photons

For direct photoproduction of two partons, there is only one generic Feynman diagram $\gamma q \to gq$ as displayed in figure 18. Unlike deep inelastic scattering, the leading order process already includes the

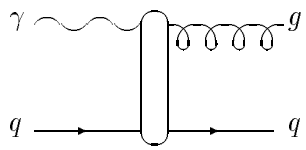

Figure 18: $2 \to 2$ *Feynman diagram for direct photoproduction.*

production of a hard gluon, which balances the transverse momentum of the scattered quark. This can either happen in the initial state (left diagram in figure 19) or in the final state (right diagram in figure 19) of this so-called "QCD Compton Scattering". Both diagrams have to be added and squared

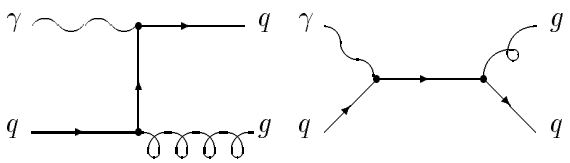

Figure 19: *Born diagrams for direct photoproduction.*

to give the full matrix element squared. In d dimensions, the result is

$$|\mathcal{M}|^2_{\gamma q \to gq}(s,t,u) = e^2 e_q^2 g^2 \mu^{4\varepsilon} T_{\gamma q \to gq}(s,t,u), \tag{3.6}$$

where the renormalization scale μ keeps the couplings dimensionless and where

$$T_{\gamma q \to gq}(s,t,u) = 8 N_C C_F (1-\varepsilon) \left[(1-\varepsilon) \left(-\frac{u}{s} - \frac{s}{u} \right) + 2\varepsilon \right]. \tag{3.7}$$

Note that the DIS interference term of the two diagrams is missing as it is proportional to $Q^2 \simeq 0$. As discussed in section 2.2, the proton not only consists of quarks but also of gluons giving rise to a "Boson Gluon Fusion" process $\gamma g \to q\bar{q}$ not shown here. The corresponding matrix element is obtained from eq. (3.6) by simply crossing the initial quark with the final gluon, or $(s \leftrightarrow t)$, and multiplying by (-1) for crossing a fermion line. Similarly, the contribution for incoming anti-quarks $\gamma \bar{q} \to g\bar{q}$ can be calculated by crossing $(s \leftrightarrow u)$. The LO direct matrix elements have been known for quite some time [Aur87, Bae89a, Böd92] and are summarized in table 2.

Process	Matrix Element $\overline{\lvert\mathcal{M}\rvert^2}$
$\gamma q \to gq$	$[\lvert\mathcal{M}\rvert^2_{\gamma q \to gq}(s,t,u)]/[4N_C]$
$\gamma \bar{q} \to g\bar{q}$	$[\lvert\mathcal{M}\rvert^2_{\gamma q \to gq}(u,t,s)]/[4N_C]$
$\gamma g \to q\bar{q}$	$-[\lvert\mathcal{M}\rvert^2_{\gamma q \to gq}(t,s,u)]/[8(1-\varepsilon)N_C C_F]$

Table 2: *Summary of* $2 \to 2$ *squared matrix elements for direct photoproduction.*

3.3 Born Matrix Elements for Resolved Photons

For resolved photoproduction of two partons, we have to calculate the four generic parton-parton scattering processes $qq' \to qq'$, $qq \to qq$, $q\bar{q} \to gg$, and $gg \to gg$. The corresponding Feynman diagrams are displayed in figure 20. The first process for the scattering of two non-identical quarks q and q'

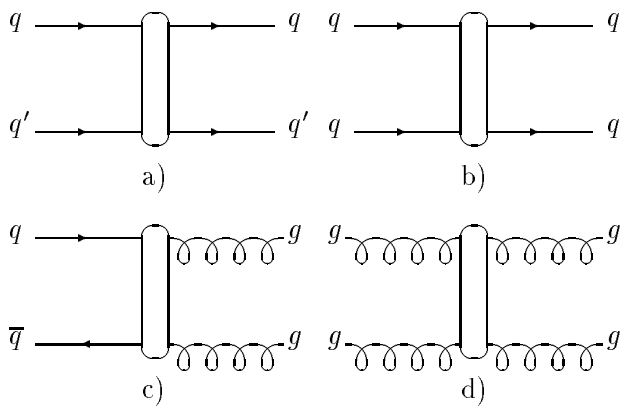

Figure 20: $2 \to 2$ *Feynman diagrams for resolved photoproduction.*

has already been calculated in 1978 by Cutler and Sivers [Cut78], shortly prior to the other processes [Com77, Owe78], and was compared to inclusive jet and hadron production at ISR energies.

Figure 21a) shows that for $qq' \to qq'$ only the one-gluon exchange between the different quarks in the t-channel contributes. The matrix element squared is given by

$$|\mathcal{M}|^2_{qq' \to qq'}(s,t,u) = g^4 \mu^{4\varepsilon} T_{qq' \to qq'}(s,t,u) \tag{3.8}$$

with

$$T_{qq' \to qq'}(s,t,u) = 4 N_C C_F \left(\frac{s^2+u^2}{t^2} - \varepsilon \right). \tag{3.9}$$

We will split off the coupling constants for the other Born matrix elements $|\mathcal{M}|^2$ as in eq. (3.8).

Equal quark flavors cannot be distinguished in the final state so that both diagrams in figure 21b) have to be added. In addition to the squares of the individual diagrams already present in the case of different quark flavors, the interference term

$$T_{qq \to qq}(s,t,u) = -8 C_F (1-\varepsilon) \left(\frac{s^2}{ut} + \varepsilon \right) \tag{3.10}$$

also contributes to the process $qq \to qq$.

Final gluons are also undistinguishable and can even couple in a non-abelian way as shown in figure 21c). The resulting matrix element for the process $q\bar{q} \to gg$ is

$$T_{q\bar{q} \to gg}(s,t,u) = 4 C_F (1-\varepsilon) \left(\frac{2 N_C C_F}{ut} - \frac{2 N_C^2}{s^2} \right) (t^2+u^2-\varepsilon s^2). \tag{3.11}$$

The diagrams for the process $gg \to gg$ in figure 21d) give

$$T_{gg \to gg}(s,t,u) = 32 N_C^3 C_F (1-\varepsilon)^2 \left(3 - \frac{ut}{s^2} - \frac{us}{t^2} - \frac{st}{u^2} \right). \tag{3.12}$$

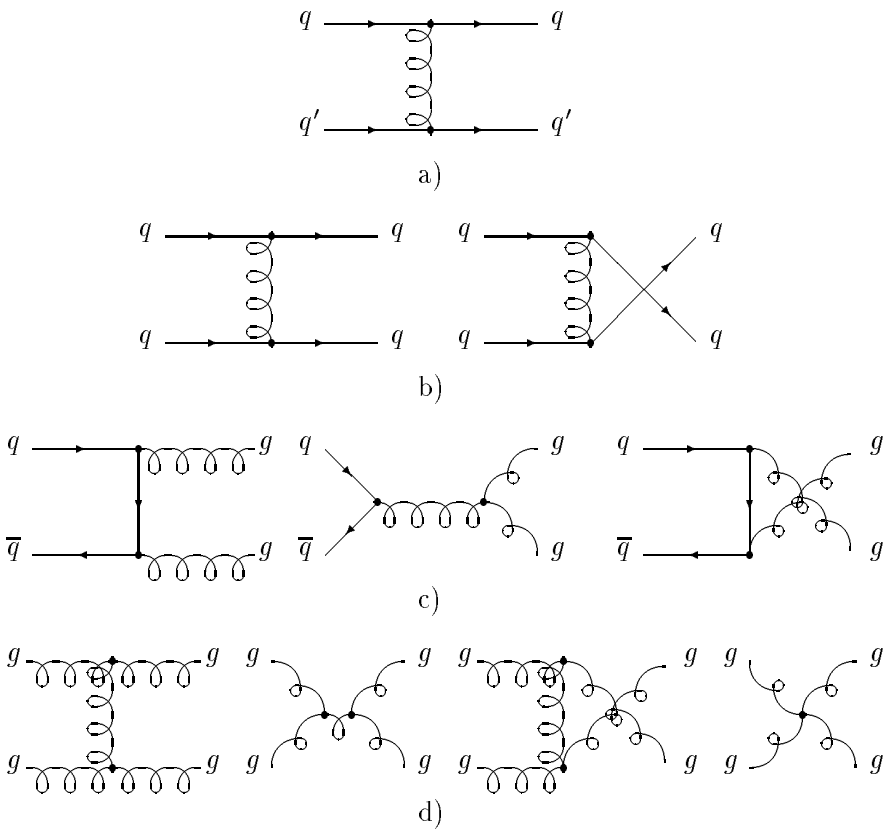

Figure 21: *Born diagrams for resolved photoproduction.*

Process	Matrix Element $\overline{\lvert\mathcal{M}\rvert^2}$
$qq' \to qq'$	$[\lvert\mathcal{M}\rvert^2_{qq'\to qq'}(s,t,u)]/[4N_C^2]$
$q\bar{q}' \to q\bar{q}'$	$[\lvert\mathcal{M}\rvert^2_{qq'\to qq'}(u,t,s)]/[4N_C^2]$
$q\bar{q} \to \bar{q}'q'$	$[\lvert\mathcal{M}\rvert^2_{qq'\to qq'}(t,s,u)]/[4N_C^2]$
$qq \to qq$	$[\lvert\mathcal{M}\rvert^2_{qq'\to qq'}(s,t,u) + \lvert\mathcal{M}\rvert^2_{qq'\to qq'}(s,u,t) + \lvert\mathcal{M}\rvert^2_{qq\to qq}(s,t,u)]/[4N_C^2]/2!$
$q\bar{q} \to q\bar{q}$	$[\lvert\mathcal{M}\rvert^2_{qq'\to qq'}(u,t,s) + \lvert\mathcal{M}\rvert^2_{qq'\to qq'}(u,s,t) + \lvert\mathcal{M}\rvert^2_{qq\to qq}(u,t,s)]/[4N_C^2]$
$q\bar{q} \to gg$	$[\lvert\mathcal{M}\rvert^2_{q\bar{q}\to gg}(s,t,u)]/[4N_C^2]/2!$
$qg \to qg$	$-[\lvert\mathcal{M}\rvert^2_{q\bar{q}\to gg}(t,s,u)]/[8(1-\varepsilon)N_C^2C_F]$
$\bar{q}g \to \bar{q}g$	$-[\lvert\mathcal{M}\rvert^2_{q\bar{q}\to gg}(t,u,s)]/[8(1-\varepsilon)N_C^2C_F]$
$gg \to q\bar{q}$	$[\lvert\mathcal{M}\rvert^2_{q\bar{q}\to gg}(s,t,u)]/[16(1-\varepsilon)^2N_C^2C_F^2]$
$gg \to gg$	$[\lvert\mathcal{M}\rvert^2_{gg\to gg}(s,t,u)]/[16(1-\varepsilon)^2N_C^2C_F^2]/2!$

Table 3: *Summary of* $2 \to 2$ *squared matrix elements for resolved photoproduction.*

All other diagrams can be obtained from the above by simple crossing relations. The complete result in d dimensions can be found in [Ell86] and is summarized in table 3.

4 Next-To-Leading Order Cross Sections

As in any calculation of next-to-leading order cross sections, we have to calculate two types of corrections in photoproduction: virtual and real corrections. For the direct case, these corrections are of $\mathcal{O}(\alpha\alpha_s^2)$, and for the resolved case, they are of $\mathcal{O}(\alpha_s^3)$. Throughout this section, direct and resolved photon results will be presented separately, but in a completely parallel way. Whereas the direct contributions have already been published [Kla93, Kla95a], the resolved contributions are presented here for the first time.

The virtual corrections consist of the interference terms of one-loop graphs with the Born graphs calculated in section 3 and will be given in section 4.1. We can still use the same phase space for two final partons as in the last section. The direct matrix elements are contained in section 4.1.1, those for resolved photons in section 4.1.2. Again, we display only the relevant master diagrams, from which all subprocesses can be deduced through crossing.

The real corrections are derived from the integration of diagrams with a third parton in the final state over regions of phase space, where this third parton causes singularities in the matrix elements. Different methods can be employed here. We choose the phase space slicing method with an invariant mass cut [Kra84] in section 4.2. Alternatively, the subtraction method could be used [Ell89, Kun92]. We calculate the three particle phase space in two different versions for final state singularities (section 4.2.1) and initial state singularities (section 4.2.4). These sections are followed by the calculation of the matrix elements for final state (sections 4.2.2 through 4.2.3) and initial state corrections (sections 4.2.5 through 4.2.8).

Finally, we demonstrate the cancellation of the infrared and collinear singularities, that show up in the virtual and real corrections separately, in section 4.3. The ultraviolet singularities in the virtual corrections are removed by counter terms in the renormalization procedure. Remaining collinear singularities in the initial states can be absorbed into the photon and proton structure functions.

4.1 Virtual Corrections

The central blobs in figures 18 and 20 can also contain loop corrections to the leading order matrix elements in figures 19 and 21. Up to $\mathcal{O}(\alpha\alpha_s^2)$, the interference terms between the direct Born diagrams T and the direct one-loop diagrams V have to be taken into account according to

$$\begin{aligned} |\mathcal{M}|^2(\mathcal{O}(\alpha\alpha_s^2)) &= |\sqrt{\alpha\alpha_s T} + \sqrt{\alpha\alpha_s^3 V}|^2 \\ &= \alpha\alpha_s T + 2\alpha\alpha_s^2\sqrt{V^* T} + \mathcal{O}(\alpha\alpha_s^3). \end{aligned} \tag{4.1}$$

Similarly, the interference terms between the resolved Born diagrams T and the resolved one-loop diagrams V have to be taken into account up to $\mathcal{O}(\alpha_s^3)$.

The inner loop momenta are unconstrained from the outer $2 \to 2$ scattering process. We can therefore still make use of the phase space calculated in section 3.1, but have to integrate over the inner degrees of freedom. At the lower and upper integration bounds, we encounter infrared (IR) and ultraviolet (UV) divergencies. Using the dimensional regularization scheme of t'Hooft and Veltman [tHo72, Bol72, Ash72, Cic72, Mar75, Lei75], we integrate in $d = 4 - 2\varepsilon$ dimensions, thus rendering the integrals finite and keeping the theory Lorentz and gauge invariant. The IR and UV poles show up as terms $\propto 1/\varepsilon^2$ and $1/\varepsilon$. As a consequence, the complete higher order cross sections have to be calculated in d dimensions up to $\mathcal{O}(\varepsilon^2)$ to ensure that no finite terms are missing.

The ultraviolet divergencies coming from infinite loop momenta can be removed by renormalizing the fields, couplings, gauge parameters, and masses in the Lagrangian, since QCD is a renormalizable field theory. This is done by multiplying the divergent parameters in the Lagrangian with renormalization constants Z_i and expanding up to the required order in the coupling constant g. The resulting counter terms then render the physical Green's functions finite. In addition to the $1/\varepsilon$ poles, universal finite contributions

$$\frac{1}{\varepsilon} - \gamma_E + \ln(4\pi) \tag{4.2}$$

are included into the counter terms according to the modified minimal subtraction ($\overline{\text{MS}}$) scheme [tHo73, Bar78], which we employ here. The coupling constant g is kept dimensionless by multiplying it with the renormalization scale μ

$$g \to g\mu^{\varepsilon}. \tag{4.3}$$

If eq. (4.3) is expanded in powers of ε and combined with single poles of the type in eq. (4.2), the renormalization procedure will produce an explicit logarithmic dependence on the renormalization scale μ

$$\frac{1}{\varepsilon}\left(\frac{4\pi\mu^2}{s}\right)^{\varepsilon} \doteq \frac{1}{\varepsilon} + \ln\frac{4\pi\mu^2}{s}, \tag{4.4}$$

that cancels the first term of the expansion of the running coupling constant

$$\alpha_s(\mu^2) = \frac{12\pi}{(33 - 2N_f)\ln\frac{\mu^2}{\Lambda^2}}\left(1 - \frac{6(153 - 19N_f)}{(33 - 2N_f)^2}\frac{\ln(\ln\frac{\mu^2}{\Lambda^2})}{\ln\frac{\mu^2}{\Lambda^2}}\right) + \cdots. \tag{4.5}$$

α_s is given here in two-loop approximation as appropriate in NLO QCD, and N_f is the number of flavors in the $q\bar{q}$ loops. We choose $\mu = \mathcal{O}(E_T)$ as for the factorization scales.

Infrared divergencies arise from small loop momenta in the virtual corrections. They have to cancel eventually against the divergencies from the emission of real soft and collinear partons according to the Kinoshita-Lee-Nauenberg theorem [Kin62, Lee64]. Finally, one obtains finite physical results in the limit $d \to 4$.

4.1.1 Virtual Corrections for Direct Photons

The one-loop corrections to the left diagram of figure 19 are shown in figure 22 and can be classified

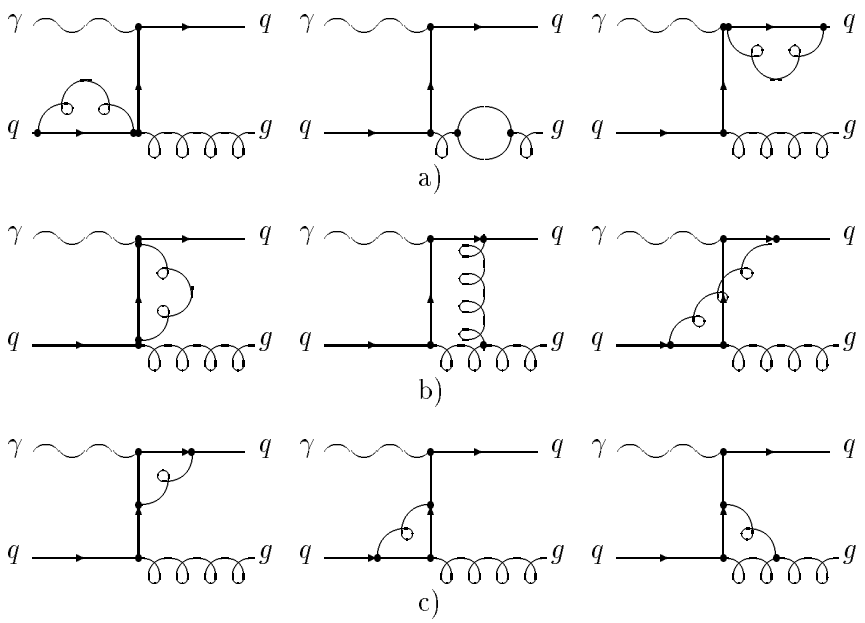

Figure 22: *Virtual diagrams for direct photoproduction. The circle in diagram a) denotes a quark, gluon, and ghost loop.*

into a) self-energy diagrams, b) propagator corrections and box diagrams, and c) vertex corrections. They contain an additional virtual gluon, which leads to an extra factor α_s. Similar diagrams are obtained for the right diagram of figure 19. As in leading order, the diagrams for the process $\gamma g \to q\bar{q}$ can be obtained from figure 22 by crossing the initial quark and the final gluon or equivalently $(s \leftrightarrow t)$ and multiplying by (-1) for the crossing of a fermion line. However, the virtual corrections can in general contain logarithms $\ln(x/s - i\eta)$ and dilogarithms $\mathrm{Li}_2(x/s)$, where x denotes different Mandelstam variables before and after crossing. The $i\eta$-prescription for Feynman propagators then takes care of additional terms of π^2, that arise in the quadratic logarithms with negative argument.

The virtual contributions have been well known for many years from $e^+e^- \to q\bar{q}g$ higher order QCD calculations [Ell81, Fab82]. For the corresponding photoproduction cross section, one substitutes $Q^2 = 0$ and performs the necessary crossings. The result can be found in [Aur87, Böd92, Kla93]. We have also compared with the results in [Gra90] for deep inelastic scattering $eq \to e'gq$ and $eg \to e'q\bar{q}$, which can be expressed by the invariants s, t, and u after setting $Q^2 = 0$. For completeness and for later use, we write the final result in the form

$$|\mathcal{M}|^2_{\gamma b \to 12}(s,t,u) = e^2 e_q^2 g^2 \mu^{4\varepsilon} \frac{\alpha_s}{2\pi} \left(\frac{4\pi\mu^2}{s}\right)^{\varepsilon} \frac{\Gamma(1-\varepsilon)}{\Gamma(1-2\varepsilon)} V_{\gamma b \to 12}(s,t,u) \tag{4.6}$$

The expression $V_{\gamma q \to gq}(s,t,u)$ is given by

$$\begin{aligned} V_{\gamma q \to gq}(s,t,u) \;=\; & \left[C_F \left(-\frac{2}{\varepsilon^2} + \frac{1}{\varepsilon}\left(2\ln\frac{-t}{s} - 3\right) + \frac{2\pi^2}{3} - 7 + \ln^2\frac{t}{u} \right) \right. \\ & \left. - \frac{N_C}{2}\left(\frac{2}{\varepsilon^2} + \frac{1}{\varepsilon}\left(\frac{11}{3} + 2\ln\frac{-t}{s} - 2\ln\frac{-u}{s}\right) + \frac{\pi^2}{3} + \ln^2\frac{t}{u} + \frac{11}{3}\ln\frac{s}{\mu^2} \right) \right. \end{aligned} \tag{4.7}$$

$$
\begin{aligned}
&+\frac{N_f}{3}\left(\frac{1}{\varepsilon}+\ln\frac{s}{\mu^2}\right)\Bigg] T_{\gamma q\to gq}(s,t,u)\\
&+8N_C C_F^2\left(-2\ln\frac{-u}{s}+4\ln\frac{-t}{s}-3\frac{s}{u}\ln\frac{-u}{s}-\left(2+\frac{u}{s}\right)\left(\pi^2+\ln^2\frac{t}{u}\right)\right.\\
&\left.-\left(2+\frac{s}{u}\right)\ln^2\frac{-t}{s}\right)\\
&-4N_C^2 C_F\left(4\ln\frac{-t}{s}-2\ln\frac{-u}{s}-\left(2+\frac{u}{s}\right)\left(\pi^2+\ln^2\frac{t}{u}\right)-\left(2+\frac{s}{u}\right)\ln^2\frac{-t}{s}\right).
\end{aligned}
$$

The contributions for incoming anti-quarks and gluons $\gamma\bar{q}\to g\bar{q}$ and $\gamma g\to q\bar{q}$ could be obtained according to table 2, if the imaginary parts were included above. The result for anti-quarks turns out to be identical to eq. (4.7), and for the gluon initiated process one obtains

$$
\begin{aligned}
V_{\gamma g\to q\bar{q}}(s,t,u) \;=\; &\Bigg[C_F\left(-\frac{2}{\varepsilon^2}-\frac{3}{\varepsilon}+\frac{2\pi^2}{3}-7+\ln^2\frac{-t}{s}+\ln^2\frac{-u}{s}\right)\\
&-\frac{N_C}{2}\left(\frac{2}{\varepsilon^2}+\frac{1}{\varepsilon}\left(\frac{11}{3}-2\ln\frac{-t}{s}-2\ln\frac{-u}{s}\right)+\frac{\pi^2}{3}+\ln^2\frac{tu}{s^2}+\frac{11}{3}\ln\frac{s}{\mu^2}\right)\\
&+\frac{N_f}{3}\left(\frac{1}{\varepsilon}+\ln\frac{s}{\mu^2}\right)\Bigg] T_{\gamma g\to q\bar{q}}(s,t,u)\\
&+8N_C C_F^2\left(2\ln\frac{-t}{s}+2\ln\frac{-u}{s}+3\frac{u}{t}\ln\frac{-t}{s}+3\frac{t}{u}\ln\frac{-u}{s}+\left(2+\frac{u}{t}\right)\ln^2\frac{-u}{s}\right.\\
&\left.+\left(2+\frac{t}{u}\right)\ln^2\frac{-t}{s}\right)\\
&-4N_C^2 C_F\left(2\ln\frac{-t}{s}+2\ln\frac{-u}{s}+\left(2+\frac{u}{t}\right)\ln^2\frac{-u}{s}+\left(2+\frac{t}{u}\right)\ln^2\frac{-t}{s}\right).
\end{aligned}
\tag{4.8}
$$

All UV poles have been cancelled by counter terms through the renormalization procedure, and the remaining IR poles are contained in the first three lines of eqs. (4.7) and (4.8). Contrary to some of the finite terms, they are proportional to the LO Born matrix elements $T_{\gamma q\to gq}$ and $T_{\gamma g\to q\bar{q}}$. The explicit dependence of the virtual corrections on the renormalization scale μ is contained in the logarithms proportional to the Born matrix elements and N_C and N_f, respectively. All terms of $\mathcal{O}(\varepsilon)$ and higher have been omitted since they do not contribute in the physical limit $d\to 4$.

4.1.2 Virtual Corrections for Resolved Photons

For the resolved virtual corrections, we show in figure 23 only the one-loop diagrams for $qq' \to qq'$ and

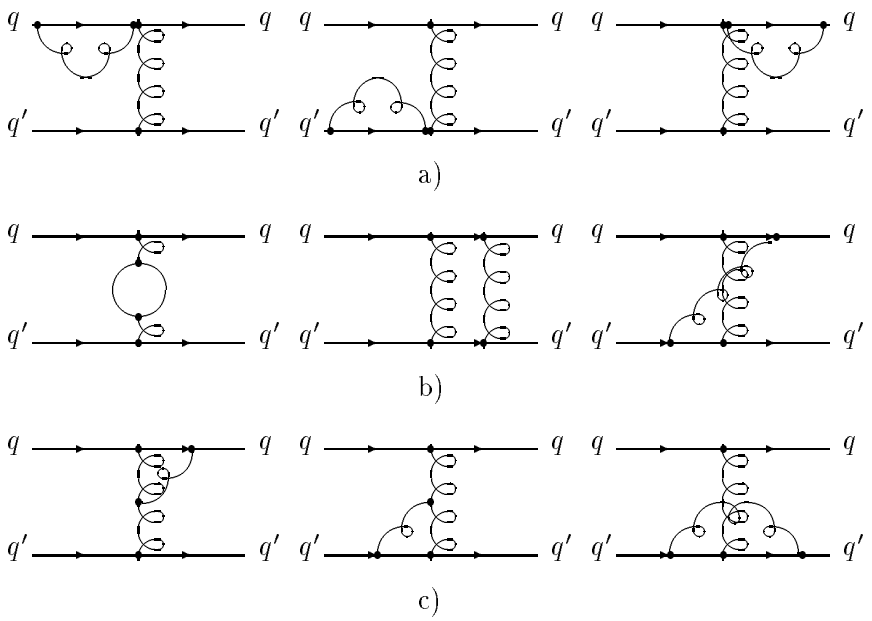

Figure 23: *Virtual diagrams for resolved photoproduction. Only the one-loop corrections to $qq' \to qq'$ are shown. The circle in diagram b) denotes a quark, gluon, and ghost loop.*

classify them again into a) self-energy diagrams, b) propagator corrections and box diagrams, and c) vertex corrections. Due to the additional gluon, these contributions are again one order higher in α_s than the Born terms as in the direct case. The complete set of diagrams can be found in [Ell86] as well as the results

$$|\mathcal{M}|^2_{ab\to 12}(s,t,u) = g^4\mu^{4\varepsilon}\frac{\alpha_s}{2\pi}\left(\frac{4\pi\mu^2}{Q^2}\right)^{\varepsilon}\frac{\Gamma(1-\varepsilon)}{\Gamma(1-2\varepsilon)}V_{ab\to 12}(s,t,u), \tag{4.9}$$

where Q^2 denotes now an arbitrary scale. For the diagrams in figure 23, we obtain

$$\begin{aligned} V_{qq'\to qq'}(s,t,u) \;=\; & \Big[C_F\left(-\frac{4}{\varepsilon^2}-\frac{1}{\varepsilon}(6+8l(s)-8l(u)-4l(t))\right. \\ & -\frac{2\pi^2}{3}-16-2l^2(t)+l(t)(6+8l(s)-8l(u)) \\ & -2\frac{s^2-u^2}{s^2+u^2}(2\pi^2+(l(t)-l(s))^2+(l(t)-l(u))^2) \\ & \left.+2\frac{s+u}{s^2+u^2}((s+u)(l(u)-l(s))+(u-s)(2l(t)-l(s)-l(u)))\right) \\ & +N_C\left(\frac{1}{\varepsilon}(4l(s)-2l(u)-2l(t))+\frac{85}{9}+\pi^2+2l(t)(l(t)+l(u)-2l(s))\right. \\ & +\frac{s^2-u^2}{2(s^2+u^2)}(3\pi^2+2(l(t)-l(s))^2+(l(t)-l(u))^2) \\ & \left.-\frac{st}{s^2+u^2}(l(t)-l(u))+\frac{2ut}{s^2+u^2}(l(t)-l(s))+\frac{11}{3}(l(-\mu^2)-l(t))\right) \\ & +\frac{N_f}{2}\left(\frac{4}{3}(l(t)-l(-\mu^2))-\frac{20}{9}\right)\Big]\,T_{qq'\to qq'}(s,t,u). \end{aligned} \tag{4.10}$$

The contributions for incoming quarks and anti-quarks of different flavor can be obtained from table 3 as well as the contribution for identical quark flavors. There one also has to include the interference term

$$\begin{aligned} V_{qq\to qq}(s,t,u) &= \left[C_F\left(-\frac{4}{\varepsilon^2}-\frac{1}{\varepsilon}(6+4l(s)-4l(t)-4l(u))-\frac{7\pi^2}{6}-16\right.\right. \\ &\quad \left.-\frac{3}{2}(l(t)+l(u))^2+2l(s)(l(t)+l(u))+2(l(t)+l(u))\right) \\ &\quad +N_C\left(\frac{1}{\varepsilon}(4l(s)-2l(t)-2l(u))+\frac{85}{9}+\frac{5}{4}(l(t)+l(u))^2\right. \\ &\quad \left.-l(t)l(u)-2l(s)(l(t)+l(u))-\frac{4}{3}(l(t)+l(u))+\frac{5}{4}\pi^2+\frac{11}{3}l(-\mu^2)\right) \\ &\quad +\frac{N_f}{2}\left(-\frac{20}{9}+\frac{2}{3}(l(t)+l(u)-2l(-\mu^2))\right) \\ &\quad \left.+\frac{1}{N_C}\left((\pi^2+(l(t)-l(u))^2)\frac{ut}{2s^2}+\frac{u}{s}l(t)+\frac{t}{s}l(u)\right)\right]T_{qq\to qq}(s,t,u). \end{aligned} \tag{4.11}$$

For incoming antiquarks, the Mandelstam variables ($s \leftrightarrow u$) have to be crossed. The first lines proportional to the color factors C_F and N_C contain the IR singular terms in the two processes discussed above. Furthermore, the complete virtual corrections are proportional to the Born matrix elements. This is not true for the case $q\bar{q} \to gg$, where the virtual corrections are given by

$$\begin{aligned} V_{q\bar{q}\to gg}(s,t,u) &= \left[C_F\left(-\frac{2}{\varepsilon^2}-\frac{3}{\varepsilon}-7-\frac{\pi^2}{3}\right)\right. \\ &\quad +N_C\left(-\frac{2}{\varepsilon^2}-\frac{11}{3\varepsilon}+\frac{11}{3}l(-\mu^2)-\frac{\pi^2}{3}\right) \\ &\quad \left.+\frac{N_f}{2}\left(\frac{4}{3\varepsilon}-\frac{4}{3}l(-\mu^2)\right)\right]T_{q\bar{q}\to gg}(s,t,u) \\ &\quad +\frac{l(s)}{\varepsilon}\left(\left(4N_C^3C_F+\frac{4C_F}{N_C}\right)\frac{t^2+u^2}{ut}-16N_C^2C_F^2\frac{t^2+u^2}{s^2}\right) \\ &\quad +\frac{8N_C^3C_F}{\varepsilon}\left(l(t)\left(\frac{u}{t}-\frac{2u^2}{s^2}\right)+l(u)\left(\frac{t}{u}-\frac{2t^2}{s^2}\right)\right) \\ &\quad -\frac{8N_CC_F}{\varepsilon}\left(\frac{u}{t}+\frac{t}{u}\right)(l(t)+l(u)) \\ &\quad +f^c(s,t,u)+f^c(s,u,t). \end{aligned} \tag{4.12}$$

Here, only parts of the IR singular terms are proportional to the Born matrix element $T_{q\bar{q}\to gg}$. The finite contributions have been put into the function

$$\begin{aligned} f^c(s,t,u) &= 8N_C^2C_F\left[\frac{l(t)l(u)}{N_C}\frac{t^2+u^2}{2tu}\right. \\ &\quad +l^2(s)\left(\frac{1}{4N_C^3}\frac{s^2}{tu}+\frac{1}{4N_C}\left(\frac{1}{2}+\frac{t^2+u^2}{tu}-\frac{t^2+u^2}{s^2}\right)-\frac{N_C}{4}\frac{t^2+u^2}{s^2}\right) \\ &\quad +l(s)\left(\left(\frac{5C_F}{4}-\frac{1}{2N_C}-\frac{1}{N_C^3}\right)-\left(N_C+\frac{1}{N_C^3}\right)\frac{t^2+u^2}{2tu}-\frac{C_F}{2}\frac{t^2+u^2}{s^2}\right) \\ &\quad +\pi^2\left(\frac{1}{8N_C}+\frac{1}{N_C^3}\left(\frac{3(t^2+u^2)}{8tu}+\frac{1}{2}\right)+N_C\left(\frac{t^2+u^2}{8tu}-\frac{t^2+u^2}{2s^2}\right)\right) \\ &\quad \left.+\left(N_C+\frac{1}{N_C}\right)\left(\frac{1}{8}-\frac{t^2+u^2}{4s^2}\right)\right. \end{aligned} \tag{4.13}$$

$$
\begin{aligned}
&+l^2(t)\left(N_C\left(\frac{s}{4t}-\frac{u}{s}-\frac{1}{4}\right)+\frac{1}{N_C}\left(\frac{t}{2u}-\frac{u}{4s}\right)+\frac{1}{N_C^3}\left(\frac{u}{4t}-\frac{s}{2u}\right)\right)\\
&+l(t)\left(N_C\left(\frac{t^2+u^2}{s^2}+\frac{3t}{4s}-\frac{5u}{4t}-\frac{1}{4}\right)-\frac{1}{N_C}\left(\frac{u}{4s}+\frac{2s}{u}+\frac{s}{2t}\right)-\frac{1}{N_C^3}\left(\frac{3s}{4t}+\frac{1}{4}\right)\right)\\
&+l(s)l(t)\left(N_C\left(\frac{t^2+u^2}{s^2}-\frac{u}{2t}\right)+\frac{1}{N_C}\left(\frac{u}{2s}-\frac{t}{u}\right)+\frac{1}{N_C^3}\left(\frac{s}{u}-\frac{u}{2t}\right)\right)\Bigg]
\end{aligned}
$$

Finally, the process $gg \to gg$ gives

$$
\begin{aligned}
V_{gg\to gg}(s,t,u) &= \left[N_C\left(-\frac{4}{\varepsilon^2}-\frac{22}{3\varepsilon}-\frac{67}{9}+\frac{11}{3}l(-\mu^2)+\frac{\pi^2}{3}\right)\right. \\
&\left.+\frac{N_f}{2}\left(\frac{8}{3\varepsilon}+\frac{20}{9}-\frac{4}{3}l(-\mu^2)\right)\right]T_{gg\to gg}(s,t,u)\\
&+\frac{32N_C^4C_F}{\varepsilon}l(s)\left(3-\frac{2tu}{s^2}+\frac{t^4+u^4}{t^2u^2}\right)\\
&+\frac{32N_C^4C_F}{\varepsilon}l(t)\left(3-\frac{2us}{t^2}+\frac{u^4+s^4}{u^2s^2}\right)\\
&+\frac{32N_C^4C_F}{\varepsilon}l(u)\left(3-\frac{2st}{u^2}+\frac{s^4+t^4}{s^2t^2}\right)\\
&+8N_C^3C_F(f^d(s,t,u)+f^d(t,u,s)+f^d(u,s,t)),
\end{aligned}
\tag{4.14}
$$

where, once more, not all IR singularities are proportional to the complete Born matrix element and the finite terms are given by the function

$$
\begin{aligned}
f^d(s,t,u) &= N_C\left[\left(\frac{2(t^2+u^2)}{tu}\right)l^2(s)+\left(\frac{4s(t^3+u^3)}{t^2u^2}-6\right)l(t)l(u)\right.\\
&\left.+\left(\frac{4}{3}\frac{tu}{s^2}-\frac{14}{3}\frac{t^2+u^2}{tu}-14-8\left(\frac{t^2}{u^2}+\frac{u^2}{t^2}\right)\right)l(s)-1-\pi^2\right]\\
&+\frac{N_f}{2}\left[\left(\frac{10}{3}\frac{t^2+u^2}{tu}+\frac{16}{3}\frac{tu}{s^2}-2\right)l(s)-\frac{s^2+tu}{tu}l^2(s)\right.\\
&\left.-2\frac{t^2+u^2}{tu}l(t)l(u)+2-\pi^2\right].
\end{aligned}
\tag{4.15}
$$

All UV singularities have already been absorbed into the Lagrangian, and terms of $\mathcal{O}(\varepsilon)$ and higher have been neglected.

As mentioned previously, the crossing of Mandelstam variables according to table 3 may change the signs of the arguments in the logarithms. This is accounted for in the definition of

$$
l(x) = \ln\left|\frac{x}{Q^2}\right|, \tag{4.16}
$$

where x may be any of the variables s, t, or u and is normalized to $Q^2 = \max(s,t,u)$. Due to the $i\eta$-prescription in the propagators, terms bilinear in the logarithms may give an extra π^2:

$$
l^2(x) = \ln^2\left(\frac{x}{Q^2}\right)-\pi^2, \text{ if } x>0, \tag{4.17}
$$

$$
l^2(x) = \ln^2\left(-\frac{x}{Q^2}\right), \quad \text{if } x<0. \tag{4.18}
$$

4.2 Real Corrections

For the calculation of the hard scattering cross section in next-to-leading order, we must include all diagrams with an additional parton in the final state. The four-vectors of these subprocesses will be labeled by $p_a p_b \to p_1 p_2 p_3$, where p_a is the momentum of the incoming photon or parton in the photon and p_b is the momentum of the incoming parton in the proton. The invariants will be denoted by $s_{ij} = (p_i + p_j)^2$ and the previously defined Mandelstam variables s, t, and u. For massless partons, the $2 \to 3$ contributions contain singularities at $s_{ij} = 0$. They can be extracted with the dimensional regularization method and cancelled against those associated with the one-loop contributions.

In order to achieve this, we go through the following steps. First, we calculate the phase space for $2 \to 3$ scattering in d dimensions and factorize it into a regular part corresponding to $2 \to 2$ scattering and a singular part corresponding to the unresolved two-parton subsystem. Next, the matrix elements for the $2 \to 3$ subprocesses are calculated in d dimensions as well. They are squared and averaged/summed over initial/final state spins and colors and can be used for incoming quarks, antiquarks, and gluons with the help of crossing.

One can distinguish three classes of singularities in photoproduction ($Q^2 \simeq 0$) depending on which propagators in the squared matrix elements vanish. Examples for these three classes are shown in figure 24. The X marks the propagator leading to the divergence. In the first graph, it is the invariant

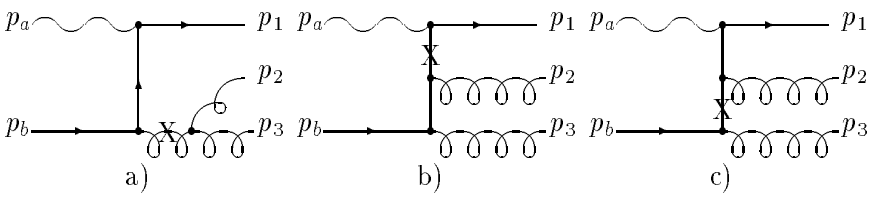

Figure 24: *Three-body diagrams with a) final state, b) photon initial state and c) proton initial state singularities.*

s_{23} given by momenta of the final state, which causes the singularity. Therefore, this divergence will be called final state singularity. The second graph becomes singular for $s_{a1} = (p_a + p_1)^2 = 0$, when the photon and the final quark momentum are parallel. This is the class of photon initial state singularities. In the third graph, the singularity occurs at $s_{b3} = (p_b + p_3)^2$, where p_b is the initial parton momentum in the proton. This stands for proton initial state singularity. Since resolved photons behave like hadrons, they produce similar initial state divergencies. The first class is familiar from calculations for jet production in e^+e^- annihilation [Fab82], the third class from jet production in deep inelastic ep scattering ($Q^2 \neq 0$) [Gra90]. The second class occurs only for direct photoproduction [Böd92].

When squaring the sum of all relevant $2 \to 3$ matrix elements, we encounter terms, where more than one of the invariants become singular, e.g. when one of the gluon momenta $p_3 \to 0$ so that $s_{23} = 0$ and $s_{b3} = 0$. These infrared singularities are disentangled by a partial fractioning decomposition, so that every term has only one vanishing denominator. This also allows the separation of the different classes of singularities in figure 24.

It turns out that the results for direct photoproduction are always proportional to the LO cross sections involved in the hard scatter

$$F, I, J_{\gamma b \to 123} = K T_{\gamma b \to 12}, \tag{4.19}$$

where F, I, and J denote final state, photon initial state and proton initial state contributions. For resolved photoproduction, this is no more true in general but only for the quark-quark scattering subprocesses with a less complicated color structure than those involving real gluons. For gluonic processes, only parts of the leading order cross sections can be factorized

$$F, I, J_{ab\to 123} = \sum_i K^{(i)} T^{(i)}_{ab\to 12}, \tag{4.20}$$

where

$$T_{ab\to 12} = \sum_i T^{(i)}_{ab\to 12} \tag{4.21}$$

is again the full Born matrix element.

As the last step, the decomposed matrix elements have to be integrated up to $s_{ij} \leq ys$. y characterizes the region, where the two partons i and j cannot be resolved. Then, the singular kernels K and $K^{(i)}$ produce terms $\propto 1/\varepsilon^2$ and $1/\varepsilon$, which will cancel against those in the virtual diagrams or be absorbed into structure functions, and finite corrections proportional to $\ln^2 y$, $\ln y$, and y^0. For small values of y, terms of $\mathcal{O}(y)$ can be neglected. In the following, we shall give the results for the different classes of singularities separately.

4.2.1 Phase Space for Three-Particle Final States

For the real corrections, we have to consider all subprocesses, which have an additional third parton in the final state attached to the $2 \to 2$ scattering process. We therefore calculate the phase space for $2 \to 3$ scattering in this section and choose as the coordinate system the center-of-mass system of partons 1 and 3 as shown in figure 25. The angle between p_a and p_1 is called θ, the azimuthal

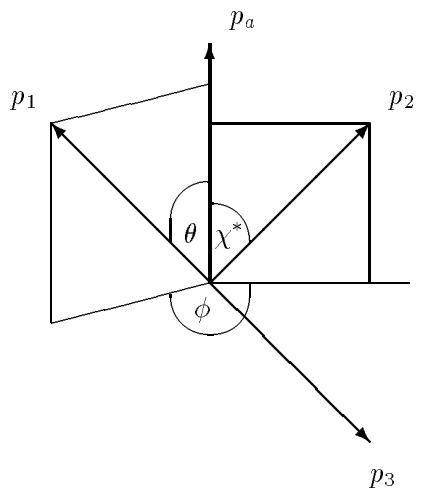

Figure 25: *Center-of-mass system of partons* 1 *and* 3 *defining the kinematic variables for the scattering of two initial into three final partons.* χ^* *is defined in the overall center-of-mass system of partons* a *and* b*.*

angle between the planes defined by p_a and p_1 and p_a and p_2 is called ϕ, and the angle χ^* between p_a and p_2 is defined in the overall center-of-mass system of the incoming partons a and b denoted by an asterisk (*). As we have to accommodate a third final particle in the scattering process, the Mandelstam variables in this section

$$s = (p_a + p_b)^2, \tag{4.22}$$

$$t = (p_a - p_1 - p_3)^2 - 2p_1p_3, \tag{4.23}$$

$$u = (p_a - p_2)^2 \tag{4.24}$$

differ slightly from the previously used ones, but still satisfy the relation $s + t + u = 0$ for massless partons. In the limit of soft ($p_3 = 0$) or collinear ($p_3 \parallel p_1$) particle emission, they can however be written in a form similar to $2 \to 2$ scattering as $t = (p_a - \overline{p}_1)^2$ and $u = (p_a - p_2)^2$. Here $\overline{p}_1 = p_1 + p_3$ represents the four-momentum of the recombined jet, and p_2 is the four-momentum of the second jet.

We start again from the general expression [Byc73]

$$\mathrm{dPS}^{(3)} = \int (2\pi)^d \prod_{i=1}^{3} \frac{\mathrm{d}^d p_i \delta(p_i^2)}{(2\pi)^{d-1}} \delta^d \left(p_a + p_b - \sum_{i=1}^{3} p_i \right) \tag{4.25}$$

and describe the final state singularity with the new variable

$$z' = \frac{p_1 p_3}{p_a p_b}. \tag{4.26}$$

We can then insert two additional δ-functions with respect to t and z'

$$\frac{\mathrm{dPS}^{(3)}}{\mathrm{d}t\mathrm{d}z'} = \int (2\pi)^d \prod_{i=1}^{3} \frac{\mathrm{d}^d p_i \delta(p_i^2)}{(2\pi)^{d-1}} \delta^d \left(p_a + p_b - \sum_{i=1}^{3} p_i \right) \delta(t + s + (p_a - p_2)^2) \delta \left(z' - \frac{2p_1p_3}{s} \right), \tag{4.27}$$

before we integrate over the $\delta(p_i^2)$ and the space-like components of the d-dimensional δ-function to eliminate p_3. The resulting expression is

$$\frac{\mathrm{dPS}^{(3)}}{\mathrm{d}t\mathrm{d}z'} = \int \frac{\mathrm{d}^{d-1}p_1\mathrm{d}^{d-1}p_2}{(2\pi)^{2d-3}2E_12E_22E_3}\delta\left(E_a+E_b-\sum_{i=1}^{3}E_i\right)\delta(t+s+(p_a-p_2)^2)\delta\left(z'-\frac{2p_1p_3}{s}\right). \quad (4.28)$$

We now decompose p_1 into its energy E_1 and angular components θ and ϕ in the center-of-mass system of partons 1 and 3, and p_2 into its components E_2^*, χ^*, and ϕ_2^* in the overall center-of-mass system with the result

$$\begin{aligned}\frac{\mathrm{dPS}^{(3)}}{\mathrm{d}t\mathrm{d}z'} &= \int \frac{1}{(2\pi)^{2d-3}8E_3}\frac{2\pi^{\frac{d-3}{2}}}{\Gamma\left(\frac{d-3}{2}\right)}E_1^{d-3}\mathrm{d}E_1\sin^{d-3}\theta\mathrm{d}\theta\sin^{d-4}\phi\mathrm{d}\phi\frac{\pi^{\frac{d-4}{2}}}{\Gamma\left(\frac{d-2}{2}\right)}{E_2^*}^{d-3}\mathrm{d}E_2^* \quad (4.29)\\ &\quad \sin^{d-3}\chi^*\mathrm{d}\chi^*\mathrm{d}\phi_2^*\delta\left(E_a+E_b-\sum_{i=1}^{3}E_i\right)\delta(t+s-2E_a^*E_2^*(1-\cos\chi^*))\delta\left(z'-\frac{4E_1^2}{s}\right).\end{aligned}$$

Integrating over the remaining δ-functions and the trivial azimuthal angle ϕ_2^* up to 2π, we arrive at

$$\frac{\mathrm{dPS}^{(3)}}{\mathrm{d}t\mathrm{d}z'} = \int \frac{(16\pi^2)^\varepsilon}{128\pi^3\Gamma(2-2\varepsilon)}z'^{-\varepsilon}u^{-\varepsilon}(t+sz')^{-\varepsilon}(b(1-b))^{-\varepsilon}\frac{\mathrm{d}b}{N_b}\sin^{-2\varepsilon}\phi\frac{\mathrm{d}\phi}{N_\phi}, \quad (4.30)$$

where we have substituted the polar angle θ by

$$b = \frac{1}{2}(1-\cos\theta), \quad (4.31)$$

and N_b and N_ϕ are the normalization factors

$$N_b = \int_0^1 \mathrm{d}b(b(1-b))^{-\varepsilon} = \frac{\Gamma^2(1-\varepsilon)}{\Gamma(2-2\varepsilon)}, \quad (4.32)$$

$$N_\phi = \int_0^\pi \sin^{-2\varepsilon}\phi\mathrm{d}\phi = \frac{\pi 4^\varepsilon\Gamma(1-2\varepsilon)}{\Gamma^2(1-\varepsilon)}. \quad (4.33)$$

Finally, we can factorize this three particle phase space into

$$\mathrm{dPS}^{(3)} = \mathrm{dPS}^{(2)}\mathrm{dPS}^{(r)}, \quad (4.34)$$

where

$$\frac{\mathrm{dPS}^{(2)}}{\mathrm{d}t} = \frac{1}{\Gamma(1-\varepsilon)}\left(\frac{4\pi s}{tu}\right)^\varepsilon\frac{1}{8\pi s} \quad (4.35)$$

is the phase space for the two observed jets with momenta $\overline{p}_1$ and p_2 already calculated in section 3.1 and

$$\mathrm{dPS}^{(r)} = \left(\frac{4\pi}{s}\right)^\varepsilon\frac{\Gamma(1-\varepsilon)}{\Gamma(1-2\varepsilon)}\frac{s}{16\pi^2}\frac{1}{1-2\varepsilon}\mathrm{d}\mu_F \quad (4.36)$$

is the phase space of the unresolved subsystem of partons 1 and 3. The integration measure is

$$\mathrm{d}\mu_F = \mathrm{d}z'z'^{-\varepsilon}\left(1+\frac{z's}{t}\right)^{-\varepsilon}\frac{\mathrm{d}b}{N_b}b^{-\varepsilon}(1-b)^{-\varepsilon}\frac{\mathrm{d}\phi}{N_\phi}\sin^{-2\varepsilon}\phi. \quad (4.37)$$

The full range of integration in $\mathrm{dPS}^{(r)}$ is given by $z' \in [0, -t/s]$, $b \in [0,1]$, and $\phi \in [0,\pi]$. The singular region is defined by the requirement that partons p_1 and p_3 are recombined, i.e. $p_3 = 0$ or p_3 parallel to p_1, so that $s_{13} = (p_1+p_3)^2 = 0$. We integrate over this region up to $s_{13} \le ys$, which restricts the range of z' to $0 \le z' \le \min\{-t/s, y\} \equiv y_F$.

4.2.2 Final State Corrections for Direct Photons

The real corrections to the QCD Compton Scattering process of figure 18 arise from two different mechanisms. Either an additional gluon can be radiated from the quark or the gluon leading to the left diagram in figure 26, or a quark-antiquark pair is emitted by a gluon as shown in the right diagram

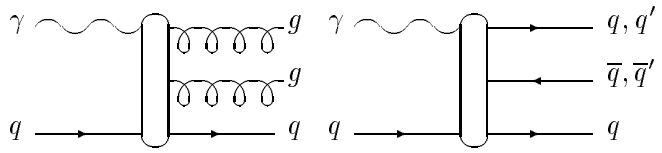

Figure 26: $2 \to 3$ *Feynman diagrams for direct photoproduction.*

of figure 26. Both cases lead to an extra factor of α_s, when the matrix elements are squared, so that all real corrections discussed in the following are of $\mathcal{O}(\alpha\alpha_s^2)$. The outgoing quark-antiquark pair can be of the same or different flavor than the incoming quark. The diagrams for incoming anti-quarks or gluons can be obtained from figure 26 by crossing a final quark or gluon line with the incoming quark line. The corresponding matrix elements can then be obtained from table 4.

Process	Matrix Element $\overline{\lvert\mathcal{M}\rvert^2}$
$\gamma q \to qgg$	$[\lvert\mathcal{M}\rvert^2_{\gamma q\to qgg}(s,t,u)]/[4N_C]/2!$
$\gamma \bar{q} \to \bar{q}gg$	$[\lvert\mathcal{M}\rvert^2_{\gamma q\to qgg}(s,t,u)]/[4N_C]/2!$
$\gamma q \to qq\bar{q}$	$[\lvert\mathcal{M}\rvert^2_{\gamma q\to qq\bar{q}}(s,t,u)]/[4N_C]$
$\gamma g \to gq\bar{q}$	$[\lvert\mathcal{M}\rvert^2_{\gamma g\to gq\bar{q}}(s,t,u)]/[8(1-\varepsilon)N_C C_F]$

Table 4: *Summary of* $2 \to 3$ *squared matrix elements for direct photoproduction.*

All possible topologies and orders of outgoing particles have to be considered for the full matrix elements of the processes, although they are not shown here explicitly. The complete result in d dimensions can be found in [Aur87] in a very compact notation not suitable to isolate the singularities. We therefore re-calculate the matrix elements with the help of REDUCE [Hea85], check their sums with the results in [Aur87], and keep only those that have singularities in a final state invariant $s_{ij} = (p_i + p_j)^2$. This can either be a soft or collinear gluon leading to a quadratic pole (left diagram of figure 26) or a collinear quark-antiquark pair leading only to a single pole (right diagram of figure 26). With the help of the singular invariant

$$z' = \frac{p_1 p_3}{p_a p_b}, \tag{4.38}$$

we can approximate the nine other invariants describing the $2 \to 3$ scattering process and express them through the $2 \to 2$ Mandelstam variables s, t, and u and the variable $b = 1/2(1 - \cos\theta)$ as defined in section 4.2.1:

$$p_a p_b = \frac{s}{2} \tag{4.39}$$

$$p_a p_1 = \frac{s}{2}\frac{-t}{s}b \tag{4.40}$$

$$p_a p_2 = \frac{s}{2}\frac{-u}{s} \tag{4.41}$$

$$p_a p_3 = \frac{s}{2}\frac{-t}{s}(1-b) \tag{4.42}$$

$$p_b p_1 = \frac{s}{2}\frac{-u}{s}b \tag{4.43}$$
$$p_b p_2 = \frac{s}{2}\frac{-t}{s} \tag{4.44}$$
$$p_b p_3 = \frac{s}{2}\frac{-u}{s}(1-b) \tag{4.45}$$
$$p_1 p_2 = \frac{s}{2}b \tag{4.46}$$
$$p_1 p_3 = \frac{s}{2}z' \tag{4.47}$$
$$p_2 p_3 = \frac{s}{2}(1-b) \tag{4.48}$$

For the subprocess $\gamma q \to qgg$, where a gluon becomes soft or collinear to the other outgoing gluon or the quark, the approximated matrix element takes the form

$$\begin{aligned} |\mathcal{M}|^2_{\gamma q\to qgg}(s,t,u) &= e^2 e_q^2 g^4 \mu^{6\varepsilon}\frac{1}{sz'}\left[4C_F\left((1-b)(1-\varepsilon)-2+\frac{-2t/s}{z'-t/s(1-b)}\right)\right. \\ &\quad \left. -4N_C\left(\frac{-t/s}{z'-t/s(1-b)}-\frac{-u/s}{z'-u/s(1-b)}-\frac{2}{z'+(1-b)}+2-b+b^2\right)\right] \\ &\quad T_{\gamma q\to gq}(s,t,u) \end{aligned} \tag{4.49}$$

with an identical result for incoming anti-quarks. The four-fermion diagram only produces a divergence from the collinear quark-antiquark pair, which can have N_f flavors

$$|\mathcal{M}|^2_{\gamma q\to qq\bar{q}}(s,t,u) = e^2 e_q^2 g^4 \mu^{6\varepsilon}\frac{1}{sz'}N_f[1-2b(1-b)(1+\varepsilon)]T_{\gamma q\to gq}(s,t,u), \tag{4.50}$$

and the gluon-initiated process $\gamma g \to gq\bar{q}$ can have a gluon that becomes soft or collinear to the quark or anti-quark

$$\begin{aligned} |\mathcal{M}|^2_{\gamma g\to gq\bar{q}}(s,t,u) &= e^2 e_q^2 g^4 \mu^{6\varepsilon}\frac{1}{sz'}\left[4C_F\left((1-b)(1-\varepsilon)-2+\frac{2}{z'+(1-b)}\right)\right. \\ &\quad \left. -2N_C\left(\frac{2}{z'+(1-b)}-\frac{-t/s}{z'-t/s(1-b)}-\frac{-u/s}{z'-u/s(1-b)}\right)\right] T_{\gamma g\to q\bar{q}}(s,t,u). \end{aligned} \tag{4.51}$$

Finally, we integrate the above matrix elements over the singular phase space $\mathrm{dPS}^{(r)}$ given in section 4.2.1. The necessary integrals are given in appendix A. The integration over ϕ in $\mathrm{dPS}^{(r)}$ is trivial, as the matrix elements do not depend on this variable. This is true for all direct and resolved photoproduction processes and for all final and initial state contributions, contrary to the case of deep-inelastic scattering. The result is

$$\int \mathrm{dPS}^{(r)}|\mathcal{M}|^2_{\gamma b\to 123}(s,t,u) = e^2 e_q^2 g^2 \mu^{4\varepsilon}\frac{\alpha_s}{2\pi}\left(\frac{4\pi\mu^2}{s}\right)^{\varepsilon}\frac{\Gamma(1-\varepsilon)}{\Gamma(1-2\varepsilon)}F_{\gamma b\to 123}(s,t,u). \tag{4.52}$$

The functions $F_{\gamma b\to 123}$ are given by

$$\begin{aligned} F_{\gamma q\to qgg}(s,t,u) &= \left[2C_F\left(\frac{1}{\varepsilon^2}-\frac{1}{2\varepsilon}\left(2\ln\frac{-t}{s}-3\right)\right.\right. \\ &\quad \left.\left. -\frac{\pi^2}{3}+\frac{7}{2}-\frac{1}{2}\ln^2\frac{-t}{s}+2\ln y_F\ln\frac{-t}{s}-2\mathrm{Li}_2\left(\frac{y_F s}{t}\right)-\ln^2 y_F-\frac{3}{2}\ln y_F\right)\right. \\ &\quad \left. -N_C\left(-\frac{2}{\varepsilon^2}-\frac{1}{\varepsilon}\left(\frac{11}{3}+\ln\frac{-t}{s}-\ln\frac{-u}{s}\right)\right.\right. \\ &\quad \left.\left. -\frac{1}{2}\ln^2\frac{-t}{s}+2\ln y_F\ln\frac{-t}{s}-2\mathrm{Li}_2\left(\frac{y_F s}{t}\right)-\frac{67}{9}+\frac{11}{3}\ln y_F+\ln^2 y_F\right.\right. \end{aligned}$$

$$+\ln^2\frac{y_F s}{-u}-\frac{1}{2}\ln^2\frac{-u}{s}+\frac{2\pi^2}{3}+2\mathrm{Li}_2\left(\frac{y_F s}{u}\right)\Bigg)\Bigg]\,T_{\gamma q\to gq}(s,t,u), \tag{4.53}$$

$$F_{\gamma q\to qq\bar{q}}(s,t,u) = N_f\left[-\frac{1}{3\varepsilon}+\frac{1}{3}\ln y_F-\frac{5}{9}\right]T_{\gamma q\to gq}(s,t,u), \tag{4.54}$$

$$\begin{aligned}F_{\gamma g\to gq\bar{q}}(s,t,u) = &\left[C_F\left(\frac{2}{\varepsilon^2}+\frac{3}{\varepsilon}-\frac{2\pi^2}{3}+7-2\ln^2 y_F-3\ln y_F\right)\right.\\ &-\frac{N_C}{2}\left(\frac{1}{\varepsilon}\left(\ln\frac{-t}{s}+\ln\frac{-u}{s}\right)+\ln^2\frac{y_F s}{-t}+\ln^2\frac{y_F s}{-u}-2\ln^2 y_F-\frac{1}{2}\ln^2\frac{-t}{s}\right.\\ &\left.\left.-\frac{1}{2}\ln^2\frac{-u}{s}+2\mathrm{Li}_2\left(\frac{y_F s}{t}\right)+2\mathrm{Li}_2\left(\frac{y_F s}{u}\right)\right)\right]T_{\gamma g\to q\bar{q}}(s,t,u).\end{aligned} \tag{4.55}$$

Terms of $\mathcal{O}(\varepsilon)$ and of $\mathcal{O}(y_F)$ have been neglected. The Spence-functions or dilogarithms Li_2 resulting from the calculation are written down explicitly even though they are also of $\mathcal{O}(y_F)$. The complete approximated $2\to 3$ matrix elements are proportional to the corresponding Born matrix elements $T_{\gamma b\to 12}$. This is also true for the exact matrix elements in four dimensions as calculated by Berends et al. [Ber81], but not for the exact d-dimensional matrix elements [Aur87].

4.2.3 Final State Corrections for Resolved Photons

For the four different generic Born diagrams of resolved photoproduction in figure 20, the real corrections all arise from an additional gluon in the final state as shown in figure 27. They are of $\mathcal{O}(\alpha_s^3)$. All

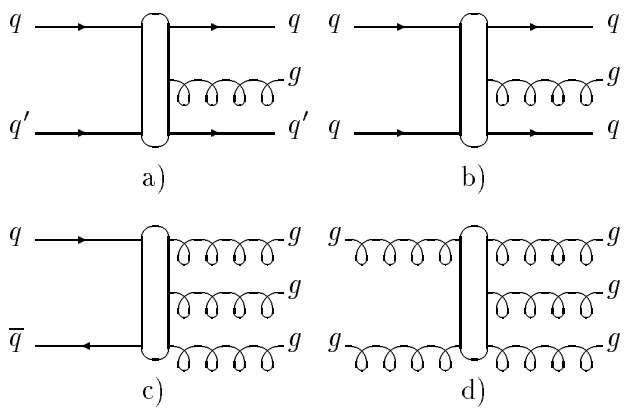

Figure 27: $2 \to 3$ *Feynman diagrams for resolved photoproduction.*

other diagrams can be obtained from figure 27 by crossing one or two outgoing gluon lines into the initial state, which leads to the gluon initiated processes with quarks in the final state, or by crossing an incoming and and outgoing quark line, which leads to the processes with incoming anti-quarks. Process c) is symmetric under the interchange of the three gluons and under the interchange of the quark and anti-quark. Process d) is completely symmetric under the interchange of any of the five gluons. The complete list of matrix elements is written down in table 5.

Process	Matrix Element $\overline{\lvert\mathcal{M}\rvert^2}$
$qq' \to qq'g$	$[\lvert\mathcal{M}\rvert^2_{qq'\to qq'g}(s,t,u)]/[4N_C^2]$
$q\bar{q}' \to q\bar{q}'g$	$[\lvert\mathcal{M}\rvert^2_{qq'\to qq'g}(u,t,s)]/[4N_C^2]$
$q\bar{q} \to \bar{q}'q'g$	$[\lvert\mathcal{M}\rvert^2_{qq'\to qq'g}(t,s,u) + \lvert\mathcal{M}\rvert^2_{q\bar{q}\to q\bar{q}g}(s,t,u)]/[4N_C^2]$
$qg \to qq'\bar{q}'$	$-[\lvert\mathcal{M}\rvert^2_{q\bar{q}\to q\bar{q}g}(t,s,u)]/[8(1-\varepsilon)N_C^2C_F]$
$qq \to qqg$	$[\lvert\mathcal{M}\rvert^2_{qq'\to qq'g}(s,t,u) + \lvert\mathcal{M}\rvert^2_{qq'\to qq'g}(s,u,t) + \lvert\mathcal{M}\rvert^2_{qq\to qqg}(s,t,u)]/[4N_C^2]/2!$
$q\bar{q} \to q\bar{q}g$	$[\lvert\mathcal{M}\rvert^2_{qq'\to qq'g}(u,t,s) + \lvert\mathcal{M}\rvert^2_{qq'\to qq'g}(u,s,t) + \lvert\mathcal{M}\rvert^2_{qq\to qqg}(u,t,s) + \lvert\mathcal{M}\rvert^2_{q\bar{q}\to q\bar{q}g}(s,t,u)]/[4N_C^2]$
$qg \to qq\bar{q}$	$-[2\lvert\mathcal{M}\rvert^2_{q\bar{q}\to q\bar{q}g}(t,s,u)]/[8(1-\varepsilon)N_C^2C_F]/2!$
$q\bar{q} \to ggg$	$[\lvert\mathcal{M}\rvert^2_{q\bar{q}\to ggg}(s,t,u)]/[4N_C^2]/3!$
$qg \to qgg$	$[-\lvert\mathcal{M}\rvert^2_{q\bar{q}\to ggg}(t,s,u)/3 + \lvert\mathcal{M}\rvert^2_{qg\to qgg}(s,t,u)]/[8(1-\varepsilon)N_C^2C_F]/2!$
$\bar{q}g \to \bar{q}gg$	$[-\lvert\mathcal{M}\rvert^2_{q\bar{q}\to ggg}(t,u,s)/3 + \lvert\mathcal{M}\rvert^2_{qg\to qgg}(u,t,s)]/[8(1-\varepsilon)N_C^2C_F]/2!$
$gg \to q\bar{q}g$	$[-\lvert\mathcal{M}\rvert^2_{qg\to qgg}(t,s,u) + \lvert\mathcal{M}\rvert^2_{gg\to q\bar{q}g}(s,t,u)]/[16(1-\varepsilon)^2N_C^2C_F^2]$
$gg \to ggg$	$[\lvert\mathcal{M}\rvert^2_{gg\to ggg}(s,t,u)]/[16(1-\varepsilon)^2N_C^2C_F^2]/3!$

Table 5: *Summary of* $2 \to 3$ *squared matrix elements for resolved photoproduction.*

In four dimensions, these matrix elements were first calculated by Gottschalk and Sivers [Got80] and by Kunszt and Pietarinen [Kun80]. The result in d dimensions was given in a compact form by Ellis and Sexton [Ell86]. We calculate the matrix elements again with the help of REDUCE [Hea85], check with the result in [Ell86], and keep only terms singular in the final state invariant z'. The result can be expressed through this variable z', b, and the Mandelstam variables s, t, and u. For quark-quark scattering of different flavors in diagram 27a), we can have a soft or collinear gluon in

the final state

$$|\mathcal{M}|^2_{qq'\to qq'g}(s,t,u) = g^6\mu^{6\varepsilon}\frac{4}{sz'}\left[(2C_F-N_C)\left(\frac{-2}{z'+(1-b)}+\frac{-t/s}{z'-t/s(1-b)}+\frac{-u/s}{z'-u/s(1-b)}\right)\right.$$
$$\left.+C_F\left((1-b)(1-\varepsilon)-2+\frac{-2u/s}{z'-u/s(1-b)}\right)\right]T_{qq'\to qq'}(s,t,u). \quad (4.56)$$

For equal flavors, there is additionally the interference contribution

$$|\mathcal{M}|^2_{qq\to qqg}(s,t,u) = g^6\mu^{6\varepsilon}\frac{4}{sz'}\left[(2C_F-N_C)\left(\frac{-2}{z'+(1-b)}+\frac{-t/s}{z'-t/s(1-b)}+\frac{-u/s}{z'-u/s(1-b)}\right)\right.$$
$$\left.+C_F\left((1-b)(1-\varepsilon)-2+\frac{2}{z'+(1-b)}\right)\right]T_{qq\to qq}(s,t,u) \quad (4.57)$$

as the final quark lines in diagram 27b) are undistinguishable and can be interchanged. The crossed diagram of quark-antiquark annihilation has an additional singularity, if the final quark-antiquark pair with N_f possible flavors becomes collinear

$$|\mathcal{M}|^2_{q\bar{q}\to q\bar{q}g}(s,t,u) = g^6\mu^{6\varepsilon}\frac{1}{sz'}N_f\left[1-2b(1-b)(1+\varepsilon)\right]T_{q\bar{q}\to gg}(s,t,u). \quad (4.58)$$

The complete matrix elements given above are proportional to the corresponding Born matrix elements $T_{ab\to 12}$. Quarks and anti-quarks can, of course, also annihilate into three final gluons as shown in figure 27c), where any pair of two gluons can produce a soft or collinear singularity:

$$|\mathcal{M}|^2_{q\bar{q}\to ggg}(s,t,u) = g^6\mu^{6\varepsilon}\frac{12}{sz'}\left[-N_C(b^2-b+2)T_{q\bar{q}\to gg}(s,t,u)\right. \quad (4.59)$$
$$+4N_CC_F$$
$$\left(\frac{-u/s}{z'-u/s(1-b)}(1-\varepsilon)\left(\frac{t^2+u^2-\varepsilon s^2}{tu}\right)\left(2N_CC_F-2N_C^2\frac{tu}{s^2}-N_C^2\frac{u^2}{s^2}\right)\right.$$
$$+\frac{1}{z'+(1-b)}(1-\varepsilon)\left(\frac{t^2+u^2-\varepsilon s^2}{tu}\right)\left(N_C^2\frac{t^2+u^2}{s^2}\right)$$
$$\left.\left.+\frac{-t/s}{z'-t/s(1-b)}(1-\varepsilon)\left(\frac{t^2+u^2-\varepsilon s^2}{tu}\right)\left(2N_CC_F-2N_C^2\frac{tu}{s^2}-N_C^2\frac{t^2}{s^2}\right)\right)\right].$$

Here, only parts of the Born matrix element $T_{q\bar{q}\to gg}$ can be factorized. The process $qg\to qgg$ can be obtained by crossing a final gluon with the incoming anti-quark or $(s\leftrightarrow t)$. In this case, either of the outgoing gluons can also be radiated from the outgoing quark leading to

$$|\mathcal{M}|^2_{qg\to qgg}(s,t,u) = g^6\mu^{6\varepsilon}\frac{4}{sz'}\left[C_F\left((1-b)(1-\varepsilon)-2\right)T_{qg\to qg}(s,t,u)\right. \quad (4.60)$$
$$-4N_CC_F$$
$$\left(\frac{-t/s}{z'-t/s(1-b)}(1-\varepsilon)\left(\frac{s^2+u^2-\varepsilon t^2}{su}\right)\left(\left(2N_CC_F-2N_C^2\frac{su}{t^2}\right)\left(-2+2\frac{C_F}{N_C}\right)\right.\right.$$
$$\left.+N_C^2\frac{s^2+u^2}{t^2}\right)$$
$$+\frac{-u/s}{z'-u/s(1-b)}(1-\varepsilon)\left(\frac{s^2+u^2-\varepsilon t^2}{su}\right)\left(2N_CC_F-2N_C^2\frac{su}{t^2}-N_C^2\frac{u^2}{t^2}\right)$$
$$\left.\left.+\frac{1}{z'+(1-b)}(1-\varepsilon)\left(\frac{s^2+u^2-\varepsilon t^2}{su}\right)\left(2N_CC_F-2N_C^2\frac{su}{t^2}-N_C^2\frac{s^2}{t^2}\right)\right)\right],$$

where again only parts of the Born matrix element $T_{qg\to qg}$ can be factorized. If also the incoming quark is crossed into the final state, the resulting quark-antiquark pair in the final state with N_f flavors can produce the collinear singularity

$$|\mathcal{M}|^2_{gg\to q\bar{q}g}(s,t,u) = g^6\mu^{6\varepsilon}\frac{1}{sz'}N_f\left[1-2b(1-b)(1+\varepsilon)\right]T_{gg\to gg}(s,t,u) \tag{4.61}$$

proportional to the full Born matrix element. Finally, the five-gluon process in figure 27d) can have three different pairs of soft or collinear gluons in the final state with the result

$$\begin{aligned}
|\mathcal{M}|^2_{gg\to ggg}(s,t,u) &= g^6\mu^{6\varepsilon}\frac{12}{sz'}\Big[-N_C\,(b^2-b+2)T_{gg\to gg}(s,t,u)\\
&\quad +16N_C^4C_F\\
&\quad \left(\frac{-t/s}{z'-t/s(1-b)}(1-\varepsilon)^2\left(3-\frac{2su}{t^2}+\frac{s^4+u^4}{s^2u^2}\right)\right.\\
&\quad +\frac{-u/s}{z'-u/s(1-b)}(1-\varepsilon)^2\left(3-\frac{2st}{u^2}+\frac{s^4+t^4}{s^2t^2}\right)\\
&\quad \left.+\frac{1}{z'+(1-b)}(1-\varepsilon)^2\left(3-\frac{2tu}{s^2}+\frac{t^4+u^4}{t^2u^2}\right)\right)\Big].
\end{aligned} \tag{4.62}$$

Only parts of the leading-order matrix element $T_{gg\to gg}$ can be factorized.

Next, the approximated matrix elements have to be integrated over the final state singularity z' in phase space up to the invariant mass cut y_F. Terms of order $\mathcal{O}(y_F)$ can be neglected if y_F is chosen sufficiently small. We use the phase space for the unobserved subsystem $\mathrm{dPS}^{(r)}$ from section 4.2.1 and find

$$\int \mathrm{dPS}^{(r)}|\mathcal{M}|^2_{ab\to 123}(s,t,u) = g^6\mu^{6\varepsilon}\frac{\alpha_s}{2\pi}\left(\frac{4\pi\mu^2}{Q^2}\right)^{\varepsilon}\frac{\Gamma(1-\varepsilon)}{\Gamma(1-2\varepsilon)}F_{ab\to 123}(s,t,u) \tag{4.63}$$

similar to the direct case. The functions $F_{ab\to 123}$ are given by

$$\begin{aligned}
F_{qq'\to qq'g}(s,t,u) &= \Big[2(2C_F-N_C)\left(-\frac{1}{2\varepsilon}(-2l(s)+l(t)+l(u))-\frac{1}{2}\left(-2l^2\left(\frac{s}{y_F}\right)\right.\right.\\
&\quad \left.+l^2\left(\frac{t}{y_F}\right)+l^2\left(\frac{u}{y_F}\right)\right)+\frac{1}{4}(-2l^2(s)+l^2(t)+l^2(u))+2\mathrm{Li}_2\left(-\left|\frac{y_FQ^2}{s}\right|\right)\\
&\quad \left.-\mathrm{Li}_2\left(-\left|\frac{y_FQ^2}{t}\right|\right)-\mathrm{Li}_2\left(-\left|\frac{y_FQ^2}{u}\right|\right)\right)\\
&\quad +2C_F\left(\frac{1}{\varepsilon^2}+\frac{1}{2\varepsilon}(3-2l(u))+\frac{1}{2}l^2(u)+\frac{7}{2}-l^2\left(\frac{u}{y_F}\right)-\frac{3}{2}\ln y_F\right.\\
&\quad \left.-\frac{\pi^2}{3}-2\mathrm{Li}_2\left(-\left|\frac{y_FQ^2}{u}\right|\right)\right)\Big]\,T_{qq'\to qq'}(s,t,u),
\end{aligned} \tag{4.64}$$

$$\begin{aligned}
F_{qq\to qqg}(s,t,u) &= \Big[2(2C_F-N_C)\left(-\frac{1}{2\varepsilon}(-2l(s)+l(t)+l(u))-\frac{1}{2}\left(-2l^2\left(\frac{s}{y_F}\right)\right.\right.\\
&\quad \left.+l^2\left(\frac{t}{y_F}\right)+l^2\left(\frac{u}{y_F}\right)\right)+\frac{1}{4}(-2l^2(s)+l^2(t)+l^2(u))+2\mathrm{Li}_2\left(-\left|\frac{y_FQ^2}{s}\right|\right)\\
&\quad \left.-\mathrm{Li}_2\left(-\left|\frac{y_FQ^2}{t}\right|\right)-\mathrm{Li}_2\left(-\left|\frac{y_FQ^2}{u}\right|\right)\right)\\
&\quad +2C_F\left(\frac{1}{\varepsilon^2}+\frac{1}{2\varepsilon}(3-2l(s))+\frac{1}{2}l^2(s)+\frac{7}{2}-l^2\left(\frac{s}{y_F}\right)-\frac{3}{2}\ln y_F\right.
\end{aligned}$$

$$-\frac{\pi^2}{3}-2\mathrm{Li}_2\left(-\left|\frac{y_F Q^2}{s}\right|\right)\Bigg)\Bigg]\,T_{qq\to qq}(s,t,u), \tag{4.65}$$

$$F_{q\bar{q}\to q\bar{q}g}(s,t,u) = N_f\left[-\frac{1}{3\varepsilon}+\frac{1}{3}\ln y_F-\frac{5}{9}\right]T_{q\bar{q}\to gg}(s,t,u), \tag{4.66}$$

$$\begin{aligned}
F_{q\bar{q}\to ggg}(s,t,u) &= \left[3N_C\left(\frac{2}{\varepsilon^2}+\frac{11}{3\varepsilon}-\frac{11}{3}\ln y_F+\frac{67}{9}-\frac{2\pi^2}{3}\right)\right]T_{q\bar{q}\to gg}(s,t,u)\\
&+6N_C C_F\left[\left(-\frac{2}{\varepsilon}l(u)+2l(u)-2l^2\left(\frac{u}{y_F}\right)+l^2(u)-4\mathrm{Li}_2\left(-\left|\frac{y_F Q^2}{u}\right|\right)\right)\right.\\
&\left(N_C^2\left(\frac{t}{u}-\frac{2t^2}{s^2}\right)-\frac{u}{t}-\frac{t}{u}\right)\\
&+\left(-\frac{2}{\varepsilon}l(s)+2l(s)-2l^2\left(\frac{s}{y_F}\right)+l^2(s)-4\mathrm{Li}_2\left(-\left|\frac{y_F Q^2}{s}\right|\right)\right)\\
&\left(N_C^2\frac{(t^2+u^2)^2}{uts^2}\right)\\
&+\left(-\frac{2}{\varepsilon}l(t)+2l(t)-2l^2\left(\frac{t}{y_F}\right)+l^2(t)-4\mathrm{Li}_2\left(-\left|\frac{y_F Q^2}{t}\right|\right)\right)\\
&\left(N_C^2\left(\frac{u}{t}-\frac{2u^2}{s^2}\right)-\frac{u}{t}-\frac{t}{u}\right)\\
&+\left(2l(u)\left(N_C^2\frac{t}{u}-\frac{s^2}{tu}\right)+2l(s)N_C^2\left(\frac{t}{u}+\frac{u}{t}\right)\right.\\
&\left.\left.+2l(t)\left(N_C^2\frac{u}{t}-\frac{s^2}{tu}\right)\right)\right],
\end{aligned} \tag{4.67}$$

$$\begin{aligned}
F_{qg\to qgg}(s,t,u) &= \left[C_F\left(\frac{1}{\varepsilon^2}+\frac{3}{2\varepsilon}-\frac{3}{2}\ln y_F+\frac{7}{2}-\frac{\pi^2}{3}\right)\right]T_{qg\to qg}(s,t,u)\\
&-N_C C_F\left[\left(-\frac{2}{\varepsilon}l(u)+2l(u)-2l^2\left(\frac{u}{y_F}\right)+l^2(u)-4\mathrm{Li}_2\left(-\left|\frac{y_F Q^2}{u}\right|\right)\right)\right.\\
&\left(N_C^2\left(\frac{s}{u}-\frac{2s^2}{t^2}\right)-\frac{u}{s}-\frac{s}{u}\right)\\
&+\left(-\frac{2}{\varepsilon}l(s)+2l(s)-2l^2\left(\frac{s}{y_F}\right)+l^2(s)-4\mathrm{Li}_2\left(-\left|\frac{y_F Q^2}{s}\right|\right)\right)\\
&\left(N_C^2\left(\frac{u}{s}-\frac{2u^2}{t^2}\right)-\frac{u}{s}-\frac{s}{u}\right)\\
&+\left(-\frac{2}{\varepsilon}l(t)+2l(t)-2l^2\left(\frac{t}{y_F}\right)+l^2(t)-4\mathrm{Li}_2\left(-\left|\frac{y_F Q^2}{t}\right|\right)\right)\\
&\left(2\frac{s^2+u^2}{t^2}+\frac{1}{N_C^2}\left(\frac{u}{s}+\frac{s}{u}\right)\right)\\
&+\left(2l(u)\left(N_C^2\frac{s}{u}-\frac{t^2}{su}\right)+2l(s)\left(N_C^2\frac{u}{s}-\frac{t^2}{su}\right)\right.\\
&\left.\left.+2l(t)\left(2+\frac{1}{N_C^2}\frac{t^2}{su}\right)\right)\right],
\end{aligned} \tag{4.68}$$

$$F_{gg\to q\bar{q}g}(s,t,u) = N_f\left[-\frac{1}{3\varepsilon}+\frac{1}{3}\ln y_F-\frac{5}{9}\right]T_{gg\to gg}(s,t,u), \tag{4.69}$$

$$\begin{aligned}
F_{gg\to ggg}(s,t,u) &= \left[3N_C\left(\frac{2}{\varepsilon^2}+\frac{11}{3\varepsilon}-\frac{11}{3}\ln y_F+\frac{67}{9}-\frac{2\pi^2}{3}\right)\right]T_{gg\to gg}(s,t,u)\\
&\quad +48N_C^4C_F\left[\left(-\frac{1}{\varepsilon}l(t)+2l(t)-l^2\left(\frac{t}{y_F}\right)+\frac{1}{2}l^2(t)-2\mathrm{Li}_2\left(-\left|\frac{y_FQ^2}{t}\right|\right)\right)\right.\\
&\quad \left(3-\frac{2us}{t^2}+\frac{u^4+s^4}{u^2s^2}\right)\\
&\quad +\left(-\frac{1}{\varepsilon}l(u)+2l(u)-l^2\left(\frac{u}{y_F}\right)+\frac{1}{2}l^2(u)-2\mathrm{Li}_2\left(-\left|\frac{y_FQ^2}{u}\right|\right)\right)\\
&\quad \left(3-\frac{2ts}{u^2}+\frac{t^4+s^4}{t^2s^2}\right)\\
&\quad +\left(-\frac{1}{\varepsilon}l(s)+2l(s)-l^2\left(\frac{s}{y_F}\right)+\frac{1}{2}l^2(s)-2\mathrm{Li}_2\left(-\left|\frac{y_FQ^2}{s}\right|\right)\right)\\
&\quad \left.\left(3-\frac{2tu}{s^2}+\frac{t^4+u^4}{t^2u^2}\right)\right].
\end{aligned} \tag{4.70}$$

All terms of $\mathcal{O}(\varepsilon)$ have been omitted since they do not contribute in the physical limit $d\to 4$.

As in the virtual corrections, we account for sign-changing arguments in the logarithms before and after crossing with the definition of

$$l(x)=\ln\left|\frac{x}{Q^2}\right|, \tag{4.71}$$

where x is any of the Mandelstam variables s, t, and u and Q^2 is an arbitrary scale chosen to be $Q^2=\max(s,t,u)$. However, there are no additional terms of π^2 in the real corrections so that

$$l^2(x)=\ln^2\left|\frac{x}{Q^2}\right| \tag{4.72}$$

for $x>0$ as well as for $x<0$.

4.2.4 Phase Space for Three-Particle Final States Revisited

Having calculated all real corrections coming from final state singularities, where the singular variable was $s_{13} = (p_1 + p_3)^2$, we now turn to the singularities that arise in the photon and proton initial states in the variables $s_{a3} = (p_a + p_3)^2$ and $s_{b3} = (p_b + p_3)^2$. The singular variables are then defined as

$$z'' = \frac{p_a p_3}{p_a p_b} \text{ and } z''' = \frac{p_b p_3}{p_a p_b}, \tag{4.73}$$

respectively. It is convenient to calculate the three-body phase space in the same center-of-mass system of the two final state particles *now called* 1 *and* 2 as in the case of final state corrections (see figure 25), where now p_3 is defined in the overall center-of-mass system of partons a and b. However, we will not choose the angle θ between the hard jet and the incoming photon or the related variable $b = 1/2(1 - \cos\theta)$ as the second independent variable. Instead it is more convenient to choose the fraction of the center-of-mass energy going into the hard subprocess $ab \to 12$

$$z_a = \frac{p_1 p_2}{p_a p_b} \in [X_a, 1] \text{ and } z_b = \frac{p_1 p_2}{p_a p_b} \in [X_b, 1], \tag{4.74}$$

respectively. In this way, the variables z_a and z_b describe the momentum of the third unobserved particle $p_3 = (1 - z_a)p_a$ and $p_3 = (1 - z_b)p_b$. They are bounded from below through the fractions of the initial electron and proton energies transferred to the partons with momenta $z_a p_a$ and $z_b p_b$ in the hard scattering

$$X_a = \frac{p_1 p_2}{k p_b} \text{ and } X_b = \frac{p_1 p_2}{p_a p}. \tag{4.75}$$

As the three-particle phase space can be calculated for photon and proton initial state singularities in exactly the same manner, we only consider the case of the photon initial state in the following. The Mandelstam variables differ slightly from those used in $2 \to 2$ scattering and final state corrections in order to accommodate the third unobserved particle radiated from the initial state

$$s = (z_a p_a + p_b)^2 = (p_1 + p_2)^2, \tag{4.76}$$

$$t = (z_a p_a - p_1)^2, \tag{4.77}$$

$$u = (z_a p_a - p_2)^2. \tag{4.78}$$

In the limit of soft ($p_3 = 0$) or collinear ($p_3 \parallel p_a$) particle emission, they satisfy the relation $s + t + u = sz'' \to 0$ for massless partons.

The calculation proceeds as follows: We insert three additional δ-functions with respect to t, z'', and z_a into the general expression

$$\mathrm{dPS}^{(3)} = \int (2\pi)^d \prod_{i=1}^{3} \frac{\mathrm{d}^d p_i \delta(p_i^2)}{(2\pi)^{d-1}} \delta^d \left(p_a + p_b - \sum_{i=1}^{3} p_i \right) \tag{4.79}$$

giving

$$\begin{aligned} \frac{\mathrm{dPS}^{(3)}}{\mathrm{d}t\mathrm{d}z''\mathrm{d}z_a} &= \int (2\pi)^d \prod_{i=1}^{3} \frac{\mathrm{d}^d p_i \delta(p_i^2)}{(2\pi)^{d-1}} \delta^d \left(p_a + p_b - \sum_{i=1}^{3} p_i \right) \\ &\quad \delta(t - (z_a p_a - p_1)^2) \delta \left(z'' - \frac{p_a p_3}{p_a p_b} \right) \delta \left(z_a - \frac{p_1 p_2}{p_a p_b} \right). \end{aligned} \tag{4.80}$$

Next, we integrate over the $\delta(p_i^2)$ and the space-like components of the d-dimensional δ-function to eliminate p_2. In the resulting expression

$$\begin{aligned} \frac{\mathrm{dPS}^{(3)}}{\mathrm{d}t\mathrm{d}z''\mathrm{d}z_a} &= \int \frac{\mathrm{d}^{d-1} p_1 \mathrm{d}^{d-1} p_3}{(2\pi)^{2d-3} 2E_1 2E_2 2E_3} \delta \left(E_a + E_b - \sum_{i=1}^{3} E_i \right) \\ &\quad \delta(t - (z_a p_a - p_1)^2) \delta \left(z'' - \frac{p_a p_3}{p_a p_b} \right) \delta \left(z_a - \frac{p_1 p_2}{p_a p_b} \right), \end{aligned} \tag{4.81}$$

we now decompose p_1 into its energy and angular components in the center-of-mass system of partons 1 and 2 and p_3 in the overall center-of-mass system

$$\begin{aligned}\frac{\mathrm{dPS}^{(3)}}{\mathrm{d}t\mathrm{d}z''\mathrm{d}z_a} &= \int \frac{1}{(2\pi)^{2d-3}8E_2}\frac{2\pi^{\frac{d-3}{2}}}{\Gamma\left(\frac{d-3}{2}\right)}E_1^{d-3}\mathrm{d}E_1\sin^{d-3}\theta\mathrm{d}\theta\sin^{d-4}\phi\mathrm{d}\phi\frac{\pi^{\frac{d-4}{2}}}{\Gamma\left(\frac{d-2}{2}\right)}E_3^{*d-3}\mathrm{d}E_3^* \\ &\quad \sin^{d-3}\chi^*\mathrm{d}\chi^*\mathrm{d}\phi_3^*\delta\left(E_a+E_b-\sum_{i=1}^{3}E_i\right)\delta(t+2z_aE_aE_1(1-\cos\theta)) \\ &\quad \delta\left(z''-\frac{2z_aE_a^*E_3^*}{s}(1-\cos\chi^*)\right)\delta\left(z_a-\frac{4z_aE_1^2}{s}\right). \end{aligned} \tag{4.82}$$

Integrating over the remaining δ-functions and the trivial azimuthal angle ϕ_2^* up to 2π, we arrive at

$$\frac{\mathrm{dPS}^{(3)}}{\mathrm{d}t\mathrm{d}z''\mathrm{d}z_a} = \int \frac{(16\pi^2)^\varepsilon}{128\pi^3\Gamma^2(1-\varepsilon)}z''^{-\varepsilon}(ut)^{-\varepsilon}(1-z'')^{-1+2\varepsilon}(1-z_a-z'')^{-\varepsilon}z_a^{-1+\varepsilon}\sin^{-2\varepsilon}\phi\frac{\mathrm{d}\phi}{N_\phi}, \tag{4.83}$$

where N_ϕ is the normalization factor given in eq. (4.33). Finally, we can factorize this three particle phase space into

$$\mathrm{dPS}^{(3)} = \mathrm{dPS}^{(2)}\mathrm{dPS}^{(r)}, \tag{4.84}$$

where $\mathrm{dPS}^{(2)}$ is the usual phase space for the two observed jets 1 and 2 from section 3.1 and

$$\mathrm{dPS}^{(r)} = \left(\frac{4\pi}{s}\right)^\varepsilon\frac{\Gamma(1-\varepsilon)}{\Gamma(1-2\varepsilon)}\frac{s}{16\pi^2}H(z'')\mathrm{d}\mu_I \tag{4.85}$$

is the phase space of the unresolved subsystem of partons a and 3. The integration measure is

$$\mathrm{d}\mu_I = \mathrm{d}z''z''^{-\varepsilon}\frac{\mathrm{d}z_a}{z_a}\left(\frac{z_a}{1-z_a}\right)^\varepsilon\frac{\mathrm{d}\phi}{N_\phi}\sin^{-2\varepsilon}\phi\frac{\Gamma(1-2\varepsilon)}{\Gamma^2(1-\varepsilon)}, \tag{4.86}$$

and the function

$$H(z'') = (1-z'')^{-1+2\varepsilon}\left(1-\frac{z''}{1-z_a}\right)^{-\varepsilon} = 1+\mathcal{O}(z'') \tag{4.87}$$

can be approximated by 1 as it leads only to negligible terms of $\mathcal{O}(y)$. The integration of $\mathrm{dPS}^{(r)}$ over $z''\in[0,-u/s]$, $z_a\in[X_a,1]$, and $\phi\in[0,\pi]$ is restricted to the singular region of z'', when partons p_a and p_3 are recombined, such that $0\le z''\le\min\{-u/s,y\}\equiv y_I$.

4.2.5 Photon Initial State Corrections for Direct Photons

Singularities from the initial direct photon arise from diagrams of type b) in figure 24. The photon here splits up into a quark-antiquark pair, and one of the two becomes a part of the photon remnant. If the (anti-)quark is collinear to the incoming photon, a simple $1/\varepsilon$ pole is produced. Quadratic $1/\varepsilon^2$ poles corresponding to soft *and* collinear singularities do not exist, since there is no direct coupling to a gluon line. In this specific case, it is therefore not necessary to perform a partial fractioning decomposition.

The matrix elements for the $2 \to 3$ processes $\gamma q \to qgg$ and $\gamma q \to qq\bar{q}$ are computed from the generic diagrams in figure 26 as in the case of final state corrections in section 4.2.2. Those for the processes with incoming anti-quarks and gluons are obtained by simple crossing of the diagrams or Mandelstam variables according to table 4. We keep only terms that are singular in the variable

$$z'' = \frac{p_a p_3}{p_a p_b} \tag{4.88}$$

and express the ten invariants for $2 \to 3$ scattering through z'', the longitudinal momentum fraction z_a transferred from the photon to the parton entering the hard subprocess, and the variables s, t, and u defined in section 4.2.4:

$$\begin{aligned}
p_a p_b &= \frac{s}{2z_a} && (4.89)\\
p_a p_1 &= \frac{s}{2z_a}\frac{-t}{s} && (4.90)\\
p_a p_2 &= \frac{s}{2z_a}\frac{-u}{s} && (4.91)\\
p_a p_3 &= \frac{s}{2z_a} z'' && (4.92)\\
p_b p_1 &= \frac{s}{2z_a}\frac{-u}{s} z_a && (4.93)\\
p_b p_2 &= \frac{s}{2z_a}\frac{-t}{s} z_a && (4.94)\\
p_b p_3 &= \frac{s}{2z_a}(1 - z_a) && (4.95)\\
p_1 p_2 &= \frac{s}{2z_a} z_a && (4.96)\\
p_1 p_3 &= \frac{s}{2z_a}\frac{-t}{s}(1 - z_a) && (4.97)\\
p_2 p_3 &= \frac{s}{2z_a}\frac{-u}{s}(1 - z_a) && (4.98)
\end{aligned}$$

Under these approximations, a singular kernel can be factorized out, which is universal for all processes of the type $\gamma b \to 123$ and describes the splitting of a boson (in this case the photon) into two fermions (i.e. the quark-antiquark pair). Consequently, a parton from the photon scatters now off the parton in the proton and the relevant parton-parton Born matrix elements show up. In the case of

$$|\mathcal{M}|^2_{\gamma q \to qgg}(s,t,u) = e^2 e_q^2 g^4 \mu^{6\varepsilon} \frac{1}{sz''}\left[z_a^2 + (1-z_a)^2 - \varepsilon\right] T_{q\bar{q}\to gg}(s,t,u), \tag{4.99}$$

it is the quark-antiquark annihilation process into two gluons. For

$$|\mathcal{M}|^2_{\gamma q \to qq\bar{q}}(s,t,u) = e^2 e_q^2 g^4 \mu^{6\varepsilon} \frac{1}{sz''}\left[z_a^2 + (1-z_a)^2 - \varepsilon\right] T_{q\bar{q}\to q\bar{q}}(s,t,u), \tag{4.100}$$

it is the process $q\bar{q} \to q\bar{q}$. The result for

$$|\mathcal{M}|^2_{\gamma g \to g q \bar{q}}(s,t,u) = e^2 e_q^2 g^4 \mu^{6\varepsilon} \frac{1}{s z''} \left[z_a^2 + (1-z_a)^2 - \varepsilon \right] T_{qg\to qg}(s,t,u) \tag{4.101}$$

is easily obtained by crossing ($s \leftrightarrow t$) in the first process and multiplying by (-1).

As the matrix elements do not depend on the variable ϕ, the integration over ϕ in $\mathrm{dPS}^{(r)}$ is as trivial as before. In addition, the integration over the simple pole in z'' can also be carried out easily. However, the integration over the momentum fraction z_a involves a convolution with the photon spectrum in the electron. Since these exist only in a parametrized form too complicated to integrate, the z_a-integration has to be done numerically and is written down explicitly in the final result

$$\int \mathrm{dPS}^{(r)} |\mathcal{M}|^2_{\gamma b \to 123}(s,t,u) = \int\limits_{X_a}^{1} \frac{\mathrm{d}z_a}{z_a} e^2 g^2 \mu^{4\varepsilon} \frac{\alpha_s}{2\pi} \left(\frac{4\pi\mu^2}{s} \right)^{\varepsilon} \frac{\Gamma(1-\varepsilon)}{\Gamma(1-2\varepsilon)} I_{\gamma b \to 123}(s,t,u). \tag{4.102}$$

The functions $I_{\gamma b \to 123}$ are given by

$$I_{\gamma q \to q g g}(s,t,u) = \left[-\frac{1}{\varepsilon} \frac{1}{2N_C} P_{q\leftarrow\gamma}(z_a) + \frac{1}{2N_C} P_{q\leftarrow\gamma}(z_a) \ln\left(y_I \frac{1-z_a}{z_a} \right) + \frac{e_q^2}{2} \right] T_{q\bar{q}\to gg}(s,t,u), \tag{4.103}$$

$$I_{\gamma q \to q q \bar{q}}(s,t,u) = \left[-\frac{1}{\varepsilon} \frac{1}{2N_C} P_{q\leftarrow\gamma}(z_a) + \frac{1}{2N_C} P_{q\leftarrow\gamma}(z_a) \ln\left(y_I \frac{1-z_a}{z_a} \right) + \frac{e_q^2}{2} \right] T_{q\bar{q}\to q\bar{q}}(s,t,u), \tag{4.104}$$

$$I_{\gamma g \to g q \bar{q}}(s,t,u) = \left[-\frac{1}{\varepsilon} \frac{1}{2N_C} P_{q\leftarrow\gamma}(z_a) + \frac{1}{2N_C} P_{q\leftarrow\gamma}(z_a) \ln\left(y_I \frac{1-z_a}{z_a} \right) + \frac{e_q^2}{2} \right] T_{qg\to qg}(s,t,u). \tag{4.105}$$

Terms of $\mathcal{O}(\varepsilon)$ and $\mathcal{O}(y)$ have been omitted as before.

The collinear $1/\varepsilon$ poles are proportional to the splitting function

$$P_{q\leftarrow\gamma}(z_a) = 2N_C e_q^2 P_{q\leftarrow g}(z_a) \tag{4.106}$$

for photons into quarks, where e_q is the fractional charge of the quark coupling to the photon and

$$P_{q\leftarrow g}(z_a) = \frac{1}{2} \left[z_a^2 + (1-z_a)^2 \right] \tag{4.107}$$

is the Altarelli-Parisi splitting function for gluons into quarks. This function appears in the evolution equation of the photon structure function as an inhomogeneous or so-called point-like term (see section 2.3). Therefore, the photon initial state singularities can be absorbed into the photon structure function. The necessary steps are well known [Böd92, Ell80]. We define the renormalized distribution function of a parton a in the electron $F_{a/e}(X_a, M_a^2)$ as

$$F_{a/e}(X_a, M_a^2) = \int_{X_a}^{1} \frac{\mathrm{d}z_a}{z_a} \left[\delta_{a\gamma}\delta(1-z_a) + \frac{\alpha}{2\pi} R_{q\leftarrow\gamma}(z_a, M_a^2) \right] F_{\gamma/e}\left(\frac{X_a}{z_a} \right), \tag{4.108}$$

where R has the general form

$$R_{a\leftarrow\gamma}(z_a, M_a^2) = -\frac{1}{\varepsilon} P_{q\leftarrow\gamma}(z_a) \frac{\Gamma(1-\varepsilon)}{\Gamma(1-2\varepsilon)} \left(\frac{4\pi\mu^2}{M_a^2} \right)^{\varepsilon} + C_{q\leftarrow\gamma}(z_a) \tag{4.109}$$

with $C = 0$ in the $\overline{\mathrm{MS}}$ scheme. The renormalized partonic cross section for $\gamma b \to$ jets is then calculated from

$$\mathrm{d}\sigma(\gamma b \to \text{jets}) = \mathrm{d}\bar{\sigma}(\gamma b \to \text{jets}) - \frac{\alpha}{2\pi} \int \mathrm{d}z_a R_{q\leftarrow\gamma}(z_a, M_a^2) \mathrm{d}\sigma(ab \to \text{jets}). \tag{4.110}$$

$d\bar{\sigma}(\gamma b \to \text{jets})$ is the higher order cross section before the subtraction procedure, and $d\sigma(ab \to \text{jets})$ contains the LO parton-parton scattering matrix elements $T_{ab\to 12}(s,t,u)$. The factor $4\pi\mu^2/M_a^2$ in eq. (4.109) is combined with the factor $4\pi\mu^2/s$ in eq. (4.102) and leads to M_a^2 dependent terms of the form

$$-\frac{1}{\varepsilon}P_{q\leftarrow\gamma}(z_a)\left[\left(\frac{4\pi\mu^2}{s}\right)^{\varepsilon}-\left(\frac{4\pi\mu^2}{M_a^2}\right)^{\varepsilon}\right]=-P_{q\leftarrow\gamma}(z_a)\ln\left(\frac{M_a^2}{s}\right), \tag{4.111}$$

so that the cross section after subtraction in eq. (4.110) will depend on the factorization scale M_a^2.

4.2.6 Proton Initial State Corrections for Direct Photons

Initial state singularities cannot only show up on the direct photon side, but also on the proton side. The parton from the proton, which undergoes the hard scattering, will then radiate a soft or collinear secondary parton. A quark can, e.g., radiate a gluon as in figure 24c), which will then not be observed but contributes to the proton remnant. As we can now have soft gluons, we find not only single but also quadratic poles in ε. After singling out the matrix elements for the diagrams in figure 26 singular in the variable

$$z''' = \frac{p_b p_3}{p_a p_b}, \tag{4.112}$$

we therefore have to decompose them with partial fractioning using REDUCE [Hea85]. The invariants are approximated quite similarly to the photon initial state corrections and are given by

$$\begin{aligned}
p_a p_b &= \frac{s}{2z_b} && (4.113)\\
p_a p_1 &= \frac{s}{2z_b}\frac{-t}{s} z_b && (4.114)\\
p_a p_2 &= \frac{s}{2z_b}\frac{-u}{s} z_b && (4.115)\\
p_a p_3 &= \frac{s}{2z_b}(1-z_b) && (4.116)\\
p_b p_1 &= \frac{s}{2z_b}\frac{-u}{s} && (4.117)\\
p_b p_2 &= \frac{s}{2z_b}\frac{-t}{s} && (4.118)\\
p_b p_3 &= \frac{s}{2z_b} z''' && (4.119)\\
p_1 p_2 &= \frac{s}{2z_b} z_b && (4.120)\\
p_1 p_3 &= \frac{s}{2z_b}\frac{-u}{s}(1-z_b) && (4.121)\\
p_2 p_3 &= \frac{s}{2z_b}\frac{-t}{s}(1-z_b) && (4.122)
\end{aligned}$$

The result for the first subprocess $\gamma q \to qgg$ turns out to be

$$\begin{aligned}
|\mathcal{M}|^2_{\gamma q\to qgg}(s,t,u) &= e^2 e_q^2 g^4 \mu^{6\varepsilon} \frac{1}{sz'''}\left[4C_F\left((1-z_b)(1-\varepsilon)-2+\frac{-2t/s}{z'''-t/s(1-z_b)}\right)\right.\\
&\quad \left. -4N_C\left(\frac{-t/s}{z'''-t/s(1-z_b)}-\frac{-u/s}{z'''-u/s(1-z_b)}\right)\right] T_{\gamma q\to gq}(s,t,u). \qquad (4.123)
\end{aligned}$$

Since the initial quark has to couple to the photon, it cannot vanish in the beam pipe. The singular kernel only describes the radiation of a gluon from the quark, factorizing the leading-order QCD Compton process $\gamma q \to gq$. According to table 4, we find the same result for incoming anti-quarks. In the four-fermion process

$$|\mathcal{M}|^2_{\gamma q\to qq\bar{q}}(s,t,u) = e^2 e_q^2 g^4 \mu^{6\varepsilon}\frac{1}{sz'''}\left[\frac{1+(1-z_b)^2}{z_b}-\varepsilon z_b\right] T_{\gamma g\to q\bar{q}}(s,t,u), \tag{4.124}$$

the initial quark necessarily produces a collinear final state quark. Thus, we have a non-diagonal transition of the quark-initiated process $\gamma q \to qq\bar{q}$ into the gluon-initiated process $\gamma g \to q\bar{q}$. The other non-diagonal transition shows up in

$$|\mathcal{M}|^2_{\gamma g\to gq\bar{q},1}(s,t,u) = e^2 e_q^2 g^4 \mu^{6\varepsilon}\frac{2}{sz'''}C_F\left[(z_b^2+(1-z_b)^2)(1+\varepsilon)-\varepsilon\right] T_{\gamma q\to gq}(s,t,u), \tag{4.125}$$

where the gluon-initiated process $\gamma g \to gq\bar{q}$ is transformed into the quark-initiated process $\gamma q \to gq$. The splitting of a gluon into a collinear quark-antiquark pair is analogous to the splitting of the direct photon in the last section. However, the gluon also possesses a non-abelian coupling to other gluons, which can become soft or collinear in

$$\begin{aligned}|\mathcal{M}|^2_{\gamma g\to gq\bar{q},2}(s,t,u) &= e^2e_q^2g^4\mu^{6\varepsilon}\frac{2}{sz'''}N_C\left[2\left(\frac{1}{z_b}+z_b(1-z_b)-2\right)\right.\\ &\left.+\frac{-t/s}{z'''-t/s(1-z_b)}-\frac{-u/s}{z'''-u/s(1-z_b)}\right]T_{\gamma g\to q\bar{q}}(s,t,u) \qquad (4.126)\end{aligned}$$

and factorizes the photon-gluon fusion process $\gamma g \to q\bar{q}$.

The complete list of proton initial state corrections given above has to be integrated over the phase space region, where parton 3 is an unobserved part of the proton remnant. The phase space for three-particle final states is taken from section 4.2.4, where $(z'' \leftrightarrow z''')$ and $(z_a \leftrightarrow z_b)$ have to be interchanged. The relevant integrals are calculated in appendix B. The result is

$$\int \mathrm{dPS}^{(r)}|\mathcal{M}|^2_{\gamma b\to 123}(s,t,u) = \int\limits_{X_b}^{1}\frac{\mathrm{d}z_b}{z_b}e^2e_q^2g^2\mu^{4\varepsilon}\frac{\alpha_s}{2\pi}\left(\frac{4\pi\mu^2}{s}\right)^{\varepsilon}\frac{\Gamma(1-\varepsilon)}{\Gamma(1-2\varepsilon)}J_{\gamma b\to 123}(s,t,u), \qquad (4.127)$$

where the functions $J_{\gamma b\to 123}$ are given by

$$\begin{aligned}J_{\gamma q\to qgg}(s,t,u) &= \left[2C_F\left(-\frac{1}{\varepsilon}\frac{1}{C_F}P_{q\leftarrow q}(z_b)+\delta(1-z_b)\left(\frac{1}{\varepsilon^2}+\frac{1}{2\varepsilon}\left(3-2\ln\frac{-t}{s}\right)+\frac{1}{2}\ln^2\frac{-t}{s}+\pi^2\right)\right.\right.\\ &+1-z_b+(1-z_b)\ln\left(y_J\frac{1-z_b}{z_b}\right)+2R_+\left(\frac{-t}{s}\right)-2\ln\left(\frac{-t}{s}\left(\frac{1-z_b}{z_b}\right)^2\right)\\ &\left.-2\frac{z_b}{1-z_b}\ln\left(1+\frac{-t}{y_Js}\frac{1-z_b}{z_b}\right)\right)\\ &-N_C\left(\delta(1-z_b)\left(\frac{1}{\varepsilon}\ln\frac{u}{t}+\frac{1}{2}\ln^2\frac{-t}{s}-\frac{1}{2}\ln^2\frac{-u}{s}\right)+2R_+\left(\frac{-t}{s}\right)-2R_+\left(\frac{-u}{s}\right)\right.\\ &-2\ln\left(\frac{-t}{s}\left(\frac{1-z_b}{z_b}\right)^2\right)+2\ln\left(\frac{-u}{s}\left(\frac{1-z_b}{z_b}\right)^2\right)\\ &\left.\left.-2\frac{z_b}{1-z_b}\ln\left(1+\frac{-t}{y_Js}\frac{1-z_b}{z_b}\right)+2\frac{z_b}{1-z_b}\ln\left(1+\frac{-u}{y_Js}\frac{1-z_b}{z_b}\right)\right)\right]\\ &T_{\gamma q\to gq}(s,t,u), \qquad (4.128)\\ J_{\gamma q\to qq\bar{q}}(s,t,u) &= \frac{1}{2}\left[-\frac{1}{\varepsilon}\frac{1}{C_F}P_{g\leftarrow q}(z_b)+\frac{1}{C_F}P_{g\leftarrow q}(z_b)\left(\ln\left(y_J\frac{1-z_b}{z_b}\right)+1\right)\right.\\ &\left.-2\frac{1-z_b}{z_b}\right]T_{\gamma g\to q\bar{q}}(s,t,u), \qquad (4.129)\\ J_{\gamma g\to gq\bar{q},1}(s,t,u) &= 2C_F\left[-\frac{1}{\varepsilon}P_{q\leftarrow g}(z_b)+P_{q\leftarrow g}(z_b)\left(\ln\left(y_J\frac{1-z_b}{z_b}\right)-1\right)+\frac{1}{2}\right]\\ &T_{\gamma q\to gq}(s,t,u), \qquad (4.130)\\ J_{\gamma g\to gq\bar{q},2}(s,t,u) &= N_C\left[-\frac{1}{\varepsilon}\frac{1}{N_C}P_{g\leftarrow g}(z_b)+\delta(1-z_b)\left(\frac{1}{\varepsilon^2}+\frac{1}{\varepsilon}\frac{1}{N_C}\left(\frac{11}{6}N_C-\frac{1}{3}N_f\right)-\frac{1}{2\varepsilon}\ln\frac{tu}{s^2}\right.\right.\\ &\left.+\frac{1}{4}\ln^2\frac{-t}{s}+\frac{1}{4}\ln^2\frac{-u}{s}+\pi^2\right)-2R_+\left(\frac{-t}{s}\right)-2R_+\left(\frac{-u}{s}\right)\\ &+2\ln\left(\frac{-t}{s}\left(\frac{1-z_b}{z_b}\right)^2\right)+2\ln\left(\frac{-u}{s}\left(\frac{1-z_b}{z_b}\right)^2\right)\\ &\left.+2\frac{z_b}{1-z_b}\ln\left(1+\frac{-t}{y_Js}\frac{1-z_b}{z_b}\right)+2\frac{z_b}{1-z_b}\ln\left(1+\frac{-u}{y_Js}\frac{1-z_b}{z_b}\right)\right.\end{aligned}$$

$$-4\left(\frac{1-z_b}{z_b}+z_b(1-z_b)\right)\ln\left(y_J\frac{1-z_b}{z_b}\right)\Bigg]\left(-\frac{N_C}{4}\right)\Bigg]T_{\gamma g\to q\bar{q}}(s,t,u). \tag{4.131}$$

Here, we have used the function

$$R_+(x) \;=\; \left(\frac{\ln\left(x\left(\frac{1-z_b}{z_b}\right)^2\right)}{1-z_b}\right)_+ \tag{4.132}$$

as an abbreviation. As the integration over z_b in eq. (4.127) runs from X_b to 1, the +-distributions [Alt78] are defined as

$$D_+[g]=\int_{X_b}^1 \mathrm{d}z_b D(z_b)g(z_b)-\int_0^1 \mathrm{d}z_b D(z_b)g(1), \tag{4.133}$$

where

$$g(z_b)=\frac{1}{z_b}F_{b'/p}\left(\frac{X_b}{z_b}\right)h(z_b), \tag{4.134}$$

and $h(z_b)$ is a regular function of z_b [Fur82]. This leads to additional terms not given here explicitly when eq. (4.133) is transformed so that both integrals are calculated in the range $[X_b,1]$.

Some of the $J_{\gamma b\to 123}$ contain infrared singularities $\propto 1/\varepsilon^2$, which must cancel against the corresponding singularities in the virtual contributions. The singular parts are decomposed in such a way that the Altarelli-Parisi kernels in four dimensions

$$P_{q\leftarrow q}(z_b) \;=\; C_F\left[\frac{1+z_b^2}{(1-z_b)_+}+\frac{3}{2}\delta(1-z_b)\right], \tag{4.135}$$

$$P_{g\leftarrow q}(z_b) \;=\; C_F\left[\frac{1+(1-z_b)^2}{z_b}\right], \tag{4.136}$$

$$P_{g\leftarrow g}(z_b) \;=\; 2N_C\left[\frac{1}{(1-z_b)_+}+\frac{1}{z_b}+z_b(1-z_b)-2\right]+\left[\frac{11}{6}N_C-\frac{1}{3}N_f\right]\delta(1-z_b), \tag{4.137}$$

$$P_{q\leftarrow g}(z_b) \;=\; \frac{1}{2}\left[z_b^2+(1-z_b)^2\right] \tag{4.138}$$

proportional to $1/\varepsilon$ are split off. They also appear in the evolution equations for the parton distribution functions in the proton in section 2.2. The singular terms proportional to these kernels are absorbed as usual into the scale dependent structure functions

$$F_{b/p}(X_b,M_b^2)=\int_{X_b}^1\frac{\mathrm{d}z_b}{z_b}\left[\delta_{bb'}\delta(1-z_b)+\frac{\alpha_s}{2\pi}R'_{b\leftarrow b'}(z_b,M_b^2)\right]F_{b'/p}\left(\frac{X_b}{z_b}\right), \tag{4.139}$$

where $F_{b'/p}(X_b/z_b)$ is the LO structure function before absorption of the collinear singularities and

$$R'_{b\leftarrow b'}(z_b,M_b^2)=-\frac{1}{\varepsilon}P_{b\leftarrow b'}(z_b)\frac{\Gamma(1-\varepsilon)}{\Gamma(1-2\varepsilon)}\left(\frac{4\pi\mu^2}{M_b^2}\right)^{\varepsilon}+C'_{b\leftarrow b'}(z_b) \tag{4.140}$$

with $C'=0$ in the $\overline{\mathrm{MS}}$ scheme. Then, the renormalized higher order hard scattering cross section $\mathrm{d}\sigma(\gamma b\to\text{jets})$ is calculated from

$$\mathrm{d}\sigma(\gamma b\to\text{ jets})=\mathrm{d}\bar{\sigma}(\gamma b\to\text{ jets})-\frac{\alpha_s}{2\pi}\int\mathrm{d}z_b R'_{b\leftarrow b'}(z_b,M_b^2)\mathrm{d}\sigma(\gamma b'\to\text{ jets}). \tag{4.141}$$

$\mathrm{d}\bar{\sigma}(\gamma b\to\text{ jets})$ is the higher order cross section before the subtraction procedure, and $\mathrm{d}\sigma(\gamma b'\to\text{ jets})$ contains the lowest order matrix elements $T_{\gamma q\to gq}(s,t,u)$ and $T_{\gamma g\to q\bar{q}}(s,t,u)$ in d dimensions. This well known factorization prescription [Ell80, Bur80, Alt82, Ell83, Arn89] removes finally all remaining collinear singularities. It is universal and leads for all processes to the same definition of structure functions if the choice concerning the regular function C' in (4.140) is kept fixed. Similar to the case of photon initial state singularities, the higher order cross sections in (4.141) will depend on the factorization scale M_b due to terms of the form $P_{b\leftarrow b'}(z_b)\ln(M_b^2/s)$.

4.2.7 Photon Initial State Corrections for Resolved Photons

We now turn back to the case of resolved photons and consider their initial state corrections. We start with the singularities on the photonic side of the hard scattering cross section. For direct photons, there was only one possible singularity coming from the splitting of the photon into a quark-antiquark pair as shown in figure 24b). However, resolved photons contribute to the hard scattering like hadrons through their partonic structure. Therefore they produce similar poles to the proton initial state singularities as in figure 24c) or those in section 4.2.6. These poles can be of quadratic strength due to the radiation of soft and collinear gluons off the quarks in the photon.

We use the same $\mathcal{O}(\alpha_s^3)$ matrix elements that were already calculated for the final state corrections of resolved photons in section 4.2.3. The relevant diagrams are those for parton-parton scattering in figure 27. As stated before, these diagrams show only the generic types and have also to be used in their crossed forms for the complete set of diagrams. All possible processes are listed in table 6 together with their matrix elements, initial spin and color averages, and statistical factors. Only the matrix elements singular in the variable $z_a'' = p_a p_3 / p_a p_b$ are kept, where p_3 is the momentum of the parton soft or collinear to the original parton in the photon with momentum p_a. Parton 3 will then be a part of the photon remnant. The matrix elements are expressed through the ten approximated invariants given in eqs. (4.89)-(4.98) and decomposed with the help of partial fractioning. It is then possible to factorize them into singular kernels and parts of the leading-order parton-parton matrix elements.

Process	Matrix Element $\overline{\lvert\mathcal{M}\rvert^2}$
$qq' \to qq'g$	$[\lvert\mathcal{M}\rvert^2_{qq'\to qq'g,1}(s,t,u) + \lvert\mathcal{M}\rvert^2_{qq'\to qq'g,2}(s,t,u)]/[4N_C^2]$
$q\bar{q}' \to q\bar{q}'g$	$[\lvert\mathcal{M}\rvert^2_{qq'\to qq'g,1}(u,t,s) + \lvert\mathcal{M}\rvert^2_{qq'\to qq'g,2}(u,t,s)]/[4N_C^2]$
$q\bar{q} \to \bar{q}'q'g$	$[\lvert\mathcal{M}\rvert^2_{qq'\to qq'g,1}(t,s,u)]/[4N_C^2]$
$qg \to qq'\bar{q}'$	$[\lvert\mathcal{M}\rvert^2_{qg\to qq'\bar{q}'}(s,t,u) + \lvert\mathcal{M}\rvert^2_{qg\to qq'\bar{q}'}(u,t,s) + \lvert\mathcal{M}\rvert^2_{qg\to qq'\bar{q}'}(t,s,u)$ $-\lvert\mathcal{M}\rvert^2_{qq'\to qq'g,2}(t,s,u)]/[8(1-\varepsilon)N_C^2C_F]$
$qq \to qqg$	$[\lvert\mathcal{M}\rvert^2_{qq'\to qq'g,1}(s,t,u) + \lvert\mathcal{M}\rvert^2_{qq'\to qq'g,1}(s,u,t) + \lvert\mathcal{M}\rvert^2_{qq\to qqg}(s,t,u)$ $+2\lvert\mathcal{M}\rvert^2_{qq'\to qq'g,2}(s,t,u)]/[4N_C^2]/2!$
$q\bar{q} \to q\bar{q}g$	$[\lvert\mathcal{M}\rvert^2_{qq'\to qq'g,1}(u,t,s) + \lvert\mathcal{M}\rvert^2_{qq'\to qq'g,1}(u,s,t) + \lvert\mathcal{M}\rvert^2_{qq\to qqg}(u,t,s)$ $+\lvert\mathcal{M}\rvert^2_{qq'\to qq'g,2}(u,t,s)]/[4N_C^2]$
$qg \to qq\bar{q}$	$[\lvert\mathcal{M}\rvert^2_{qg\to qq'\bar{q}'}(s,t,u) + \lvert\mathcal{M}\rvert^2_{qg\to qq'\bar{q}'}(s,u,t) + \lvert\mathcal{M}\rvert^2_{qg\to qq\bar{q}}(s,t,u)$ $+\lvert\mathcal{M}\rvert^2_{qg\to qq'\bar{q}'}(u,t,s) + \lvert\mathcal{M}\rvert^2_{qg\to qq'\bar{q}'}(t,u,s) + \lvert\mathcal{M}\rvert^2_{qg\to qq\bar{q}}(u,t,s)$ $+\lvert\mathcal{M}\rvert^2_{qg\to qq'\bar{q}'}(t,s,u) + \lvert\mathcal{M}\rvert^2_{qg\to qq'\bar{q}'}(u,s,t) + \lvert\mathcal{M}\rvert^2_{qg\to qq\bar{q}}(t,s,u)$ $-2\lvert\mathcal{M}\rvert^2_{qq'\to qq'g,2}(t,s,u)]/[8(1-\varepsilon)N_C^2C_F]/2!$
$q\bar{q} \to ggg$	$[\lvert\mathcal{M}\rvert^2_{q\bar{q}\to ggg}(s,t,u)]/[4N_C^2]/3!$
$qg \to qgg$	$[-\lvert\mathcal{M}\rvert^2_{q\bar{q}\to ggg}(t,s,u)/3 + \lvert\mathcal{M}\rvert^2_{qg\to qgg,1}(s,t,u) + \lvert\mathcal{M}\rvert^2_{qg\to qgg,2}(s,t,u)]/[8(1-\varepsilon)N_C^2C_F]/2!$
$\bar{q}g \to \bar{q}gg$	$[-\lvert\mathcal{M}\rvert^2_{q\bar{q}\to ggg}(t,u,s)/3 + \lvert\mathcal{M}\rvert^2_{qg\to qgg,1}(u,t,s) + \lvert\mathcal{M}\rvert^2_{qg\to qgg,2}(u,t,s)]/[8(1-\varepsilon)N_C^2C_F]/2!$
$gg \to q\bar{q}g$	$[-\lvert\mathcal{M}\rvert^2_{qg\to qgg,1}(t,s,u) + \lvert\mathcal{M}\rvert^2_{gg\to q\bar{q}g}(s,t,u)]/[16(1-\varepsilon)^2N_C^2C_F^2]$
$gg \to ggg$	$[\lvert\mathcal{M}\rvert^2_{gg\to ggg}(s,t,u)]/[16(1-\varepsilon)^2N_C^2C_F^2]/3!$

Table 6: *Summary of* $2 \to 3$ *squared matrix elements for resolved photoproduction.*

Let us start with the process $qq' \to qq'g$ in figure 27a). Here, the final gluon can be soft or collinear to the incoming quark a

$$\lvert\mathcal{M}\rvert^2_{qq'\to qq'g,1}(s,t,u) \quad = \quad g^6\mu^{6\varepsilon}\frac{2}{sz''}$$

$$\left[(2C_F - N_C)\left(\frac{-2}{z''+(1-z_a)} + \frac{-t/s}{z''-t/s(1-z_a)} + \frac{-u/s}{z''-u/s(1-z_a)}\right)\right.$$
$$\left. + C_F\left((1-z_a)(1-\varepsilon) - 2 + \frac{-2u/s}{z''-u/s(1-z_a)}\right)\right] T_{qq'\to qq'}(s,t,u), \quad (4.142)$$

so that the original quark will also participate in the Born process $qq' \to qq'$. However, the quark can also go into the photon remnant. It will then radiate a gluon that scatters from the quark b with different flavor

$$|\mathcal{M}|^2_{qq'\to qq'g,2}(s,t,u) = g^6\mu^{6\varepsilon}\frac{1}{sz''}\left[\frac{1+(1-z_a)^2}{z_a} - \varepsilon z_a\right] T_{qg\to qg}(s,t,u). \quad (4.143)$$

For equal flavors in figure 27b), the interference contribution

$$\begin{aligned}|\mathcal{M}|^2_{qq\to qqg}(s,t,u) &= g^6\mu^{6\varepsilon}\frac{2}{sz''} \\ &\left[(2C_F - N_C)\left(\frac{-2}{z''+(1-z_a)} + \frac{-t/s}{z''-t/s(1-z_a)} + \frac{-u/s}{z''-u/s(1-z_a)}\right)\right. \\ &\left. + C_F\left((1-z_a)(1-\varepsilon) - 2 + \frac{2}{z''+(1-z_a)}\right)\right] T_{qq\to qq}(s,t,u) \quad (4.144)\end{aligned}$$

has the same kernel for the color factor $(2C_F - N_C)$, but a crossed version for the color factor C_F, and is proportional to the Born interference contribution $T_{qq\to qq}$. If the final gluon is crossed into the initial state for the processes $qg \to qq'\bar{q}'$ and $qg \to qq\bar{q}$ with unlike and like quark flavors, it can split up into a collinear quark-antiquark pair quite similar to the splitting of direct photons in section 4.2.5. Consequently, the singular kernels in

$$|\mathcal{M}|^2_{qg\to qq'\bar{q}'}(s,t,u) = g^6\mu^{6\varepsilon}\frac{2}{sz''}C_F\left[(z_a^2+(1-z_a)^2)(1+\varepsilon) - \varepsilon\right] T_{qq'\to qq'}(s,t,u) \quad (4.145)$$

and

$$|\mathcal{M}|^2_{qg\to qq\bar{q}}(s,t,u) = g^6\mu^{6\varepsilon}\frac{4}{sz''}C_F\left[(z_a^2+(1-z_a)^2)(1+\varepsilon) - \varepsilon\right] T_{qq\to qq}(s,t,u) \quad (4.146)$$

are the same as in eqs. (4.99)-(4.101), and we have the quark-quark scattering processes $qq' \to qq'$ and $qq \to qq$ on the tree level. The additional factor of $(1+\varepsilon)$ is due to the averaging of initial gluon spins with $1/(2(1-\varepsilon)) \simeq 1/2(1+\varepsilon)$, whereas the photons were averaged just by $1/2$. The third process to be considered is taken from figure 27c). Obviously, only a gluon can go into the photon remnant so that in

$$\begin{aligned}|\mathcal{M}|^2_{q\bar{q}\to ggg}(s,t,u) &= g^6\mu^{6\varepsilon}\frac{6}{sz''}\left[C_F\left((1-z_a)(1-\varepsilon)-2\right)T_{q\bar{q}\to gg}(s,t,u)\right. \quad (4.147)\\ &+4N_CC_F \\ &\left(\frac{-u/s}{z''-u/s(1-z_a)}(1-\varepsilon)\left(\frac{t^2+u^2-\varepsilon s^2}{tu}\right)\left(2N_CC_F - 2N_C^2\frac{tu}{s^2} - N_C^2\frac{u^2}{s^2}\right)\right. \\ &+\frac{1}{z''+(1-z_a)}(1-\varepsilon)\left(\frac{t^2+u^2-\varepsilon s^2}{tu}\right)\left(\left(2N_CC_F - 2N_C^2\frac{ut}{s^2}\right)\left(-2+2\frac{C_F}{N_C}\right)\right. \\ &\left.+N_C^2\frac{t^2+u^2}{s^2}\right) \\ &\left.\left.+\frac{-t/s}{z''-t/s(1-z_a)}(1-\varepsilon)\left(\frac{t^2+u^2-\varepsilon s^2}{tu}\right)\left(2N_CC_F - 2N_C^2\frac{tu}{s^2} - N_C^2\frac{t^2}{s^2}\right)\right)\right]\end{aligned}$$

we find the same simple pole for the color factor C_F as in eq. (4.142) and still have quark-antiquark annihilation into gluons in the Born process. The double poles are, however, more complicated and

factorize only parts of the Born matrix elements. If a final gluon is crossed into the initial state, a soft or collinear gluon can also be radiated from the initial gluon

$$\begin{aligned}|\mathcal{M}|^2_{qg\to qgg,1}(s,t,u) &= g^6\mu^{6\varepsilon}\frac{8}{sz''}\left[N_C\left(\frac{1}{z_a}+z_a(1-z_a)-2\right)T_{qg\to qg}(s,t,u)\right.\\ &\quad -2N_CC_F\\ &\quad \left(\frac{-u/s}{z''-u/s(1-z_a)}(1-\varepsilon)\left(\frac{s^2+u^2-\varepsilon t^2}{su}\right)\left(2N_CC_F-2N_C^2\frac{su}{t^2}-N_C^2\frac{u^2}{t^2}\right)\right.\\ &\quad +\frac{1}{z''+(1-z_a)}(1-\varepsilon)\left(\frac{s^2+u^2-\varepsilon t^2}{su}\right)\left(2N_CC_F-2N_C^2\frac{us}{t^2}-N_C^2\frac{s^2}{t^2}\right)\\ &\quad \left.\left.+\frac{-t/s}{z''-t/s(1-z_a)}(1-\varepsilon)\left(\frac{s^2+u^2-\varepsilon t^2}{su}\right)\left(N_C^2\frac{s^2+u^2}{t^2}\right)\right)\right], \end{aligned} \tag{4.148}$$

leaving a new kernel and a partly factorizable $qg\to qg$ scattering process behind. Alternatively, the quark can go into the photon remnant

$$|\mathcal{M}|^2_{qg\to qgg,2}(s,t,u) = g^6\mu^{6\varepsilon}\frac{1}{sz''}\left[\frac{1+(1-z_a)^2}{z_a}-\varepsilon z_a\right]T_{gg\to gg}(s,t,u), \tag{4.149}$$

which leads to a $gg\to gg$ Born process. For collinear quarks, only a single divergence is possible. The next kernel for $gg\to q\bar{q}g$ is already known from $qg\to qq'\bar{q}'$ and $qg\to qq\bar{q}$

$$|\mathcal{M}|^2_{gg\to q\bar{q}g}(s,t,u) = g^6\mu^{6\varepsilon}\frac{2}{sz''}C_F\left[(z_a^2+(1-z_a)^2)(1+\varepsilon)-\varepsilon\right]T_{qg\to qg}(s,t,u), \tag{4.150}$$

where a gluon splits into a quark-antiquark pair, but now with a different leading-order matrix element $qg\to qg$. Finally in

$$\begin{aligned}|\mathcal{M}|^2_{gg\to ggg}(s,t,u) &= g^6\mu^{6\varepsilon}\frac{12}{sz''}\left[N_C\left(\frac{1}{z_a}+z_a(1-z_a)-2\right)T_{gg\to gg}(s,t,u)\right.\\ &\quad +8N_C^4C_F\\ &\quad \left(\frac{-t/s}{z''-t/s(1-z_a)}(1-\varepsilon)^2\left(3-\frac{2su}{t^2}+\frac{s^4+u^4}{s^2u^2}\right)\right.\\ &\quad +\frac{-u/s}{z''-u/s(1-z_a)}(1-\varepsilon)^2\left(3-\frac{2st}{u^2}+\frac{s^4+t^4}{s^2t^2}\right)\\ &\quad \left.\left.+\frac{1}{z''+(1-z_a)}(1-\varepsilon)^2\left(3-\frac{2tu}{s^2}+\frac{t^4+u^4}{t^2u^2}\right)\right)\right], \end{aligned} \tag{4.151}$$

it is clear that the Born process must also be completely gluonic and we can only have the gluon splitting into two gluons as in $qg\to qgg$. All these contributions have to be considered several times and also in crossed forms according to table 6.

What remains to be done is the integration over the phase space of particle 3 in a region, where it can be considered a part of the photon remnant. We do so with the help of the phase space $\mathrm{dPS}^{(r)}$ calculated in section 4.2.4 and leave the z_a-integration for numerics. Again, the reason is the analytically not integrable form of the photonic parton densities that have to be convoluted with the matrix elements. The result is

$$\int \mathrm{dPS}^{(r)}|\mathcal{M}|^2_{ab\to 123}(s,t,u) = \int\limits_{X_a}^{1}\frac{\mathrm{d}z_a}{z_a}g^4\mu^{4\varepsilon}\frac{\alpha_s}{2\pi}\left(\frac{4\pi\mu^2}{Q^2}\right)^{\varepsilon}\frac{\Gamma(1-\varepsilon)}{\Gamma(1-2\varepsilon)}I_{ab\to 123}(s,t,u). \tag{4.152}$$

The integrated matrix elements are put into the functions $I_{ab\to 123}$:

$$
\begin{aligned}
I_{qq'\to qq'g,1}(s,t,u) &= \Bigg[(2C_F - N_C)\left(\delta(1-z_a)\left(-\frac{1}{2\varepsilon}(-2l(s)+l(t)+l(u))\right.\right.\\
&\quad \left.+\frac{1}{4}(-2l^2(s)+l^2(t)+l^2(u))\right)+\frac{z_a}{(1-z_a)_+}(-2l(s)+l(t)+l(u))\\
&\quad +2\frac{z_a}{1-z_a}\ln\left(1+\frac{|s|}{y_I Q^2}\frac{1-z_a}{z_a}\right)-\frac{z_a}{1-z_a}\ln\left(1+\frac{|t|}{y_I Q^2}\frac{1-z_a}{z_a}\right)\\
&\quad \left.-\frac{z_a}{1-z_a}\ln\left(1+\frac{|u|}{y_I Q^2}\frac{1-z_a}{z_a}\right)\right)\\
&\quad +C_F\left(-\frac{1}{\varepsilon}\frac{1}{C_F}P_{q\leftarrow q}(z_a)+\delta(1-z_a)\left(\frac{1}{\varepsilon^2}+\frac{1}{2\varepsilon}(3-2l(u))\right.\right.\\
&\quad \left.+\frac{1}{2}l^2(u)+\pi^2\right)+1-z_a+(1-z_a)\ln\left(y_I\frac{1-z_a}{z_a}\right)+2R_+\left(\left|\frac{u}{Q^2}\right|\right)\\
&\quad \left.-2l\left(u\left(\frac{1-z_a}{z_a}\right)^2\right)-2\frac{z_a}{1-z_a}\ln\left(1+\frac{|u|}{y_I Q^2}\frac{1-z_a}{z_a}\right)\right)\Bigg]\\
&\quad T_{qq'\to qq'}(s,t,u), \qquad (4.153)\\
I_{qq'\to qq'g,2}(s,t,u) &= \frac{1}{2}\left[-\frac{1}{\varepsilon}\frac{1}{C_F}P_{g\leftarrow q}(z_a)+\frac{1}{C_F}P_{g\leftarrow q}(z_a)\left(\ln\left(y_I\frac{1-z_a}{z_a}\right)+1\right)\right.\\
&\quad \left.-2\frac{1-z_a}{z_a}\right]T_{qg\to qg}(s,t,u), \qquad (4.154)\\
I_{qq\to qqg}(s,t,u) &= \Bigg[(2C_F - N_C)\left(\delta(1-z_a)\left(-\frac{1}{2\varepsilon}(-2l(s)+l(t)+l(u))\right.\right.\\
&\quad \left.+\frac{1}{4}(-2l^2(s)+l^2(t)+l^2(u))\right)+\frac{z_a}{(1-z_a)_+}(-2l(s)+l(t)+l(u))\\
&\quad +2\frac{z_a}{1-z_a}\ln\left(1+\frac{|s|}{y_I Q^2}\frac{1-z_a}{z_a}\right)-\frac{z_a}{1-z_a}\ln\left(1+\frac{|t|}{y_I Q^2}\frac{1-z_a}{z_a}\right)\\
&\quad \left.-\frac{z_a}{1-z_a}\ln\left(1+\frac{|u|}{y_I Q^2}\frac{1-z_a}{z_a}\right)\right)\\
&\quad +C_F\left(-\frac{1}{\varepsilon}\frac{1}{C_F}P_{q\leftarrow q}(z_a)+\delta(1-z_a)\left(\frac{1}{\varepsilon^2}+\frac{1}{2\varepsilon}(3-2l(s))\right.\right.\\
&\quad \left.+\frac{1}{2}l^2(s)+\pi^2\right)+1-z_a+(1-z_a)\ln\left(y_I\frac{1-z_a}{z_a}\right)+2R_+\left(\left|\frac{s}{Q^2}\right|\right)\\
&\quad \left.-2l\left(s\left(\frac{1-z_a}{z_a}\right)^2\right)-2\frac{z_a}{1-z_a}\ln\left(1+\frac{|s|}{y_I Q^2}\frac{1-z_a}{z_a}\right)\right)\Bigg]\\
&\quad T_{qq\to qq}(s,t,u), \qquad (4.155)\\
I_{qg\to qq'\bar{q}'}(s,t,u) &= 2C_F\left[-\frac{1}{\varepsilon}P_{q\leftarrow g}(z_a)+P_{q\leftarrow g}(z_a)\left(\ln\left(y_I\frac{1-z_a}{z_a}\right)-1\right)+\frac{1}{2}\right]\\
&\quad T_{qq'\to qq'}(s,t,u), \qquad (4.156)\\
I_{qg\to qq\bar{q}}(s,t,u) &= 4C_F\left[-\frac{1}{\varepsilon}P_{q\leftarrow g}(z_a)+P_{q\leftarrow g}(z_a)\left(\ln\left(y_I\frac{1-z_a}{z_a}\right)-1\right)+\frac{1}{2}\right]\\
&\quad T_{qq\to qq}(s,t,u), \qquad (4.157)\\
I_{q\bar{q}\to ggg}(s,t,u) &= \left[3C_F\left(-\frac{1}{\varepsilon}\frac{1}{C_F}P_{q\leftarrow q}(z_a)+\delta(1-z_a)\left(\frac{1}{\varepsilon^2}+\frac{3}{2\varepsilon}+\pi^2\right)\right.\right.\\
&\quad \left.\left.+1-z_a+(1-z_a)\ln\left(y_I\frac{1-z_a}{z_a}\right)\right)\right]T_{q\bar{q}\to gg}(s,t,u)\\
&\quad +3N_C C_F\left[\left(\delta(1-z_a)\left(-\frac{2}{\varepsilon}l(t)+2l(t)+l^2(t)\right)+4R_+\left(\left|\frac{t}{Q^2}\right|\right)\right.\right.
\end{aligned}
$$

$$
\begin{aligned}
& -4l\left(t\left(\frac{1-z_a}{z_a}\right)^2\right) - 4\frac{z_a}{1-z_a}\ln\left(1+\frac{|t|}{y_I Q^2}\frac{1-z_a}{z_a}\right)\Bigg) \\
& \left(N_C^2\left(\frac{u}{t}-\frac{2u^2}{s^2}\right)-\frac{u}{t}-\frac{t}{u}\right) \\
& + \left(\delta(1-z_a)\left(-\frac{2}{\varepsilon}l(s)+2l(s)+l^2(s)\right)+4R_+\left(\left|\frac{s}{Q^2}\right|\right)\right. \\
& -4l\left(s\left(\frac{1-z_a}{z_a}\right)^2\right) - 4\frac{z_a}{1-z_a}\ln\left(1+\frac{|s|}{y_I Q^2}\frac{1-z_a}{z_a}\right)\Bigg) \\
& \left(2\frac{t^2+u^2}{s^2}+\frac{1}{N_C^2}\left(\frac{u}{t}+\frac{t}{u}\right)\right) \\
& + \left(\delta(1-z_a)\left(-\frac{2}{\varepsilon}l(u)+2l(u)+l^2(u)\right)+4R_+\left(\left|\frac{u}{Q^2}\right|\right)\right. \\
& -4l\left(u\left(\frac{1-z_a}{z_a}\right)^2\right) - 4\frac{z_a}{1-z_a}\ln\left(1+\frac{|u|}{y_I Q^2}\frac{1-z_a}{z_a}\right)\Bigg) \\
& \left(N_C^2\left(\frac{t}{u}-\frac{2t^2}{s^2}\right)-\frac{u}{t}-\frac{t}{u}\right) \\
& +\delta(1-z_a)\left(2l(t)\left(N_C^2\frac{u}{t}-\frac{s^2}{tu}\right)+2l(s)\left(2+\frac{1}{N_C^2}\frac{s^2}{tu}\right)\right. \\
& \left.\left.+2l(u)\left(N_C^2\frac{t}{u}-\frac{s^2}{tu}\right)\right)\right], \qquad (4.158)
\end{aligned}
$$

$$
\begin{aligned}
I_{qg\to qgg,1}(s,t,u) \;=\; & \Big[2N_C\left(-\frac{1}{\varepsilon}\frac{1}{N_C}P_{g\leftarrow g}(z_a)\right. \\
& +\delta(1-z_a)\left(\frac{1}{\varepsilon^2}+\frac{1}{\varepsilon}\frac{1}{N_C}\left(\frac{11}{6}N_C-\frac{1}{3}N_f\right)+\pi^2\right) \\
& \left.+2\ln\left(y_I\frac{1-z_a}{z_a}\right)\left(\frac{1}{z_a}+z_a(1-z_a)-1\right)\right)\Big]T_{qg\to qg}(s,t,u) \\
& -2N_C C_F\left[\left(\delta(1-z_a)\left(-\frac{2}{\varepsilon}l(t)+2l(t)+l^2(t)\right)+4R_+\left(\left|\frac{t}{Q^2}\right|\right)\right.\right. \\
& -4l\left(t\left(\frac{1-z_a}{z_a}\right)^2\right) - 4\frac{z_a}{1-z_a}\ln\left(1+\frac{|t|}{y_I Q^2}\frac{1-z_a}{z_a}\right)\Bigg) \\
& \left(N_C^2\frac{(s^2+u^2)^2}{ust^2}\right) \\
& + \left(\delta(1-z_a)\left(-\frac{2}{\varepsilon}l(s)+2l(s)+l^2(s)\right)+4R_+\left(\left|\frac{s}{Q^2}\right|\right)\right. \\
& -4l\left(s\left(\frac{1-z_a}{z_a}\right)^2\right) - 4\frac{z_a}{1-z_a}\ln\left(1+\frac{|s|}{y_I Q^2}\frac{1-z_a}{z_a}\right)\Bigg) \\
& \left(N_C^2\left(\frac{u}{s}-\frac{2u^2}{t^2}\right)-\frac{u}{s}-\frac{s}{u}\right) \\
& + \left(\delta(1-z_a)\left(-\frac{2}{\varepsilon}l(u)+2l(u)+l^2(u)\right)+4R_+\left(\left|\frac{u}{Q^2}\right|\right)\right. \\
& -4l\left(u\left(\frac{1-z_a}{z_a}\right)^2\right) - 4\frac{z_a}{1-z_a}\ln\left(1+\frac{|u|}{y_I Q^2}\frac{1-z_a}{z_a}\right)\Bigg)
\end{aligned}
$$

$$
\begin{aligned}
&\left(N_C^2\left(\frac{s}{u}-\frac{2s^2}{t^2}\right)-\frac{u}{s}-\frac{s}{u}\right)\\
&+\delta(1-z_a)\left(2l(t)N_C^2\left(\frac{u}{s}+\frac{s}{u}\right)+2l(s)\left(N_C^2\frac{u}{s}-\frac{t^2}{su}\right)\right.\\
&\left.+2l(u)\left(N_C^2\frac{s}{u}-\frac{t^2}{su}\right)\right)\Bigg], \qquad (4.159)\\
I_{qg\to qgg,2}(s,t,u) &= \frac{1}{2}\left[-\frac{1}{\varepsilon}\frac{1}{C_F}P_{g\leftarrow q}(z_a)+\frac{1}{C_F}P_{g\leftarrow q}(z_a)\left(\ln\left(y_I\frac{1-z_a}{z_a}\right)+1\right)\right.\\
&\left.-2\frac{1-z_a}{z_a}\right]T_{gg\to gg}(s,t,u), \qquad (4.160)\\
I_{gg\to q\bar{q}g}(s,t,u) &= 2C_F\left[-\frac{1}{\varepsilon}P_{q\leftarrow g}(z_a)+P_{q\leftarrow g}(z_a)\left(\ln\left(y_I\frac{1-z_a}{z_a}\right)-1\right)+\frac{1}{2}\right]\\
&T_{qg\to qg}(s,t,u), \qquad (4.161)\\
I_{gg\to ggg}(s,t,u) &= \Bigg[3N_C\left(-\frac{1}{\varepsilon}\frac{1}{N_C}P_{g\leftarrow g}(z_a)\right.\\
&+\delta(1-z_a)\left(\frac{1}{\varepsilon^2}+\frac{1}{\varepsilon}\frac{1}{N_C}\left(\frac{11}{6}N_C-\frac{1}{3}N_f\right)+\pi^2\right)\\
&\left.+2\ln\left(y_I\frac{1-z_a}{z_a}\right)\left(\frac{1}{z_a}+z_a(1-z_a)-1\right)\right)\Bigg]T_{gg\to gg}(s,t,u)\\
&+12N_C^4C_F\left[\left(\delta(1-z_a)\left(-\frac{2}{\varepsilon}l(t)+4l(t)+l^2(t)\right)+4R_+\left(\left|\frac{t}{Q^2}\right|\right)\right.\right.\\
&\left.-4l\left(t\left(\frac{1-z_a}{z_a}\right)^2\right)-4\frac{z_a}{1-z_a}\ln\left(1+\frac{|t|}{y_IQ^2}\frac{1-z_a}{z_a}\right)\right)\\
&\left(3-\frac{2us}{t^2}+\frac{u^4+s^4}{u^2s^2}\right)\\
&+\left(\delta(1-z_a)\left(-\frac{2}{\varepsilon}l(u)+4l(u)+l^2(u)\right)+4R_+\left(\left|\frac{u}{Q^2}\right|\right)\right.\\
&\left.-4l\left(u\left(\frac{1-z_a}{z_a}\right)^2\right)-4\frac{z_a}{1-z_a}\ln\left(1+\frac{|u|}{y_IQ^2}\frac{1-z_a}{z_a}\right)\right)\\
&\left(3-\frac{2ts}{u^2}+\frac{t^4+s^4}{t^2s^2}\right)\\
&+\left(\delta(1-z_a)\left(-\frac{2}{\varepsilon}l(s)+4l(s)+l^2(s)\right)+4R_+\left(\left|\frac{s}{Q^2}\right|\right)\right.\\
&\left.-4l\left(s\left(\frac{1-z_a}{z_a}\right)^2\right)-4\frac{z_a}{1-z_a}\ln\left(1+\frac{|s|}{y_IQ^2}\frac{1-z_a}{z_a}\right)\right)\\
&\left.\left(3-\frac{2tu}{s^2}+\frac{t^4+u^4}{t^2u^2}\right)\right]. \qquad (4.162)
\end{aligned}
$$

The absorption of the collinear poles $1/\varepsilon$ proportional to the different Altarelli-Parisi splitting functions is handled in a completely analogous way as in section 4.2.6 for proton initial state corrections. The only difference is that the poles are absorbed into the photon structure function and not the proton structure function. As always, we omit terms of higher order in ε and the invariant mass cut-off y.

4.2.8 Proton Initial State Corrections for Resolved Photons

Finally, the next-to-leading order $\mathcal{O}(\alpha_s^3)$ resolved photoproduction cross section receives also initial state corrections on the proton side. It is, however, not necessary to calculate these contributions again. The relevant diagrams in figure 27 are the same as in the last section as is the singularity structure in figure 24c). This is due to the fact that resolved photons behave like hadrons.

The proton initial state formulæ are obtained from those in section 4.2.7 by interchanging ($z'' \leftrightarrow z'''$) and ($z_a \leftrightarrow z_b$), so that we consider matrix elements that are singular in the variable

$$z''' = \frac{p_b p_3}{p_a p_b}. \tag{4.163}$$

The parton b in the proton gives a fraction

$$z_b = \frac{p_1 p_2}{p_a p_b} \tag{4.164}$$

of its momentum to the $2 \to 2$ hard scattering process and the rest of $(1 - z_b)$ to particle 3 in the proton remnant. The list of approximated invariants is the same as in section 4.2.6 for proton initial state corrections of direct photons, and the list of contributing matrix elements is the same as in table 6.

The integration over the singular region of phase space gives

$$\int \mathrm{dPS}^{(r)} |\mathcal{M}|^2_{ab\to 123}(s,t,u) = \int\limits_{X_b}^{1} \frac{\mathrm{d}z_b}{z_b} g^4 \mu^{4\varepsilon} \frac{\alpha_s}{2\pi} \left(\frac{4\pi\mu^2}{Q^2}\right)^{\varepsilon} \frac{\Gamma(1-\varepsilon)}{\Gamma(1-2\varepsilon)} J_{ab\to 123}(s,t,u), \tag{4.165}$$

where the z_b-integration is done numerically to allow for inclusion of the proton structure function. The functions

$$J_{ab\to 123}(s,t,u) = I_{ab\to 123}(s,t,u) \tag{4.166}$$

are identical to those from the last chapter. For the IR singularities and finite contributions proportional to the $\delta(1 - z_b)$-function, the integration can of course be carried out trivially. Thus, these singularities cancel against those from the virtual corrections for resolved photoproduction. The collinear singularities proportional to the Altarelli-Parisi splitting functions are now absorbed into the proton structure functions and not the photon structure functions as before.

4.3 Finite Next-To-Leading Order Cross Sections

We conclude this section with a summary of all singularities that appeared in the next-to-leading order cross section of jet photoproduction. There were three types of singularities:

- UV singularities in the virtual corrections
- IR singularities in the virtual and real corrections
- Collinear singularities in the initial state real corrections

All of them were regularized dimensionally by going from four to $d = 4 - 2\varepsilon$ dimensions, where the regulator ε had a positive sign for the ultraviolet (UV) and a negative sign for the infrared (IR) divergencies.

The ultraviolet divergencies were encountered in the calculation of the virtual diagrams in section 4.1. The diagrams had an additional inner "virtual" particle and were classified into self-energy diagrams, propagator corrections, box diagrams, and vertex corrections. The inner loop momenta could not be observed and had to be integrated up to infinity. The resulting UV singularities could be removed by renormalizing the fields, couplings, gauge parameters, and masses in the Lagrangian through multiplicative renormalization constants Z_i, which show up in perturbation theory as counter terms order by order in the strong coupling α_s. The counter terms were not given explicitly, so that all matrix element formulæ in section 4.1 are already UV-divergence free and all fields, couplings etc. have to be considered physical and renormalized. As an example, the counter term for the QCD Compton graph $\gamma q \to gq$ has the form

$$\begin{aligned} |\mathcal{M}|^2_{\gamma q \to gq, CT}(s,t,u) &= e^2 e_q^2 g^2 \mu^{4\varepsilon} \frac{\alpha_s}{2\pi} \left(\frac{4\pi\mu^2}{s}\right)^{\varepsilon} \frac{\Gamma(1-\varepsilon)}{\Gamma(1-2\varepsilon)} \\ &\quad \left(\frac{1}{\varepsilon} + \ln\frac{s}{\mu^2}\right) \left(\frac{1}{3}N_f - \frac{11}{6}N_C\right) T_{\gamma q \to gq}(s,t,u) \end{aligned} \tag{4.167}$$

in the $\overline{\text{MS}}$ scheme and leads to a logarithmic dependence of the cross section on the renormalization scale μ.

The second type of singularities, IR divergencies, were produced at the lower end of the loop integration in the virtual corrections and through soft or collinear real particle emission in the real corrections. They were written down explicitly throughout the last sections and have to cancel according to the Kinoshita-Lee-Nauenberg theorem [Kin62, Lee64]. We demonstrate this cancellation separately for direct and resolved photoproduction in tables 7 and 8.

There is only one generic $2 \to 2$ diagram $\gamma q \to gq$ in direct photoproduction as shown in figure 18, from which the photon-gluon fusion process can be deduced with the help of crossing relations. Therefore we show only this process in table 7, but for the three contributing color factors C_F, N_C, and N_f. The real corrections for the first two classes come from the process $\gamma q \to qgg$ and are equally divided among final and initial state singularities. The last class, however, occurs only in the splitting of the final gluon into an additional quark-antiquark pair with N_f flavors. This is the reason why no initial state singularity is present here.

For resolved photoproduction, we have the four generic processes in figure 20. They are presented in table 8 and divided further into color factor classes. All other processes can be obtained through crossing. The real corrections for quark-quark scattering with different and like flavors arise simply from the emission of an additional gluon and factorize the complete Born matrix element. Final and initial state corrections contribute at equal parts. For processes involving more gluons, the situation is

Process	Color Factor	NLO Correction	Singular Parts of Matrix Elements
$\gamma q \to gq$	C_F	Virtual Corr.	$\left[-\frac{2}{\varepsilon^2} - \frac{1}{\varepsilon}(3 - 2l(t))\right] T_{\gamma q \to gq}(s,t,u)$
		Final State	$\left[+\frac{1}{\varepsilon^2} + \frac{1}{2\varepsilon}(3 - 2l(t))\right] T_{\gamma q \to gq}(s,t,u)$
		Initial State	$\left[+\frac{1}{\varepsilon^2} + \frac{1}{2\varepsilon}(3 - 2l(t))\right] T_{\gamma q \to gq}(s,t,u)$
	N_C	Virtual Corr.	$\left[-\frac{1}{\varepsilon^2} - \frac{1}{2\varepsilon}\left(\frac{11}{3} - 2l(s) + 2l(t) - 2l(u)\right)\right] T_{\gamma q \to gq}(s,t,u)$
		Final State	$\left[+\frac{1}{\varepsilon^2} + \frac{1}{2\varepsilon}\left(\frac{11}{3} - \ l(s) + \ l(t) - \ l(u)\right)\right] T_{\gamma q \to gq}(s,t,u)$
		Initial State	$\left[\quad +\frac{1}{2\varepsilon}\left(\quad - \ l(s) + \ l(t) - \ l(u)\right)\right] T_{\gamma q \to gq}(s,t,u)$
	N_f	Virtual Corr.	$+\frac{1}{3\varepsilon} T_{\gamma q \to gq}(s,t,u)$
		Final State	$-\frac{1}{3\varepsilon} T_{\gamma q \to gq}(s,t,u)$

Table 7: *Cancellation of IR singularities from virtual, final state, and initial state NLO corrections for the direct partonic subprocesses and different color factors.*

more complex. In $q\bar{q} \to gg$, an additional gluon leads to different color factors depending on whether it is radiated in the initial state (C_F) or the final state (N_C). A final gluon can also split up into N_f flavors accounting for half of the real corrections in the class N_f. The other half comes from the process $qg \to qgg$, where the initial gluon splits up into a quark-antiquark pair with N_f flavors. So far, the factorization property of $q\bar{q} \to gg$ holds. However, the logarithmic contributions to the emission of a third initial or final gluon in the color classes 1, $8N_C^3 C_F$, and $8N_C C_F$ only factorize parts of the leading order cross section. In the completely gluonic process $gg \to gg$ it does not matter where the third gluon is radiated (color class N_C). Still, a final gluon can split up into N_f flavors or an initial gluon can have come from N_f different quarks. Finally, the logarithmic contributions proportional to $32N_C^4 C_F$ only factorize parts of the Born cross section, but are symmetric under cyclic permutations of the Madelstam variables as a completely symmetric process must be.

The third and last class of singularities are those in the initial state from collinear real particle emission. Although they are generally classified as infrared singularities as well, they are not included in the tables 7 and 8 above. These single poles proportional to the Altarelli-Parisi splitting functions $P_{q \leftarrow q}(\mathrm{z})$, $P_{g \leftarrow q}(z)$, $P_{q \leftarrow g}(z)$, and $P_{g \leftarrow g(z)}$ do not cancel against similar poles from virtual corrections. They are absorbed into the renormalized photon and proton structure functions according to the $\overline{\mathrm{MS}}$ scheme and leave behind a logarithmic dependence of the hard cross section on the factorization scales M_a and M_b.

The finite next-to-leading order cross section for the photoproduction of two jets was given in section 2.5 as

$$\frac{\mathrm{d}^3\sigma}{\mathrm{d}E_T^2 \mathrm{d}\eta_1 \mathrm{d}\eta_2} = \sum_b x_a F_{a/e}(x_a, M_a^2) x_b F_{b/p}(x_b, M_b^2) \frac{\mathrm{d}\sigma}{\mathrm{d}t}(ab \to p_1 p_2) \tag{4.168}$$

with the partonic cross section

$$\frac{\mathrm{d}\sigma}{\mathrm{d}t}(ab \to p_1 p_2) = \frac{1}{2s} \overline{|\mathcal{M}|^2} \frac{\mathrm{dPS}^{(2)}}{\mathrm{d}t}. \tag{4.169}$$

We can now return to the physical four dimensions letting $\varepsilon \to 0$ everywhere in the calculation. The strong coupling constant α_s and the parton densities in the electron $F_{a/e}(x_a, M_a^2)$ and in the proton $F_{b/p}(x_b, M_b^2)$ are renormalized and defined in the $\overline{\mathrm{MS}}$ scheme.

Process	Color Factor	NLO Correction	Singular Parts of Matrix Elements
$qq' \to qq'$	C_F	Virtual Corr.	$\left[-\frac{4}{\varepsilon^2} - \frac{1}{\varepsilon}(6 + 8l(s) - 8l(u) - 4l(t))\right] T_{qq'\to qq'}(s,t,u)$
		Final State	$\left[+\frac{2}{\varepsilon^2} + \frac{1}{\varepsilon}(3 + 4l(s) - 4l(u) - 2l(t))\right] T_{qq'\to qq'}(s,t,u)$
		Initial State	$\left[+\frac{2}{\varepsilon^2} + \frac{1}{\varepsilon}(3 + 4l(s) - 4l(u) - 2l(t))\right] T_{qq'\to qq'}(s,t,u)$
	N_C	Virtual Corr.	$\left[+\frac{1}{\varepsilon}(4l(s) - 2l(u) - 2l(t))\right] T_{qq'\to qq'}(s,t,u)$
		Final State	$\left[-\frac{1}{\varepsilon}(2l(s) - l(u) - l(t))\right] T_{qq'\to qq'}(s,t,u)$
		Initial State	$\left[-\frac{1}{\varepsilon}(2l(s) - l(u) - l(t))\right] T_{qq'\to qq'}(s,t,u)$
$qq \to qq$	C_F	Virtual Corr.	$\left[-\frac{4}{\varepsilon^2} - \frac{1}{\varepsilon}(6 + 4l(s) - 4l(t) - 4l(u))\right] T_{qq\to qq}(s,t,u)$
		Final State	$\left[+\frac{2}{\varepsilon^2} + \frac{1}{\varepsilon}(3 + 2l(s) - 2l(t) - 2l(u))\right] T_{qq\to qq}(s,t,u)$
		Initial State	$\left[+\frac{2}{\varepsilon^2} + \frac{1}{\varepsilon}(3 + 2l(s) - 2l(t) - 2l(u))\right] T_{qq\to qq}(s,t,u)$
	N_C	Virtual Corr.	$\left[+\frac{2}{\varepsilon}(2l(s) - l(t) - l(u))\right] T_{qq\to qq}(s,t,u)$
		Final State	$\left[-\frac{1}{\varepsilon}(2l(s) - l(t) - l(u))\right] T_{qq\to qq}(s,t,u)$
		Initial State	$\left[-\frac{1}{\varepsilon}(2l(s) - l(t) - l(u))\right] T_{qq\to qq}(s,t,u)$
$q\bar{q} \to gg$	C_F	Virtual Corr.	$\left[-\frac{2}{\varepsilon^2} - \frac{3}{\varepsilon}\right] T_{q\bar{q}\to gg}(s,t,u)$
		Initial State	$\left[+\frac{2}{\varepsilon^2} + \frac{3}{\varepsilon}\right] T_{q\bar{q}\to gg}(s,t,u)$
	N_C	Virtual Corr.	$\left[-\frac{2}{\varepsilon^2} - \frac{11}{3\varepsilon}\right] T_{q\bar{q}\to gg}(s,t,u)$
		Final State	$\left[+\frac{2}{\varepsilon^2} + \frac{11}{3\varepsilon}\right] T_{q\bar{q}\to gg}(s,t,u)$
	N_f	Virtual Corr.	$+\frac{2}{3\varepsilon} T_{q\bar{q}\to gg}(s,t,u)$
		Final State	$-\frac{1}{3\varepsilon} T_{q\bar{q}\to gg}(s,t,u)$
		Initial State	$-\frac{1}{3\varepsilon} T_{q\bar{q}\to gg}(s,t,u)$
	1	Virtual Corr.	$+\frac{1}{\varepsilon} l(s) \left(\left(4N_C^3 C_F + \frac{4C_F}{N_C} \right) \frac{t^2+u^2}{tu} - 16 N_C^2 C_F^2 \frac{t^2+u^2}{s^2} \right)$
		Final State	$-\frac{1}{2\varepsilon} l(s) \left(\left(4N_C^3 C_F + \frac{4C_F}{N_C} \right) \frac{t^2+u^2}{tu} - 16 N_C^2 C_F^2 \frac{t^2+u^2}{s^2} \right)$
		Initial State	$-\frac{1}{2\varepsilon} l(s) \left(\left(4N_C^3 C_F + \frac{4C_F}{N_C} \right) \frac{t^2+u^2}{tu} - 16 N_C^2 C_F^2 \frac{t^2+u^2}{s^2} \right)$
	$8N_C^3 C_F$	Virtual Corr.	$+\frac{1}{\varepsilon} \left(l(t) \left(\frac{u}{t} - \frac{2u^2}{s^2} \right) + l(u) \left(\frac{t}{u} - \frac{2t^2}{s^2} \right) \right)$
		Final State	$-\frac{1}{2\varepsilon} \left(l(t) \left(\frac{u}{t} - \frac{2u^2}{s^2} \right) + l(u) \left(\frac{t}{u} - \frac{2t^2}{s^2} \right) \right)$
		Initial State	$-\frac{1}{2\varepsilon} \left(l(t) \left(\frac{u}{t} - \frac{2u^2}{s^2} \right) + l(u) \left(\frac{t}{u} - \frac{2t^2}{s^2} \right) \right)$
	$8N_C C_F$	Virtual Corr.	$-\frac{1}{\varepsilon} \left(\frac{u}{t} + \frac{t}{u} \right) (l(t) + l(u))$
		Final State	$+\frac{1}{2\varepsilon} \left(\frac{u}{t} + \frac{t}{u} \right) (l(t) + l(u))$
		Initial State	$+\frac{1}{2\varepsilon} \left(\frac{u}{t} + \frac{t}{u} \right) (l(t) + l(u))$
$gg \to gg$	N_C	Virtual Corr.	$\left[-\frac{4}{\varepsilon^2} - \frac{22}{3\varepsilon}\right] T_{gg\to gg}(s,t,u)$
		Final State	$\left[+\frac{2}{\varepsilon^2} + \frac{11}{3\varepsilon}\right] T_{gg\to gg}(s,t,u)$
		Initial State	$\left[+\frac{2}{\varepsilon^2} + \frac{11}{3\varepsilon}\right] T_{gg\to gg}(s,t,u)$
	N_f	Virtual Corr.	$+\frac{4}{3\varepsilon} T_{gg\to gg}(s,t,u)$
		Final State	$-\frac{2}{3\varepsilon} T_{gg\to gg}(s,t,u)$
		Initial State	$-\frac{2}{3\varepsilon} T_{gg\to gg}(s,t,u)$
	$32N_C^4 C_F$	Virtual Corr.	$+\frac{1}{\varepsilon} \left(l(s) \left(3 - 2\frac{tu}{s^2} + \frac{t^4+u^4}{t^2u^2} \right) + \text{cycl. perm.} \right)$
		Final State	$-\frac{1}{2\varepsilon} \left(l(s) \left(3 - 2\frac{tu}{s^2} + \frac{t^4+u^4}{t^2u^2} \right) + \text{cycl. perm.} \right)$
		Initial State	$-\frac{1}{2\varepsilon} \left(l(s) \left(3 - 2\frac{tu}{s^2} + \frac{t^4+u^4}{t^2u^2} \right) + \text{cycl. perm.} \right)$

Table 8: *Cancellation of IR singularities from virtual, final state, and initial state NLO corrections for the resolved partonic subprocesses and different color factors.*

5 Numerical Results

In this section we present numerical results for single and dijet NLO cross sections in complete photoproduction, as they were defined in section 2.5. We use the analytical results that have been calculated in leading order in section 3 and in next-to-leading order in section 4. All UV, IR, and collinear initial state singularities cancelled or could be removed through a renormalization procedure, leading to finite results in four dimensions.

The cross section formulæ are implemented in a FORTRAN computer program, which consists of four main parts as explained in table 9. The first part contains the analytical results of sections

Part No.	Number of Jets	Contributions
1	2	Analytical contributions in LO and NLO
2	2	Numerical contributions in jet cone 1
3	2	Numerical contributions in jet cone 2
4	3	Numerical contributions outside jet cones

Table 9: *Organization of the FORTRAN program into four main parts.*

3 and 4, and the numerical parts are needed for an implementation of the Snowmass jet definition (see section 5.1). Obviously, the third part is only needed for two-jet cross sections. For one-jet cross sections, this region of phase space is included in part four.

The main task of the computer program is to integrate over different parameters. For example, total or partly differential cross sections are integrated over E_T, η_1 and/or η_2. Furthermore, the momentum fractions of the initial photon in the electron x_a, the parton in the photon y_a, and the parton in the proton x_b have to be integrated. Additional momentum fractions z_a and z_b appear in the initial state corrections. Finally, the numerical contributions have to be integrated over the phase space of the third parton E_{T_3}, η_3, and ϕ_3. The two δ-functions for the momentum fractions of the partons going into the hard $2 \to 2$ scattering X_a and X_b,

$$\delta\left(X_a - \frac{1}{2E_e}\sum_i E_{T_i} e^{-\eta_i}\right) \text{ and } \delta\left(X_b - \frac{1}{2E_p}\sum_i E_{T_i} e^{\ \eta_i}\right), \tag{5.1}$$

reduce the total number of integrations by two. The non-trivial task of computing up to seven-dimensional integrals is solved with the Monte Carlo routine VEGAS written by G.P. Lepage [Lep78], which adapts the spacing of the integration bins to the size of the integrand in the bin. We implement our program in FORTRAN77 language on a HP 9000/735 workstation, run under the UNIX operating system HP-UX. An older version was implemented on an IBM 3270 mainframe with operating sytem MVS/ESA.

The input parameters for our predictions will be kept constant throughout this chapter, if not stated otherwise. All cross sections are for HERA conditions, where electrons of energy $E_e = 26.7$ GeV collide with protons of energy $E_p = 820$ GeV. Positive rapidities η correspond to the proton direction. We use the Weizsäcker-Williams approximation of eq. (2.13) with $Q^2_{\max} = 4$ GeV^2 as in the ZEUS experiment, but do not restrict the range of longitudinal photon momentum x_a in the electron. For the parton densities in the proton, we choose the recent next-to-leading order parametrization CTEQ3 in the $\overline{\text{MS}}$ scheme, which already includes HERA deep inelastic scattering data. The newest CTEQ4 parametrizations have become available too late for this thesis, but they do not differ significantly from CTEQ3. The corresponding Λ value of $\Lambda^{(4)} = 239$ MeV is also used in the two-loop calculation

of the strong coupling constant α_s with four flavors. We do not use the one-loop approximation for leading order calculations, because the effects of the next-to-leading order hard scattering contributions are then isolated. The parton densities in the photon are taken from the NLO fit of GRV and transformed from the DIS_γ into the $\overline{\mathrm{MS}}$ scheme. The renormalization and factorization scales are equal to E_T. We use the Snowmass jet definition with $R = 1$, no jet double counting, and no R_{sep} parameter. This makes the cross sections independent of the phase space slicing parameter y, which is fixed at $y = 10^{-3}$. This value is sufficiently small to justify the omission of $\mathcal{O}(y)$ terms in the analytical calculation (see section 5.1).

In section 5.1, we check our analytical results with respect to y-cut independence and with two different existing programs for direct and resolved one-jet production. Section 5.2 contains studies of the dependence of the cross sections on renormalization and factorization scales and on various cancellation mechanisms. Theoretical predictions for one- and two-jet cross sections are presented in sections 5.3 and 5.4, before we conclude this section with a comparison of our calculation to data from the H1 and ZEUS collaborations in section 5.5.

5.1 Check of the Analytical Results

The first check of our analytical results for the photoproduction of jets in next-to-leading order of QCD has already been given in section 4.3. There it has been shown that all infrared divergencies cancel in a consistent way between the virtual and the real corrections, giving a finite cross section in four dimensions. We have therefore missed none of the singular terms. This cancellation mechanism could only work since we integrated the $2 \to 3$ matrix elements over regions, where two final state particles or an initial and a final state particle had an invariant mass $s_{ij} = (p_i + p_j)^2$ smaller than a fraction $y_{F,I,J}$ of the center-of-mass energy s. Naturally, this leads to a dependence of the cross sections on these phase space slicing parameters $y_{F,I,J}$. We choose $y_{\text{cut}} = y_F = y_I = y_J$ in the following.

One possibility to deal with the dependence of the cross section on the invariant mass cut-off y_{cut} is to use it as a definition for the experimentally observed jets. As we noted already in section 2.4, the experimental jet definition has only a correspondence in theory beyond the leading order. Furthermore, we mentioned a special kind of algorithm, i.e. the JADE cluster algorithm, which uses exactly the invariant mass criterion to cluster hadrons into jets. For e^+e^--experiments, one can then identify the theoretical (partonic) with the experimental (hadronic) cut-off

$$y_{\text{cut}}^{\text{theory}} = y_{\text{cut}}^{\text{experiment}} \tag{5.2}$$

and implement our analytical formulæ into a FORTRAN computer program. In this case, the corresponding cross sections are for *exclusive* dijet production.

The numerical value of y_{cut} is constrained in a two-fold manner. First, the real corrections contain simple and quadratic logarithmic terms $\ln y_{\text{cut}}$, $\ln^2 y_{\text{cut}}$, coming from the single and quadratic $1/\varepsilon$ poles, which force the cross section to become negative for $y_{\text{cut}} < 10^{-2}$. Therefore one should choose $y_{\text{cut}} \geq 10^{-2}$. Second, we have always assumed the singular region to be small in the real corrections. This means we have omitted terms like $y_{\text{cut}} \ln y_{\text{cut}}$, y_{cut}, ... This forces us to take $y_{\text{cut}} \ll 1$. The typical value for the JADE algorithm is therefore given by $y_{\text{cut}} \simeq 10^{-2}$.

The omitted terms of $\mathcal{O}(y_{\text{cut}})$ can be calculated numerically to improve the precision of the calculation. This makes it necessary to include the full and un-approximated $2 \to 3$ matrix elements in the FORTRAN program, which are then integrated numerically in the region between the analytical cut-off $y_{\text{cut}}^{\text{theory}}$ and the experimental cut-off $y_{\text{cut}}^{\text{experiment}}$. It is important to note that the full $2 \to 3$ matrix elements have to be integrated *after partial fractioning*. Regions, where a single invariant is small but is not a pole in the matrix element, cannot be neglected. The theoretical invariant mass cut is then reduced to a purely technical variable, on which the physical prediction will no more depend. If one integrates over the phase space outside the experimental cut-off as well, one arrives at *inclusive* dijet cross sections. In this case, the full $2 \to 3$ matrix elements contribute as a leading-order process through the production of three jets, where the third jet is unobserved.

At HERA, we have to deal with a partly hadronic process, for which cluster algorithms are not well suited. We will therefore follow the two experiments H1 and ZEUS and use the Snowmass cone algorithm, where hadrons i are combined into a single jet, if they lie inside a cone in azimuth-rapidity space from the jet center. The experimental cone size R was already defined in section 2.4

$$R_i = \sqrt{(\eta_i - \eta_J)^2 + (\phi_i - \phi_J)^2} \leq R \tag{5.3}$$

and will be chosen to be $R = 1$ in the following. As R takes the role of $y_{\text{cut}}^{\text{experiment}}$, we expect the sum of the analytical two-body and numerical three-body cross sections to be independent of $y_{\text{cut}}^{\text{theory}}$. This is the second decisive test of our analytical results.

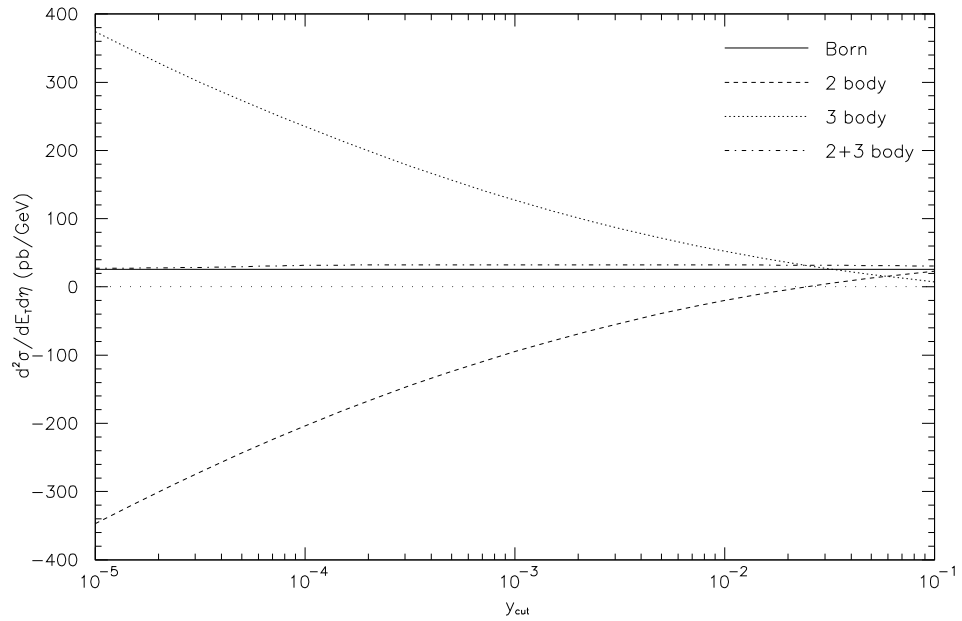

Figure 28: *Inclusive single-jet cross section $d^2\sigma/dE_T d\eta$ for direct photons at $E_T = 20$ GeV and $\eta = 1$, as a function of $y_{\rm cut}$. The analytical (dashed) and numerical (dotted) contributions have a quadratic logarithmic dependence on $y_{\rm cut}$, which cancels in the full next-to-leading order result (dot-dashed curve).*

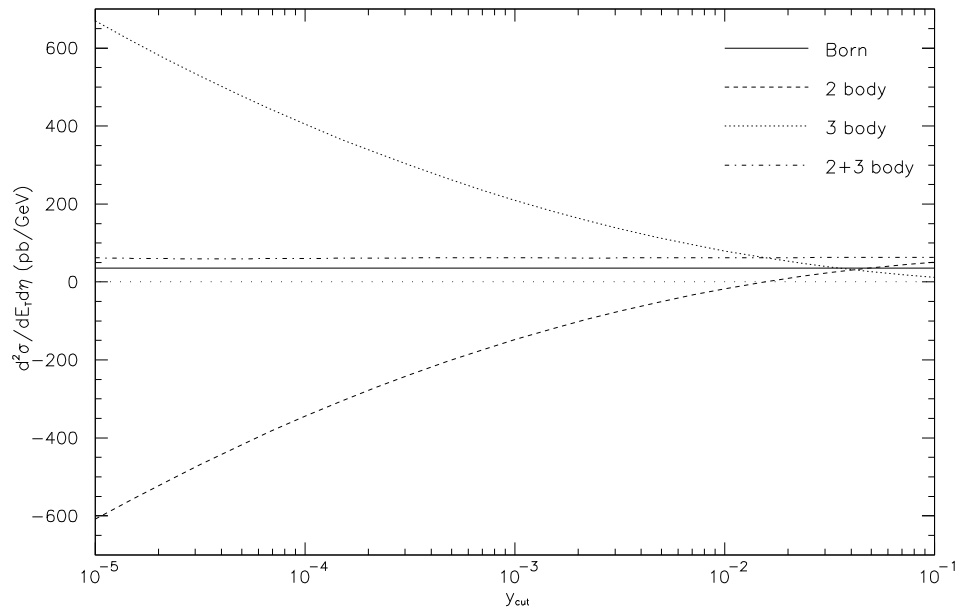

Figure 29: *Inclusive single-jet cross section $d^2\sigma/dE_T d\eta$ for resolved photons at $E_T = 20$ GeV and $\eta = 1$, as a function of $y_{\rm cut}$. Again the sum of two-body (dashed) and three-body (dotted) curves is $y_{\rm cut}$-independent (dot-dashed curve) like the leading order (full) curve.*

In figure 28 we plot the inclusive single-jet cross section $\mathrm{d}^2\sigma/\mathrm{d}E_T\mathrm{d}\eta$ for direct photons at $E_T = 20$ GeV and $\eta = 1$ as a function of y_{cut}. The leading order prediction (full curve) is trivially independent of y_{cut}. The analytical two-body contributions (dashed curve) exhibit a quadratic logarithmic dependence on y_{cut} and turn negative below $y_{\mathrm{cut}} = 2.3 \cdot 10^{-2}$. We add the numerical contributions inside and outside the jet cone into the three-body contributions (dotted curve), which are also quadratically logarithmically dependent on y_{cut}, but positive. The sum of two- and three-body contributions is the full inclusive next-to-leading order result (dot-dashed curve) and is independent of y_{cut}. This proves that the y_{cut}-dependent finite terms in our analytical results are correct. Towards very small values of $y_{\mathrm{cut}} \simeq 10^{-5}$, the dot-dashed curve drops slightly. This is due to the limited accuracy in the numerical integration of the three-body contributions and can be remedied with increased computer power.

Figure 29 is the analogue to figure 28 for resolved photoproduction. The two-body curve turns negative at a slightly smaller value of $y_{\mathrm{cut}} = 1.5 \cdot 10^{-2}$. As the number of contributing partonic subprocesses is much larger than in the direct case, more computer time was needed for similar statistical accuracy.

The ultimate test for our analytical and numerical results consists in the comparison of our prediction with existing predictions, that were obtained by Bödeker [Böd92] (direct case) and by Salesch [Sal93] (resolved case) with different methods. This can only be done for the single-jet inclusive cross section $\mathrm{d}^2\sigma/\mathrm{d}E_T\mathrm{d}\eta$, since dijet cross sections are not available. Bödeker's results are obtained with the subtraction method of Ellis et al. [Ell89] to cancel soft and collinear singularities. Salesch calculated finite cone corrections in addition to the results by Aversa et al. [Ave88], who used the so-called small cone approximation. Here, a small jet cone radius δ is used to slice the phase space and isolate the final state divergencies. The dependence on δ cancels, when the finite cone corrections are added. We take exactly the same parameters in our calculation and in the reference calculations. Furthermore, we choose $y_{\mathrm{cut}} = 10^{-3}$ to ensure that we are not sensitive to the omission of terms of $\mathcal{O}(y_{\mathrm{cut}})$.

The E_T dependence is checked in figure 30 with Bödeker for direct photons and in figure 31 with Salesch for resolved photons at $\eta = 1$. Our prediction (full curve) agrees with the older calculations (open circles) at a level better than 1%. The numerical statistics are so good that the error bars in Bödeker's and Salesch's programs are not seen. For comparison, we include the leading order dotted curves, where the predictions are identical.

We compare the same inclusive single-jet cross section as a rapidity distribution for $E_T = 20$ GeV. We choose now a linear scale for the ordinate in figures 32 for direct and 33 for resolved photoproduction. This makes it possible to see the error bars in the reference calculations (open circles) which are at the same level as the agreement between the different programs. Errors of $\sim 1\%$ present in our program are not shown. With more computer time, the agreement would certainly be even better.

From these comparisons, we conclude that also the cut-independent finite terms in our analytical results and in our numerical FORTRAN program are correct. Even more, it was possible to check the transverse energy, rapidity, and other distributions not shown here for every single direct and resolved partonic subprocess. We found perfect agreement everywhere.

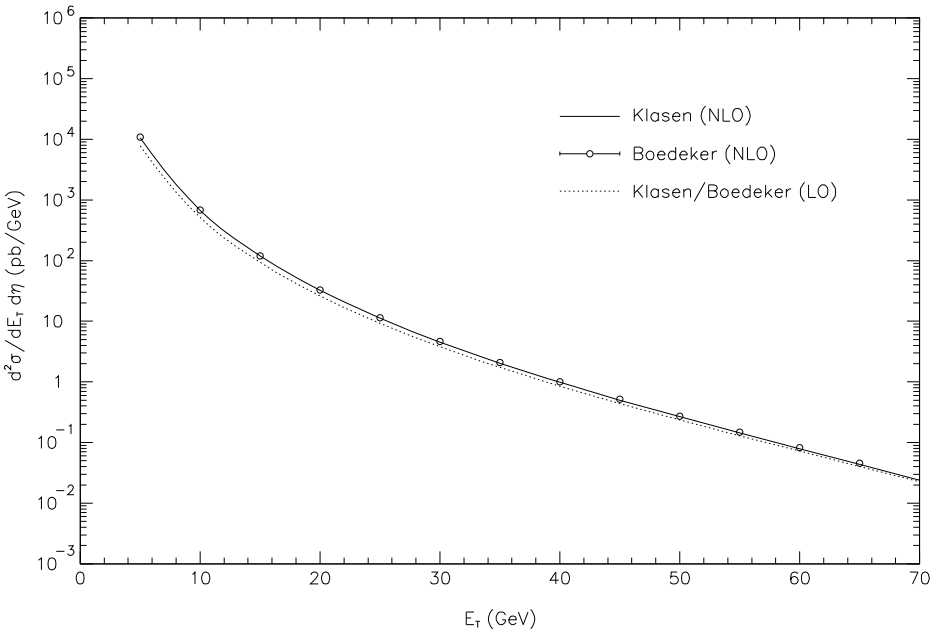

Figure 30: *Inclusive single-jet cross section $d^2\sigma/dE_T d\eta$ for direct photons at $\eta = 1$, as a function of E_T. The subtraction method results (open circles) agree with our phase space slicing prediction (full curve).*

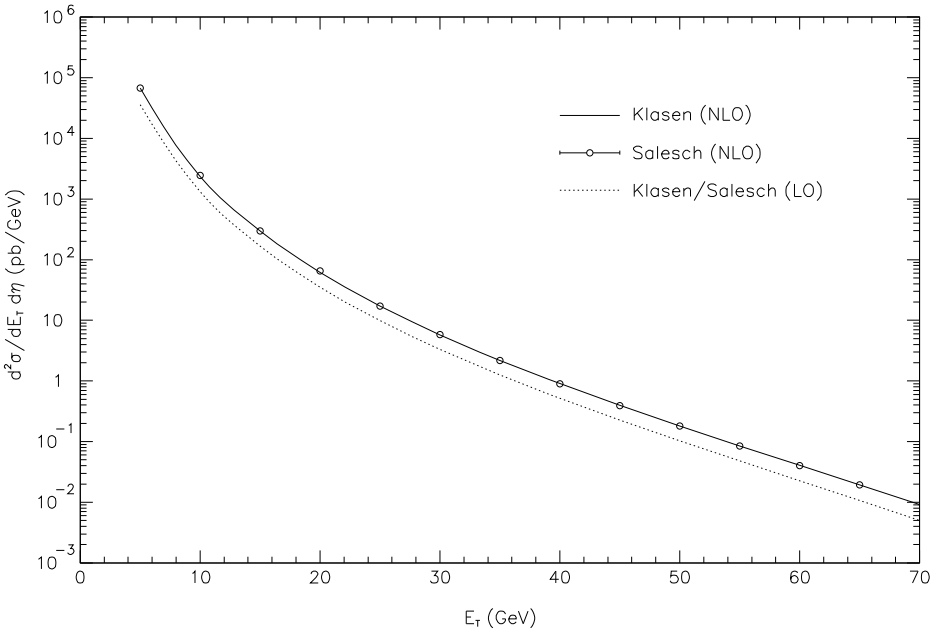

Figure 31: *Inclusive single-jet cross section $d^2\sigma/dE_T d\eta$ for resolved photons at $\eta = 1$, as a function of E_T. The small cone approximation and finite cone corrections (open circles) agree with our invariant mass cut method (full curve). The leading order (dotted) curve is shown for comparison.*

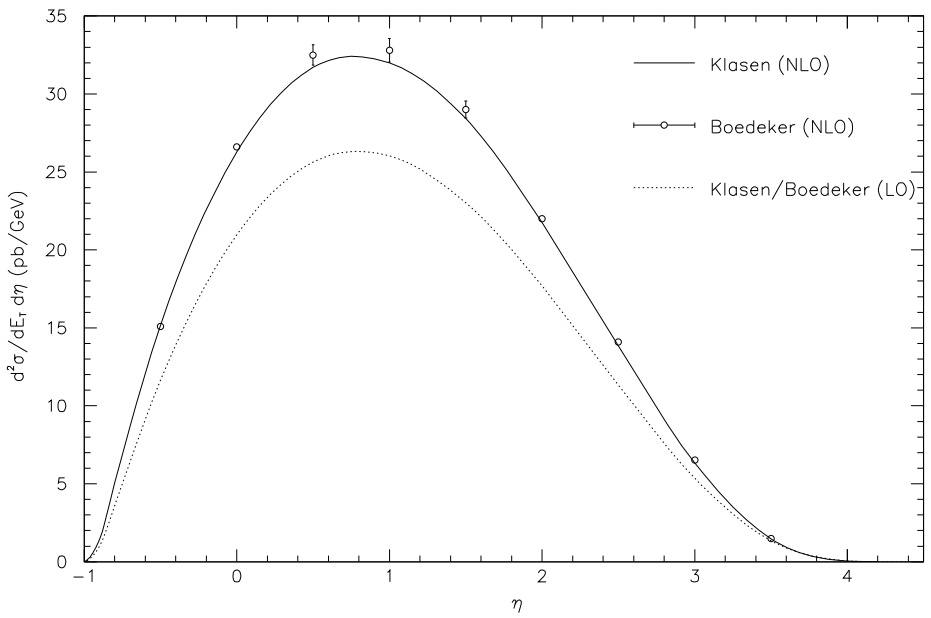

Figure 32: *Inclusive single-jet cross section $d^2\sigma/dE_T d\eta$ for direct photons at $E_T = 20$ GeV, as a function of η. Our predictions (full curve) agree with Bödeker's predictions (open circles).*

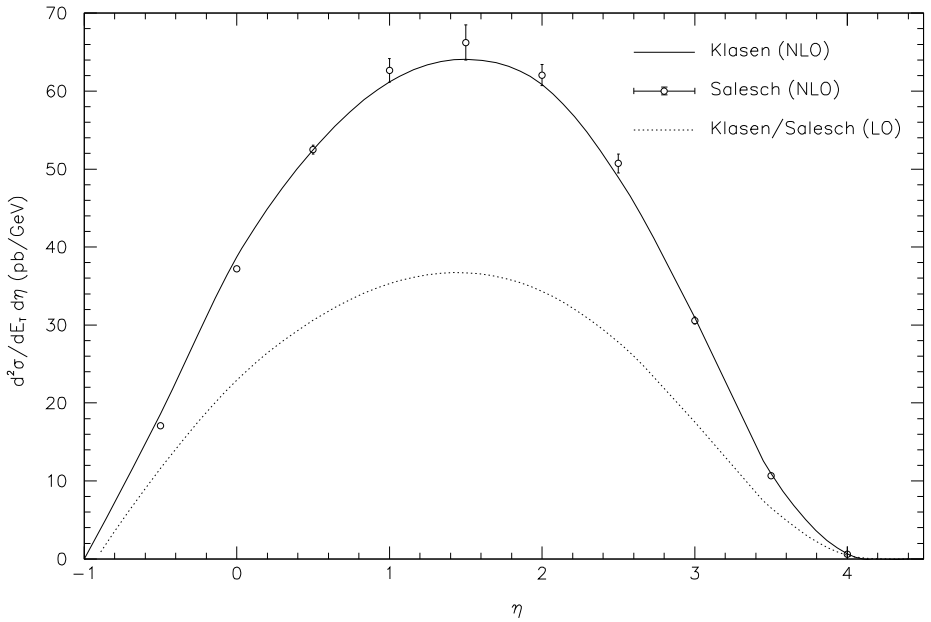

Figure 33: *Inclusive single-jet cross section $d^2\sigma/dE_T d\eta$ for resolved photons at $E_T = 20$ GeV, as a function of η. Good agreement is seen for Salesch's (open circles) and our calculation (full curve). The leading order (dotted) curve is shown for comparison.*

5.2 Renormalization- and Factorization-Scale Dependences

From the numerical checks in section 5.1, we can now be sure to have a reliable computer program for the calculation of jet cross sections in photoproduction. We will use this program here to study the dependence of these cross sections on the three relevant scales:

- the renormalization scale μ
- the factorization scale for the photon M_a
- the factorization scale for the proton M_b

We expect a reduced dependence in next-to-leading order for all three scales with respect to the leading order. As stated in sections 4.1, 2.2, and 2.3, we take μ, M_a, and M_b to be of $\mathcal{O}(E_T)$. Therefore, we will always plot the single-jet inclusive cross section $\mathrm{d}^2\sigma/\mathrm{d}E_T\mathrm{d}\eta$ as a function of scale/E_T in the following. Direct and resolved photoproduction will be presented separately at a fixed transverse jet energy of $E_T = 20$ GeV and at a rapidity of $\eta = 1$, where the cross sections are at their maximum.

We start with the dependence on the renormalization scale μ. Leading order $\mathcal{O}(\alpha\alpha_s)$ cross sections depend on μ only through the running of the strong coupling constant $\alpha_s(\mu^2)$, which has to be implemented in the one-loop approximation

$$\alpha_s(\mu^2) = \frac{12\pi}{(33 - 2N_f)\ln\frac{\mu^2}{\Lambda^2}} \tag{5.4}$$

for consistency. The results are shown as dotted curves in figures 34 and 35. For direct photons, the curve drops by one half when going from $\mu = 1/4E_T$ to $\mu = 4E_T$. The resolved photon hard cross section is one order higher in α_s ($\mathcal{O}(\alpha_s^2)$) and therefore drops even by a factor of four. This strong $1/\ln(\mu^2)$-behavior is slightly weakened in the two-loop approximation

$$\alpha_s(\mu^2) = \frac{12\pi}{(33 - 2N_f)\ln\frac{\mu^2}{\Lambda^2}}\left(1 - \frac{6(153 - 19N_f)}{(33 - 2N_f)^2}\frac{\ln(\ln\frac{\mu^2}{\Lambda^2})}{\ln\frac{\mu^2}{\Lambda^2}}\right), \tag{5.5}$$

where one adds further logarithmic terms in μ^2. These curves are shown in dashed form in figures 34 and 35. However, going from one-loop to two-loop α_s affects not so much the shape but the overall normalization. The cross sections are reduced by 20% in the direct and by almost 40% in the resolved case. Although not physically relevant, the dashed curves can be compared to the full curves and enable us to see solely the effect of the explicit logarithmic terms

$$\frac{1}{\varepsilon}\left(\frac{4\pi\mu^2}{s}\right)^{\varepsilon} \doteq \frac{1}{\varepsilon} + \ln\frac{4\pi\mu^2}{s}, \tag{5.6}$$

that appear in the one-loop corrections to the hard cross section in section 4.1. They cancel partly the α_s-dependence, so that the full curves in figures 34 and 35 are much flatter compared to the leading order curves with one- and two-loop α_s. The direct curve varies by only 20% and exhibits a maximum near $\mu/E_T \simeq 1/2$. According to the principle of minimal sensitivity [Ste81, Ste81a], $\mu = 1/2E_T$ would then be the optimal scale. The dependence of the resolved photoproduction cross section is also weakened and amounts to a factor of two in NLO. It meets the one-loop LO result at $\mu \simeq 1/2E_T$. This scale is sometimes preferred since the NLO corrections are small in its vicinity.

The next scale that we will study is the factorization scale in the photon M_a. It separates the soft parton content in the photon given by the parton distribution function $F_{a/\gamma}(y_a, M_a^2)$ from the hard partonic cross section $\mathrm{d}\sigma_{ab}(ab \to \text{jets})$. As discussed in section 2.3, direct and resolved processes are

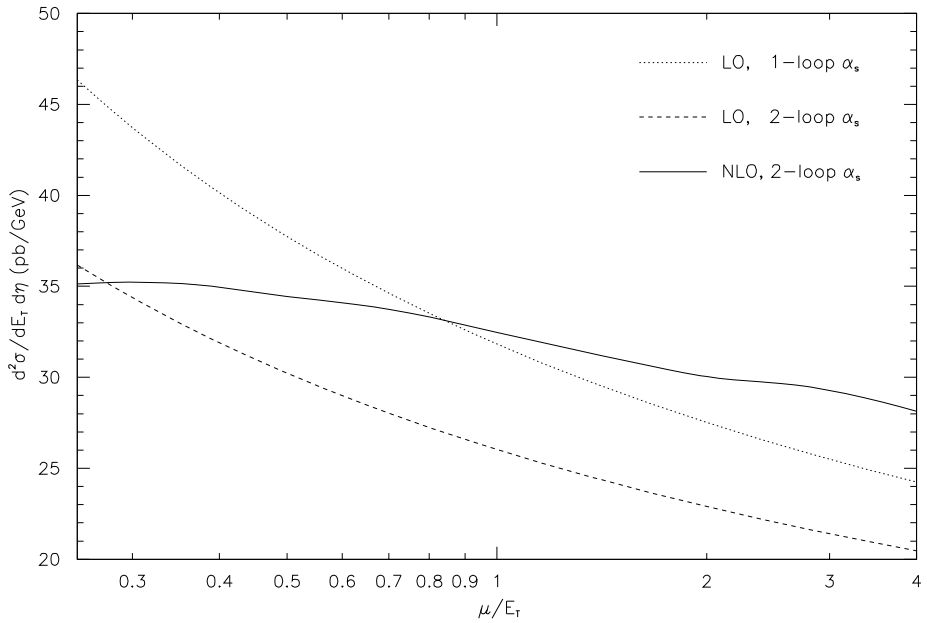

Figure 34: *Inclusive single-jet cross section $d^2\sigma/dE_T d\eta$ for direct photons at $E_T = 20$ GeV and $\eta = 1$, as a function of μ/E_T. From $\mu = 1/4E_T$ to $\mu = 4E_T$, the leading order predictions drop by one half. The two-loop curve (dashed) is 20% smaller than the one-loop curve (dotted). The next-to-leading order (full) curve only varies by 20%.*

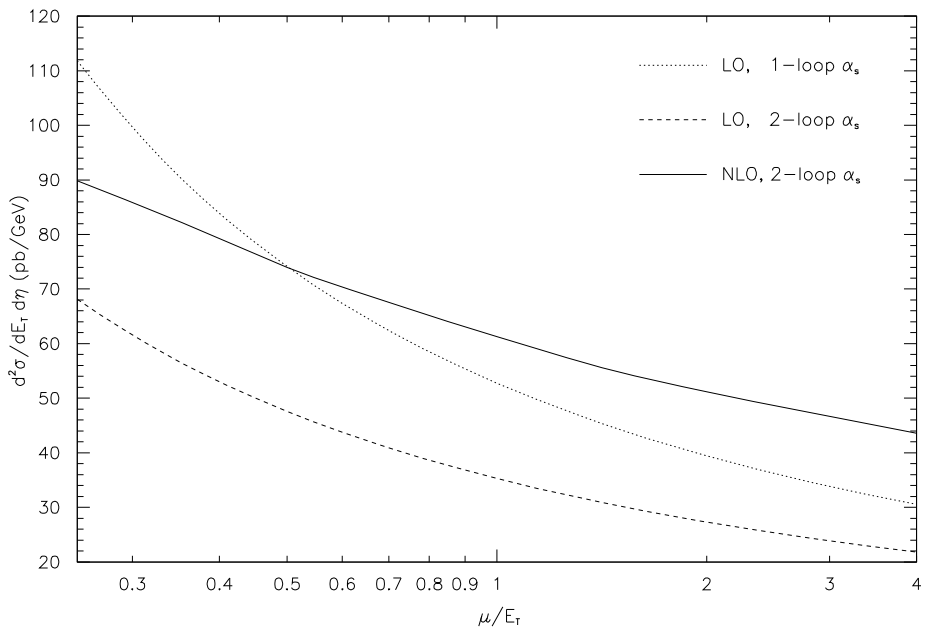

Figure 35: *Inclusive single-jet cross section $d^2\sigma/dE_T d\eta$ for resolved photons at $E_T = 20$ GeV and $\eta = 1$, as a function of μ/E_T. From $\mu = 1/4E_T$ to $\mu = 4E_T$, the leading order predictions drop by a factor of four. The two-loop curve (dashed) is 40% smaller than the one-loop curve (dotted). The next-to-leading order (full) curve only varies by a factor of two.*

only separable in leading order. The direct parton distribution is then simply a δ-function $\delta(1-y_a)$ and does not depend on any scale. This can be seen from the dotted curve in figure 36. The resolved part depends, however, strongly on the scale M_a as could already be inferred from e^+e^--data on the F_2^γ structure function in figure 11. We expect the M_a-dependence to be dominated by the asymptotic pointlike contribution to F_2^γ

$$F_2^\gamma(x_B, M_a^2) = \alpha\left[\frac{1}{\alpha_s(M_a^2)}a(x_B) + b(x_B)\right] \tag{5.7}$$

that was already presented in eq. (2.29) and behaves like $\ln M_a^2$. Clearly we see this behavior in the leading order dot-dashed curve in figure 36, which is identical to the dotted curve in figure 37 and is obtained with the GRV photon distributions. As the GRV distributions are fitted in the DIS_γ-scheme, we transform them into the $\overline{\mathrm{MS}}$ scheme by adding the correct finite terms independent of M_a. The renormalization scheme dependence was studied by Bödeker, Kramer, and Salesch [Böd94] and will not be studied here again. The main result is that the dependence disappears in next-to-leading order, because the transformation of the resolved part is compensated through scheme dependent terms in the initial state singularities of the direct photon. The renormalization of the singularities in section 4.2.5

$$F_{a/\gamma}(y_a, M_a^2) = \int_{y_a}^1 \frac{\mathrm{d}z_a}{z_a}\left[\delta_{a\gamma}\delta(1-z_a) + \frac{\alpha}{2\pi}R_{q\leftarrow\gamma}(z_a, M_a^2)\right]F_{\gamma/\gamma}\left(\frac{y_a}{z_a}\right) \tag{5.8}$$

gave also rise to scale dependent terms

$$R_{a\leftarrow\gamma}(z_a, M_a^2) = -\frac{1}{\varepsilon}P_{q\leftarrow\gamma}(z_a)\frac{\Gamma(1-\varepsilon)}{\Gamma(1-2\varepsilon)}\left(\frac{4\pi\mu^2}{M_a^2}\right)^\varepsilon \tag{5.9}$$

through the $1/\varepsilon$ pole

$$-\frac{1}{\varepsilon}P_{q\leftarrow\gamma}(z_a)\left[\left(\frac{4\pi\mu^2}{s}\right)^\varepsilon - \left(\frac{4\pi\mu^2}{M_a^2}\right)^\varepsilon\right] = -P_{q\leftarrow\gamma}(z_a)\ln\left(\frac{M_a^2}{s}\right). \tag{5.10}$$

We can see this negative logarithmic behavior ($-\ln M_a^2$) in the dashed curve in figure 36 for next-to-leading order direct photoproduction. It has the opposite sign than the LO resolved contribution, so that the sum of both will eventually be almost independent of M_a (full curve in figure 36). The next-to-leading order resolved contribution has a similar, but slightly steeper shape than the leading order and is shown as a full curve in figure 37. Therefore, the dependence of the complete NLO calculation on the photon factorization scale is slightly stronger than in the full line of figure 36. The difference will be compensated in next-to-next-to-leading order (NNLO) of direct photoproduction, which is beyond the scope of our calculation.

For the proton, we have a similar scale M_b as in the photon case that separates the soft and the hard part of the hadronic and partonic cross sections. Of course, the proton is not point-like and does not have a direct component. The scale dependence of the proton distribution functions $F_{b/p}(x_b, M_b^2)$ is governed by the DGLAP-equations. If we solve them iteratively, we can assume that in

$$\frac{\mathrm{d}F_{b/p}(x_b, M_b^2)}{\mathrm{d}\ln M_b^2} = \frac{\alpha_s^{(0)}}{2\pi}\int_{x_b}^1 \frac{\mathrm{d}z_b}{z_b}P_{b\leftarrow b'}\left(\frac{x_b}{z_b}\right)F_{b/p}^{(0)}(z_b) \tag{5.11}$$

the starting distributions $F_{b/p}^{(0)}(z_b)$ and the coupling constant $\alpha_s^{(0)}$ are scale independent. Then, the integral over $\mathrm{d}\ln M_b^2$ can be carried out leading to a simple logarithmic behavior

$$F_{b/p}(x_b, M_b^2) = \frac{\alpha_s^{(0)}}{2\pi}\int_{x_b}^1 \frac{\mathrm{d}z_b}{z_b}P_{b\leftarrow b'}\left(\frac{x_b}{z_b}\right)F_{b/p}^{(0)}(z_b)\ln\left(\frac{M_b^2}{s}\right). \tag{5.12}$$

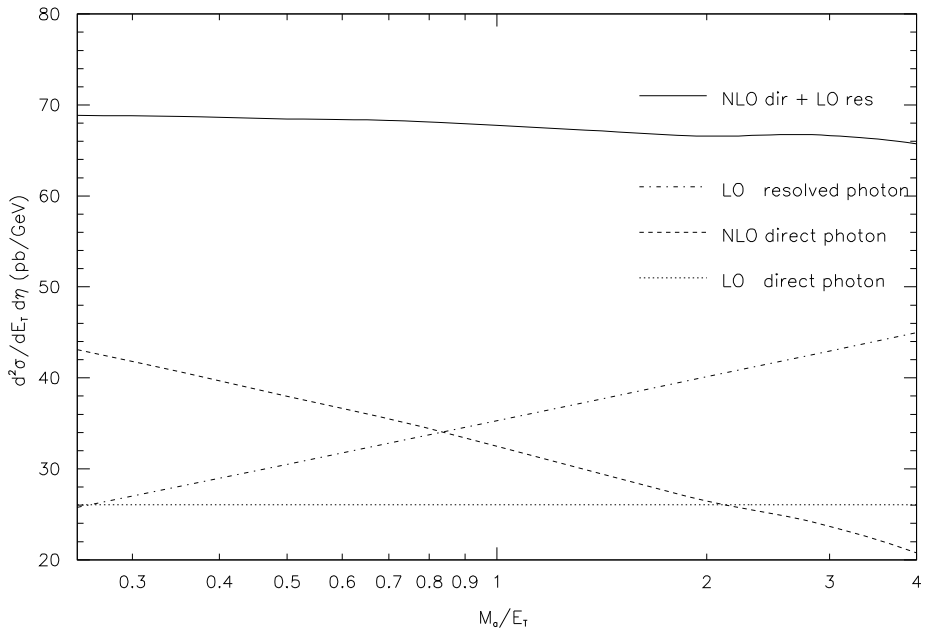

Figure 36: *Inclusive single-jet cross section $d^2\sigma/dE_T d\eta$ for direct photons at $E_T = 20$ GeV and $\eta = 1$, as a function of M_a/E_T. The LO direct curve (dotted) is independent of M_a as is the sum (full curve) of NLO direct (dashed) and LO resolved (dot-dashed) contributions.*

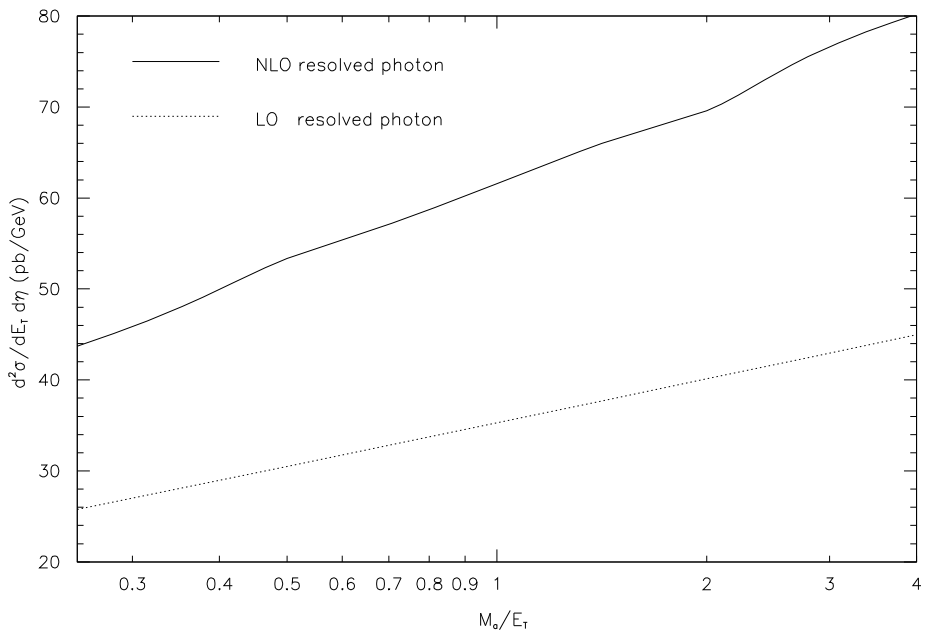

Figure 37: *Inclusive single-jet cross section $d^2\sigma/dE_T d\eta$ for resolved photons at $E_T = 20$ GeV and $\eta = 1$, as a function of M_a/E_T. The logarithmic behavior of the resolved part is slightly steeper in NLO (full curve) than in LO (dotted curve).*

For the LO resolved photon contribution, this approximation is obviously good enough as can be seen from the dotted curve in figure 39. The cross section drops by 20% when going from $M_b = 1/4E_T$ to $M_b = 4E_T$. Of course, the full solution of the DGLAP equations is not so simple, and the LO direct photon contribution in figure 38 deviates slightly from a simply logarithmic graph. The variation of the cross section here amounts only to 6.5%. In next-to-leading order, initial state singularities arise as in the photon case and are absorbed into the proton structure function

$$F_{b/p}(x_b, M_b^2) = \int_{x_b}^1 \frac{\mathrm{d}z_b}{z_b} \left[\delta_{bb'}\delta(1-z_b) + \frac{\alpha_s}{2\pi} R'_{b\leftarrow b'}(z_b, M_b^2) \right] F_{b'/p}\left(\frac{x_b}{z_b}\right). \tag{5.13}$$

Again, finite terms accompany the pole in the $\overline{\mathrm{MS}}$ scheme

$$R'_{b\leftarrow b'}(z_b, M_b^2) = -\frac{1}{\varepsilon} P_{b\leftarrow b'}(z_b) \frac{\Gamma(1-\varepsilon)}{\Gamma(1-2\varepsilon)} \left(\frac{4\pi\mu^2}{M_b^2}\right)^{\varepsilon}, \tag{5.14}$$

which depend on M_b^2 through

$$-\frac{1}{\varepsilon} P_{b\leftarrow b'}(z_b) \left[\left(\frac{4\pi\mu^2}{s}\right)^{\varepsilon} - \left(\frac{4\pi\mu^2}{M_b^2}\right)^{\varepsilon} \right] = -P_{b\leftarrow b'}(z_b) \ln\left(\frac{M_b^2}{s}\right). \tag{5.15}$$

These logarithms cancel the leading logarithmic behavior of the parton distribution functions in the proton. Consequently, the full next-to-leading order curves in figures 38 and 39 depend only very weakly on the renormalization scale M_b in the proton. Finally, we consider the total scale dependence for complete photoproduction in figure 40. The dependence of the inclusive single-jet cross section on $M = \mu = M_a = M_b$ is dominated by the renormalization scale dependence in the one-loop (dotted curve) and two-loop (dashed curve) approximation for α_s. Since resolved photoproduction is more important than direct photoproduction at $E_T = 20$ GeV, figure 40 resembles figure 35 more than figure 34. The total scale dependence is reduced by almost a factor of two in next-to-leading order (full curve).

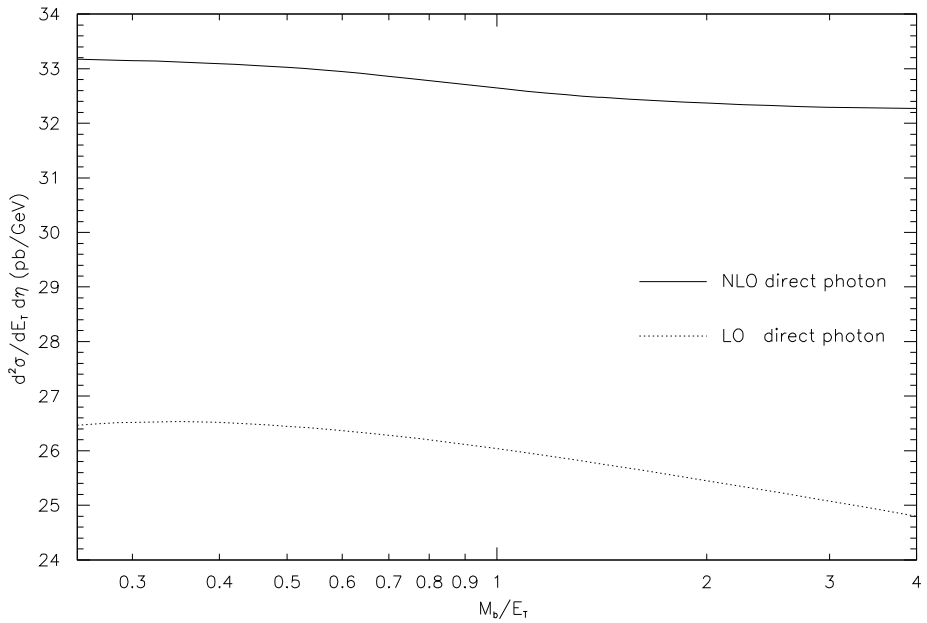

Figure 38: *Inclusive single-jet cross section $d^2\sigma/dE_T d\eta$ for direct photons at $E_T = 20$ GeV and $\eta = 1$, as a function of M_b/E_T. The weak behavior of the LO (dotted) curve is even more reduced in NLO (full curve).*

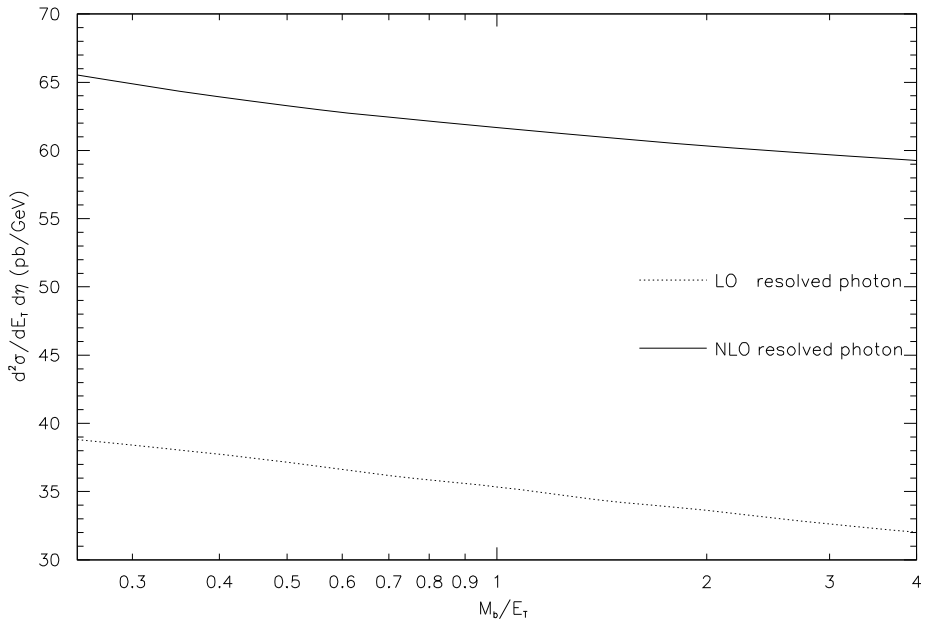

Figure 39: *Inclusive single-jet cross section $d^2\sigma/dE_T d\eta$ for resolved photons at $E_T = 20$ GeV and $\eta = 1$, as a function of M_b/E_T. The approximately logarithmic dependence in LO (dotted curve) is reduced in NLO (full curve).*

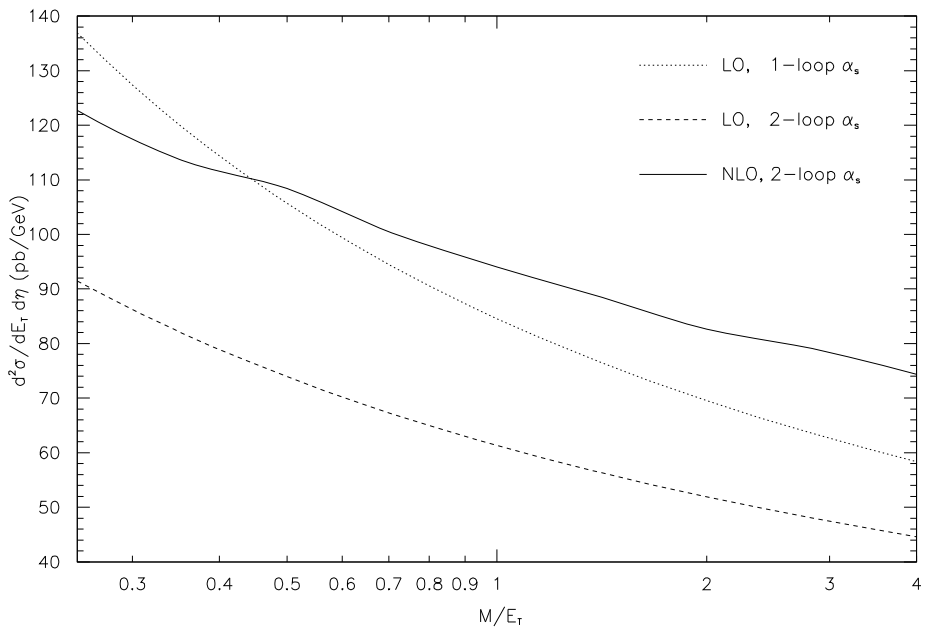

Figure 40: *Complete inclusive single-jet cross section $d^2\sigma/dE_T d\eta$ at $E_T = 20$ GeV and $\eta = 1$, as a function of M/E_T for $M = \mu = M_a = M_b$. The strong dependence in LO (dotted and dashed curves) is reduced in NLO (full curve).*

5.3 One-Jet Cross Sections

In the last section, we have studied the dependence of the inclusive single-jet cross section on the various scales, which cannot be predicted from theory. It was shown that the next-to-leading order cross section is much less dependent on the renormalization and factorization scales than the leading order cross section, due to cancellation mechanisms. We continue to study one-jet cross sections here, but shift the emphasis towards experimentally relevant distributions. The two main experimental observables in the double differential cross section

$$\frac{\mathrm{d}^2\sigma}{\mathrm{d}E_T\mathrm{d}\eta} = \sum_b \int_{x_{a,\min}}^1 \mathrm{d}x_a x_a F_{a/e}(x_a, M_a^2) x_b F_{b/p}(x_b, M_b^2) \frac{4E_e E_T}{2x_a E_e - E_T e^{-\eta}} \frac{\mathrm{d}\sigma}{\mathrm{d}t}(ab \to p_1 p_2) \qquad (5.16)$$

are the hardness or transverse energy E_T of the observed jet and its orientation in the detector, i.e. the angle θ it forms with the beam axis. Instead of this angle, we use the pseudorapidity $\eta = -\ln[\tan(\theta/2)]$ as usual. As the electron is only weakly deflected, it stays in the beam pipe like the proton remnant. Therefore, the jets are homogeneously distributed in the azimuthal angle ϕ, and we have integrated over ϕ in the theoretical prediction. The single-jet cross sections for direct photoproduction have already been published [Kla95a], those for resolved photoproduction are unpublished.

We start with distributions in the jet transverse energy E_T, which is at the same time a measure for the resolution of partons within the photon and the proton. In figure 41, we plot the direct photon contribution for transverse energies between 5 and 70 GeV. In this interval, the cross section drops by almost six orders of magnitude. The next-to-leading order curves are always above the leading order predictions. To separate the curves for three different rapidities, we multiplied those for $\eta = 0$ and $\eta = 2$ by factors of 0.1 and 0.5, respectively. At $\eta = 0$, the phase space restricts the accessible range in E_T to $E_T < 50$ GeV. The so-called k-factor, i.e. the ratio of NLO to LO, drops from 1.8 at 5 GeV to 1.2 at 70 GeV for $\eta = 1$, so that the higher order corrections are more important at small scales, where the strong coupling α_s is large. Had we calculated the leading order with one-loop α_s, the correction would, however, not be so large.

The corresponding curves for resolved photoproduction are shown in figure 42. Here, the curves for $\eta = 1$ and $\eta = 2$ lie closer to each other in spite of the rescaling for $\eta = 2$. This already hints at a broader maximum in the rapidity distribution compared to the direct case (see below). The NLO and LO curves lie further apart due to the large k-factor of about 1.8 over the whole E_T-range. This can be understood from the non-perturbative nature of resolved photons, where higher order corrections are more important at all scales due to the many channels involved.

The rapidity distribution for direct photons is presented in figure 43 at a transverse energy of $E_T = 20$ GeV. In the available phase space of $\eta \in [-1; 4]$, the cross section exhibits a rather broad maximum and steep edges. The k-factor is 1.25 in the central region.

We have already mentioned that the corresponding distribution for resolved photons is expected to have an even broader maximum. This proves to be true in figure 44, where the maximum is also slightly shifted in the proton direction from $\eta = 1$ to $\eta = 1.5$. The reason can be found in the lower longitudinal momentum of photon components with respect to a direct photon. The next-to-leading order cross section is about 80% larger than the leading order cross section, which is compatible to the observation of a large k-factor from the E_T-distribution above.

We now look at the interplay of direct and resolved photoproduction in inclusive single-jet cross sections. Figures 45 and 46 present the leading order and next-to-leading order predictions for complete photoproduction (full curves), which are the sums of the direct (dotted) and resolved (dashed) curves already presented above. The rapidity of the observed jet is fixed at $\eta = 1$. Obviously, the

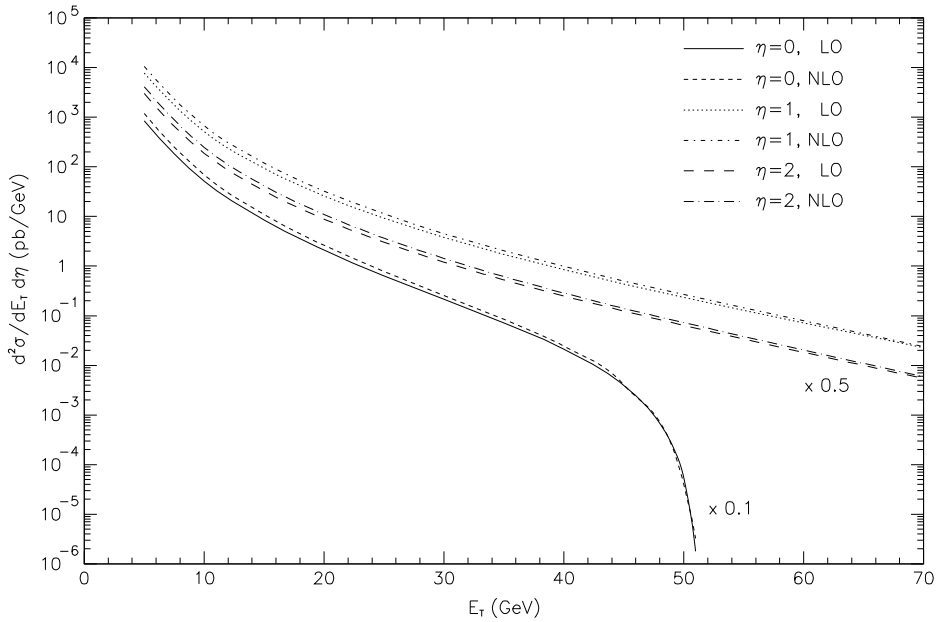

Figure 41: *Inclusive single-jet cross section $d^2\sigma/dE_T d\eta$ for direct photons as a function of E_T for various rapidities $\eta = 0, 1, 2$ in LO and NLO. The cross section for $\eta = 0$ ($\eta = 2$) is multiplied by a factor of* 0.1 (0.5).

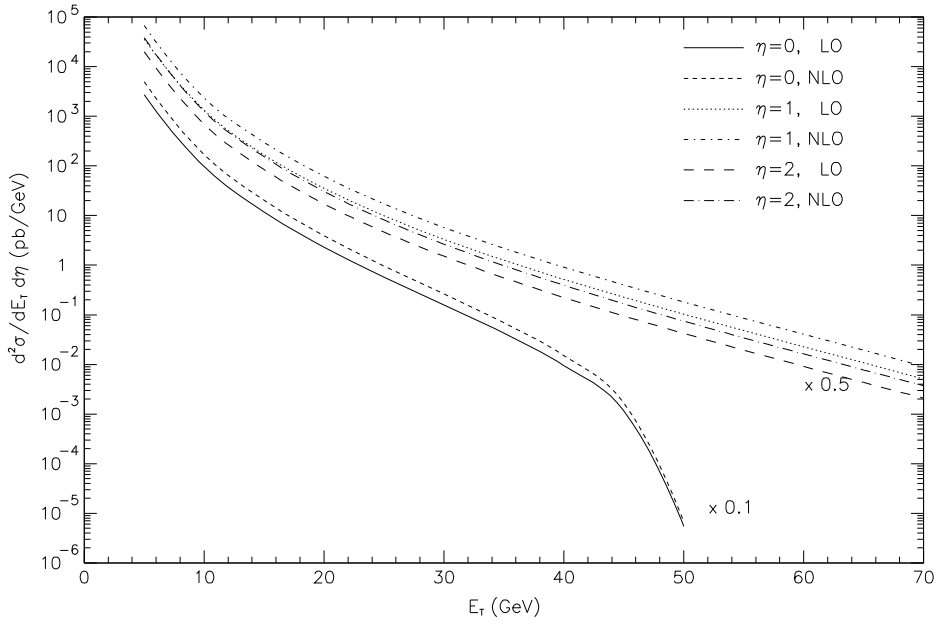

Figure 42: *Inclusive single-jet cross section $d^2\sigma/dE_T d\eta$ for resolved photons as a function of E_T for various rapidities $\eta = 0, 1, 2$ in LO and NLO. The cross section for $\eta = 0$ ($\eta = 2$) is multiplied by a factor of* 0.1 (0.5).

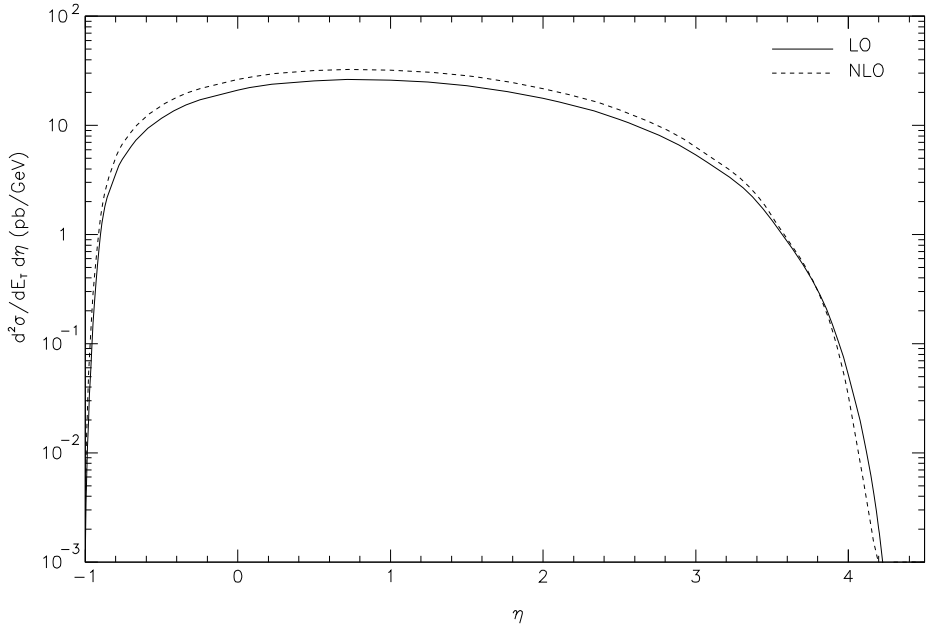

Figure 43: *Inclusive single-jet cross section $d^2\sigma/dE_T d\eta$ for direct photons as a function of η for $E_T = 20$ GeV in LO and NLO.*

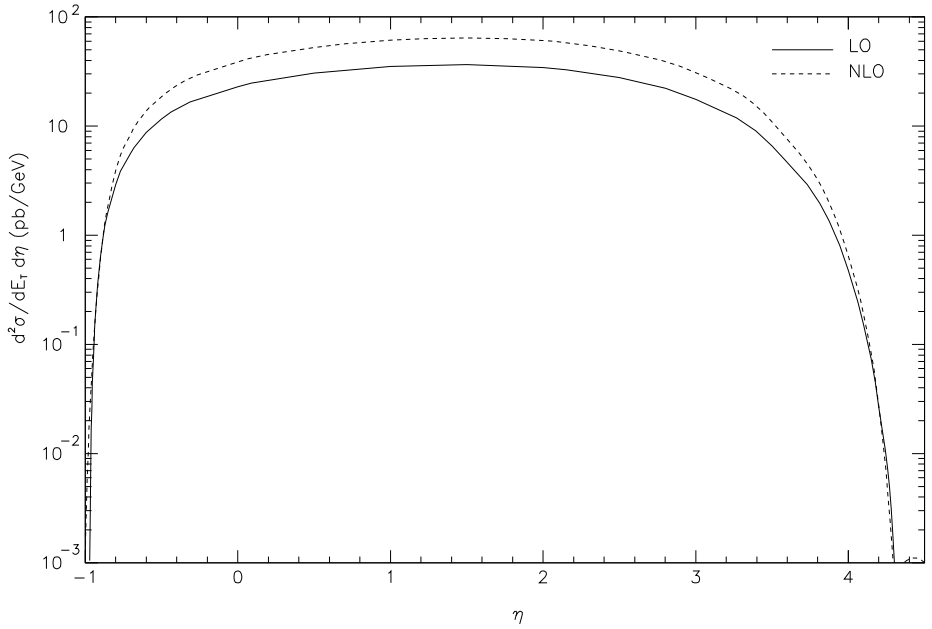

Figure 44: *Inclusive single-jet cross section $d^2\sigma/dE_T d\eta$ for resolved photons as a function of η for $E_T = 20$ GeV in LO and NLO.*

resolved photon component is dominating at low transverse energies due to the photon structure function and unimportant at large transverse energies, where the perturbative point-like coupling is large. In leading order, the intersection of the resolved and direct curves lies near 26 GeV and is shifted towards 37 GeV in next-to-leading order. The resolved process has larger NLO corrections than the direct process, so that the region, in which the latter is important, moves to higher E_T.

The rapidity distributions for full photoproduction are shown as full curves in figures 47 and 48 for leading and next-to-leading order at a transverse energy of $E_T = 20$ GeV. One expects the direct photon to be important mostly in the electron direction at small or negative rapidities. This behavior can be seen in both figures, but only close to the boundary of phase space below $\eta = 0$.

In figures 49 and 50, we plot the dependence of the single-jet inclusive cross section on the jet cone size R in the Snowmass convention [Hut92]. As discussed in section 2.4, a theoretical definition for jets containing more than one parton is only possible in next-to-leading order. Therefore only the full curves depend on R, whereas the leading order curves are constant. The dependence has the functional form of the next-to-leading order result [Sal93, Kra94]

$$\frac{\mathrm{d}^2\sigma}{\mathrm{d}E_T \mathrm{d}\eta} = a + b \ln R + cR^2, \tag{5.17}$$

For the direct photon contribution in figure 49, the leading and higher order predictions are equal at $R \simeq 1$ for one-loop α_s (dotted) and at $R \simeq 0.6$ for two-loop α_s (dashed). For the resolved photon contribution in figure 50, the situation is different. The stable points lie at $R \simeq 0.7$ for one-loop (dotted) and $R \simeq 0.12$ for two-loop α_s.

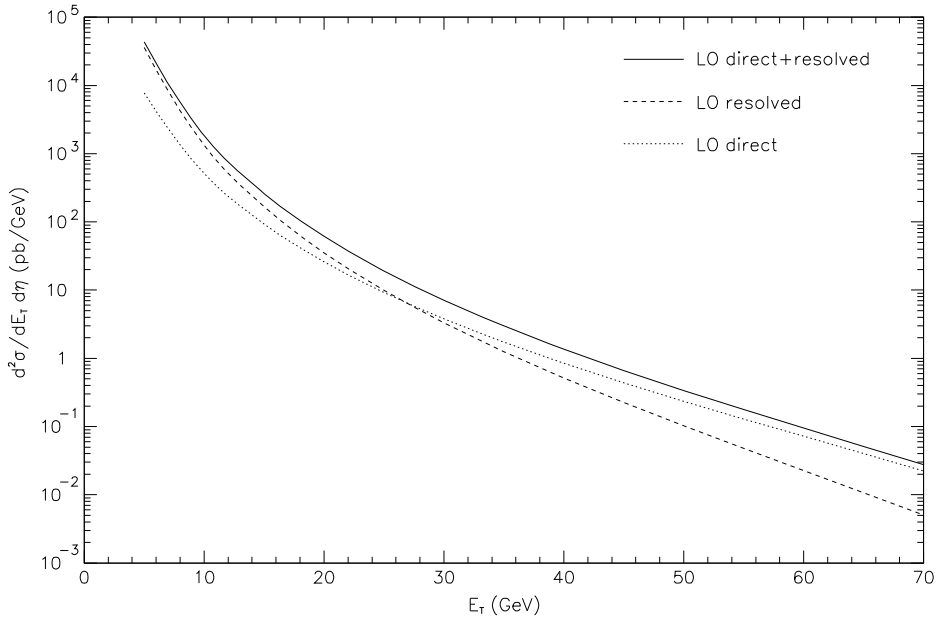

Figure 45: *Inclusive single-jet cross section $d^2\sigma/dE_T d\eta$ for complete photoproduction at $\eta = 1$, as a function of E_T. The full curve is the sum of the LO direct (dotted) and LO resolved (dashed) contributions.*

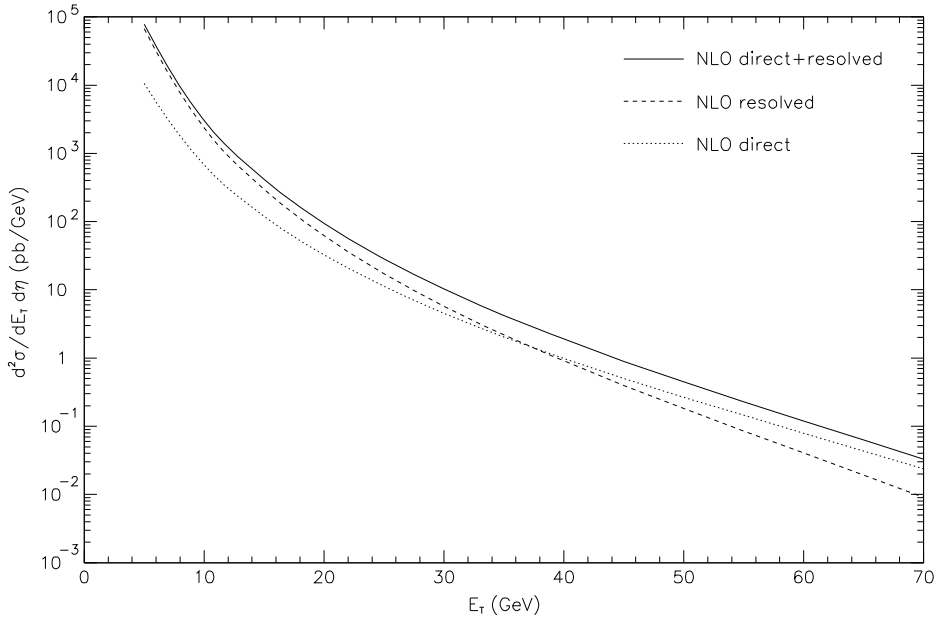

Figure 46: *Inclusive single-jet cross section $d^2\sigma/dE_T d\eta$ for complete photoproduction at $\eta = 1$, as a function of E_T. The full curve is the sum of the NLO direct (dotted) and NLO resolved (dashed) contributions.*

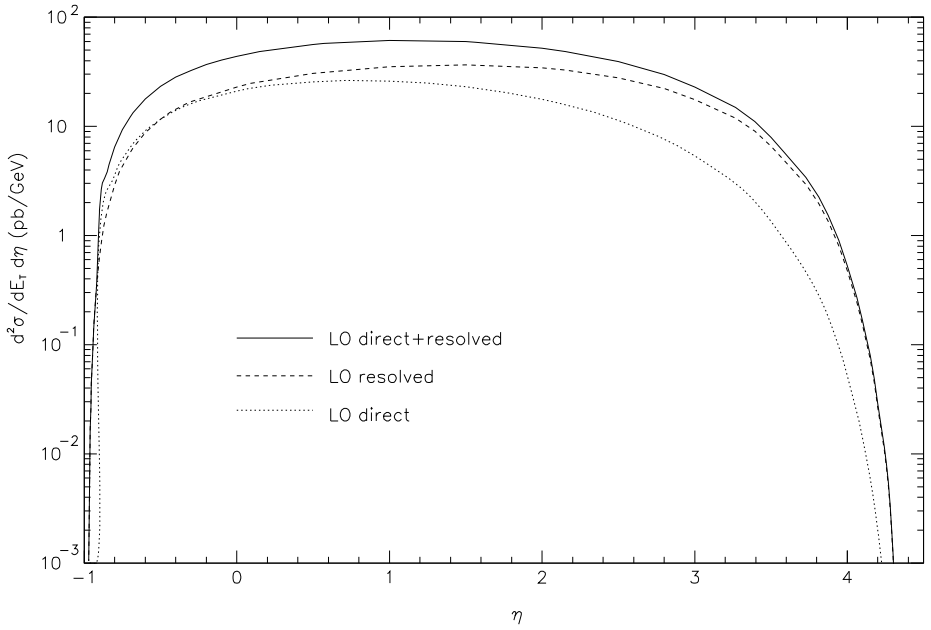

Figure 47: *Inclusive single-jet cross section $d^2\sigma/dE_T\,d\eta$ for complete photoproduction at $E_T = 20$ GeV, as a function of η. The full curve is the sum of the LO direct (dotted) and LO resolved (dashed) contributions.*

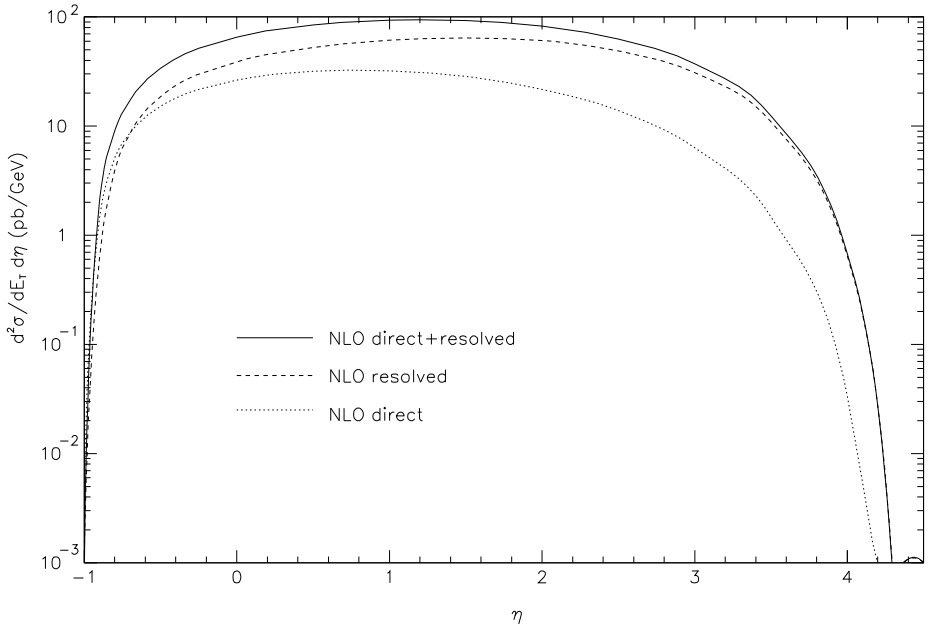

Figure 48: *Inclusive single-jet cross section $d^2\sigma/dE_T\,d\eta$ for complete photoproduction at $E_T = 20$ GeV, as a function of η. The full curve is the sum of the NLO direct (dotted) and NLO resolved (dashed) contributions.*

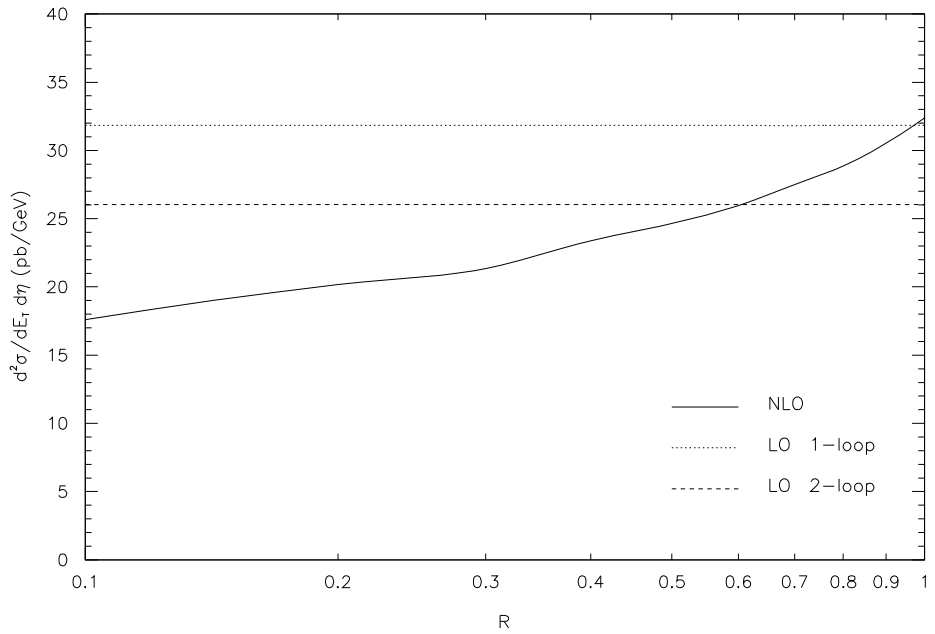

Figure 49: *Inclusive single-jet cross section $d^2\sigma/dE_T d\eta$ for direct photons at $E_T = 20$ GeV and $\eta = 1$, as a function of the jet cone size R. Only the NLO (full) curve and not the LO curves with one- (dotted) or two-loop (dashed) α_s depends on R.*

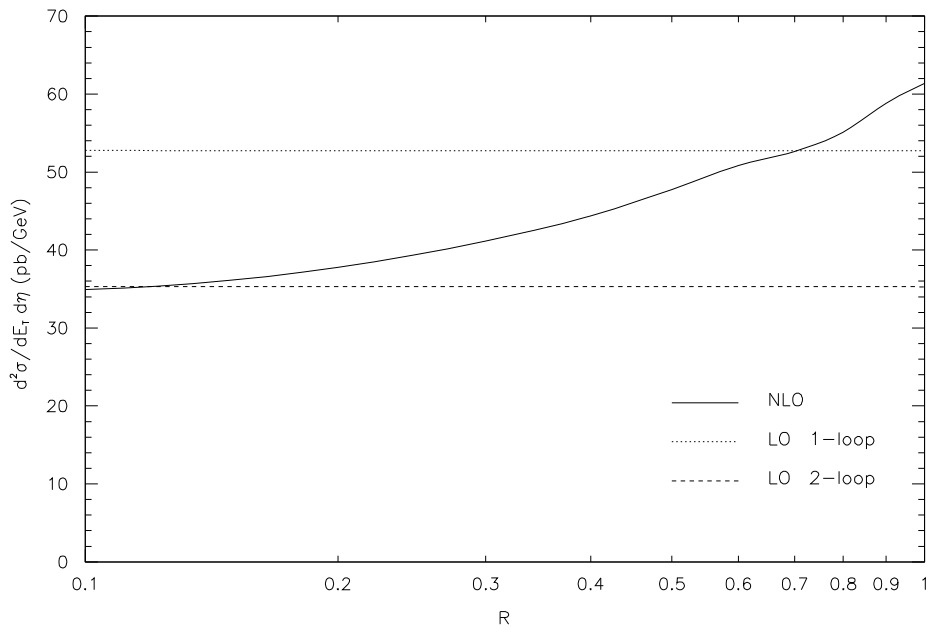

Figure 50: *Inclusive single-jet cross section $d^2\sigma/dE_T d\eta$ for resolved photons at $E_T = 20$ GeV and $\eta = 1$, as a function of the jet cone size R. Only the NLO (full) curve and not the LO curves with one- (dotted) or two-loop (dashed) α_s depends on R.*

5.4 Two-Jet Cross Sections

We now turn to two-jet cross sections, where one does not integrate over the second rapidity η_2 or, alternatively, over the momentum fraction x_a of the parton in the electron. The differential cross section

$$\frac{\mathrm{d}^3\sigma}{\mathrm{d}E_T^2\mathrm{d}\eta_1\mathrm{d}\eta_2} = \sum_b x_a F_{a/e}(x_a, M_a^2) x_b F_{b/p}(x_b, M_b^2) \frac{\mathrm{d}\sigma}{\mathrm{d}t}(ab \to p_1 p_2) \tag{5.18}$$

then yields the maximum of information possible on the parton distributions and is better suited to constrain them than the observation of inclusive single-jets. Since dijet production is a more exclusive process than one-jet production, the cross sections are smaller and require higher luminosity or longer running time in the experiments. This is the reason why H1 and ZEUS have only recently started to analyze dijet data and why we can present here the first theoretical calculation for complete dijet photoproduction.

It is important to note that only in leading order the transverse energies of the two observed jets balance ($E_{T_1} = E_{T_2} = E_T$). In next-to-leading order inclusive cross sections, there may be a third unobserved jet which must have full freedom to become infinitely soft. Therefore, the transverse energies of both jets cannot be observed without spoiling infrared safety. This is an artifact of fixed order perturbation theory and will go away in $\mathcal{O}(\alpha\alpha_s^3)$, where one may as well have a fourth jet. We will calculate similar distributions as in the last section, i.e. in the transverse energy *of the first jet*, E_{T_1}, and in both observable rapidities η_1 and η_2. Yet, the rapidities η_1 and η_2 always belong to the two jets with largest transverse energy in the event. As in the one-jet case, the direct distributions have already been presented in a recent paper [Kla95a], whereas the resolved and complete cross sections are shown here for the first time.

First, we look at the distributions in the transverse energy E_{T_1} in figure 51 for direct photons. We fix η_1 at $\eta_1 = 1$ and η_2 at three different values of $\eta_2 = 0,\ 1,\ 2$. The curves for $\eta_2 = 0$ and $\eta_2 = 2$ are rescaled by factors of 0.1 and 0.5 as before. We expect the dijet cross sections to be smaller than the single-jet cross sections in figure 41. Indeed, for E_T, $E_{T_1} = 5$ GeV and η, η_1, $\eta_2 = 1$, the cross section drops by almost an order of magnitude from 10.6 nb to 1.29 nb. The k-factors in dijet production are basically the same as in single-jet production. There is, however, one novel feature: for $\eta_2 = 0$, the third jet in next-to-leading order opens up some additional phase space, so that E_{T_1} can go up to $E_{T_1} < 55$ GeV instead of only 39 GeV in leading order.

A similar behavior is seen for resolved photoproduction in figure 52. At the lowest value of $E_{T_1} = 5$ GeV and back-to-back jets ($\eta_1 = \eta_2 = 1$), the two-jet cross section (4.91 nb) is even more than one order of magnitude smaller than the one-jet cross section (67.5 nb). The ratio of NLO to LO is 1.7 for resolved photons over the whole E_{T_1}-range. The phase space for $\eta_2 = 0$ increases from $E_{T_1} = 39$ GeV to $E_{T_1} = 50$ GeV. This slightly smaller value is due to the reduced center-of-mass energy in resolved photoproduction, as some of the energy always goes into the photon remnant.

Next, we present the dependence of the cross sections on the two rapidities in form of the three-dimensional lego-plots 53 and 54. The leading order is always shown on the left side and is completely symmetric in η_1 and η_2. For the next-to-leading order cross sections on the right hand sides of figures 53 and 54, this is no longer exactly true due to the presence of a "trigger" jet with transverse energy E_{T_1}, which is fixed at $E_{T_1} = 20$ GeV. The next-to-leading order lego-plots are only approximately symmetric. This can best be seen at the bottom of the contour plots, where at least one of the two observed jets is far off the central region. The NLO predictions are considerably larger than the LO predictions, especially in the resolved case.

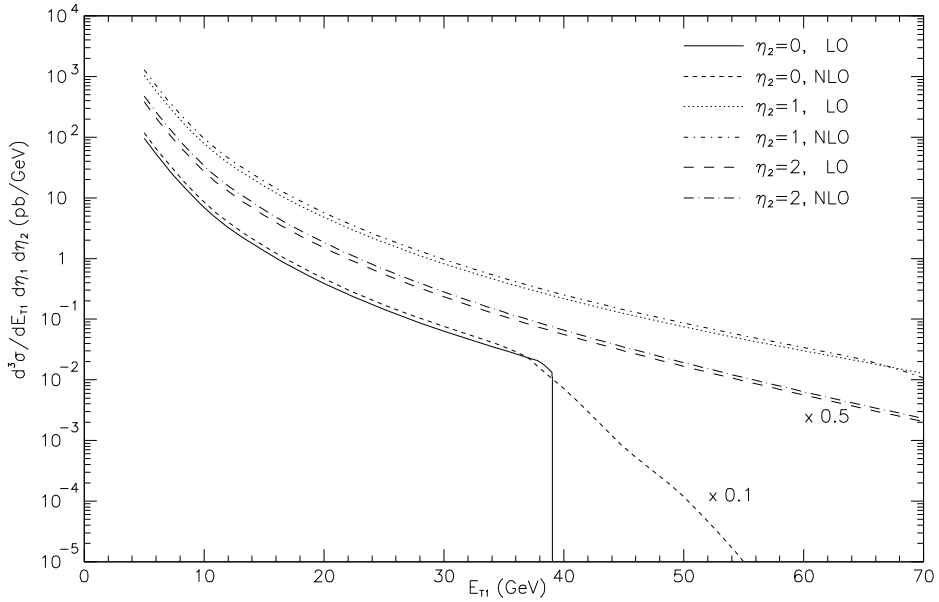

Figure 51: *Inclusive dijet cross section* $d^3\sigma/dE_{T_1}d\eta_1 d\eta_2$ *for direct photons as a function of* E_{T_1} *for* $\eta_1 = 1$ *and three values of* $\eta_2 = 0, 1, 2$. *The cross section for* $\eta_2 = 0$ *(*$\eta_2 = 2$*) is multiplied by 0.1 (0.5).*

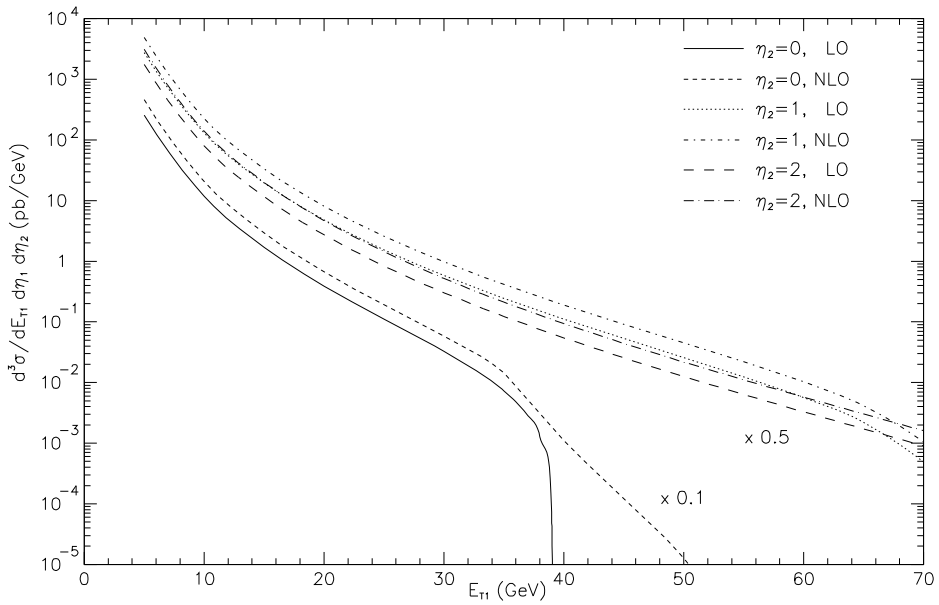

Figure 52: *Inclusive dijet cross section* $d^3\sigma/dE_{T_1}d\eta_1 d\eta_2$ *for resolved photons as a function of* E_{T_1} *for* $\eta_1 = 1$ *and three values of* $\eta_2 = 0, 1, 2$. *The cross section for* $\eta_2 = 0$ *(*$\eta_2 = 2$*) is multiplied by 0.1 (0.5).*

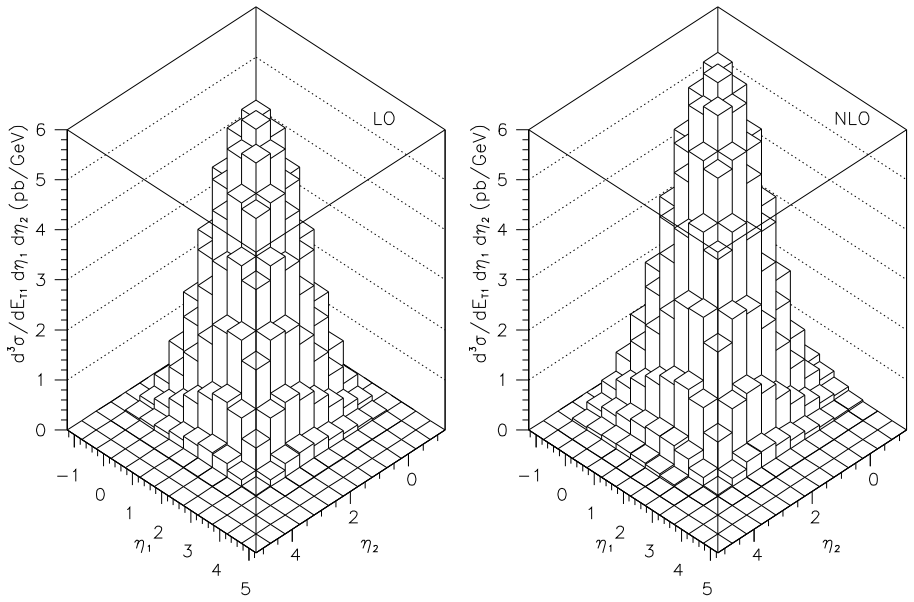

Figure 53: *Inclusive dijet cross section* $d^3\sigma/dE_{T_1}d\eta_1 d\eta_2$ *at* $E_{T_1} = 20$ *GeV for direct photons, as a function of* η_1 *and* η_2*. The LO plot (left) is exactly symmetric, the NLO plot (right) only approximately.*

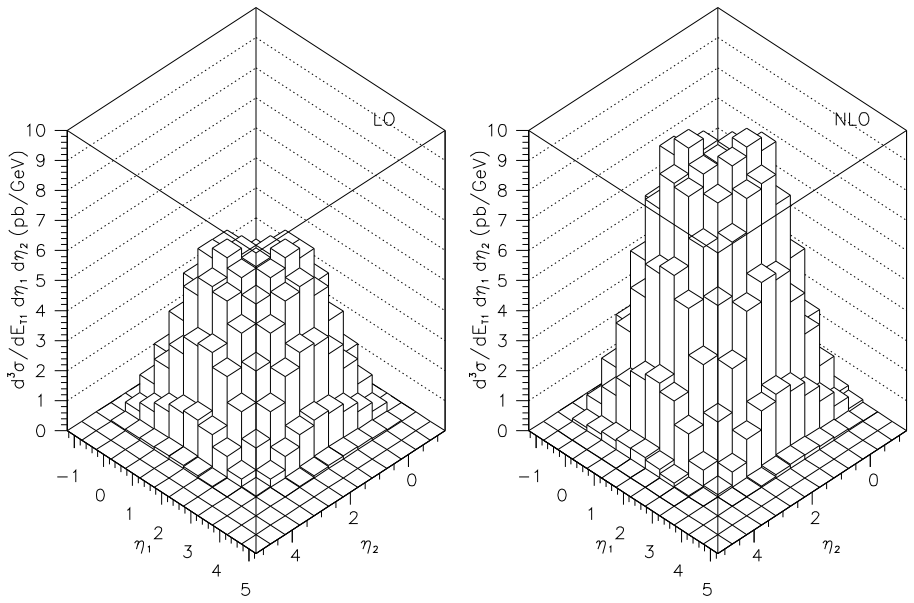

Figure 54: *Inclusive dijet cross section* $d^3\sigma/dE_{T_1}d\eta_1 d\eta_2$ *at* $E_{T_1} = 20$ *GeV for resolved photons, as a function of* η_1 *and* η_2*. The LO plot (left) is exactly symmetric, the NLO plot (right) only approximately.*

This becomes even clearer when we plot the projections of the lego-plots for fixed $\eta_1 = 0,\ 1,\ 2$ and 3. In figure 55, we plot the leading and next-to-leading order distributions in η_2 for direct photoproduction. It is clearly seen that the second jet tends to be back-to-back with the first jet, since the maximum always occurs at $\eta_2 \simeq \eta_1$. However, at $\eta_1 = 3$ this is no more permitted by phase space. We obtain the same k-factor of 1.25 in the central regions as in single-jet production.

The η_2-distributions for resolved photons in figure 56 are considerably broader than those in figure 55 due to the smearing of the hard cross sections with the distribution function of partons in the photon. The maxima of the plots are also not so much dominated by kinematics but more by the quark and gluon structure of the photon in different x regimes. They do not lie at $\eta_2 = \eta_1$ any more. Therefore, dijet rapidity distributions are best suited to constrain the photon structure. We will come back to this point in the next section 5.5, when we compare similar plots to data from ZEUS. The k-factors range from 1.65 in the central regions to more than 3 in the proton forward direction. The shapes of the distributions are very similar in LO and in NLO. The absolute values make, however, an important difference.

Direct and resolved contributions are now added to give physical, complete photoproduction results. The dijet cross section is first plotted as a function of the transverse energy E_{T_1}. Figure 57 gives the LO result, figure 58 the NLO result. Like the direct and resolved cross sections alone, the full two-jet cross sections are about an order of magnitude smaller than the one-jet cross sections (see figures 45 and 46). The point where direct and resolved contributions are equally important is lowered towards $E_{T_1} = 20$ GeV in leading order and $E_{T_1} = 30$ GeV in next-to-leading order, so that direct photons are better observed in dijet production.

If one plots the complete two-jet cross sections as a function of η_2, the different behaviors of direct and resolved photons add up to the full curves in figures 59 and 60. These plots are best suited to decide in which rapidity regions one can look best for the resolved photon structure. We have already seen that this will be in situations where the two jets are not back-to-back, e.g. for $\eta_1 = 0$ and positive η_2 in the upper left plots of figures 59 and 60. On the other hand, the proton structure can best be studied with direct photons, when the cross section is not folded with another distribution. A possible scenario is $\eta_1 = 0$ and negative values of η_2. This is especially interesting for the small-x components of the proton like the gluons and the quark sea. Another interesting observation is that the relative importance of direct and resolved processes changes dramatically when calculating dijet photoproduction in next-to-leading order $\mathcal{O}(\alpha\alpha_s^2)$: resolved processes are much more important at $E_{T_1} = 20$ GeV than one would have guessed from a leading order estimate.

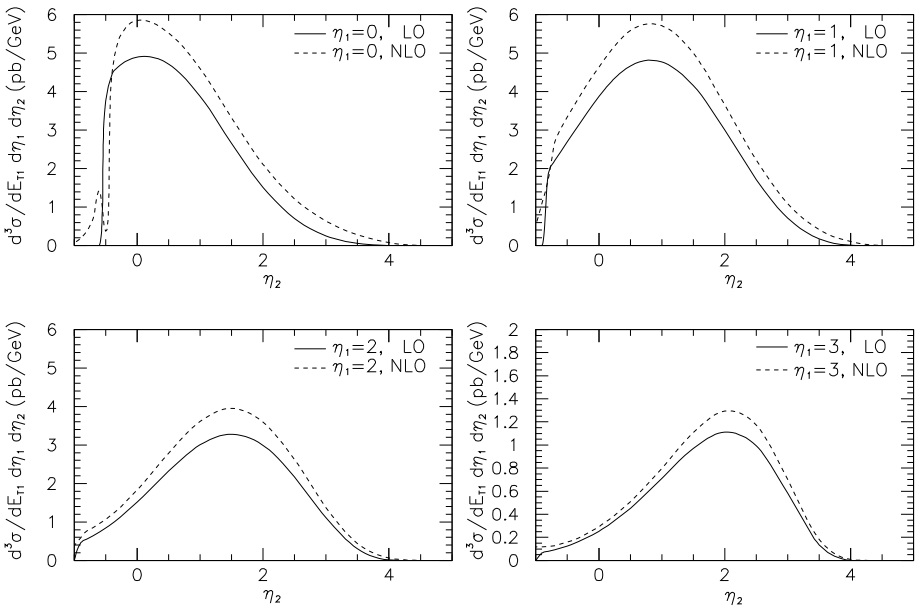

Figure 55: *Projections of the LO (full curves) and NLO (dashed curves) triple differential dijet cross section for direct photons at $E_{T_1} = 20$ GeV and fixed values of $\eta_1 = 0,\ 1,\ 2,$ and 3, as a function of η_2.*

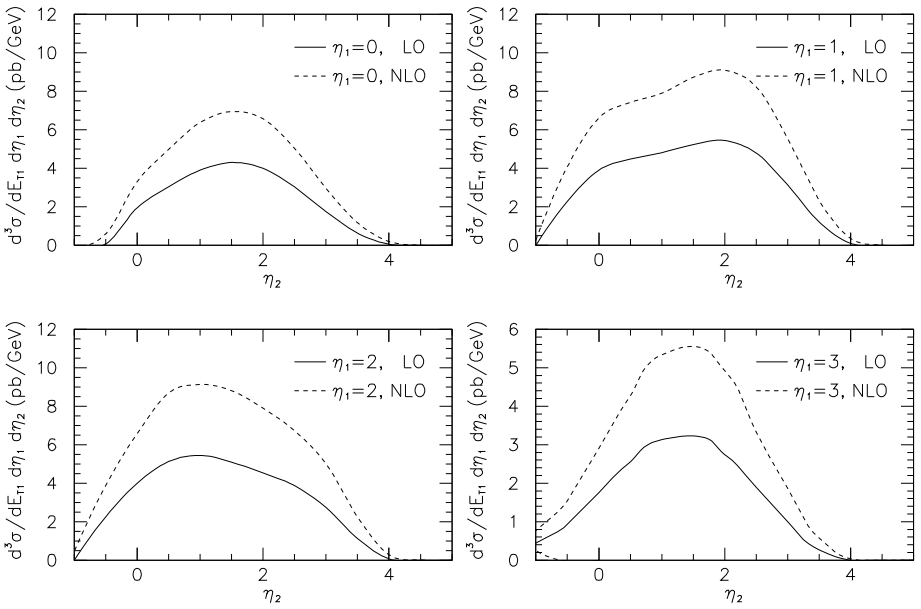

Figure 56: *Projections of the LO (full curves) and NLO (dashed curves) triple differential dijet cross section for resolved photons at $E_{T_1} = 20$ GeV and fixed values of $\eta_1 = 0,\ 1,\ 2,$ and 3, as a function of η_2.*

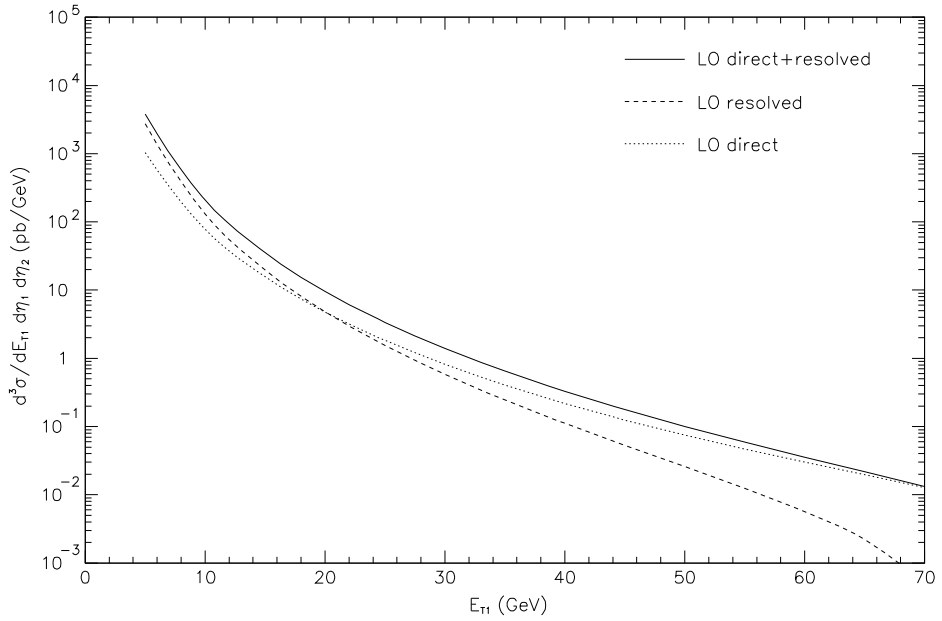

Figure 57: *Inclusive dijet cross section $d^3\sigma/dE_{T_1}d\eta_1 d\eta_2$ for full photoproduction at $\eta_1 = \eta_2 = 1$ as a function of E_{T_1}. The full curve is the sum of the LO direct (dotted) and LO resolved (dashed) contributions.*

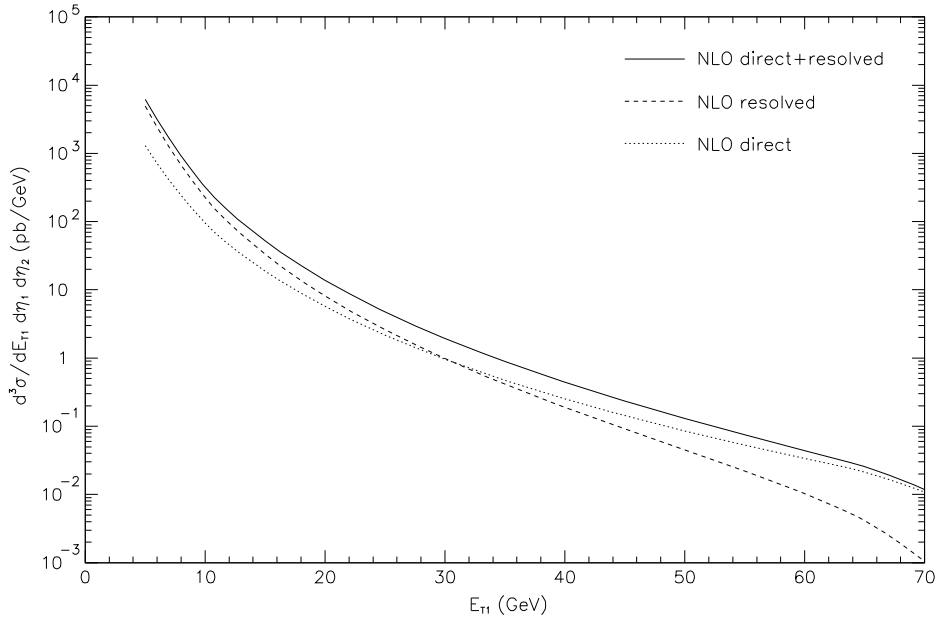

Figure 58: *Inclusive dijet cross section $d^3\sigma/dE_{T_1}d\eta_1 d\eta_2$ for full photoproduction at $\eta_1 = \eta_2 = 1$ as a function of E_{T_1}. The full curve is the sum of the NLO direct (dotted) and NLO resolved (dashed) contributions.*

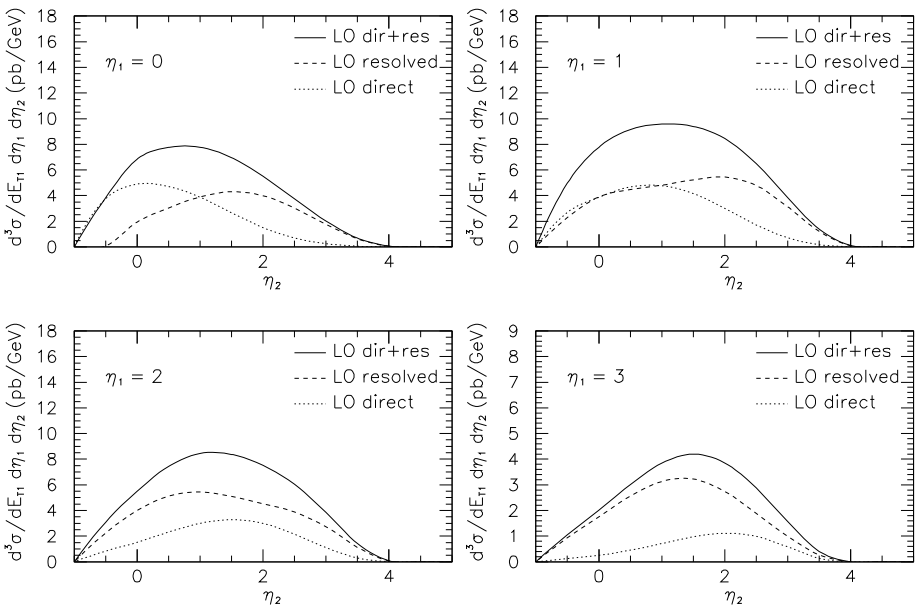

Figure 59: *Projections of the complete triple differential dijet cross section at $E_{T_1} = 20$ GeV and fixed values of $\eta_1 = 0,\ 1,\ 2,$ and 3, as a function of η_2. The full curve is the sum of the LO direct (dotted) and LO resolved (dashed) contributions.*

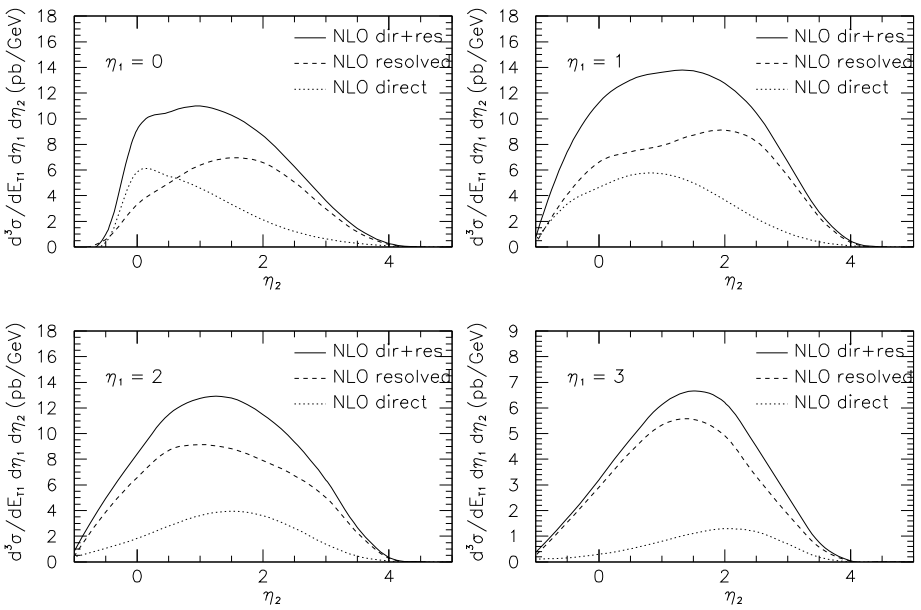

Figure 60: *Projections of the complete triple differential dijet cross section at $E_{T_1} = 20$ GeV and fixed values of $\eta_1 = 0,\ 1,\ 2,$ and 3, as a function of η_2. The full curve is the sum of the NLO direct (dotted) and NLO resolved (dashed) contributions.*

5.5 Comparison to H1 and ZEUS Data

Finally, we compare our next-to-leading order calculation to one- and two-jet data from the H1 and ZEUS collaborations at HERA. Both collaborations have continuously studied the photoproduction of jets since HERA started running in 1992 and published interesting papers on many aspects of this subject. In this section, we will restrict the maximum virtuality and the energy of the photon radiated by the electron to $Q^2_{\max} = 0.01\ (4)\ \mathrm{GeV}^2$ and $x_a \in [0.25, 0.7]$ ($[0.2, 0.85]$) as in the H1 (ZEUS) experiment.

The inclusive single-jet cross section is shown in figure 61 as a function of the transverse energy of the jet E_T and integrated over $\eta \in [-1, 2]$ and $\eta \in [-1, 1]$, respectively. The two curves are separated from each other by rescaling the latter with a factor of 0.1. The agreement with the 1993 data from H1 [Bou95] is good, especially at larger E_T. One also has to keep in mind that the systematic errors and energy scale uncertainty are not included in the experimental error bars throughout this section.

Next, we consider the rapidity distributions of the one-jet cross section $\mathrm{d}\sigma/\mathrm{d}\eta$ in figure 62, where we integrate over three different regions in E_T: $E_T > 7$ GeV, $E_T > 11$ GeV, and $E_T > 15$ GeV. The predictions agree with the H1 data except in the forward region at low E_T. It was shown by A. Bouniatian that hadronization corrections are large in this region [Bou95]. Accounting in addition for multiple interactions or the underlying event also changes the jet shapes and the determination of the transverse jet energy [Oh96, Ste96]. After these corrections, the data points lie on top of the theoretical curves [Bou95].

Figure 63 shows the single-jet cross section as a function of E_T compared to data from the ZEUS detector at HERA [Der95]. We integrate over the same rapidity ranges as in the case of H1 and divide the curves for $\eta \in [-1, 1]$ by a factor of 10 to separate the two results. We observe even better agreement in the ZEUS case than in the H1 case. For the range of $\eta \in [-1, 1]$, the data are slightly better described with the GS photon structure functions.

In the ZEUS rapidity distributions in figure 64, we observe again an enhancement of data over the prediction in the forward region at low E_T. Otherwise, the curves lie within the experimental error bars. As in the last plot, the GS parton distributions seem to be slightly favored by the data compared to the GRV parton distributions.

The last two plots contain preliminary dijet data from the ZEUS collaboration [Der96a]. The cross sections $\mathrm{d}\sigma/\mathrm{d}\overline{\eta}$ are plotted as a function of the average rapidity $\overline{\eta} = 1/2(\eta_1 + \eta_2)$ of the two observed jets and integrated over the difference in rapidity $\Delta\eta \in [-0.5, 0.5]$ and over $E_{T_{1,2}} > 6$ GeV. As the experimental constraint on the transverse energies of both jets is not infrared safe in next-to-leading order of perturbative QCD, we allow the second jet to have less than 6 GeV if the third unobserved particle is soft (i.e. has a transverse energy of less than 1 GeV). Through this procedure we avoid a dependence of the theoretical prediction on the y-cut. We separate "direct" and "resolved" photoproduction with the new variable

$$x_\gamma^{\mathrm{OBS}} = \frac{\sum_i E_{T_i} e^{-\eta_i}}{2 x_a E_e}, \tag{5.19}$$

which measures the fraction of the photon energy that goes into the production of the two hard jets.

Figure 65 shows the "direct" cross section for $x_\gamma^{\mathrm{OBS}} > 0.75$. In a previous publication, we compared the corresponding ZEUS 1993 data to our predictions, which then only included the LO resolved contributions for the GRV and GS photon parton densities [Kla96]. The 1994 ZEUS data are analyzed with three different jet algorithms, EUCELL, PUCELL, KTCLUS (see section 2.4). The latter two algorithms are expected to give very similar results. The theoretical predictions are given for two

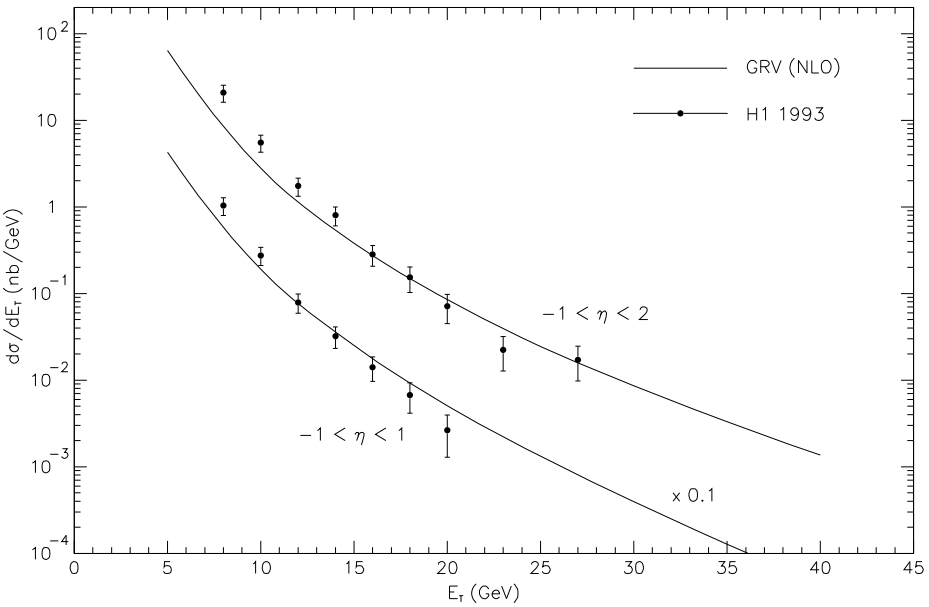

Figure 61: *Inclusive single-jet cross section $d\sigma/dE_T$ as a function of E_T integrated over two different rapidity ranges. Our next-to-leading order predictions are compared to 1993 data from H1.*

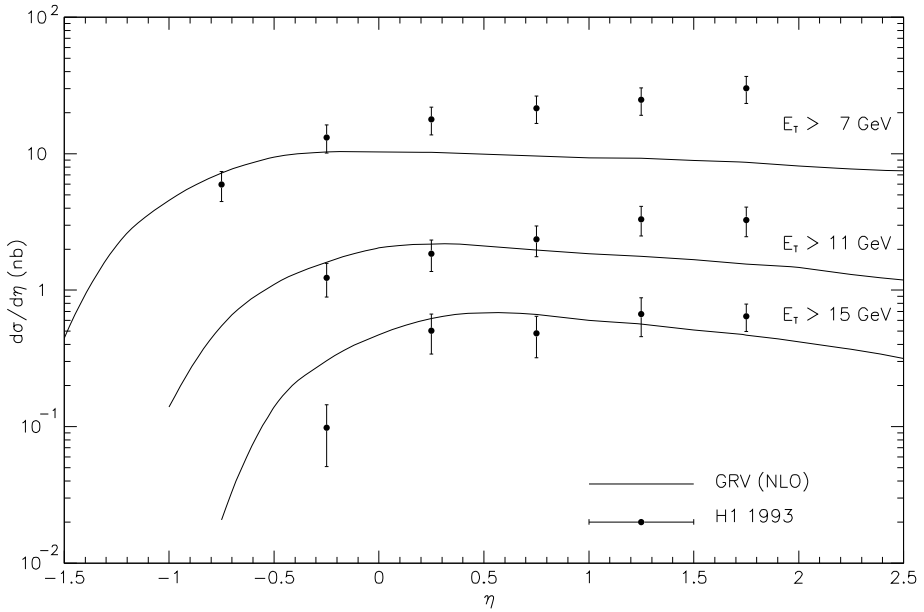

Figure 62: *Inclusive single-jet cross section $d\sigma/d\eta$ as a function of η integrated over three different ranges in E_T. Our next-to-leading order predictions are compared to 1993 data from H1.*

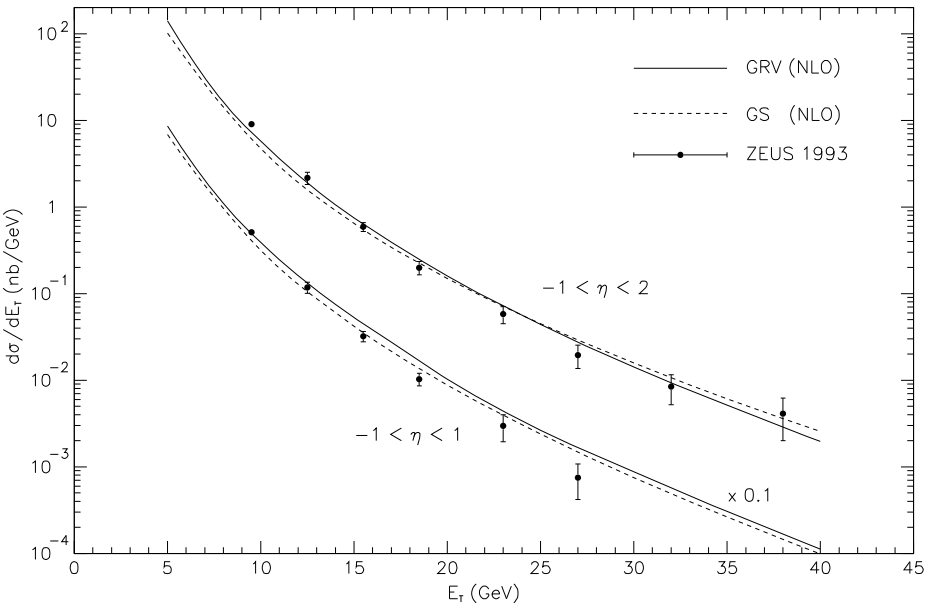

Figure 63: *Inclusive single-jet cross section $d\sigma/dE_T$ as a function of E_T integrated over two different rapidity ranges. Our next-to-leading order predictions with GRV and GS photon structure functions are compared to 1993 data from ZEUS.*

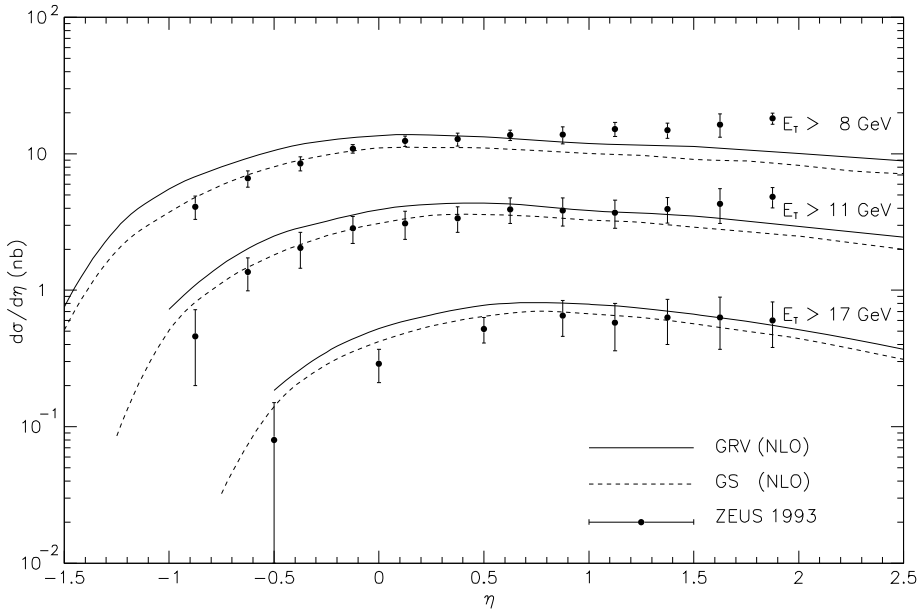

Figure 64: *Inclusive single-jet cross section $d\sigma/d\eta$ as a function of η integrated over three different ranges in E_T. Our next-to-leading order predictions with GRV and GS photon structure functions are compared to 1993 data from ZEUS.*

different R_{sep} parameters in order to match the theoretical and experimental jet definitions. The EUCELL results correspond to a value of $R_{\mathrm{sep}} = 2.0$, whereas the PUCELL and KTCLUS results correspond to $R_{\mathrm{sep}} = 1.0$. The absolute normalization, the shape, and the variation with respect to the different jet algorithms agree well between theory and data.

The "resolved" photon dijet cross section is given in figure 66 for $x_\gamma^{\mathrm{OBS}} \in [0.3, 0.75]$. Here, only the shapes and the jet definition variation behave in the same way in our calculation and in the data. The overall normalization is not well determined. This may be due to the large uncertainty of ± 0.5 nb of the preliminary data in the calorimeter energy scale, the influence of the underlying event, or multiple interactions.

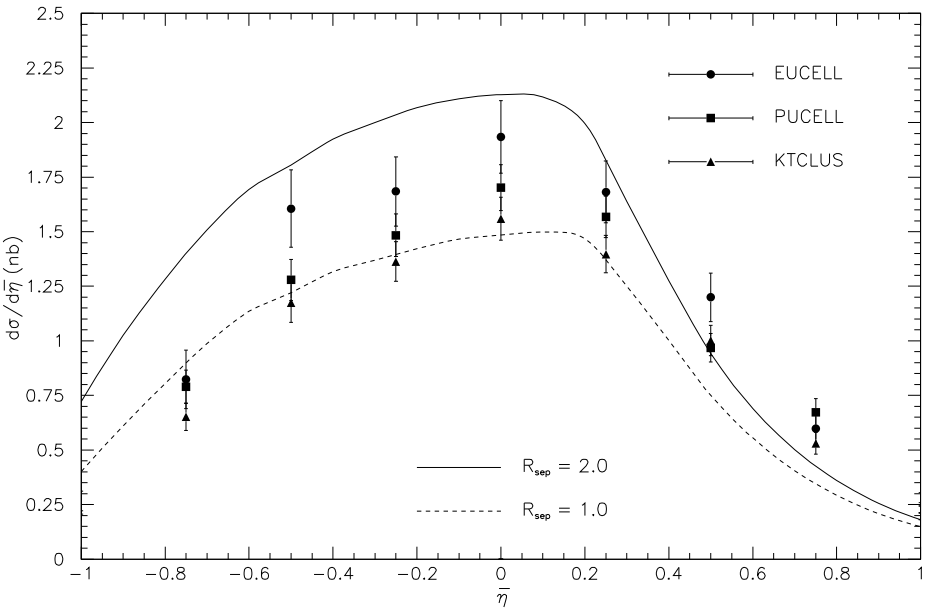

Figure 65: *Inclusive dijet cross section* $d\sigma/d\overline{\eta}$ *at* $x_\gamma^{\rm OBS} > 0.75$ *as a function of* $\overline{\eta}$ *and integrated over* $\Delta\eta \in [-0.5, 0.5]$ *and* $E_T > 6$ *GeV. Our next-to-leading order predictions with* $R_{\rm sep} = 2.0$ *and* $R_{\rm sep} = 1.0$ *are compared to preliminary 1994 data from ZEUS with three different jet algorithms.*

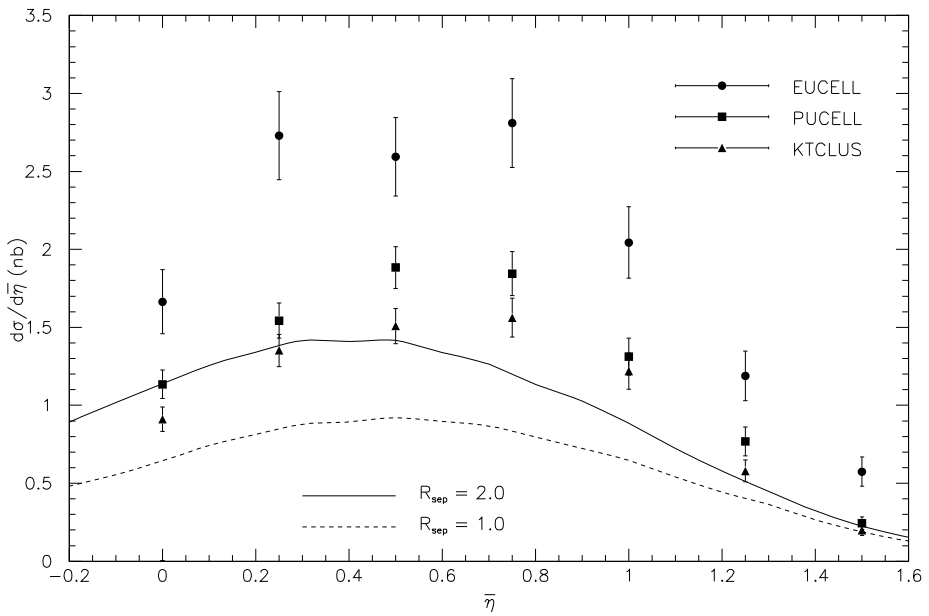

Figure 66: *Inclusive dijet cross section* $d\sigma/d\overline{\eta}$ *at* $x_\gamma^{\rm OBS} \in [0.3, 0.75]$ *as a function of* $\overline{\eta}$ *and integrated over* $\Delta\eta \in [-0.5, 0.5]$ *and* $E_T > 6$ *GeV. Our next-to-leading order predictions with* $R_{\rm sep} = 2.0$ *and* $R_{\rm sep} = 1.0$ *are compared to preliminary 1994 data from ZEUS with three different jet algorithms.*

6 Summary and Outlook

In this thesis we have presented for the first time the next-to-leading order resolved photon contribution to dijet production at HERA and a complete next-to-leading order calculation of direct and resolved photoproduction of one and two jets. The results are of great importance not only as a test of quantum chromodynamics (QCD), but also for the measurement of the proton and photon parton densities currently performed at DESY in Hamburg.

First, we embedded the perturbatively calculable photon-parton scattering in the experimentally observable electron-proton scattering process, using the Weizsäcker-Williams approximation and universal structure functions for the proton and the photon. For these structure functions, we chose recent next-to-leading order parametrizations from the CTEQ and GRV collaborations. Special emphasis was given to experimental and theoretical ambiguities in the Snowmass jet definition.

The hard photon-parton scattering cross section was calculated in leading and in next-to-leading order. The analytical calculation included the tree-level Born matrix elements, the virtual corrections with one internal loop, and the real corrections with the radiation of a third particle in the initial or final states. We integrated the latter over singular regions of phase space up to an invariant mass cut y. This was done in d dimensions in order to regularize the soft and collinear divergencies. All infrared singularities cancelled, as they must according to the Kinoshita-Lee-Nauenberg theorem. The ultraviolet poles in the virtual corrections and the collinear poles in the initial state corrections were absorbed into the Lagrangian and the structure functions, respectively.

The cross sections proved to be independent of the technical y-cut and less dependent on the renormalization and factorization scales, when added to the regular three-body contributions and integrated numerically. Excellent agreement was found in inclusive single-jet predictions with the existing programs of Bödeker and Salesch. We extensively studied the direct, resolved, and complete one- and two-jet distributions in the transverse energies and rapidities of the observed jets as well as the dependence on the jet cone size R. Finally, we compared similar distributions to inclusive and dijet data from H1 and ZEUS and found good agreement.

It is possible to extend the work presented here in a number of different ways. First, the comparison with dijet data from ZEUS has just started. One should also look at average rapidity distributions at larger transverse energies as well as at distributions in the relative angle between the two jets, in the transverse energy, and in the dijet mass. The same is desirable for H1 dijet data, which is not yet available. Second, this calculation can also easily be applied to photon-photon cross sections in e^+e^- scattering, which opens a wide field of jet production studies at TRISTAN, LEP, LEPII, and the planned Next Linear Collider (NLC). Whereas our calculation is restricted to the single-resolved and double-resolved processes, a complete calculation is already available [Kle96b]. Third, our program can be used to predict single and dijet cross sections in proton-proton and proton-antiproton scattering at the TEVATRON at Fermilab in Chicago or at the designated LHC at CERN in Geneva. An interesting topic here is the enhancement of inclusive jet data over next-to-leading order theory predictions at very large transverse energies, which might signal the existence of subquarks.

Acknowledgements

It is a pleasure to thank

— Prof. Dr. G. Kramer for the idea to this very interesting study as well as his constant advice and support during the preparation of this dissertation. His expertise in elementary particle phenomenology and insight into mathematical and technical problems of higher order QCD calculations have always been of great help to me.

— T. Kleinwort and S.G. Salesch for their fruitful collaboration,

— J. Binnewies and T. Kleinwort for a careful reading of the manuscript,

— J. Binnewies, P. Büttner, B. Pötter, and T. Kleinwort for a very pleasant working atmosphere at the II. Institut für Theoretische Physik der Universität Hamburg,

— A. Bouniatian for providing me with the 1993 H1 single-jet data and with information on the hadronization corrections in the forward direction at low E_T,

— M. Erdmann, F. Ferrarrotto, H. Rick, and B. Stella for comments on the H1 dijet analysis,

— C. Glasman and J. Terron for providing me with the 1993 and preliminary 1994 ZEUS single-jet data and interesting discussions on inclusive jet production,

— J. Butterworth and L. Feld for providing me with the 1993 and preliminary 1994 ZEUS dijet data and a fruitful collaboration on the matching of jet definitions within the "Workshop on Future Physics at HERA" during 1995 and 1996,

— B. Oh for comments on the ZEUS dijet analysis,

— E.-L. Bohnen and the DESY User Consulting Group for providing a working UNIX computing environment on the HP 9000/735 workstations,

— D. Michelsen for his valuable hardware and software support,

— the Bundesministerium für Bildung und Wissenschaft, Forschung und Technologie (BMBF), Bonn, Germany, for financial support under contract 05 7HH92P(0), and

— the European Union for financial support within the program "Human Capital and Mobility" through the network "Physics at High Energy Colliders" under contract CHRX-CT93-0357 (DG12 COMA).

Last, but not least, I wish to thank my wife Elke for her great support and encouragement during the last years.

A Phase Space Integrals for Final State Singularities

This appendix contains the formulæ needed to integrate the real $2 \to 3$ matrix elements in sections 4.2.2 and 4.2.3 over phase space regions with final state singularities. To this aim, we have defined in section 4.2.1 a measure

$$\int \mathrm{d}\mu_F = \int_0^{y_F} \mathrm{d}z' z'^{-\varepsilon} \left(1 + \frac{z's}{t}\right)^{-\varepsilon} \int_0^1 \frac{\mathrm{d}b}{N_b} b^{-\varepsilon} (1-b)^{-\varepsilon} \int_0^\pi \frac{\mathrm{d}\phi}{N_\phi} \sin^{-2\varepsilon}\phi, \tag{A.1}$$

which contains all variables associated with the phase space of the unobserved subsystem $\overline{p}_1 = p_1 + p_3$. The integral over the azimuthal angle ϕ is trivial, as the matrix elements are independent of ϕ.

We give the results for the four generic types of integrals in the following:

$$\begin{aligned} f_1(a) &= \int \mathrm{d}\mu_F \frac{1}{z'} \frac{a}{z'+ab} = \int \mathrm{d}\mu_F \frac{1}{z'} \frac{a}{z'+a(1-b)} \\ &= \frac{1}{2\varepsilon^2} + \frac{1}{\varepsilon}\left(-1 - \frac{1}{2}\ln a\right) + \ln a - \frac{1}{2}\ln^2 \frac{y_F}{a} + \frac{1}{4}\ln^2 a - \mathrm{Li}_2\left(-\frac{y_F}{a}\right) - \frac{\pi^2}{6} + \mathcal{O}(\varepsilon), \end{aligned} \tag{A.2}$$

$$\begin{aligned} f_2(a) &= \int \mathrm{d}\mu_F \frac{1}{z'}(1-b)(1-\varepsilon) \\ &= -\frac{1}{2\varepsilon} + \frac{1}{2} + \frac{1}{2}\ln y_F + \mathcal{O}(\varepsilon), \end{aligned} \tag{A.3}$$

$$\begin{aligned} f_3(a) &= \int \mathrm{d}\mu_F \frac{1}{z'} \\ &= -\frac{1}{\varepsilon} + \ln y_F + \mathcal{O}(\varepsilon), \end{aligned} \tag{A.4}$$

$$\begin{aligned} f_4(a) &= \int \mathrm{d}\mu_F \frac{1}{z'}(1-b+b^2) \\ &= -\frac{5}{6\varepsilon} + \frac{5}{6}\ln y_F - \frac{1}{18} + \mathcal{O}(\varepsilon). \end{aligned} \tag{A.5}$$

Terms of order ε have been omitted since they vanish in the limit $d \to 4$.

B Phase Space Integrals for Initial State Singularities

In this appendix, we calulate the formulæ needed to integrate the real $2 \to 3$ matrix elements in sections 4.2.5 through 4.2.8 over phase space regions with initial state singularities. The integration measure was defined in section 4.2.4 and is given by

$$\int \mathrm{d}\mu_I = \int_0^{y_I} \mathrm{d}z'' z''^{-\varepsilon} \int_{X_a}^1 \frac{\mathrm{d}z_a}{z_a} \left(\frac{z_a}{1-z_a}\right)^{\varepsilon} \int_0^{\pi} \frac{\mathrm{d}\phi}{N_\phi} \sin^{-2\varepsilon}\phi \frac{\Gamma(1-2\varepsilon)}{\Gamma^2(1-\varepsilon)}. \tag{B.1}$$

The integration variables are associated with the phase space of the unobserved particle p_3. The integral over the azimuthal angle ϕ is again trivial, as the matrix elements do not depend on ϕ. The longitudinal momentum fraction z_a is integrated over numerically, since the cross sections still have to be folded with the parton densities. These are contained in the functions $g(z_a)$ below.

We give the results for the four generic types of integrals in the following:

$$\begin{aligned}
i_1(a) &= \int \mathrm{d}\mu_I g(z_a) \frac{1}{z''} \frac{a}{z'' + a(1-z_a)} \\
&= \int_{X_a}^1 \frac{\mathrm{d}z_a}{z_a} g(z_a) \left[-\frac{1}{\varepsilon} - \frac{1}{\varepsilon} \frac{z_a}{(1-z_a)_+} + \left(\frac{\ln\left(a\left(\frac{1-z_a}{z_a}\right)^2\right)}{1-z_a} \right)_+ - \ln\left(a\left(\frac{1-z_a}{z_a}\right)^2\right) \right. \\
&\qquad \left. - \frac{z_a}{1-z_a} \ln\left(1 + \frac{a(1-z_a)}{y_I z_a}\right) + \ln\left(y_I\left(\frac{1-z_a}{z_a}\right)\right) \right] \\
&\quad + \qquad g(1) \left[\frac{1}{2\varepsilon^2} - \frac{1}{2\varepsilon} \ln a + \frac{1}{4} \ln^2 a + \frac{\pi^2}{2} \right] + \mathcal{O}(\varepsilon),
\end{aligned} \tag{B.2}$$

$$\begin{aligned}
i_2(a) &= \int \mathrm{d}\mu_I g(z_a) \frac{1}{z''} \\
&= \int_{X_a}^1 \frac{\mathrm{d}z_a}{z_a} g(z_a) \left[-\frac{1}{\varepsilon} + \ln\left(y_I \frac{1-z_a}{z_a}\right) \right] + \mathcal{O}(\varepsilon),
\end{aligned} \tag{B.3}$$

$$\begin{aligned}
i_3(a) &= \int \mathrm{d}\mu_I g(z_a) \frac{1}{z''} (1-z_a)(1-\varepsilon) \\
&= \int_{X_a}^1 \frac{\mathrm{d}z_a}{z_a} g(z_a) \left[-\frac{1}{\varepsilon}(1-z_a) + (1-z_a) + (1-z_a) \ln\left(y_I \frac{1-z_a}{z_a}\right) \right] + \mathcal{O}(\varepsilon),
\end{aligned} \tag{B.4}$$

$$\begin{aligned}
i_4(a) &= \int \mathrm{d}\mu_I g(z_a) \frac{1}{z''} \left(\frac{z_a^2 - 2z_a + 2 - \varepsilon z_a^2}{z_a} \right) \frac{1}{1-\varepsilon} \\
&= \int_{X_a}^1 \frac{\mathrm{d}z_a}{z_a} g(z_a) \left[-\frac{1}{\varepsilon} \frac{z_a^2 - 2z_a + 2}{z_a} + \frac{z_a^2 - 2z_a + 2}{z_a} \ln\left(y_I \frac{1-z_a}{z_a}\right) - 2\frac{1-z_a}{z_a} \right] + \mathcal{O}(\varepsilon).
\end{aligned} \tag{B.5}$$

Terms of order ε have again been omitted.

References

[Abr91] H. Abramowicz, K. Charchula, A. Levy
Parametrization of Parton Distributions in the Photon
Phys. Lett. **B269** (1991) 458

[Abr92] H. Abramowicz et al.
Parton Distributions in the Photon
J. Mod. Phys. **A8** (1992) 1005

[Abt93] I. Abt et al., H1 Collaboration
Measurement of Inclusive Jet Cross-Sections in Photoproduction at HERA
Phys. Lett. **B314** (1993) 436

[Ada94] D. Adams et al., E683 Collaboration
Observation of Jet Production by Real Photons
Phys. Rev. Lett. **72** (1994) 2337

[Ahm92] T. Ahmed et al., H1 Collaboration
Hard Scattering in γp Interactions
Phys. Lett. **B297** (1992) 205

[Ahm93] T. Ahmed et al., H1 Collaboration
Total Photoproduction Cross-Section Measurement at HERA Energies
Phys. Lett. **B299** (1993) 374

[Aid96] S. Aid et al., H1 Collaboration
Jets and Energy Flow in Photon-Proton Collisions at HERA
Z. Phys. **C70** (1996) 17

[Ali80] A. Ali, E. Pietarinen, G. Kramer, J. Willrodt
A QCD Analysis of the High Energy e^+e^- Data from PETRA
Phys. Lett. **B93** (1980) 155

[Alt77] G. Altarelli, G. Parisi
Asymptotic Freedom in Parton Language
Nucl. Phys. **B126** (1977) 298

[Alt78] G. Altarelli, R.K. Ellis, G. Martinelli
Leptoproduction and Drell-Yan Processes beyond the Leading Approximation in Chromodynamics
Nucl. Phys. **B143** (1978) 521

[Alt82] G. Altarelli
Partons in Quantum Chromodynamics
Phys. Rep. **81** (1982) 1

[Ama78] D. Amati, R. Petronzio, G. Veneziano
Relating Hard QCD Processes through Universality of Mass Singularities
Nucl. Phys. **B140** (1978) 54

[Ama78a] D. Amati, R. Petronzio, G. Veneziano
Relating Hard QCD Processes through Universality of Mass Singularities (II)
Nucl. Phys. **B146** (1978) 29

[And80] B. Andersson, G. Gustafson, T. Sjöstrand
A Three-Dimensional Model for Quark and Gluon Jets
Z. Phys. **C6** (1980) 235

[Arn89] P.B. Arnold, M. Hall Reno
The Complete Computation of High-p_T W and Z Production in Second Order QCD
Nucl. Phys. **B319** (1989) 37

[Ash72] J.F. Ashmore
A Method of Gauge-Invariant Regularization
Lett. Nuov. Cim. **4** (1972) 289

[Aug86] E. Auge et al., NA14 Collaboration
High-energy Photoproduction of Large Transverse Momentum π^0 Mesons: a Quantitative Test of QCD
Phys. Lett **168B** (1986) 163

[Aur87] P. Aurenche, R. Baier, A. Douiri, M. Fontannaz, D. Schiff
Scheme Invariant Higher Order QCD Predictions for Large p_T Photoproduction Reactions
Nucl. Phys. **B286** (1987) 553

[Aur92] P. Aurenche, P. Chiapetta, M. Fontannaz, J.P. Guillet, E. Pilon
Higher Order QCD Corrections to the Photoproduction of a Direct Photon at HERA
Z. Phys. **C56** (1992) 589

[Aur94] P. Aurenche, M. Fontannaz, J.P. Guillet
Parton Distributions in the Photon
Z. Phys. **C64** (1994) 621

[Aur94a] P. Aurenche, M. Fontannaz, J.P. Guillet
On the Photoproduction of Jets at HERA
Phys. Lett. **B338** (1994) 98

[Aur95] P. Aurenche, A. Finch, M. Greco, D.J. Miller (eds.)
$\gamma\gamma$ Physics at Linear Colliders
Talks given at 2nd general meeting LEP2 physics workshop, Geneva (1995)

[Ave88] F. Aversa, P. Chiappetta, M. Greco, J.P. Guillet
Higher Order Corrections to QCD Jets
Phys. Lett. **B210** (1988) 225

[Bae89] H. Baer, J. Ohnemus, J.F. Owens
Expectations for Two- and Three-Jet Events at HERA
Z. Phys. **C42** (1989) 657

[Bae89a] H. Baer, J. Ohnemus, J.F. Owens
Next-to-Leading-Logarithm Calculation of Jet Photoproduction
Phys. Rev. **D40** (1989) 2844

[Bar78] W.A. Bardeen, A.J. Buras, D.W. Duke, T. Muta
Deep-Inelastic Scattering Beyond the Leading Order in Asymptotically Free Gauge Theories
Phys. Rev. **D18** (1978) 3998

[Bar79] W.A. Bardeen, A.J. Buras
Higher Order Asymptotic Freedom Corrections to Photon-Photon Scattering
Phys. Rev. **D20** (1979) 166, **D21** (1980) 2041(E)

[Bar86] W. Bartel et al.
Experimental Studies on Multijet Production in e^+e^- Annihilation at PETRA Energies
Z. Phys. **C33** (1986) 23

[Ben87] H.-U. Bengtsson, T. Sjöstrand
The Lund Monte Carlo for Hadronic Processes: PYTHIA Version 4.8
Comp. Phys. Comm. **46** (1987) 43

[Ber81] F.A. Berends, R. Kleiss, P. De Causmaecker, R. Gastmans, T.T. Wu
Single Bremsstrahlung Processes in Gauge Theories
Phys. Lett. **103B** (1981) 124

[Bin95] J. Binnewies, B.A. Kniehl, G. Kramer
Pion and Kaon Production in e^+e^- and ep Collisions at Next-To-Leading Order
Phys. Rev. **D52** (1995) 4947

[Bin96] J. Binnewies, B.A. Kniehl, G. Kramer
Neutral Kaon Production in e^+e^-, ep and $p\bar{p}$ Collisions at Next-To-Leading Order
Phys. Rev. **D53** (1996) 3573

[Bjo69] J.D. Bjorken, E.A. Paschos
Inelastic Electron-Proton and γ-Proton Scattering and the Structure of the Nucleon
Phys. Rev. **185** (1969) 1975

[Blo37] F. Bloch, A. Nordsieck
Note on the Radiation Field of the Electron
Phys. Rev. **52** (1937) 54

[Böd92] D. Bödeker
Der Beitrag des direkten Photons zur Photoproduktion von Jets in Elektron-Proton-Kollisionen zur Ordnung $\alpha\alpha_s^2$
Ph.D. Thesis, University of Hamburg, Hamburg (1992)

[Böd92a] D. Bödeker
Jet Photoproduction at HERA in Next-To-Leading Order QCD
Phys. Lett. **B292** (1992) 164

[Böd93] D. Bödeker
QCD Corrections to Inclusive Jet Photoproduction via Direct Photons
Z. Phys. **C59** (1993) 501

[Böd94] D. Bödeker, G. Kramer, S.G. Salesch
Inclusive Jet Production at HERA: Next-To-Leading Order QCD Corrections to the Resolved and Direct Photon Contribution
Z. Phys. **C63** (1994) 471

[Bol72] C.G. Bollini, J.J. Giambiagi
Lowest Order "Divergent" Graphs in ν-Dimensional Space
Phys. Lett. **40B** (1972) 566

[Bou95] A. Bouniatian
Studies of Hard Scattering in Photoproduction at the ep Storage Ring HERA with the H1 Detector
Ph.D. Thesis, University of Hamburg, Hamburg, DESY FH1K-95-04 (1995)

[Bur80] A. Buras
Asymptotic Freedom in Deep Inelastic Processes in the Leading Order and Beyond
Rev. Mod. Phys. **52** (1980) 199

[But96] J. Butterworth, L. Feld, M. Klasen, G. Kramer
Matching Experimental and Theoretical Jet Definitions for Photoproduction at HERA
To be published in Proc. of the DESY Workshop on "Future Physics at HERA" (1996), hep-ph/9608481

[Byc73] E. Byckling, K. Kajantie
Particle Kinematics
John Wiley & Sons, London (1973)

[Cat91] S. Catani, Y.L. Dokshitzer, M. Olsson, G. Turnock, B.R. Webber
New Clustering Algorithm for Multi-Jet Cross-Sections in e^+e^- Annihilation
Phys. Lett. **B269** (1991) 432

[Che75] M.-S. Chen, P. Zerwas
Equivalent-Particle Approximations in Electron and Photon Processes of Higher-Order QED
Phys. Rev. **D12** (1975) 187

[Cic72] G. M. Cicuta, E. Montaldi
Analytic Renormalization Via Continuous Space Dimension
Lett. Nuovo Cim. **4** (1972) 329

[Com77] B.L. Combridge, J. Kripfganz, J. Ranft
Hadron Production at Large Transverse Momentum and QCD
Phys. Lett. **B70** (1977) 234

[Cur56] R.B. Curtis
Meson Production by Electrons
Phys. Rev. **104** (1956) 211

[Cur80] G. Curci, W. Furmanski, R. Petronzio
Evolution of Parton Densities Beyond Leading Order: The Nonsinglet Case
Nucl. Phys. **B175** (1980) 27

[Cut78] R. Cutler, D. Sivers
One Gluon Exchange Quark Scattering and Large p_T Inclusive data
Phys. Rev. **D17** (1978) 196

[Dal57] R.H. Dalitz, D.R. Yennie
Pion Production in Electron-Proton Collisions
Phys. Rev. **105** (1957) 1598

[Der92] M. Derrick et al., ZEUS Collaboration
Observation of Hard Scattering in Photoproduction at HERA
Phys. Lett. **B297** (1992) 404

[Der94] M. Derrick et al., ZEUS Collaboration
Observation of Direct Processes in Photoproduction at HERA
Phys. Lett. **B322** (1994) 287

[Der95] M. Derrick et al., ZEUS Collaboration
Inclusive Jet Differential Cross-Sections in Photoproduction at HERA
Phys. Lett. **B342** (1995) 417

[Der95a] M. Derrick et al., ZEUS Collaboration
Dijet Cross-Sections in Photoproduction at HERA
Phys. Lett. **B348** (1995) 665

[Der95b] M. Derrick et al., ZEUS Collaboration
Study of the Photon Remnant in Resolved Photoproduction at HERA
Phys. Lett. **B354** (1995) 163

[Der96] M. Derrick et al., ZEUS Collaboration
Dijet Angular Distributions in Direct and Resolved Photoproduction at HERA
DESY 96-094 (1996)

[Der96a] M. Derrick et al., ZEUS Collaboration
Dijet Cross Sections in Photoproduction at HERA
Talk given at XXVIII International Conference on High Energy Physics, Warsaw (1996)

[Dev84] A. Devoto, D.W. Duke
Table of Integrals and Formulae for Feynman Diagram Calculations
Riv. Nuov. Cim. **7/6** (1984) 1

[Dok77] Y. Dokshitzer
Calculation of the Structure Functions for Deep Inelastic Scattering and e^+e^- Annihilation by Perturbation Theory in Quantum Chromodynamics
Soviet. Phys. JETP **46** (1977) 641

[Ell78] R.K. Ellis, H. Georgi, M. Machacek, H.D. Politzer, G.G. Ross
Factorization and the Parton Model in QCD
Phys. Lett. **78B** (1978) 281

[Ell79] R.K. Ellis, H. Georgi, M. Machacek, H.D. Politzer, G.G. Ross
Perturbation Theory and the Parton Model in QCD
Nucl. Phys. **B152** (1979) 285

[Ell80] R.K. Ellis, M.A. Furman, H.E. Haber, I. Hinchcliffe
Large Corrections to High p_T Hadron-Hadron Scattering in QCD
Nucl. Phys. **B173** (1980) 397

[Ell81] R.K. Ellis, D.A. Ross, A.E. Terrano
The Perturbative Calculation of Jet Structure in e^+e^- Annihilation
Nucl. Phys. **B178** (1981) 421

[Ell83] R.K. Ellis, G. Martinelli, R. Petronzio
Lepton Pair Production at Large Transverse Momentum in Second Order QCD
Nucl. Phys. **B211** (1983) 106

[Ell86] R.K. Ellis, J.C. Sexton
QCD Radiative Corrections to Parton-Parton Scattering
Nucl. Phys. **B269** (1986) 445

[Ell89] S.D. Ellis, Z. Kunszt, D.E. Soper
One-Jet Inclusive Cross Section at Order α_s^3: Gluons Only
Phys. Rev. **D40** (1989) 2188

[Ell89a] S.D. Ellis, Z. Kunszt, D.E. Soper
The One Jet Inclusive Cross-Section at Order α_s^3: Gluons Only
Phys. Rev. Lett. **62** (1989) 726

[Ell93] S.D. Ellis, D.E. Soper
Successive Combination Jet Algorithm for Hadron Collisions
Phys. Rev. **D48** (1993) 3160

[Fab82] K. Fabricius, G. Kramer, G. Schierholz, I. Schmitt
Higher Order Perturbative QCD Calculation of Jet Cross Sections in e^+e^- Annihilation
Z. Phys. **C11** (1982) 315

[Fer24] E. Fermi
Über die Theorie des Stoßes zwischen Atomen und elektrisch geladenen Teilchen
Z. Phys. **29** (1924) 315

[Fey69] R.P. Feynman
Very High-Energy Collisions of Hadrons
Phys. Rev. Lett. **23** (1969) 1415

[Fie78] R.D. Field, R.P. Feynman
A Parametrization of the Properties of Quark Jets
Nucl. Phys. **B136** (1978) 1

[Fon96] M. Fontannaz
Private Communication

[For93] J.R. Forshaw, R.G. Roberts
Determining the Gluon Distributions in the Proton and Photon from Two Jet Production at HERA
Phys. Lett. **B319** (1993) 539

[Fri93] S. Frixione, M.L. Mangano, P. Nason, G. Ridolfi
Improving the Weizsäcker-Williams Approximation in Electron-Proton Collisions
Phys. Lett. **B319** (1993) 339

[Fur80] W. Furmanski, R. Petronzio
Singlet Parton Densities beyond Leading Order
Phys. Lett. **97B** (1980) 437

[Fur82] M.A. Furman
Study of a Nonleading QCD Correction to Hadron Calorimeter Reactions
Nucl. Phys. **B197** (1982) 413

[Glü84] M. Glück, K. Grassie, E. Reya
Detailed QCD Analysis of the Photon Structure Function
Phys. Rev. **D30** (1984) 1447

[Glü92] M. Glück, E. Reya, A. Vogt
Parton Structure of the Photon Beyond the Leading Order
Phys. Rev. **D45** (1992) 3986

[Glü95] M. Glück, E. Reya, A. Vogt
Dynamical Parton Distributions of the Proton and Small-x Physics
Z. Phys. **C67** (1995) 433

[Gor92] L.E. Gordon, J.K. Storrow
The Parton Distribution Functions of the Photon and the Structure Function $F_2^\gamma(x, Q^2)$
Z. Phys. **C56** (1992) 307

[Gor92a] L.E. Gordon, J.K. Storrow
The Single Jet Inclusive Cross-Section at HERA in Next-To-Leading Order QCD Phys. Lett. **B291** (1992) 320

[Gor96] L.E. Gordon, J.K. Storrow
New Parton Distribution Functions for the Photon
ANL-HEP-PR-96-33 (1996), hep-ph/9607370

[Got80] T. Gottschalk, D. Sivers
Basic Processes and Formalism for the Hadronic Production of Three Large p_T Jets
Phys. Rev. **D21** (1980) 102

[Gra90] D. Graudenz
Der Drei-Jet-Wirkungsquerschnitt zur Ordnung α_s^2 in der tief-inelastischen Elektron-Proton-Streuung
Ph.D. thesis, University of Hamburg, Hamburg, DESY T-90-01 (1990)

[Gri72] V.N. Gribov, L.N. Lipatov
Deep Inelastic ep Scattering in Perturbation Theory
Sov. J. Nucl. Phys. **15** (1972) 438

[Gri72a] V.N. Gribov, L.N. Lipatov
e^+e^- Pair Annihilation and Deep Inelastic ep Scattering in Perturbation Theory
Sov. J. Nucl. Phys. **15** (1972) 675

[Gro73] D.J. Gross, F. Wilczek
Ultraviolet Behavior of Non-Abelian Gauge Theories
Phys. Rev. Lett. **30** (1973) 1343

[Hea85] A.C. Hearn
REDUCE User's Manual, Version 3.2
Rand Publication CP78 (Rev. 4/85)

[Hoy79] P. Hoyer, P. Osland, H.G. Sander, T.F. Walsh, P.M. Zerwas
Quantum Chromodynamics and Jets in e^+e^-
Nucl. Phys. **B161** (1979) 349

[Hum81] B. Humpert, W.L. van Neerven
Infrared and Mass Regularization in AF Field Theories (I). Φ_6^3
Nucl. Phys. **B178** (1981) 498

[Hum81a] B. Humpert, W.L. van Neerven
Infrared and Mass Regularization in AF Field Theories (II). QCD
Nucl. Phys. **B184** (1981) 225

[Hum82] B. Humpert, W.L. van Neerven
Diagrammatic Mass Factorization
Phys. Rev. **D25** (1982) 2593

[Hut92] J.E. Huth et al.
Toward a Standardization of Jet Definitions
Proc. of the 1990 DPF Summer Study on High Energy Physics, Snowmass, Colorado, edited by E.L. Berger, World Scientific, Singapore (1992) 134

[Joo67] H. Joos
A Remark on the Photoproduction of Vector Mesons
Phys. Lett. **24B** (1967) 103

[Joo67a] H. Joos
Vector Mesons and the Electromagnetic Interactions of Hadrons
DESY 67/13 (1967)

[Kin62] T. Kinoshita
Mass Singularities of Feynman Amplitudes
J. Math. Phys. **3** (1962) 650

[Kla93] M. Klasen
Der Drei-Jet-Wirkungsquerschnitt zur Ordnung $\alpha\alpha_s^2$ in der Photoproduktion bei HERA-Energien
Diploma Thesis, University of Würzburg, Würzburg (1993)

[Kla95] M. Klasen, G. Kramer, S.G. Salesch
Photoproduction of Jets at HERA: Comparison of Next-To-Leading Order Calculation with ZEUS Data
Z. Phys. **C68** (1995) 113

[Kla95a] M. Klasen, G. Kramer
Inclusive Dijet Production at HERA: Direct Photon Cross Sections in Next-To-Leading Order QCD
DESY 95-226 (1995), to be published in Z. Phys. **C**

[Kla96] M. Klasen, G. Kramer
Dijet Cross Sections in Photon-Proton Collisions
Phys. Lett. **B366** (1996) 385

[Kle96] T. Kleinwort, G. Kramer
Inclusive Two Jet Cross-Sections in $\gamma\gamma$ Processes at e^+e^- Colliders
Phys. Lett. **B370** (1996) 141

[Kle96a] T. Kleinwort, G. Kramer
Inclusive One and Two Jet Cross-Sections in $\gamma\gamma$ Reactions at e^+e^- Colliders
DESY 96-035 (1996), to be published in Nucl. Phys. **B**

[Kle96b] T. Kleinwort
Inklusive 1- und 2-Jet Wirkungsquerschnitte in Photon-Photon Kollisionen in nächstführender Ordnung der QCD
Ph.D. thesis, University of Hamburg, Hamburg, DESY 96-195 (1996)

[Kra84] G. Kramer
Theory of Jets in Electron-Positron Annihilation
Springer Tracts in Mod. Phys., Vol. 102, Springer, Berlin (1984)

[Kra94] G. Kramer, S.G. Salesch
Single Jet Photoproduction at HERA in Next-To-Leading Order QCD
Z. Phys. **C61** (1994) 277

[Kra96] D. Krakauer, ZEUS Collaboration
http://www-zeus.desy.de/~krakauer/disp/96_list.html, 96_91GeV_FBcal_dijet.ps

[Kra96a] D. Krakauer, ZEUS Collaboration
http://www-zeus.desy.de/~krakauer/disp/96_list.html, 96_noblob_550.ps

[Kun80] Z. Kunszt, E. Pietarinen
Production of Three Large p_T Jets in Hadron-Hadron Collisions
Nucl. Phys. **B164** (1980) 45

[Kun92] Z. Kunszt, D.E. Soper
Calculation of Jet Cross Sections in Hadron Collisions at Order α_s^3
Phys. Rev. **D46** (1992) 192

[Lai95] H.L. Lai, J. Botts, J. Huston, J.G. Morin, J.F. Owens, J.W. Qiu, W.K. Tung, H. Weerts
Global QCD Analysis and the CTEQ Parton Distributions
Phys. Rev. **D51** (1995) 4763

[Lai96] H.L. Lai, J. Huston, S. Kuhlmann, F. Olness, J. Owens, D. Soper, W.K. Tung, H. Weerts
Improved Parton Distributions from Global Analysis of Recent Deep Inelastic Scattering and Inclusive Jet Data
MSUHEP-60426, CTEQ-604 (1996), hep-ph/9606399

[Lee64] T.D. Lee, M. Nauenberg
Degenerate Systems and Mass Singularities
Phys. Rev. **133B** (1964) 1549

[Lei75] G. Leibbrandt
Introduction to the Technique of Dimensional Regularization
Rev. Mod. Phys. **47** (1975) 849

[Lep78] G.P. Lepage
A New Algorithm for Adaptive Multidimensional Integration
J. Comp. Phys. **27** (1978) 192

[Lib79] S.B. Libby, G. Sterman
Cancellation of Infrared Divergences in Massive Quark Potential Scattering
Phys. Rev. **D19** (1979) 2468

[Mar75] W.J. Marciano, A. Sirlin
Dimensional Regularization of Infrared Divergences
Nucl. Phys. **B88** (1975) 86

[Mar92] G. Marchesini, B.R. Webber, G. Abbiendi, I.G. Knowles, M.H. Seymour, L. Stanco
HERWIG: A Monte Carlo Event Generator for Simulating Hadron Emission Reactions with Interfering Gluons. Version 5.1 - April 1991
Comp. Phys. Comm. **67** (1992) 465

[Mar94] A.D. Martin, W.J. Stirling, R.G. Roberts
Parton Distributions of the Proton
Phys. Rev. **D50** (1994) 6734

[Mar95] A.D. Martin, W.J. Stirling, R.G. Roberts
Pinning Down the Glue in the Proton
Phys. Lett. **B354** (1995) 155

[Mar96] A.D. Martin
The Partonic Structure of the Proton

Talk given at the 2nd Krakow Epiphany Conference on "Proton Structure", Krakow (1996), hep-ph/9605271

[Mar96a] A.D. Martin, R.G. Roberts, W.J. Stirling
Parton Distributions: A Study of the new HERA Data, α_s, the Gluon and $p\overline{p}$ Jet Production
DTP/96/44, RAL-TR-96-037 (1996), hep-ph/9606345

[Mue78] A.H. Mueller
Cut Vertices and their Renormalization: A Generalization of the Wilson Expansion
Phys. Rev. **D18** (1978) 3705

[Mue81] A.H. Mueller
Perturbative QCD at High Energies
Phys. Rep. **73** (1981) 237

[Nor37] A. Nordsieck
The Low Frequency Radiation of a Scattered Electron
Phys. Rev. **52** (1937) 59

[Oh96] B. Oh
Private Communication

[Owe78] J.F. Owens, E. Reya, M. Glück
Detailed Quantum Chromodynamic Predictions for High p_T Processes
Phys. Rev. **D18** (1978) 1501

[Owe80] J.F. Owens
Photoproduction of Large-Transverse Momentum Hadronic Jets
Phys. Rev. **D21** (1980) 54

[Par76] G. Parisi
Proc. 11th Rencontre de Moriond on Weak Interactions and Neutrino Physics, edited by J. Tran Thanh Van, Flaine (1976)

[Pau92] E. Paul
Hard Photoproduction of Multiparticle Hadronic Final States
DESY 92-026 (1992)

[Plo95] H. Plothow-Besch
The Parton Distribution Function Library
Int. J. Mod. Phys. **A10** (1995) 2901

[Pol73] H.D. Politzer
Reliable Perturbative Results for Strong Interactions?
Phys. Rev. Lett. **30** (1973) 1346

[Pol77] H.D. Politzer
QCD off the Lightcone and the Demise of the Transverse Momentum Cut-off
Phys. Lett. **70B** (1977) 430

[Pol77a] H.D. Politzer
Gluon Corrections to Drell-Yan Processes
Nucl. Phys. **B129** (1977) 301

[Sak60] J.J. Sakurai
Theory of Strong Interactions
Ann. Phys. **11** (1960) 1

[Sal93] S.G. Salesch
Photoproduktion von Jets bei HERA mit aufgelösten Photonen bis zur Ordnung $\mathcal{O}(\alpha\alpha_s^2)$
Ph.D. thesis, University of Hamburg, Hamburg, DESY 93-196 (1993)

[Sch95] G.A. Schuler, T. Sjöstrand
Low and High Mass Components of the Photon Distribution Functions
Z. Phys. **C68** (1995) 607

[Sey95] M.H. Seymour
Jets in QCD
Talk given at the 10^{th} topical workshop on proton-antiproton collider physics, Batavia, IL (1995), hep-ph/9506421

[Sjö96] T. Sjöstrand, J.K. Storrow, A. Vogt
Parton Distributions of Real and Virtual Photons
J. Phys. **G22** (1996) 893

[Ste77] G. Sterman, S. Weinberg
Jets from Quantum Chromodynamics
Phys. Rev. Lett. **39** (1977) 1436

[Ste81] P.M. Stevenson
Resolution of the Renormalization Scheme Ambiguity in Perturbative QCD
Phys. Lett. **100B** (1981) 61

[Ste81a] P.M. Stevenson
Optimized Perturbation Theory
Phys. Rev. **D23** (1981) 2916

[Ste96] M. Steenbock
Untersuchung des Energieflusses außerhalb von Jets in der Photon-Proton-Streuung bei HERA
Ph.D. thesis, University of Hamburg, Hamburg (1996)

[tHo72] G. t'Hooft, M. Veltman
Regularization and Renormalization of Gauge Fields
Nucl. Phys. **B44** (1972) 189

[tHo72a] G. t'Hooft
Unpublished remark. See, however:
Proc. Colloquium on Renormalization of Yang-Mills Fields and Applications to Particle Physics, edited by C.P. Korthals-Altes, Marseilles (1972)

[tHo73] G. t'Hooft
Dimensional Regularization and the Renormalization Group
Nucl. Phys. **B61** (1973) 455

[Wei34] C.F.v. Weizsäcker
Ausstrahlung bei Stößen sehr schneller Elektronen
Z. Phys. **88** (1934) 612

[Wil34] E.J. Williams
Nature of the High Energy Particles of Penetrating Radiation and Status of Ionization and Radiation Formulae
Phys. Rev. **45** (1934) 729

[Wil35] E.J. Williams
Correlation of Certain Collision Problems with Radiation Theory
Kgl. Danske Vidensk. Selskab. Mat.-fys. Medd. **XIII** (1935) N4

[Wit77] E. Witten
Anomalous Cross-Section for Photon-Photon Scattering in Gauge Theories
Nucl. Phys. **B120** (1977) 189

[Yen61] D.R. Yennie, S.C. Frautschi, H. Suura
The Infrared Divergence Phenomena and High-Energy Processes
Ann. Phys. **13** (1961) 379

List of Figures

1 Direct Photoproduction of Two Jets as Seen by the ZEUS Detector . . . 3
2 Resolved Photoproduction of Two Jets as Seen by the ZEUS Detector . . . 3
3 Electron-Proton Scattering with Single Photon Exchange . . . 6
4 Electron-Proton Scattering in the Parton Model . . . 9
5 Partonic Subprocesses Contributing to Deep Inelastic Scattering . . . 10
6 Experimental Constraints on the Gluon in Different Regions of x . . . 11
7 x Dependence of Different Parton Distributions in the Proton . . . 12
8 Generic Diagrams for Direct and Resolved Photoproduction . . . 13
9 Different Diagrams Contributing to the Photon Structure Function . . . 14
10 $\gamma^*\gamma$ Scattering in the Vector Meson Dominance Model . . . 14
11 Recent Data on the Photon Structure Function from TRISTAN and LEP . . . 16
12 x Dependence of Different u Quark Parametrizations in the Photon . . . 16
13 x Dependence of Different Gluon Parametrizations in the Photon . . . 17
14 Jet Cone Definition According to the Snowmass Convention . . . 19
15 Jet Cone Definition with an Additional Parameter R_{sep} . . . 20
16 Regions in x_a, x_b Accessible in the Photoproduction of Jets . . . 24
17 Center-of-Mass System for $2 \to 2$ Scattering . . . 28
18 Generic $2 \to 2$ Feynman Diagram for Direct Photoproduction . . . 29
19 Born Diagrams for Direct Photoproduction . . . 29
20 Generic $2 \to 2$ Feynman Diagrams for Resolved Photoproduction . . . 30
21 Born Diagrams for Resolved Photoproduction . . . 31
22 Virtual Diagrams for Direct Photoproduction . . . 35
23 Virtual Diagrams for Resolved Photoproduction . . . 37
24 Different Types of Singularities in Three-Body Diagrams . . . 40
25 Center-of-Mass System for $2 \to 3$ Scattering . . . 42
26 Generic $2 \to 3$ Feynman Diagrams for Direct Photoproduction . . . 44
27 Generic $2 \to 3$ Feynman Diagrams for Resolved Photoproduction . . . 47
28 y_{cut}-Independence for Direct Photoproduction . . . 74
29 y_{cut}-Independence for Resolved Photoproduction . . . 74
30 Comparison of E_T-Dependence with Bödeker for Direct Photons . . . 76
31 Comparison of E_T-Dependence with Salesch for Resolved Photons . . . 76
32 Comparison of η-Dependence with Bödeker for Direct Photons . . . 77
33 Comparison of η-Dependence with Salesch for Resolved Photons . . . 77
34 Renormalization Scale Dependence for Direct Photoproduction . . . 79
35 Renormalization Scale Dependence for Resolved Photoproduction . . . 79
36 Photon Factorization Scale Dependence for Direct and Complete Photoproduction . . . 81
37 Photon Factorization Scale Dependence for Resolved Photoproduction . . . 81
38 Proton Factorization Scale Dependence for Direct Photoproduction . . . 82
39 Proton Factorization Scale Dependence for Resolved Photoproduction . . . 83
40 Total Scale Dependence for Complete Photoproduction . . . 83
41 E_T-Dependence of Single-Jet Cross Section for Direct Photons . . . 85
42 E_T-Dependence of Single-Jet Cross Section for Resolved Photons . . . 85
43 η-Dependence of Single-Jet Cross Section for Direct Photons . . . 86
44 η-Dependence of Single-Jet Cross Section for Resolved Photons . . . 86
45 E_T-Dependence of Single-Jet Cross Section for Complete Photoproduction in LO . . . 88
46 E_T-Dependence of Single-Jet Cross Section for Complete Photoproduction in NLO . . . 88
47 η-Dependence of Single-Jet Cross Section for Complete Photoproduction in LO . . . 89
48 η-Dependence of Single-Jet Cross Section for Complete Photoproduction in NLO . . . 89
49 Jet Cone Size Dependence of Single-Jet Cross Section for Direct Photons . . . 90

50 Jet Cone Size Dependence of Single-Jet Cross Section for Resolved Photons 90
51 E_T-Dependence of Dijet Cross Section for Direct Photoproduction 92
52 E_T-Dependence of Dijet Cross Section for Resolved Photoproduction 92
53 Lego-Plot of Dijet Cross Section for Direct Photoproduction 93
54 Lego-Plot of Dijet Cross Section for Resolved Photoproduction 93
55 Rapidity Dependence of Dijet Cross Section for Direct Photoproduction 95
56 Rapidity Dependence of Dijet Cross Section for Resolved Photoproduction 95
57 E_T-Dependence of Dijet Cross Section for Complete Photoproduction in LO 96
58 E_T-Dependence of Dijet Cross Section for Complete Photoproduction in NLO 96
59 Rapidity Dependence of Dijet Cross Section for Complete Photoproduction in LO . . 97
60 Rapidity Dependence of Dijet Cross Section for Complete Photoproduction in NLO . 97
61 Comparison of E_T-Dependence in Single-Jet Cross Sections with H1 Data 99
62 Comparison of η-Dependence in Single-Jet Cross Sections with H1 Data 99
63 Comparison of E_T-Dependence in Single-Jet Cross Sections with ZEUS Data 100
64 Comparison of η-Dependence in Single-Jet Cross Sections with ZEUS Data 100
65 Comparison of $\overline{\eta}$-Dependence in Dijet Cross Sections with ZEUS Data at large x_γ^{OBS} . 102
66 Comparison of $\overline{\eta}$-Dependence in Dijet Cross Sections with ZEUS Data at small x_γ^{OBS} . 102

List of Tables

1 Overview of Phase Space Parametrizations and Matrix Elements 23
2 Squared $2 \to 2$ Matrix Elements for Direct Photoproduction 29
3 Squared $2 \to 2$ Matrix Elements for Resolved Photoproduction 31
4 Squared $2 \to 3$ Matrix Elements for Direct Photoproduction 44
5 Final State $2 \to 3$ Matrix Elements for Resolved Photoproduction 47
6 Initial State $2 \to 3$ Matrix Elements for Resolved Photoproduction 60
7 Cancellation of IR Singularities for Direct Photoproduction 68
8 Cancellation of IR Singularities for Resolved Photoproduction 69
9 Organization of the FORTRAN Program 71